

Jan Seebeck

Carrier-Phonon Interaction in Semiconductor Quantum Dots



Universität Bremen

Carrier-Phonon Interaction in Semiconductor Quantum Dots

**Dissertation
zur Erlangung des akademischen Grades**

**Doktor der Naturwissenschaften
(Dr. rer. nat)**

**am Fachbereich Physik/Elektrotechnik
der Universität Bremen**

vorgelegt von

**Dipl. Phys.
Jan Seebeck**

Vom Fachbereich Physik/Elektrotechnik der Universität Bremen
genehmigte Dissertation

Eingereicht am: 27. Januar 2009

Promotionskolloquium: 10. März 2009

1. Gutachter: Prof. Dr. F. Jahnke, Universität Bremen

2. Gutachter: Prof. Dr. H.C. Schneider, TU Kaiserslautern

weitere Prüfer: Prof. Dr. G. Czycholl, Universität Bremen

Prof. Dr. J. Falta, Universität Bremen

“Unless you test yourself, you stagnate. Unless you try to go way beyond what you’ve been able to do before, you won’t develop and grow. When you go for it 100%, when you don’t have the fear of ‘what if I fail’, that’s when you learn. That’s when you’re really living.”

(Mark Allen, triathlete)

Abstract

In recent years semiconductor quantum dots have been studied extensively due to their wide range of possible applications, predominantly for light sources. For successful applications, efficient carrier scattering processes as well as a detailed understanding of the optical properties are of central importance. The aims of this thesis are theoretical investigations of carrier scattering processes in InGaAs/GaAs quantum dots on a quantum-kinetic basis. A consistent treatment of quasi-particle renormalizations and carrier kinetics for non-equilibrium conditions is presented, using the framework of non-equilibrium Green's functions.

The focus of our investigations is the interaction of carriers with LO phonons. Important for the understanding of the scattering mechanism are the corresponding quasi-particle properties. Starting from a detailed study of quantum-dot polarons, scattering and dephasing processes are discussed for different temperature regimes. The inclusion of polaron and memory effects turns out to be essential for the description of the carrier kinetics in quantum-dot systems. They give rise to efficient scattering channels and the obtained results are in agreement with recent experiments. Furthermore, a consistent treatment of the carrier-LO-phonon and the carrier-carrier interaction is presented for the optical response of semiconductor quantum dots, both giving rise to equally important contributions to the dephasing.

Beside the conventional GaAs material system, currently GaN based light sources are of high topical interest due to their wide range of possible emission frequencies. In this material additionally intrinsic properties like piezoelectric fields and strong band-mixing effects have to be considered. For the description of the optical properties of InN/GaN quantum dots a procedure is presented, where the material properties obtained from an atomistic tight-binding approach are combined with a many-body theory for non-equilibrium conditions.

Contents

1 Prologue	1
<hr/>	
I Introduction	
2 Physics of semiconductor quantum dots	5
2.1 Structural properties	6
2.2 Application in laser structures	7
2.3 Goals of this thesis	10
<hr/>	
II Theory	
3 Many-body theory	15
3.1 Hamiltonian and many-body hierarchy	16
3.2 Non-equilibrium Green's functions	20
3.3 Kadanoff-Baym equations	27
3.4 Two-time formalism	29
3.5 Generalized Kadanoff-Baym ansatz	31
4 Many-body interactions	35
4.1 Coulomb interaction	35
4.2 Carrier-phonon interaction	42
4.3 Light-matter interaction	48
<hr/>	
III Application	
5 Carrier-phonon scattering	53
5.1 The polaron problem	54
5.2 The phonon-bottleneck controversy	69
5.3 The steady-state discussion	78
5.4 Theory-experiment comparison for the low-temperature regime	88

6 Optical experiments	97
6.1 Linear absorption and optical gain	98
6.2 Time-resolved photoluminescence	107
7 Nitride semiconductors	113
7.1 Envelope wave function model	115
7.2 Tight-binding wave-function model	120
7.3 Nitride polarons	131
7.4 Optical properties	136
8 Conclusion	145

IV Appendix

A Envelope wave function model and additional material	151
A.1 Envelope wave function model	151
A.2 RPA screening for inhomogeneous systems	154
A.3 Dipole matrix elements	156
B Parameters and numerics	161
B.1 Material parameters	161
B.2 Wurtzite crystal structure	162
B.3 KMS condition in the time domain	163
B.4 Lifting the Coulomb singularity	164
B.5 Numerical methods	164
Bibliography	165

1 Prologue

The term *nanotechnology* describes the possibility to design structures on a nanometer length scale, providing a wide range of possible applications for everyday life. Semiconductor-based nano-structured devices can be divided into three categories: electronics, spintronics, and photonics.

A prominent charge-transport device is the transistor and the pursuit for its miniaturization has not yet stopped. Nowadays transistor sizes of 45 nm can be realized [1], almost reaching the borderline where quantum-mechanical effects like the Coulomb blockade regime [2, 3] become important. Promising new concepts are investigated in current research, for example molecular-transport devices [4–6] and graphene sheets [7]. In spintronics additionally the electron spin is exploited to control the electric current. For example, applications of the giant-magneto-resistance effect [8, 9] include the read heads of nowadays computer harddisks and magnetic RAM devices [10].

Besides electronics and spintronics, the manipulation of the optical properties of nano-scale devices is of intense topical interest. Optically active nanocrystals made by chemical synthesis can be functionalized to monitor specific proteins, providing new insight into fundamental mechanisms of life-science and biotechnology [11]. Probably the key applications in the field of photonics are lasers and light emitting devices (LEDs). In information technology semiconductor lasers are well established for data storage and optical communication networks. The energy consumption for electrical illumination can be reduced using LEDs. For example, replacing recandescent lamps by LED could save 30 coal power plants in the US alone [12], corresponding to 8 power plants in Germany.

The key ingredient in the light emitters utilized for the applications discussed above is an active medium where the energy provided to the system is efficiently transformed into light. One approach to optimize the quantum efficiency of these devices is to increase the carrier confinement and use so-called quantum-dot structures, which are often regarded as artificial atoms due to their discrete energy spectrum. Using quantum dots as active medium one expects lower pump power and a better temperature stability. The central goal of this thesis is to gain more insight into the fundamental physical processes involved in quantum-dot structures to be able to make progress towards more efficient and reliable light emitting devices.

Part I

Introduction

2 Physics of semiconductor quantum dots

The broad interest of current research in nanostructures arises from their wide range of possible applications. Especially quantum dots (QDs) that exhibit a confinement of carriers in all three spacial dimensions are investigated due to their discrete energy spectrum. For the fabrication of QDs various experimental techniques are available [13]. Among them are approaches that provide the confinement potential by metallic gate electrodes [3], the chemical synthesis of nano-crystals [14], or epitaxial semiconductor structures [15, 16]. Each approach has advantages for particular applications. Single-electron transistors can be realized via gate electrodes [3], colloidal QDs can be functionalized as biological markers [11], and semiconductor QDs are best suited for integrated semiconductor devices [17].

For laser devices several advantages are expected from using an ensemble of QDs as optical gain medium. Among them are lower threshold powers, a better temperature stability, and the possibility to engineer the emission wave length to a large extend. To understand the optical properties of QDs, on the one hand experimental techniques have been developed for addressing single QDs. They allow for example to study the electronic fine structure [18], multi-exciton complexes [19, 20], and the coupling between two QDs [21, 22]. On the other hand, progress has also been made in fabricating microcavities to confine the light field. Various approaches to achieve high quality factors are presented [23–25], ranging from microdiscs, micropillars to photonic crystals. By placing single QD emitters into a microcavity the spontaneous emission from QDs can be controlled by exploiting the Purcell effect [26]. This enables the fabrication of single-photon sources, which are of high topical interest due to their potential application in quantum cryptography. The interaction of single emitters with the cavity modes is currently subject of intense research in the field of cavity QED [23].

Laser devices and single-photon sources can be considered as key applications for semiconductor QDs. Of particular importance for these applications are scattering processes and many-body effects in QDs due to the carrier-carrier and the carrier-phonon interaction, which are studied in this thesis. The following chapter is intended to introduce the properties of QDs and the physics involved in laser devices in more detail. Starting from the structural properties of QDs and their electronic properties, the light-matter interaction with the cavity modes and important carrier-scattering processes are discussed.

2.1 Structural properties

In semiconductor systems a confinement of the free carrier motion can be achieved by embedding a low band-gap material into a high band-gap material. For optoelectronic devices predominantly the InGaAs/GaAs material system is used, as the bandgap can be engineered to match the transmission wave length of glass fibers. Depending on the geometry of the embedded nanostructure, a carrier confinement in one to three spatial dimension can be obtained. The corresponding nanostructures are denoted as quantum wells (QW), quantum wires and quantum dots (QD), as schematically depicted in Fig. 2.1.

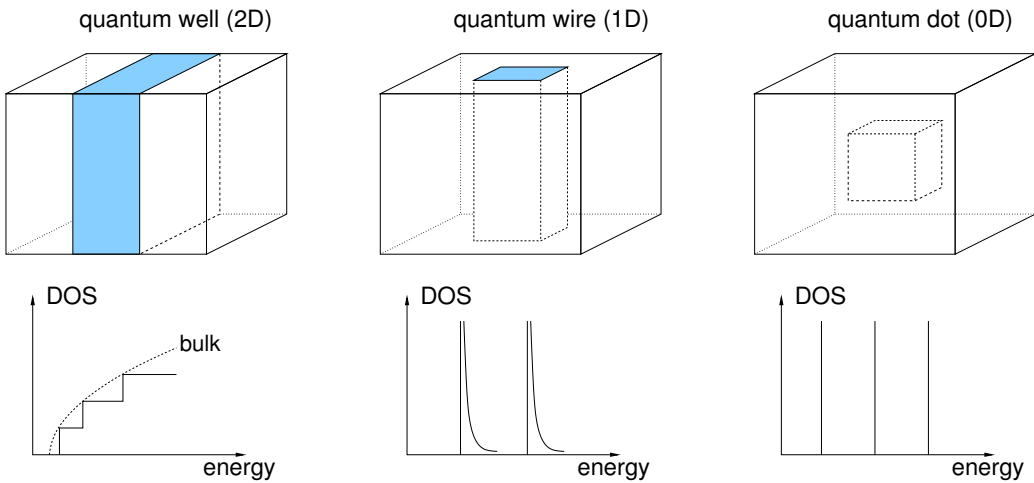


Fig. 2.1: Illustration of semiconductor nanostructures with reduced dimensionality and the corresponding density of states for free particles.

The motivation for the carrier confinement is an enhancement of the density of states (DOS). For non-interacting carriers the DOS is also given in Fig. 2.1. The advantage of QW structures over bulk semiconductors is clearly indicated by the larger DOS at the band edge. A further enhancement of the DOS can be obtained by using QDs. They exhibit a δ -like density of states and are therefore often referred to as artificial atoms. One particular advantage of QDs for practical applications is that their energy spectrum can be engineered according to particular needs. As can be seen easily from a simple particle-in-a-box model, the energy spectrum of a QD strongly depends on the system size. Therefore semiconductor QDs are favorable candidates for applications in light-emitting devices.

In this thesis we consider self-assembled semiconductor QDs fabricated in the Stranski-Krastanov growth mode [15, 16] using molecular beam epitaxy or metal-organic vapor-phase epitaxy. The self-assembled QDs form by growing a material *A* compressively strained upon a substrate of material *B*. At some critical thickness the strain energy due to the lattice mismatch relaxes by redistribution of atoms and island formation [15, 16]. A characteristic feature of this type of QDs is a residual wetting layer (WL) of material *A*, as

shown in Fig. 2.2a. Depending on the material composition and on growth parameters like temperature and material flux, a variety of different QD geometries can be fabricated [16]. For the InGaAs/GaAs material system we consider flat lens-shaped QDs which typically exhibit a diameter of 10-30 nm and an height-to-diameter aspect ratio of 0.3-0.4. The random distribution of QDs on the WL plane typically amounts to a density of the order of 10^{10} - 10^{11} cm $^{-2}$.

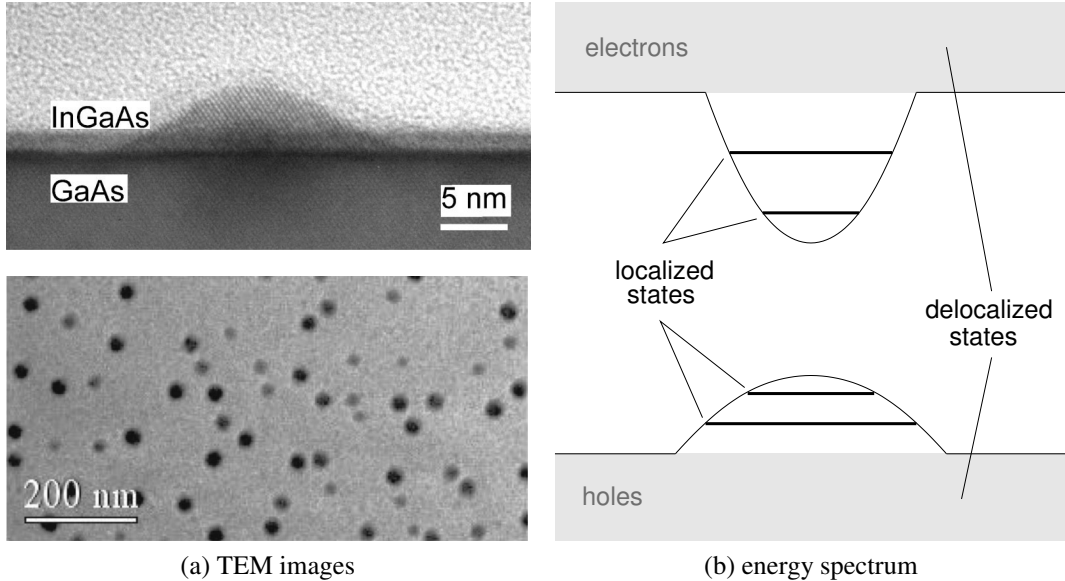


Fig. 2.2: Cross-section and bright-field TEM image (a) and schematic energy spectrum (b) of self-assembled InGaAs/GaAs QDs. TEM images taken from Ref. [27] (Reprinted with permission. Copyright 2002, American Physical Society.).

2.2 Application in laser structures

In this thesis we consider light-emitting devices as key application for semiconductor QDs, especially laser structures where QDs act as active medium. These devices show a complicated interplay of various physical mechanisms. On the one hand, the geometry and the material used to build a laser structure determine the electronic structure for free particles as well as the optical modes of the cavity. On the other hand, excitation induced effects and vibrations of the underlying crystal structure give rise to carrier-scattering processes and many-body renormalizations. In the following the interplay of these properties will be discussed in more detail.

From the geometry of self-assembled semiconductor QDs, consisting of a WL with islands on top as shown in Fig. 2.2a, the free energy spectrum can already be understood qualita-

tively. The WL provides a confinement of carriers in growth direction and a free carrier motion perpendicular to the growth direction, similar to a quantum well. At the position of the islands the height of the low-band-gap material increases, lowering the ground state energy, and therefore giving rise to an additional in-plane confinement potential. Thus, the energy spectrum contains localized (3D confined) QD states that are located energetically below a quasi continuum of 2D WL states. This is schematically shown in Fig. 2.2b. As demonstrated by Wojs et al. [28], the in-plane-confinement potential resulting from a flat, lens-shaped QD geometry is in good approximation parabolic. For the corresponding wave functions one might introduce an envelope-function approach and additionally separate the envelope into growth-direction and growth-plane part. In this case the Schrödinger equation for the part in growth direction reduces to the 1D quantum-well problem. Furthermore, the in-plane part for the bound states can be described by 2D harmonic-oscillator states which are known from literature [29]. A more detailed discussion of this model is given in App. A.1.

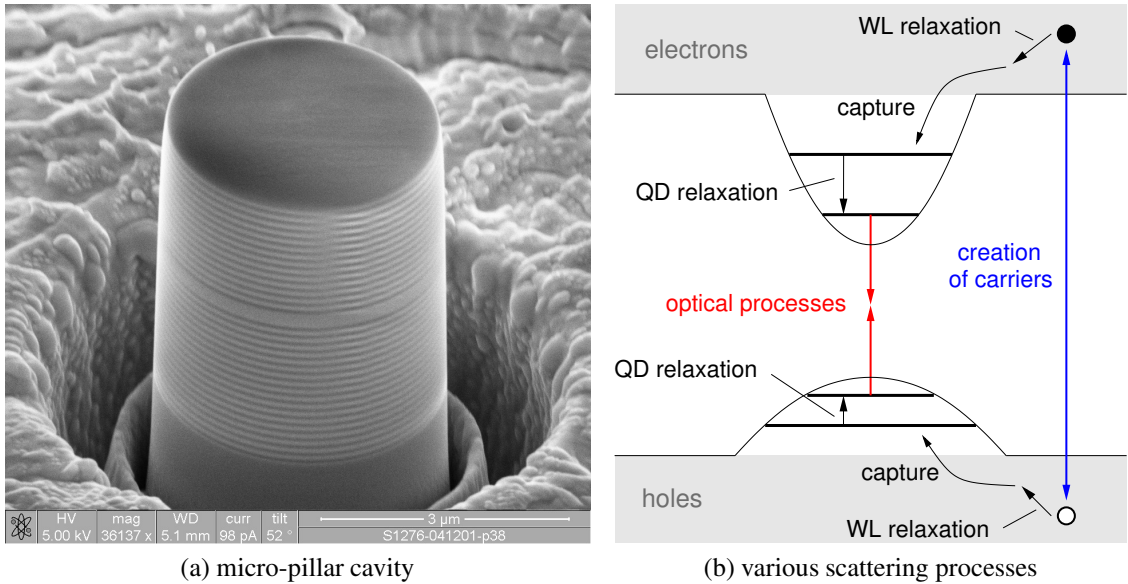


Fig. 2.3: SEM image of a semiconductor micro-pillar cavity (a) and schematic summary of carrier scattering processes in self-assembled QDs (b). SEM picture courtesy of H. Lohmeyer and Prof. J. Gutowski, University of Bremen.

Beside the GaAs material system nitride-based nanostructures are currently of high topical interest. Their wide band gap allows for laser structures with possible emission frequencies ranging from the amber to the UV. In contrast to the InGaAs/GaAs material system, the underlying wurtzite crystal structure of nitride semiconductors demands for a more accurate calculation of the electronic structure. For example the inclusion of strong band-mixing effects and intrinsic electrostatic fields is of central importance. Appropriate methods are

continuum approaches like $\mathbf{k} \cdot \mathbf{p}$ calculations [30, 31] or atomistic approaches like tight-binding calculations [32, 33]. An introduction to the tight-binding approach is given in Chap. 7.2.

Besides the active medium, an important component of a semiconductor laser is the cavity, as it provides the confinement of the light field and the optical feedback for stimulated emission. Two different types of semiconductor lasers need to be distinguished. In conventional edge-emitting laser diodes, the feedback for the laser mode is provided by a cavity which is formed by the cleaved end faces of the device. The cavity of these devices shows a low reflectivity due to the jump of the refractive index from the semiconductor material to air, which results in a short cavity lifetime and requires a large gain of the active material to compensate for the losses. Another approach that provides a much better light confinement is used for so-called vertical-cavity surface-emitting laser (VCSEL) structures, where the cavity is realized as a spacer layer between a top and a bottom distributed Bragg reflector (DBR). As an example, a micropillar structure is shown in Fig. 2.3a. Bragg mirrors consist of layers with alternating refractive index which results in constructive interference for particular wave lengths, depending on the layer thickness. In analogy to the electronic band structure a photonic bandgap appears, the so-called stop-band. A spacer layer between top and bottom DBR acts as a defect in the photonic bandstructure, leading to light confinement. Thus, a microcavity can be realized where the optical mode is restricted to a very small volume. Placing QDs inside the spacer layer of such cavities gives rise to a very efficient light-matter coupling [23]. For example the spontaneous emission rate into the cavity mode can be increased beyond its value for emission into free space. The increase itself grows with a larger quality factor of the cavity or a smaller mode volume. This is known as the Purcell effect. An effective feedback of the cavity requires a spectral overlap of the optical transition energies in the active medium with the cavity mode. At this point the complex interplay of light-matter interaction and carrier scattering becomes obvious.

To successfully use QDs as light emitters requires efficient scattering channels that lead to a population of the QD ground state for recombination processes. On the other hand fast carrier scattering also leads to a dephasing of optical coherences, resulting in renormalizations of the optical response of the QDs. These renormalizations are important for laser devices due to the required spectral overlap of the laser transition with the cavity mode as outlined above. A summary of scattering processes that occur in QDs is schematically shown in Fig. 2.3b. The carrier generation at energetically higher states is followed by capture and relaxation processes towards the energetically lowest states. Experimental insight into carrier scattering processes is obtained by ultra-fast optical pump-probe spectroscopy, ranging from absorption measurements to advanced two-color pump-probe and four-wave-mixing experiments [34]. The dominant mechanisms for carrier redistribution and dephasing are carrier-carrier and carrier-phonon collisions. Their relative strength depends on the temperature and the carrier density. In carrier-carrier collisions two particles are involved and energy can be transferred from one scattering partner to the other one. For carrier-phonon collisions the transferred energy depends on the phonon mode.

As an example, the phonon bandstructure for bulk GaAs is depicted in Fig. 2.4. Around the Γ point, the acoustic modes depend linearly on the phonon momentum. In contrast, the optical modes show a rather flat dispersion and from their DOS we can infer that they provide an efficient mechanism for energy dissipation. For embedded nanostructures also surface modes and confined modes are present [35–37]. At low densities the QDs represent a small perturbation in the crystal structure of the surrounding matrix. Therefore, one expects the restriction to bulk phonon modes to be a good approximation. Moreover, the discrete energy spectrum of confined phonon modes leads qualitatively to similar results as the interaction with dispersionless LO phonons.

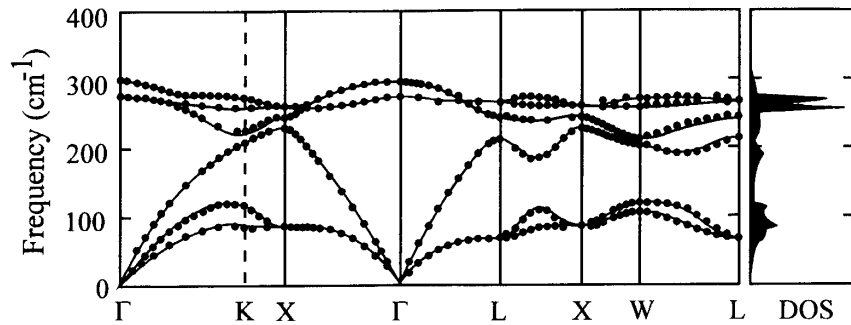


Fig. 2.4: Phonon bandstructure for GaAs and the corresponding density of states. Image taken from Ref. [38] (Reprinted with permission. Copyright 1991, American Physical Society.).

2.3 Goals of this thesis

As outlined above, carrier scattering and dephasing of optical coherences strongly influence the emission properties of QD-based laser devices. The dominant scattering channels arise from carrier-carrier and carrier-phonon collisions. Especially the contribution from the interaction of confined carriers with LO phonons is of particular interest. For bulk semiconductors it has been shown that the LO phonons provide efficient relaxation channels [39]. In self-assembled QD structures that exhibit a discrete component in their energy spectrum, interesting new physical questions arise. Prohibited carrier scattering was predicted on the ground of perturbation theory due to the mismatch between the free-carrier transition energies and the LO-phonon energy. This is also known as the phonon-bottleneck effect. Experimental results that are presented in the literature are controversial [40–43] and a lively debate in favor and against the bottleneck interpretation is taking place. In this thesis we investigate the carrier-phonon interaction in QD systems in more detail.

Especially the quasi-particle renormalizations due to interactions and their influence on the carrier scattering are discussed.

Besides carrier scattering, the dephasing of optical coherences plays an important role for laser applications. In the low-temperature regime the interaction with LA phonons dominates the dephasing, but at elevated temperatures also LO phonons significantly contribute [44–46]. Therefore also in this case the influence of quasi-particle renormalizations due to the carrier-phonon interaction is of interest. Moreover, for the high carrier densities that are present in a laser device also carrier-carrier collisions have to be considered. A consistent treatment of both interactions is presented and optical absorption spectra are studied to compare the contributions from the carrier-carrier and the carrier-LO-phonon interaction.

For practical applications currently the wide bandgap GaN material system is intensively studied. In comparison to GaAs, this material shows specific properties like the wurtzite crystal structure, intrinsic electrostatic fields, and strong band-mixing effects. Beside many-body effects, they also influence the optical response [47–49]. In this case the combination of material properties and quasi-particle renormalizations is of interest. An approach is presented where this combined influence on the optical absorption is studied, starting from an atomistic tight-binding calculation.

For the theoretical investigation we chose the framework of non-equilibrium Green's functions, which allows a microscopic description of the temporal evolution of carriers for non-equilibrium situations. After a general introduction in Chap. 3.2, the treatment of the interaction mechanisms is discussed in Chap. 4. The main advantage of non-equilibrium Green's functions is the consistent treatment of quasi-particle renormalizations and carrier kinetics. First, the quasi-particle renormalization for the carrier-LO-phonon interaction, the so-called polaron, is discussed in Chap. 5.1. In a second step scattering processes including polaron effects as well as their long-time behavior for the room- and the low temperature regime are studied in Chap. 5.2–5.3. Our theoretical findings can also be observed experimentally, and in Chap. 5.4 a theory-experiment comparison is presented. In contrast to carrier scattering, Chap. 6 focuses on optical experiments. The influence of carrier-carrier scattering and polaron effects on the dephasing of optical coherences is investigated in Chap. 6.1 and optical absorption spectra are presented. Also time-dependent photoluminescence spectra are discussed in Chap. 6.2. Finally, we present in Chap. 7 a method to include the nitride-specific material properties in a many-body theory. Here we start from an atomistic tight-binding model for the single-particle states and calculate polaron properties, as well as linear optical absorption spectra including the influence of Coulomb effects and carrier-phonon scattering.

Part II

Theory

3 Many-body theory

A semiconductor crystal typically consists of 10^{23} atoms per cm^3 . This large amount of lattice atoms and electrons interacting with each other prevents a direct solution of the full Schrödinger equation. Instead, a statistical framework is necessary to describe properties of the interacting many-particle system on a quantum mechanical basis. In quantum statistics, physical observables are represented by the expectation value of Hermitian operators. They are calculated as the ensemble average of identical systems where in general the full statistical operator has to be known. Its direct calculation could be done only for a few heuristic systems like ideal quantum gases. However, it turns out that the explicit knowledge of the full statistical operator is not necessary when applying quantum field theoretical methods.

In the following the quantum statistical description of a semiconductor is presented. Different methods are discussed but the main focus is on non-equilibrium Green's functions (NGF). This method enables us to handle arbitrary non-equilibrium conditions which in general are present when performing for example optical experiments. The application of Green's functions to quantum field theory was first developed by Feynman [50, 51, 52] formulating quantum electrodynamics. Further progress was made in developing quantum chromodynamics in the field of elementary-particle physics. Within this context the extension to non-equilibrium conditions was introduced by Keldysh [53], Baym and Kadanoff [54]. In its non-relativistic version, the NGF method was also applied to semiconductor physics and electrical [55, 56], optical [57, 58], and transport [6, 59, 60] properties have been described successfully.

In the following, first the Hamiltonian and the physical observables which are important to describe an optically excited semiconductor are introduced. Prior to a detailed introduction of the NGF technique and its diagrammatic representation, alternative approaches to describe many-body systems are discussed. The final equations of motion that are obtained from the NGF approach are the Kadanoff-Baym equations. Solution strategies for their two-time version as well as the reduction to one-time equations by the help of the generalized Kadanoff-Baym ansatz are presented. Finally the carrier-carrier and the carrier-LO-phonon interaction as well as the construction of self-energies is discussed.

3.1 Hamiltonian and many-body hierarchy

The starting point for the description of a semiconductor is the Hamiltonian

$$\hat{H} = \hat{T}_e + \hat{T}_i + \hat{H}_{e-e} + \hat{H}_{i-i} + \hat{H}_{e-i}, \quad (3.1)$$

which includes the kinetic contributions \hat{T} of the electrons and ions as well as the bare Coulomb interaction \hat{H}_{e-e} , \hat{H}_{i-i} and \hat{H}_{e-i} among them. This Hamiltonian describes chemical bonds, the preferred crystal structure, electronic and vibrational properties as well as excitation effects. Since the treatment of the many-body interaction on the ab-initio level is not feasible, some simplifying assumptions are made.

We assume that the equilibrium positions \mathbf{R}_0 of the ions and the corresponding crystal structure are known. Furthermore, the electron-ion and the ion-ion interaction are each mapped onto an effective single-particle potential $V_{e-i}(\mathbf{r}-\mathbf{R})$ and $V_{i-i}(\mathbf{R}-\mathbf{R}')$, respectively. Here \mathbf{R} denotes the position of the ions and \mathbf{r} that of the electrons. The properties of the solid with the ions being in their equilibrium position defines the semiconductor ground state. In the following this ground state is assumed to be known and electronic excitations as well as corrections due to lattice distortions $\mathbf{Q} = \mathbf{R} - \mathbf{R}_0$ are treated explicitly by many-body methods.

The free carrier motion together with the lattice-periodic equilibrium contribution $V_{e-i}(\mathbf{r} - \mathbf{R}_0)$ of the electron-ion interaction potential usually is included in the Hamiltonian $\hat{H}_e(\mathbf{r})$ which describes the bandstructure. Corrections to the equilibrium contribution due to lattice distortions \mathbf{Q} are treated as perturbation in terms of the electron-phonon interaction $\hat{H}_{e-ph}(\mathbf{Q}, \mathbf{r})$. Within the Born-Oppenheimer approximation the kinetic energy of the ions together with an expansion of the interaction potential $V_{i-i}(\mathbf{R} - \mathbf{R}')$ up to second order (harmonic approximation) yields the vibrational properties $\hat{H}_{ph}(\mathbf{Q})$ of the solid [61, 62]. One obtains a set of uncoupled harmonic oscillators that describe phonons. Higher order terms in the expansion represent anharmonic corrections and give rise effects like the thermal expansion of the solid and the phonon-phonon interaction, which is not considered here. Using these approximations, the Hamiltonian (3.1) is replaced by

$$\hat{H} = \left[\hat{H}_e(\mathbf{r}) + \hat{H}_{ph}(\mathbf{Q}) + \hat{H}_{e-ph}(\mathbf{Q}, \mathbf{r}) \right] + \hat{H}_{e-e}(\mathbf{r}), \quad (3.2)$$

where the term in brackets is a so-called Fröhlich-type Hamiltonian. In second quantization

the single components read

$$\hat{H}_e = \sum_1 \epsilon_1 \hat{a}_1^\dagger \hat{a}_1 , \quad (3.3)$$

$$\hat{H}_{ph} = \sum_{\mathbf{q}, \xi} \hbar \omega_\xi(\mathbf{q}) \left(\hat{b}_{\mathbf{q}, \xi}^\dagger \hat{b}_{\mathbf{q}, \xi} + \frac{1}{2} \right) , \quad (3.4)$$

$$\hat{H}_{e-ph} = \sum_{1,2} \sum_{\mathbf{q}, \xi} M_{12}^\xi(\mathbf{q}) \left(\hat{b}_{\mathbf{q}, \xi} + \hat{b}_{-\mathbf{q}, \xi}^\dagger \right) \hat{a}_1^\dagger \hat{a}_2 , \quad (3.5)$$

$$\hat{H}_{e-e} = \frac{1}{2} \sum_{1234} V_{1234} \hat{a}_1^\dagger \hat{a}_2^\dagger \hat{a}_3 \hat{a}_4 , \quad (3.6)$$

where the electron operators are expanded into an eigenfunction basis $|1\rangle$ and the phonon operators are expanded into plane waves $|\mathbf{q}\rangle$. The creation and annihilation operators for electrons and phonons are denoted as $\hat{a}_1^{(\dagger)}$ and $\hat{b}_{\mathbf{q}, \xi}^{(\dagger)}$, respectively. In this short-hand notation the electron states are described by the index $1 \in \{\alpha, \lambda, s\}$ which contains the state index α , the band index λ , and the spin s . As eigenfunctions $|1\rangle$ the non-interacting single-particle wave-functions discussed in Chap. A.1 will be used in later chapters, but for the following discussion no explicit basis is necessary. Correspondingly, phonons are described by the wave-vector \mathbf{q} and the phonon mode ξ .

In the Coulomb interaction matrix-elements V_{1234} only the interaction among carriers is considered. The interaction with the rigid lattice is included in the band-structure ϵ_1 and the contribution due to lattice displacements gives rise to the carrier-phonon interaction $M_{12}^\xi(\mathbf{q})$. In addition to the Hamiltonian (3.2) of the solid, the dipole interaction

$$\hat{H}_D = \sum_{1,2} \sum_{\mathbf{q}} \mathbf{d}_{12}(\mathbf{q}) \mathbf{E}_q \hat{a}_1^\dagger \hat{a}_2 \quad (3.7)$$

is considered with \mathbf{E}_q being a classical light field and $\mathbf{d}_{12}(\mathbf{q})$ denoting the corresponding dipole coupling. A detailed discussion of all interaction matrix-elements is given below in Chap. 4.

In quantum mechanics, physical observables are calculated by tracing the corresponding Hermitian operator \hat{A} with the statistical operator $\hat{\rho}$,

$$\langle \hat{A} \rangle = \text{Tr}(\hat{\rho} \hat{A}) . \quad (3.8)$$

Interesting physical observables in semiconductor physics are the carrier density n and the macroscopic polarization \mathbf{P} ,

$$n = \sum_1 \langle \hat{a}_1^\dagger \hat{a}_1 \rangle , \quad (3.9)$$

$$\mathbf{P}_q = \sum_{1 \neq 2} \mathbf{d}_{12}(\mathbf{q}) \langle \hat{a}_1^\dagger \hat{a}_2 \rangle . \quad (3.10)$$

For these observables the knowledge of the reduced single particle density matrix $\rho_{12} = \langle \hat{a}_1^\dagger \hat{a}_2 \rangle$ is sufficient. Restricting to contributions that are diagonal in the state index, the reduced single particle density matrix contains, with respect to its band indices, population functions on its diagonal and transition amplitudes on its off-diagonal. This is easily seen for a two-band semiconductor model containing conduction band c and valence band v ,

$$\rho_{\alpha\alpha} = \begin{pmatrix} \langle \hat{c}_\alpha^\dagger \hat{c}_\alpha \rangle & \langle \hat{v}_\alpha^\dagger \hat{c}_\alpha \rangle \\ \langle \hat{c}_\alpha^\dagger \hat{v}_\alpha \rangle & \langle \hat{v}_\alpha^\dagger \hat{v}_\alpha \rangle \end{pmatrix} = \begin{pmatrix} f_\alpha^c & \psi_\alpha \\ \psi_\alpha^* & f_\alpha^v \end{pmatrix}. \quad (3.11)$$

Also higher order correlation functions that are not represented by the single-particle density matrix might be of interest, for example the probability of the process $\langle \hat{a}_\beta^\dagger \hat{a}_\alpha \hat{b}_q^\dagger \rangle$ where the emission of a phonon is correlated to the transition of an electron from state α to state β . The explicit calculation of such many-particle correlations is not considered in the following.

The temporal evolution of the reduced density matrix is obtained by applying the chain rule, using the equation of motion for the creation and annihilation operators according to Heisenberg's equation of motion

$$i\hbar \frac{d}{dt} \hat{a}^{(\dagger)} = [\hat{a}^{(\dagger)}, \hat{H}], \quad (3.12)$$

and considering the anti-commutation relations

$$[\hat{a}_1, \hat{a}_2^\dagger]_+ = \delta_{1,2}, \quad (3.13)$$

$$[\hat{a}_1^{(\dagger)}, \hat{a}_2^{(\dagger)}]_+ = 0 \quad (3.14)$$

for fermions. This leads to the so-called many-body hierarchy problem. Due to the Coulomb interaction, two-operator expectation values couple to four-operator expectation values which couple to six-operator expectation values and so on. Similarly the carrier-phonon interaction couples two-operator expectation values to three-operator expectation values which couple to four- and five-operator expectation values and so on. If both, carrier-carrier and carrier-phonon interaction, are considered also mixing occurs. In principle, this hierarchy has to be considered up to infinite order. To deal with the many-body hierarchy, several approximate truncation schemes have been developed.

The simplest way of truncating the hierarchy at a certain order N is based on Wick's theorem [63], which states that an expectation value with an even number N of operators can be decomposed into the sum of all possible combinations of two-operator expectation values¹. On the four-operator level this corresponds to a Hartree-Fock like factorization [62, 64]

$$\langle \hat{a}_1^\dagger \hat{a}_2^\dagger \hat{a}_3 \hat{a}_4 \rangle = \langle \hat{a}_1^\dagger \hat{a}_4 \rangle \langle \hat{a}_2^\dagger \hat{a}_3 \rangle - \langle \hat{a}_1^\dagger \hat{a}_3 \rangle \langle \hat{a}_2^\dagger \hat{a}_4 \rangle. \quad (3.15)$$

¹Note, that the ordering of operators remains and that each permutation required for the contraction yields a change of sign according to the commutation relations.

The factorization at a certain order is somewhat arbitrary as all contributions from higher orders are neglected. A more consistent approach is the cluster expansion technique introduced by Fricke [65, 66], where N -particle expectation values $\langle N \rangle$ are expanded into a factorized part and correlations $\langle \dots \rangle^c$. On the four-particle level this corresponds to

$$\langle 1 \rangle = \langle 1 \rangle^c \quad (3.16a)$$

$$\langle 2 \rangle = \langle 1 \rangle \langle 1 \rangle + \langle 2 \rangle^c \quad (3.16b)$$

$$\langle 3 \rangle = \langle 1 \rangle \langle 1 \rangle \langle 1 \rangle + \langle 1 \rangle \langle 2 \rangle^c + \langle 3 \rangle^c \quad (3.16c)$$

$$\langle 4 \rangle = \langle 1 \rangle \langle 1 \rangle \langle 1 \rangle \langle 1 \rangle + \langle 1 \rangle \langle 1 \rangle \langle 2 \rangle^c + \langle 1 \rangle \langle 3 \rangle^c + \langle 4 \rangle^c . \quad (3.16d)$$

The equations of motion for the correlations are derived successively using Heisenberg's equation of motion. Alternatively, also a diagram technique is presented in Refs. [65, 66]. Within this approach the hierarchy of correlations is truncated rather than the hierarchy of expectation values. Hence, in contrast to a truncation that simply neglects higher order correlations, the cluster expansion consistently includes all collision terms as well as energy renormalizations from higher correlation functions up to N -particle order. Correspondingly, this approach might be interpreted as an N -particle theory that includes all N -particle processes. Carrier-phonon scattering [66] and light-matter interaction processes like photoluminescence [67, 68] have been described successfully using this method. For example photoluminescence involves recombination processes of two carriers, one electron and one hole, by whose annihilation a photon is emitted. Thus, one expects the restriction to few-particle correlations to be a good approximation.

Another physical argument for truncating the many-body hierarchy is found in semiconductor optics. Here, effects are usually classified according to the contributing order N of the optical light field. So-called $\chi^{(N)}$ regimes are introduced. For this situation, Axt and Stahl [69, 70] developed the dynamics-controlled truncation scheme (DCT) which consistently takes into account all coherent correlations up to the N -th order in the optical field. This scheme was successfully applied to describe for example the coherent dynamics in four-wave-mixing experiments [71, 72]. However, this approach is limited to coherent excitations. The consistent inclusion of incoherent effects like carrier scattering is difficult.

Truncation schemes are useful if the system under consideration provides a limiting parameter like the order of the optical field or the number of particles involved. The disadvantage is that the cutoff of the many-body hierarchy introduces artifacts in the sense that energy renormalizations and dephasing are not included for the highest order of the correlations that are taken into account. They are provided by even higher correlations. If many-particle processes are important, like in case of dressing an electron by the interaction with phonons, a more powerful approach is necessary. Therefore, in the following the technique of non-equilibrium Green's functions is presented. In this approach one restricts to a certain class of interaction processes by choosing a selfenergy. Due to the iterative structure of the Dyson equation, which is derived in the following, interaction processes are included up to infinite order. Within this framework the complex interplay of many-body renormal-

izations and carrier kinetics can be studied systematically. Furthermore, for example the DCT equations and their extension beyond the coherent regime can be formulated using GFs [71, 73, 74].

3.2 Non-equilibrium Green's functions

The theory of non-equilibrium Green's functions is based on the idea of deriving a closed set of equations for the two-point correlation function $\langle \hat{\Psi}(2) \hat{\Psi}^\dagger(1) \rangle$ which represents the probability of adding a particle in state $1 = \{r_1, t_1, s_1\}$ prior to removing one in state 2. Physically, this correlation function describes the propagation of a particle and therefore it is called propagator. Similarly a hole propagator $\langle \hat{\Psi}^\dagger(2) \hat{\Psi}(1) \rangle$ can be defined, representing a generalization of the single-particle density matrix.

In this chapter, the theory of NGF is outlined in a rather compact fashion. More detailed reviews on non-equilibrium Green's functions can be found for example in Refs. [61, 75–77].

Quantum statistics

For the discussion, a Hamiltonian of the form

$$\hat{H} = [\hat{H}_0 + \hat{H}_{\text{int}}] + \hat{H}_{\text{ext}}(t), \quad (3.17)$$

is considered, including a non-interacting part \hat{H}_0 an interacting part \hat{H}_{int} and an explicitly time dependent perturbation $\hat{H}_{\text{ext}}(t)$. Note, that the Hamiltonian (3.2) is of this form, with $\hat{H}_{\text{ext}}(t)$ specified below.

The expectation value of an arbitrary operator in the Schrödinger picture is given by

$$\langle \hat{A} \rangle = \langle \Phi_S(t) | \hat{A}_S | \Phi_S(t) \rangle. \quad (3.18)$$

After transformation into the Dirac picture one has

$$|\Phi_S(t)\rangle = S(t, t_0) |\Phi_0(t_0)\rangle, \quad (3.19)$$

$$\hat{A}_D(t) = U^\dagger(t, t_0) \hat{A}_S U(t, t_0). \quad (3.20)$$

The temporal evolution of the states is determined by the external perturbation and that of the operators given by the free and the interacting part of the Hamiltonian according to

$$S(t, t_0) = T e^{-\frac{i}{\hbar} \int_{t_0}^t dt' \hat{H}_{\text{ext}}(t')}, \quad (3.21)$$

$$U(t, t_0) = e^{-\frac{i}{\hbar} [\hat{H}_0 + \hat{H}_{\text{int}}](t-t_0)}. \quad (3.22)$$

The operator T ensures chronological ordering of all operators from right to left. Now, Eq. (3.18) can be cast into

$$\langle \hat{A} \rangle = \langle \Phi_0 | S(-\infty, \infty) T \left\{ S(\infty, -\infty) \hat{A}_D(t) \right\} | \Phi_0 \rangle , \quad (3.23)$$

when considering the semi-group property $S(t_1, t_2) = S(t_1, t_3) S(t_3, t_2)$ of the time evolution operator and choosing $t_0 = -\infty$ for the initial time. One finds the right part ordered chronologically and the left part ordered anti-chronologically. To apply quantum field theoretical methods like Feynman's diagram rules [50, 51], a uniform time ordering is required. This could be achieved by introducing the so-called Keldysh time contour \mathcal{C} and the corresponding Keldysh time \underline{t} . On this contour the operators are, with respect to the real time, chronologically ordered on the upper branch t_+ and anti-chronologically ordered on the lower branch t_- . This is schematically depicted in Fig. 3.1.

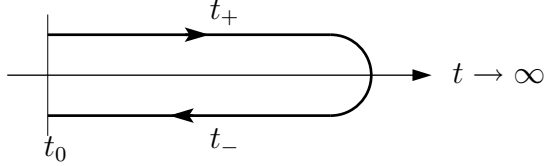


Fig. 3.1: Keldysh time contour \mathcal{C} for the temporal evolution from the initial time $t = t_0$ to $t = \infty$ and back. With respect to the real time, the upper branch t_+ is ordered chronologically while the lower branch t_- is ordered anti-chronologically.

By introducing the Keldysh contour one artificially distinguishes between an external perturbation on the upper branch $\hat{H}_{\text{ext}}(t_+)$ and a perturbation on the lower branch $\hat{H}_{\text{ext}}(t_-)$. Defining the contour-ordered expectation value as

$$\langle \hat{A}(\underline{t}) \rangle_{\mathcal{C}} = \frac{\text{Tr} \left\{ \rho_D T_{\mathcal{C}} \left[S_{\mathcal{C}} \hat{A}_D(\underline{t}) \right] \right\}}{\text{Tr} \{ \rho_D S_{\mathcal{C}} \}} , \quad (3.24)$$

the original expectation value (3.23) is recovered in the physical limit $\hat{H}_{\text{ext}}(t_+) = \hat{H}_{\text{ext}}(t_-)$. The corresponding contour-ordered time-evolution operator contains the forward evolution S_+ on the upper branch and the backward evolution S_- on the lower branch,

$$S_{\mathcal{C}} = S_+ S_- = T_{\mathcal{C}} \exp \left(-\frac{i}{\hbar} \int_{\mathcal{C}} d\underline{\tau} \hat{H}_{\text{ext}}(\underline{\tau}) \right) , \quad (3.25)$$

which in the physical limit reduces to $S_{\mathcal{C}} = 1$.

Carrier Green's function

For the calculation of single particle expectation values it is sufficient to know the single-particle Green's function

$$G(\underline{1}, \underline{2}) = -\frac{i}{\hbar} n_2 \frac{\text{Tr} \left\{ \rho_0 T_C [S_C \hat{\Psi}(\underline{2}) \hat{\Psi}^\dagger(\underline{1})] \right\}}{\text{Tr} \{ \rho_0 S_C \}}. \quad (3.26)$$

Here, the argument $\underline{1}$ includes the branch index $n_1 \in \{+1, -1\}$ of the Keldysh time, where $+1$ denotes the upper branch and -1 the lower one. With respect to the branch index, the Keldysh GF has the matrix structure

$$G(\underline{1}, \underline{2}) = \begin{pmatrix} G(1_+, 2_+) & G(1_+, 2_-) \\ G(1_-, 2_+) & G(1_-, 2_-) \end{pmatrix}. \quad (3.27)$$

The diagonal elements are the chronologically and the anti-chronologically ordered GFs, whereas the non-diagonal elements are given by the propagators:

$$G(1_+, 2_+) = -\frac{i}{\hbar} \langle T[\hat{\Psi}(1_+) \hat{\Psi}^\dagger(2_+)] \rangle = G(1, 2), \quad (3.28)$$

$$G(1_-, 2_-) = -\frac{i}{\hbar} \langle \tilde{T}[\hat{\Psi}(1_-) \hat{\Psi}^\dagger(2_-)] \rangle = \tilde{G}(1, 2), \quad (3.29)$$

$$G(1_+, 2_-) = \frac{i}{\hbar} \langle \hat{\Psi}^\dagger(2_-) \hat{\Psi}(1_+) \rangle = -G^<(1, 2), \quad (3.30)$$

$$G(1_-, 2_+) = -\frac{i}{\hbar} \langle \hat{\Psi}(1_-) \hat{\Psi}^\dagger(2_+) \rangle = G^>(1, 2). \quad (3.31)$$

From a linear combination of the propagators the retarded and advanced GF are defined,

$$G^R(1, 2) = \Theta(t_1 - t_2) [G^>(1, 2) - G^<(1, 2)], \quad (3.32)$$

$$G^A(1, 2) = -\Theta(t_2 - t_1) [G^>(1, 2) - G^<(1, 2)]. \quad (3.33)$$

Since also the (anti-)chronologically ordered GF can be expressed in terms of propagators according to

$$G(1, 2) = \Theta(t_1 - t_2) G^>(1, 2) + \Theta(t_2 - t_1) G^<(1, 2), \quad (3.34)$$

$$\tilde{G}(1, 2) = \Theta(t_2 - t_1) G^>(1, 2) + \Theta(t_1 - t_2) G^<(1, 2), \quad (3.35)$$

only two elements of the Keldysh matrix are independent. Frequently used properties of these GFs are:

$$[G^{\geqslant}(1, 2)]^\dagger = -G^{\geqslant}(2, 1), \quad (3.36)$$

$$[G^R(1, 2)]^\dagger = G^A(2, 1). \quad (3.37)$$

Schwinger functional derivative technique and Dyson equation

To obtain a set of equations for a perturbation expansion of the contour-ordered GF, the functional derivative technique introduced by Schwinger is employed [61, 77]. Alternatively a unitary transformation might be used, which enables to use Wick's theorem and to derive Dyson's equation as in equilibrium theory [78, 79].

For the following derivation the Hamiltonian

$$\hat{H} = \hat{H}_{\text{ph}} + \hat{H}_0 + \hat{H}_{\text{e-e}} + \hat{H}_{\text{e-i}} \quad (3.38)$$

is considered. The single components in real-space representation and second quantization read

$$\hat{H}_0 = \int d\underline{x}_1 \hat{\Psi}^\dagger(\underline{1}) h(\underline{1}) \hat{\Psi}(\underline{1}), \quad (3.39)$$

$$\hat{H}_{\text{e-e}} = \frac{1}{2} \int d\underline{x}_1 \int d\underline{x}_2 \hat{\Psi}^\dagger(\underline{1}) \hat{\Psi}^\dagger(\underline{2}) V(\underline{1}, \underline{2}) \hat{\Psi}(\underline{2}) \hat{\Psi}(\underline{1}), \quad (3.40)$$

$$\hat{H}_{\text{e-i}} = \int d\underline{x}_1 V_{\text{e-i}}(\underline{1}) \hat{\Psi}^\dagger(\underline{1}) \hat{\Psi}(\underline{1}) \quad (3.41)$$

with $\underline{x} \in \{\mathbf{r}, s\}$, $\int d\underline{x} = \sum_s \int d^3r$ and

$$h(\underline{1}) = -\frac{\hbar^2}{2m} \nabla^2 + \mathbf{dE}(\mathbf{r}_1, \underline{t}_1), \quad (3.42)$$

$$V(\underline{1}, \underline{2}) = \frac{e^2}{4\pi\varepsilon_0} \frac{1}{|\mathbf{r}_1 - \mathbf{r}_2|} \delta(\underline{t}_1 - \underline{t}_2), \quad (3.43)$$

$$V_{\text{e-i}}(\underline{1}) = -\frac{Ze^2}{4\pi\varepsilon_0} \int d\mathbf{R} \frac{\hat{N}_0(\mathbf{R}) + \Delta\hat{N}(\mathbf{R})}{|\mathbf{r}_1 - \mathbf{R}|}. \quad (3.44)$$

Note, that in the Hamiltonian all particles are considered explicitly and hence no background screening is included in the interaction potentials. According to the Born-Oppenheimer approximation the ions are decoupled from the electrons. The kinetic part and the ion-ion interaction are summarized in the phonon Hamiltonian \hat{H}_{ph} which in harmonic approximation is given by Eq. 3.4. The phonon Hamiltonian describes the equilibrium positions of the ions, which can be determined from the minima of the Born-Oppenheimer energy surface (cf. Refs. [62, 80]). However, their explicit values are not necessary for the following discussion.

The ion density $\hat{N} = \hat{N}_0 + \Delta\hat{N}$ entering the electron-ion interaction potential $V_{\text{e-i}}$ is split into an equilibrium part \hat{N}_0 and a fluctuation part $\Delta\hat{N}$. As $V_{\text{e-i}}$ represents an effective single-particle potential for the electrons, the equilibrium part describes the lattice-periodic potential which enters the band structure. The fluctuation part gives rise to the carrier-phonon interaction. As external perturbation we consider the Hamiltonian

$$\hat{H}_{\text{ext}} = \int d^3r \left\{ \left[\hat{n}(\mathbf{r}) - \hat{N}(\mathbf{r}) \right] U_{\text{ext}}(\mathbf{r}, t) + \hat{N}(\mathbf{r}) J_{\text{ext}}(\mathbf{r}, t) \right\} \quad (3.45)$$

which includes the coupling of the total carrier density to an electrostatic potential $U_{\text{ext}}(\mathbf{r}, t) = e \phi_{\text{ext}}(\mathbf{r}, t)$ as well as an external source $J_{\text{ext}}(\mathbf{r}, t)$ that can be interpreted as a mechanical force acting only on the ionic lattice. Here, the electron density operator is denoted as $\hat{n}(\underline{1}) = \hat{\Psi}^\dagger(\underline{1})\hat{\Psi}(\underline{1})$ and the total charge density is given by $e\hat{\rho}$ with $\hat{\rho} = \hat{n} - \hat{N}$.

The time dependence of the creation and annihilation operators for carriers is found using Heisenberg's equation of motion. Applying the chain rule, the equation of motion for the Keldysh GF (3.26) with respect to the first time is then given by

$$i\hbar \frac{\partial}{\partial t_1} G(\underline{1}, \underline{2}) = \delta(\underline{1} - \underline{2}) + [h(\underline{1}) - U_{\text{ext}}(\underline{1})] G(\underline{1}, \underline{2}) - i\hbar \int d\underline{3} n_3 V(\underline{1}, \underline{3}) \left\langle (\hat{n}(\underline{3}) - \hat{N}(\underline{3})) \hat{\psi}(\underline{1}) \hat{\psi}^\dagger(\underline{2}) \right\rangle, \quad (3.46)$$

where a four-point correlation function appears which in addition to the two-particle carrier GF also contains a term involving the ion density. Analogous, the equation of motion with respect to the second time can be obtained. At this point, the many-body hierarchy problem is explicitly present. The basic idea to deal with the many-body hierarchy is to consider the response of the system to the external perturbation U_{ext} by means of applying Schwinger's functional derivative technique. In terms of response theory, the GF is considered as a functional $G[U_{\text{ext}}(t)]$ whose derivative with respect to the external perturbation is given by

$$\frac{\delta G(\underline{1}, \underline{2})}{\delta U_{\text{ext}}(\underline{3})} = - \left\langle (\hat{n}(\underline{3}) - \hat{N}(\underline{3})) \hat{\psi}(\underline{1}) \hat{\psi}^\dagger(\underline{2}) \right\rangle + G(\underline{1}, \underline{2}) \left\langle \hat{n}(\underline{3}) - \hat{N}(\underline{3}) \right\rangle. \quad (3.47)$$

Here, the GF itself acts as a generating functional for higher order correlation functions. The second term on the right-hand side of Eq. (3.47) can be identified as a Hartree interaction which is lumped into an effective potential

$$U_{\text{eff}}(\underline{1}) = U_{\text{ext}}(\underline{1}) - i\hbar n_1 \int d\underline{3} V(\underline{1}, \underline{3}) \left\langle \hat{n}(\underline{3}) - \hat{N}(\underline{3}) \right\rangle. \quad (3.48)$$

Via the functional derivative the selfenergy is defined as

$$i\hbar \int d\underline{3} n_3 V(\underline{1}, \underline{3}) \frac{\delta G(\underline{1}, \underline{2})}{\delta U_{\text{ext}}(\underline{3})} \equiv \int d\underline{3} \Sigma(\underline{1}, \underline{3}) G(\underline{3}, \underline{2}). \quad (3.49)$$

Using this definition of the selfenergy, the structure of a Dyson equation equation

$$\left[i\hbar \frac{\partial}{\partial t_1} - h(\underline{1}) - U_{\text{eff}}(\underline{1}) \right] G(\underline{1}, \underline{2}) - \int d\underline{3} \Sigma(\underline{1}, \underline{3}) G(\underline{3}, \underline{2}) = \delta(\underline{1}, \underline{2}) \quad (3.50)$$

is obtained from the equation of motion (3.46). In the non-interacting case, i.e. $\Sigma(\underline{1}, \underline{2}) = 0$, the free inverse GF

$$G_0^{-1}(\underline{1}, \underline{2}) = \left[i\hbar \frac{\partial}{\partial t_1} - h(\underline{1}) - U_{\text{eff}}(\underline{1}) \right] \delta(\underline{1}, \underline{2}) \quad (3.51)$$

can be identified. Successive application of the functional derivative then yields a fundamental set of equations where the hierarchy problem is eliminated formally. In the following this somewhat lengthy calculation is skipped and only the basic steps are outlined. Details are presented for example in Refs. [61, 80]. Using the definition $\int d\mathbf{3} G(1, 3) G^{-1}(3, 2) = \delta(1 - 2)$ of the inverse GF we may write

$$\frac{\delta G(\underline{1}, \underline{2})}{\delta U_{\text{ext}}(\underline{3})} = \iiint d\underline{4} d\underline{5} d\underline{6} G(\underline{1}, \underline{4}) \frac{\delta G^{-1}(\underline{4}, \underline{5})}{\delta U_{\text{eff}}(\underline{6})} \frac{\delta U_{\text{eff}}(\underline{6})}{\delta U_{\text{ext}}(\underline{3})} G(\underline{5}, \underline{2}). \quad (3.52)$$

The expression Eq. (3.49) for the selfenergy together with the definition of the vertex function

$$\Gamma(\underline{1}, \underline{2}, \underline{3}) = \frac{\delta G^{-1}(\underline{1}, \underline{2})}{\delta U_{\text{eff}}(\underline{3})} \quad (3.53)$$

and the dielectric function

$$\varepsilon^{-1}(\underline{1}, \underline{2}) = \frac{\delta U_{\text{eff}}(\underline{1})}{\delta U_{\text{ext}}(\underline{2})} = \delta(\underline{1} - \underline{2}) + \int d\underline{3} V(\underline{1}, \underline{3}) \frac{\delta \langle \hat{n}(\underline{3}) - \hat{N}(\underline{3}) \rangle}{\delta U_{\text{ext}}(\underline{2})} \quad (3.54)$$

yields the final expression (3.59d) for the selfenergy. Note, that the screening of the bare Coulomb interaction contains an electronic and an ionic contribution. Evaluating the dielectric function further, we find

$$\begin{aligned} \varepsilon^{-1}(\underline{1}, \underline{2}) &= \delta(\underline{1} - \underline{2}) + \iint d\underline{4} d\underline{5} \varepsilon^{-1}(\underline{5}, \underline{3}) P(\underline{4}, \underline{5}) V(\underline{4}, \underline{1}) \\ &\quad - \int d\underline{4} \frac{\delta \langle \hat{N}(\underline{4}) \rangle}{\delta U_{\text{ext}}(\underline{2})} V(\underline{4}, \underline{1}), \end{aligned} \quad (3.55)$$

where the electronic polarization function

$$P(\underline{1}, \underline{2}) = -i\hbar n_1 \frac{\delta \langle \hat{n}(\underline{1}) \rangle}{\delta U_{\text{eff}}(\underline{2})} \quad (3.56)$$

is introduced. The evaluation of the functional derivative of the ion density yields

$$-\frac{\delta \langle \hat{N}(\underline{2}) \rangle}{\delta U_{\text{ext}}(\underline{1})} = \frac{\delta \langle \hat{\rho}(\underline{1}) \rangle}{\delta J_{\text{ext}}(\underline{2})} = D(\underline{1}, \underline{2}) + \iint d\underline{3} d\underline{4} P(\underline{1}, \underline{3}) V(\underline{3}, \underline{4}) \frac{\delta \langle \hat{\rho}(\underline{4}) \rangle}{\delta J_{\text{ext}}(\underline{2})}, \quad (3.57)$$

which contains the ion density-density correlation function

$$i\hbar D(\underline{1}, \underline{2}) = \langle \Delta \hat{N}(\underline{1}) \Delta \hat{N}(\underline{2}) \rangle. \quad (3.58)$$

Solving Eq. (3.57) for $\frac{\delta \hat{\rho}}{\delta J}$ and inserting into Eq. (3.55) yields the interaction given by Eq. 3.59c, containing the usual screened Coulomb interaction (3.59b) and a carrier-phonon contribution.

3 Many-body theory

In summary, the following fundamental set of equations is found, whose diagrammatic representation is depicted in Fig. 3.2:

Dyson equation

$$G(\underline{1}, \underline{2}) = G_0(\underline{1}, \underline{2}) + \iint d\underline{3} d\underline{4} G_0(\underline{1}, \underline{3}) \Sigma(\underline{3}, \underline{4}) G(\underline{4}, \underline{2}), \quad (3.59a)$$

$$W_e(\underline{1}, \underline{2}) = V(\underline{1}, \underline{2}) + \iint d\underline{3} d\underline{4} V(\underline{1}, \underline{3}) P(\underline{3}, \underline{4}) W_e(\underline{4}, \underline{2}); \quad (3.59b)$$

Screened interaction

$$W(\underline{1}, \underline{2}) = W_e(\underline{1}, \underline{2}) + \iint d\underline{3} d\underline{4} W_e(\underline{1}, \underline{3}) D(\underline{3}, \underline{4}) W_e(\underline{4}, \underline{2}); \quad (3.59c)$$

Selfenergy and polarization function

$$\Sigma(\underline{1}, \underline{2}) = -i\hbar n_1 \iint d\underline{3} d\underline{4} G(\underline{1}, \underline{3}) \Gamma(\underline{3}, \underline{2}, \underline{4}) W(\underline{4}, \underline{1}), \quad (3.59d)$$

$$P(\underline{1}, \underline{2}) = i\hbar n_1 \iint d\underline{3} d\underline{4} G(\underline{1}, \underline{3}) \Gamma(\underline{3}, \underline{4}, \underline{2}) G(\underline{4}, \underline{1}); \quad (3.59e)$$

Vertex function

$$\begin{aligned} \Gamma(\underline{1}, \underline{2}, \underline{3}) &= -\delta(\underline{1}, \underline{2}) \delta(\underline{1}, \underline{3}) \\ &\quad + \iiint d\underline{4} d\underline{5} d\underline{6} d\underline{7} \frac{\delta \Sigma(\underline{1}, \underline{2})}{\delta G(\underline{4}, \underline{5})} G(\underline{4}, \underline{6}) \Gamma(\underline{6}, \underline{7}, \underline{3}) G(\underline{7}, \underline{5}). \end{aligned} \quad (3.59f)$$

In case of $D(\underline{1}, \underline{2}) = 0$, corresponding to a rigid lattice, the equations reduce to the purely electronic part. The influence of a lattice displacements enters the theory via the ion density-density correlation function $D(\underline{1}, \underline{2})$ which is a N -body quantity as it depends on the actual position of all ions. Note, that so far no equation for this correlation function is given. Its evaluation in general can only be done approximately [80]. Considering the Fröhlich Hamiltonian, the evaluation of the correlation function $D(\underline{1}, \underline{2})$ is shown in Chap. 4.2, giving rise to so-called phonon interaction lines. Furthermore, even though the vertex function Γ is formally the same as in the purely electronic case, additional contributions are included. The selfenergy (3.59d') contains the full interaction W . Therefore, the functional derivative $\frac{\delta \Sigma}{\delta G}$ also introduces mixed diagrams that include Coulomb and phonon interaction lines, in addition to diagrams with only one type of interaction line.

$$\underline{1} \xrightarrow{\text{---}} \underline{2} = \underline{1} \xrightarrow{\text{---}} \underline{2} + \underline{1} \xrightarrow{\text{---}} \begin{matrix} 3 \\ \Sigma \end{matrix} \xrightarrow{\text{---}} \underline{2} \quad (3.59\text{a}')$$

$$\underline{1} \xrightarrow{\text{wavy}} \underline{2} = \underline{1} \xrightarrow{\text{wavy}} \underline{2} + \underline{1} \xrightarrow{\text{---}} \begin{matrix} 3 \\ P \end{matrix} \xrightarrow{\text{wavy}} \underline{2} \quad (3.59\text{b}')$$

$$\underline{1} \xrightarrow{\text{wavy}} \underline{2} = \underline{1} \xrightarrow{\text{wavy}} \underline{2} + \underline{1} \xrightarrow{\text{---}} \begin{matrix} 3 \\ D \end{matrix} \xrightarrow{\text{wavy}} \underline{2} \quad (3.59\text{c}')$$

$$\underline{1} \circledcirc \underline{2} = \underline{1} \xrightarrow{\text{---}} \begin{matrix} 4 \\ \text{---} \\ 3 \end{matrix} \underline{2} \quad (3.59\text{d}')$$

$$\underline{1} \boxed{P} \underline{2} = \underline{1} \xleftarrow{\text{---}} \begin{matrix} 3 \\ \Gamma \\ 4 \end{matrix} \underline{2} \quad (3.59\text{e}')$$

$$\begin{matrix} 1 \\ \Delta \\ 2 \end{matrix} = - \frac{1}{2} = \begin{matrix} \bullet \\ \underline{2} \end{matrix} = \begin{matrix} 3 \\ \Delta \end{matrix} + \begin{matrix} 1 & 4 & 6 \\ \boxed{\frac{\delta \Sigma}{\delta G}} & \xrightarrow{\text{---}} & \Gamma \\ 2 & 5 & 7 \end{matrix} \quad (3.59\text{f}')$$

Fig. 3.2: Diagrammatic representation of the fundamental set of equations.

3.3 Kadanoff-Baym equations

The Keldysh contour was introduced to ensure the time ordering of operators, which allowed to derive the fundamental set of equations (3.59). In this chapter the Keldysh contour is unfolded. From the Dyson equation for the Keldysh GF the so-called Kadanoff-Baym equations are obtained with the help of the Langreth-Wilkins theorems [79]. They are the starting point for further calculations.

As shown in Chap. 3.2, the Keldysh matrix (3.27) contains only two independent elements. In the following the lesser and the retarded GF are used. This is motivated by the fact that the time-diagonal lesser GF $G^<$ corresponds to the single particle density matrix and the retarded GF G^R represents to the quasi-particle spectrum (see Chap. 5.1). Both properties are connected, which is properly included in the Keldysh matrix.

Langreth-Wilkins theorems

For the derivation we consider the matrix product

$$X(\underline{1}, \underline{2}) = \int d\underline{3} \ A(\underline{1}, \underline{3}) \ B(\underline{3}, \underline{2}) . \quad (3.60)$$

and split the time integration along the Keldysh contour \mathcal{C} into two separate integrations along the upper and the lower branch,

$$\int_{\mathcal{C}} d\underline{t} = \int_{-\infty}^{+\infty} dt_+ - \int_{-\infty}^{+\infty} dt_- . \quad (3.61)$$

The components of the Keldysh GF are chosen by fixing the outer contour indices. Following this procedure and considering the definitions of retarded and advanced GF given by Eqs. (3.32)–(3.33) we find the relations

$$(AB)^{\geqslant} = A^R B^{\geqslant} + A^{\geqslant} B^A , \quad (3.62a)$$

$$(AB)^{R,A} = A^{R,A} B^{R,A} . \quad (3.62b)$$

Additionally one has to keep in mind that the greater/lesser components vanish for those quantities which are instantaneous on the Keldysh contour. By definition the two branch indices of these components are different and we have

$$[A^\delta(\underline{1}, \underline{2})]^{\geqslant} = A^\delta(1_\mp, 2_\pm) \delta_{\mp, \pm} \delta(t_1 - t_2) = 0 . \quad (3.63)$$

The argument given for a single integration along the time contour can be extended easily to multiple integrations.

Kadanoff-Baym equations

The Kadanoff-Baym equations (KBE) are obtained from the Dyson equation (3.59) together with the Langreth-Wilkins theorems. From the Dyson equation with respect to the time derivative of the first and the second argument we find:

1st Kadanoff-Baym equations

$$\int d\underline{3} [G_0^{-1}(1, 3) - \Sigma^R(1, 3)] G^R(3, 2) = \delta(1, 2) , \quad (3.64a)$$

$$\int d\underline{3} \left\{ [G_0^{-1}(1, 3) - \Sigma^R(1, 3)] G^<(3, 2) - \Sigma^<(1, 3) G^A(3, 2) \right\} = 0 ; \quad (3.64b)$$

2nd Kadanoff-Baym equations

$$\int d3 G^A(1,3) [G_0^{-1}(3,2) - \Sigma^A(3,2)] = \delta(1,2), \quad (3.65a)$$

$$\int d3 G^<(1,3) \left\{ [G_0^{-1}(3,2) - \Sigma^A(3,2)] - G^R(1,3) \Sigma^<(3,2) \right\} = 0. \quad (3.65b)$$

These equations are given in matrix notation and both sets are connected by Hermitian conjugation. Therefore, the time derivative in Eq. (3.64), contained in G_0^{-1} , has to be understood as acting to the left. The KBE form a coupled set of integro-differential equations that are non-local in space and time. Furthermore, the coupling of quasi-particle properties (G^R) and quasi-particle kinetics ($G^<$), which is intrinsically included in the Keldysh matrix, is found explicitly in the KBE.

3.4 Two-time formalism

Provided the initial conditions are known, the KBE (3.64)–(3.65) describe the propagation of the system anywhere in the two-time plane. Since the time diagonal of the lesser GF corresponds to the single-particle density matrix it is favorable to parametrize the evolution in the two-time plane into an evolution along and away from the time diagonal according to $G(t_1, t_2) = G(t, t - \tau)$ with

$$t = t_1, \quad \frac{\partial}{\partial t} = \frac{\partial}{\partial t_1} + \frac{\partial}{\partial t_2}, \quad (3.66)$$

$$\tau = t_1 - t_2, \quad \frac{\partial}{\partial \tau} = -\frac{\partial}{\partial t_2}. \quad (3.67)$$

Within this parametrization the evolution away from the time diagonal is given by the 2nd KBE whereas the evolution along the time diagonal is given by the sum of 1st and 2nd KBE. For the evolution parallel to the time diagonal we obtain

$$i\hbar \frac{\partial}{\partial t} G^{<,R}(t, t - \tau) = \Sigma^\delta(t) G^{<,R}(t, t - \tau) - G^{<,R}(t, t - \tau) \Sigma^\delta(t - \tau) \\ + i\hbar \frac{\partial}{\partial t} G^{<,R}(t, t - \tau) \Big|_{\text{coll}} \quad (3.68)$$

with the 2-time collision terms

$$i\hbar \frac{\partial}{\partial t} G^R(t, t - \tau) \Big|_{\text{coll}} = \int_{t-\tau}^t dt' [\Sigma^R(t, t') G^R(t', t - \tau) - G^R(t, t') \Sigma^R(t', t - \tau)] , \quad (3.69)$$

$$\begin{aligned} i\hbar \frac{\partial}{\partial t} G^<(t, t - \tau) \Big|_{\text{coll}} &= \int_{-\infty}^t dt' [\Sigma^R(t, t') G^<(t', t - \tau) + \Sigma^<(t, t') G^A(t', t - \tau) \\ &\quad - G^R(t, t') \Sigma^<(t', t - \tau) - G^<(t, t') \Sigma^A(t', t - \tau)] . \end{aligned} \quad (3.70)$$

For simplicity only the time arguments are written explicitly. With respect to other indices the equations are to be understood in matrix notation. For any point $(t, t - \tau)$ in the two-time plane, the time derivative of G has the structure of a matrix product $\Sigma \cdot G$ or $G \cdot \Sigma$. Correspondingly, the time integration involves the 2nd argument of the 1st matrix and the 1st argument of the 2nd matrix. Schematically this is depicted in Fig. 3.3 for the term $\Sigma \cdot G$. Furthermore, all functions could be mapped onto the sub-diagonal half-plane by Hermitian conjugation and using the properties (3.36)–(3.37) of the GFs.

To specify the initial conditions for the correlated many-particle system in general is a complicated task on its own. For plasma physics this is discussed for example in Refs. [81, 82]. In case of a homogeneous semiconductor and considering the carrier-phonon interaction, Gartner et al. [83] have shown² that for the unexcited semiconductor the solution of the KBE is given by the propagation with respect to the relative time only,

$$i\hbar \frac{\partial}{\partial \tau} G^R(\tau) = \delta(\tau) + \int_0^\tau dt' \Sigma^R(\tau - t') G^R(t') . \quad (3.71)$$

This completely defines the initial correlations prior to excitation. An optical pulse would initiate a propagation along the time-diagonal according to the collision terms (3.68)–(3.70). Alternatively, for the situation where all non-local correlations are dephased also an incoherent steady-state population obeying the condition $\frac{dG^<}{dt} = \frac{dG^R}{dt} = 0$ might be considered, cf. the discussion in Chap. 5.3 and Chap. 5.1.5.

The numerical implementation of the two-time KBE (3.68)–(3.70) is very demanding, even on nowadays supercomputers. It requires a large amount of computer memory to store all two-time GFs. For certain cases the GFs decay sufficiently fast away from the time diagonal and one could restrict the calculation to a certain memory depth. In general this is not the case and therefore numerical two-time calculations only provide insight into the early time regime (1 ps) after optical pulse excitation.

²Considering G^R and Σ^R state- and band-diagonal as well as only depending on the relative time, G^R and Σ^R commute and hence the right-hand side in Eqs. (3.68) and (3.69) vanishes.

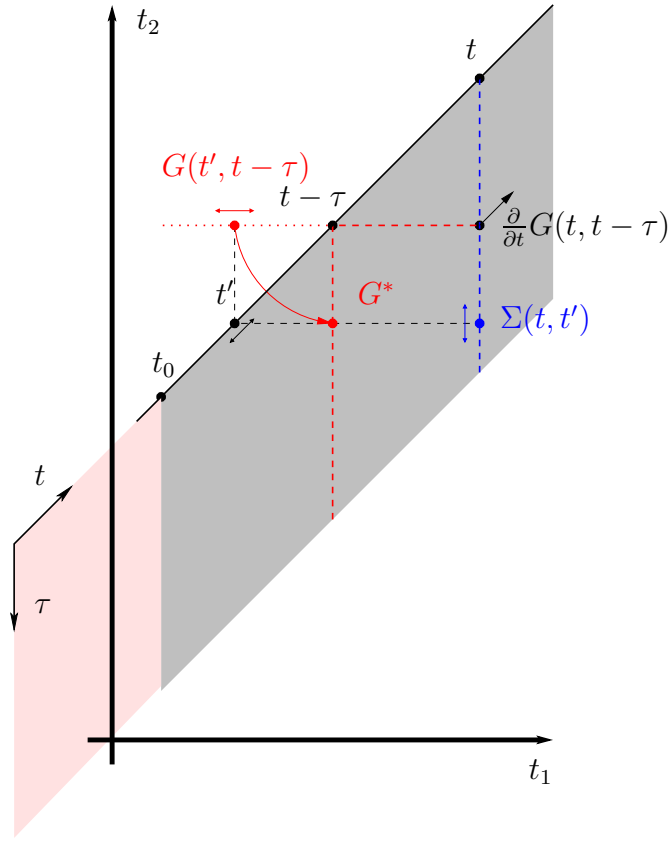


Fig. 3.3: Parametrization of the two-time plane into main time and relative time. Also the integration boundaries, the memory depth (gray area), and the initial conditions prior to an optical pulse around t_0 (pink area) are depicted.

3.5 Generalized Kadanoff-Baym ansatz

Since we are mainly interested in the time-diagonal elements of the lesser GF, $G^<(t, t)$, it would be advantageous to directly have a closed set of equations for them. From the two-time KBE (3.68)–(3.70) the time diagonal limit is obtained for $\tau = 0$. Using the definition of retarded and advanced GF, Eqs. (3.33)–(3.32), the collision terms on the time diagonal read

$$i\hbar \frac{\partial}{\partial t} G^<(t, t) \Big|_{\text{coll}} = \int_{-\infty}^t dt' [\Sigma^>(t, t') G^<(t', t) + \Sigma^<(t, t') G^>(t', t) - G^>(t, t') \Sigma^<(t', t) - G^<(t, t') \Sigma^>(t', t)]. \quad (3.72)$$

Note, that the GFs are again given in matrix notation. Lipavský et al. [84–87] have shown that the propagators $G^{\gtrless}(t_1, t_2)$ anywhere in the two time plane can be reconstructed from

their time diagonal elements $G^{\geq}(t, t)$ by an iterative procedure using the identity

$$\begin{aligned}
 G^{\geq}(t_1, t_2) = & i\hbar [G^R(t_1, t_2) G^{\geq}(t_2, t_2) - G^{\geq}(t_1, t_1) G^A(t_1, t_2)] \\
 & + \Theta(t_1 - t_2) \int_{t_2}^{t_1} dt_3 \int_{-\infty}^{t_2} dt_4 \\
 & \times G^R(t_1, t_3) [\Sigma^R(t_3, t_4) G^{\geq}(t_4, t_2) + \Sigma^{\geq}(t_3, t_4) G^A(t_4, t_2)] \\
 & + \Theta(t_2 - t_1) \int_{t_1}^{t_2} dt_3 \int_{-\infty}^{t_1} dt_4 \\
 & \times [G^{\geq}(t_1, t_4) \Sigma^A(t_4, t_3) + G^R(t_1, t_4) \Sigma^{\geq}(t_4, t_3)] G^A(t_3, t_2).
 \end{aligned} \tag{3.73}$$

In the non-interacting case only the first term contributes,

$$G^{\geq}(t_1, t_2) = i\hbar [G^R(t_1, t_2) G^{\geq}(t_2, t_2) - G^{\geq}(t_1, t_1) G^A(t_1, t_2)]. \tag{3.74}$$

This corresponds to the generalized Kadanoff-Baym ansatz (GKBA) which is widely used to map two-time propagators onto the time diagonal by the help of two-time spectral GFs. The assumption behind the GKBA is that the interaction is weak and that the dominant contribution to the reconstruction (3.73) is provided by the time-diagonal elements. Furthermore, a capable model for the retarded/advanced GF is required to gain practical advantage over a two-time calculation.

As pointed out by Schäfer and Wegener [61], even in the non-interacting case the GKBA (3.74) is not unique. For the two-time propagator we consider a reconstruction of the form $G^{\geq}(t_1, t_2) = i\hbar [G^a(t_1, t_2) G^{\geq}(t_2, t_2) - G^{\geq}(t_1, t_1) G^b(t_1, t_2)]$. Within the Hartree-Fock approximation, where the selfenergy is instantaneous, we find that in Eq. (3.74) G^R and G^A can be replaced by any linear combination of them since the two-time objects G^a and G^b only have to obey the relation $G^a + G^b = G^R - G^A$. The actual choice (3.74) is guided by the causality requirement and the idea of obtaining a maximum of retardation and correlation effects. By interchanging G^R and G^A , a minimum of retardation is obtained, corresponding to the Markov approximation. This ansatz we refer to as the reverse GKBA

$$G^{\geq}(t_1, t_2) = i\hbar [G^{\geq}(t_1, t_1) G^R(t_1, t_2) - G^A(t_1, t_1) G^{\geq}(t_2, t_2)]. \tag{3.75}$$

Schematically, the mapping onto the time diagonal is shown in Fig. 3.4a where the horizontal projection corresponds to the GKBA and the vertical projection to the reverse GKBA.

A deeper understanding of the GKBA can be obtained from the correction terms in the iterative reconstruction equation (3.73). As an example, the integration region in the two-time plane for the retarded part is depicted graphically in Fig. 3.4b. We find that the selfenergy (shaded area) connects both time integrations occurring in Eq. (3.73). In addition to a decay of the retarded/advanced GFs away from the time diagonal that might limit the integration (dashed lines), Špička et al. [84–87] pointed out that the selfenergy only contributes within a finite strip along the time-diagonal (dark shaded area) due to finite

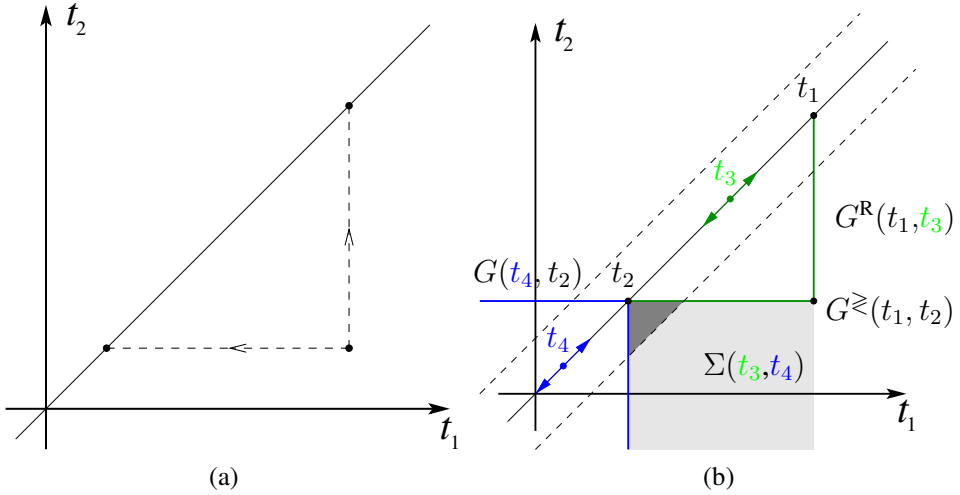


Fig. 3.4: Reconstruction of a two-time propagator $G^>(t_1, t_2)$ from its time-diagonal elements by the help of two-time spectral GFs for (a) the non-interacting case (GKBA) and (b) corrections due to the interaction.

decoherence times of many-body correlations. This means that the inner time-scales of the system provide a limit of the corrections to the GKBA. Therefore, depending on the processes under consideration and the parameters of the system, the GKBA might be a good approximation even in case of strong interaction. Physically, the correction terms in Eq. (3.73) describe the memory of non-local many-body correlations that is neglected within the GKBA. Unfortunately, beside theoretical considerations up to now no verification of this concept is presented in literature. However, the reconstruction of two-time propagators is still a debated topic where also new quasi-particle concepts are introduced, see for example Refs. [87–89].

4 Many-body interactions

The formalism of non-equilibrium GFs presented so far is rather general. In this chapter the selfenergies for the different interaction processes taken into account are specified. Starting from the choice of a vertex function (3.59f) the class of selfenergies (3.59f) is generated. Since the construction is performed on the Keldysh contour, the Keldysh matrix has to be decomposed along the same lines as for the carrier GF. For the selfenergy under consideration, usually simplifying approximations are applied. This has to be done carefully to avoid inconsistencies in the resulting equations. A detailed discussion on the choice of the vertex function for Coulomb scattering is presented for example in [90].

In the following, a collection of all selfenergy diagrams used throughout this thesis is given. The basic interaction vertices, interaction matrix elements as well as properties that are specific to the semiconductor system are discussed. At this point explicitly semiconductor properties enter the description via the wavefunctions and single-particle energies of the states that are used for an eigenfunction expansion. Note, that the calculations presented in the following do not contain all given selfenergies at the same time. The diagrams that are used are indicated explicitly.

The discussed interaction processes for carriers include the Coulomb interaction up to the second order Born approximation (SBA) and the carrier-phonon interaction in random-phase approximation (RPA). Carrier spins are considered on the basis of two non-interacting sub-systems. For the optical excitation, the light-matter interaction is considered in dipole approximation.

4.1 Coulomb interaction

The basic interaction vertex for the carrier-carrier interaction in eigenfunction representation is a two-particle vertex where a carrier is scattered from state $|1\rangle$ to state $|4\rangle$ while another carrier is scattered from $|2\rangle$ to $|3\rangle$. This is described by the interaction matrix

element

$$\begin{aligned} V_{1234} &= \frac{e^2}{4\pi\varepsilon_0\varepsilon_B} \int d^3r \int d^3r' \hat{\Psi}_1^*(\mathbf{r}) \hat{\Psi}_2^*(\mathbf{r}') \frac{1}{|\mathbf{r} - \mathbf{r}'|} \hat{\Psi}_3(\mathbf{r}') \hat{\Psi}_4(\mathbf{r}) \\ &= \frac{e^2}{4\pi\varepsilon_0\varepsilon_B} \int d^3q \frac{1}{q^2} \langle 1 | e^{i\mathbf{qr}} | 4 \rangle \langle 2 | e^{-i\mathbf{qr}} | 3 \rangle . \end{aligned} \quad (4.1)$$

In the second line, the Fourier expansion of the Coulomb potential was used. Schematically the basic Coulomb interaction vertex is depicted in Fig. 4.1, where the overlap integrals are represented as triangles.

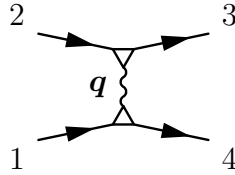


Fig. 4.1: Basic interaction vertex for the carrier-Coulomb interaction in eigenfunction representation.

For the overlap integrals, in the following a diagonal approximation with respect to the band indices is assumed, $\langle 1 | e^{i\mathbf{qr}} | 4 \rangle = \langle \phi_\alpha^\lambda | e^{i\mathbf{qr}} | \phi_\beta^{\lambda'} \rangle \approx \langle \phi_\alpha^\lambda | e^{i\mathbf{qr}} | \phi_\beta^{\lambda'} \rangle \delta_{\lambda=\lambda'}$. Strictly speaking this is only true for $\mathbf{q} = 0$ due to the orthogonality of the states. However, for the vicinity of the Γ -point, i.e. for low \mathbf{q} , we expect this to be a good approximation. This approximation should not be confused with the envelope-function approximation [64], as it is independent of a particular representation of the wave functions. It is for example also applied to the approach discussed in Chap. 7.2, where we use tight-binding wavefunctions.

Hartree and RPA selfenergy

The lowest order selfenergy contributions to the Kadanoff-Baym equations (3.64)–(3.65) are given by the Hartree and the RPA terms. Within the functional derivative technique, the Hartree selfenergy

$$\Sigma^H(\underline{1}, \underline{1}) = -i\hbar n_1 \int d\underline{3} V(\underline{1}, \underline{3}) G(\underline{3}, \underline{3}^+) \quad (4.2)$$

arises from the equation of motion, cf. Eq. (3.47). In contrast, the RPA terms are obtained from the 1st order vertex function, i.e. the δ -part and the corresponding selfenergy and polarization function read

$$\Sigma^{RPA}(\underline{1}, \underline{2}) = i\hbar n_1 G(\underline{1}, \underline{2}) W_e(\underline{2}, \underline{1}), \quad (4.3)$$

$$P^{RPA}(\underline{1}, \underline{2}) = -i\hbar n_1 G(\underline{1}, \underline{2}) G(\underline{2}, \underline{1}). \quad (4.4)$$

Note, that the screened interaction W_e contains the polarization function. The diagrammatic representation of these terms is depicted in Fig. 4.2.

For the RPA terms, unfolding the Keldysh contour yields

$$\Sigma^{\geq, \text{RPA}}(1, 2) = i\hbar G^{\geq}(1, 2) W_e^{\leq}(2, 1), \quad (4.5)$$

$$P^{\geq, \text{RPA}}(1, 2) = -i\hbar G^{\geq}(1, 2) G^{\leq}(2, 1). \quad (4.6)$$

As the Hartree selfenergy is instantaneous with respect to the Keldysh time, the corresponding greater/lesser components vanish. The corresponding retarded selfenergy reads

$$\Sigma^{\text{R}, \text{H}}(1, 1) = -i\hbar \int d3 V(1, 3) G^<(3, 3^+). \quad (4.7)$$

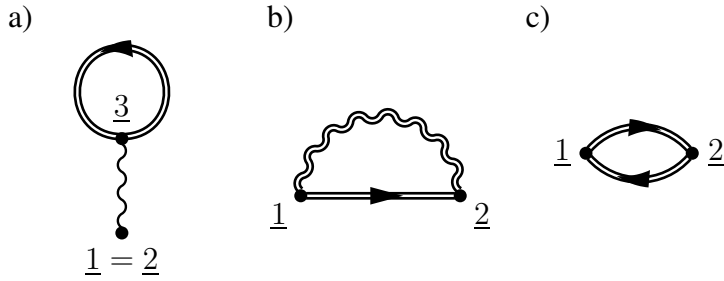


Fig. 4.2: Hartree selfenergy for the Coulomb interaction (a) as well as the RPA selfenergy (b) and the RPA polarization bubble (c).

Hartree-Fock selfenergy

If screening effects are neglected and only the bare Coulomb interaction is considered, the Hartree and Fock terms are obtained from the RPA result. They are also known as direct and exchange contributions. The greater/lesser components vanish due to the instantaneous nature of the bare Coulomb interaction and one obtains for the retarded components in eigenfunction representation

$$\Sigma_{12}^{\text{H}, \text{R}}(t_1, t_2) = -i\hbar \delta(t_1 - t_2) \sum_{34} V_{1432} G_{34}^<(t_1), \quad (4.8)$$

$$\Sigma_{12}^{\text{F}, \text{R}}(t_1, t_2) = i\hbar \delta(t_1 - t_2) \sum_{34} V_{1423} G_{34}^<(t_1). \quad (4.9)$$

The corresponding diagrammatic representation is depicted in Fig. 4.3. Note, that these diagrams are only intended to illustrate the index structure as no diagram rules are involved.

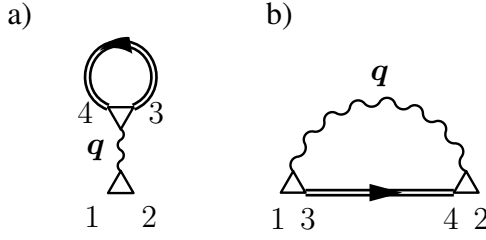


Fig. 4.3: Self consistent (a) direct Coulomb selfenergy (Hartree) and (b) exchange Coulomb selfenergy (Fock) in eigenfunction representation.

That these are indeed the diagrams representing the direct and the exchange Coulomb interaction is seen easily when considering the Dyson equation (3.46). From a factorization of the two-particle GF into uncorrelated one-particle GFs one immediately recovers the Hartree and Fock terms. In this sense, the direct term describes the mean-field interaction of a single carrier with all others whereas the exchange term arises from particle exchange.

For the QD-WL system, some comments on the Hartree contributions are appropriate. First, the selfenergy Σ_{kk} for WL states vanishes due to charge neutrality. The corresponding selfenergy for QD states reads

$$\begin{aligned} \Sigma_{mm}^{\lambda\lambda} = -i\hbar & \left\{ \sum_{\mathbf{R}, \mathbf{R}'} \sum_{m', \lambda'} \sum_{\mathbf{q}} V_{mm'm'm}^{\lambda\lambda'} G_{m'}^{<, \lambda'} \langle m | e^{-i\mathbf{q}\mathbf{r}} | m \rangle \langle m' | e^{i\mathbf{q}\mathbf{r}} | m' \rangle e^{i\mathbf{q}(\mathbf{R}-\mathbf{R}')} \right. \\ & \left. + \sum_{\mathbf{R}} \sum_{\mathbf{k}, \lambda'} \sum_{\mathbf{q}} V_{m\mathbf{k}\mathbf{k}m}^{\lambda\lambda'} G_{\mathbf{k}}^{<, \lambda'} \langle m | e^{-i\mathbf{q}\mathbf{r}} | m \rangle \langle \mathbf{k} | e^{i\mathbf{q}\mathbf{r}} | \mathbf{k} \rangle e^{i\mathbf{q}\mathbf{R}} \right\}, \quad (4.10) \end{aligned}$$

when classifying the internal indices into QD and WL contributions. The averaging over the random QD positions \mathbf{R}, \mathbf{R}' is performed like in disordered system theory,

$$\sum_{\mathbf{R}, \mathbf{R}'} f(\mathbf{R}) g(\mathbf{R}') = \sum_{\mathbf{R} \neq \mathbf{R}'} f(\mathbf{R}) g(\mathbf{R}') + \sum_{\mathbf{R}} f(\mathbf{R}) g(\mathbf{R}). \quad (4.11)$$

We obtain an uncorrelated average of the two random variables (first term) and a correlated average (second term). In our case, the uncorrelated part gives rise to a $\mathbf{q} = 0$ contribution. Due to charge neutrality this term cancels with the term originating from the WL, where due to momentum conservation also a $\mathbf{q} = 0$ appears. Therefore, only the intra-dot contribution

$$\Sigma_{mm}^{\lambda\lambda}(t) = -i\hbar \sum_{m', \lambda'} V_{mm'm'm}^{\lambda\lambda'} G_{m'}^{<, \lambda'}(t). \quad (4.12)$$

has to be considered in the Hartree selfenergy. A detailed discussion on this subject can be found in Refs. [91, 92].

The diagrams for the Hartree interaction contain the unscreened interaction and the full GF. Thus, for non-homogeneous systems like QDs in principle also non-diagonal GFs $G_{\mathbf{k},\mathbf{k}'}$ have to be considered. From a physical point of view these contributions are important, as they provide for QD carriers the screening of the Hartree interaction due to the presence of WL carriers. To include these contributions we choose an equivalent approach, where we restrict to diagonal GFs in the Hartree loop, while considering a screened interaction. In our case the Lindhard screening is used, which we discuss below. A detailed discussion of the corresponding diagrams is presented in Refs. [91, 92].

RPA screening

The starting point for the inclusion of the screened Coulomb interaction is the equation of motion for the plasmon GF (3.59e). In the following we use the RPA polarization function (4.4). After unfolding the Keldysh contour, we find for the retarded plasmon GF and the polarization propagator

$$W_e^R(1, 2) = V(1, 2) + V(1, 3) P^R(3, 4) W_e^R(4, 2), \quad (4.13)$$

$$P^R(1, 2) = \left[G^R(1, 2) G^<(2, 1) + G^<(1, 2) G^A(2, 1) \right]. \quad (4.14)$$

When using the retarded GF in pole approximation¹, the GKBA and assuming time-independent populations, we obtain the well known Lindhard screening [61, 62],

$$W_q^{R,A}(\omega) = \frac{V_q}{\varepsilon_q(\omega)}, \quad \varepsilon_q(\omega) = 1 - V_q P_q(\omega), \quad (4.15a)$$

$$P_q^R(\omega) = \frac{1}{A} \sum_{\mathbf{k}, \lambda} \frac{f_{\mathbf{k}-\mathbf{q}}^\lambda - f_\mathbf{k}^\lambda}{\hbar(\omega + i\delta) + \epsilon_{\mathbf{k}-\mathbf{q}}^\lambda - \epsilon_\mathbf{k}^\lambda}. \quad (4.15b)$$

A detailed derivation is given in App. A.2. In our calculations the static limit ($\omega \rightarrow 0$) is used. This way, the instantaneous bare Coulomb interaction is replaced by a screened instantaneous interaction.

The validity of the Lindhard screening in the form (4.15a) is restricted to systems that obey momentum conservation. Hence, for QD systems in principle a screened Coulomb potential W_{q_1, q_2}^R , as outlined in App. A.2, has to be considered. Such calculations require computational resources that exceed even nowadays supercomputers. Therefore, in the following only contributions from WL carriers are taken into account. This is a reasonable approximation for the high carrier density regime, which is considered for example in gain calculations (cf. Chap. 6.1). For a low QD density, in this case the number of QD carriers

¹A free GF that might include renormalized energies, i.e. $\epsilon_0 + \Delta - i\gamma$.

that contribute to the screening is also low in comparison to the number of carriers in the WL.

Furthermore, the static limit does not contain dynamical screening effects which describe the build-up of plasmon resonances due to the temporal evolution of carrier populations. Their inclusion requires the solution of the equations of motion for the plasmon propagator $W^{\gtrless}(1, 2) = W^R(1, 3) P^{\gtrless}(3, 4) W^A(4, 2)$. Corresponding calculations are presented for example in Refs. [93–96]. It is shown that these effects are restricted to the early time regime (≈ 500 fs after carrier excitation).

Screened-exchange and Coulomb-hole selfenergy

A first step beyond the Hartree-Fock approximation (4.8)–(4.9) is to consider terms that are linear in the screened instantaneous interaction $W_e^{R/A}$. In the linear case the greater/lesser components vanish, $W_e^{\gtrless} = 0$, as these terms are at least of second order in the interaction. Instantaneous contributions are contained in the retarded selfenergy, which in general is given by

$$\begin{aligned}\Sigma^R(1, 2) &= \Sigma^\delta(1, 2) + \Theta(t_1 - t_2) [\Sigma^>(1, 2) - \Sigma^<(1, 2)] \\ &= \Sigma(1, 2) - \Sigma^<(1, 2).\end{aligned}\quad (4.16)$$

Note, that Σ denotes the time-ordered selfenergy, according to the notation introduced in Chap. 3.2. Using the RPA selfenergy (4.5) and considering the assumptions discussed above, we find

$$\begin{aligned}\frac{1}{i\hbar} \Sigma^R(1, 2) &= G(1, 2) W_e(2, 1) - G^<(1, 2) W_e^>(2, 1) \\ &= [G^R(1, 2) + G^<(1, 2)] [W_e^A(2, 1) + W_e^>(2, 1)] - G^<(1, 2) W_e^>(2, 1) \\ &= [G^R(1, 2) + G^<(1, 2)] W_e^A(2, 1) \\ &= \frac{1}{2} [G^>(1, 2) + G^<(1, 2)] W_e^A(2, 1),\end{aligned}\quad (4.17)$$

where in the last line we used the definition $\Theta(0) = \frac{1}{2}$. Performing an eigenfunction expansion, the selfenergy reads

$$\begin{aligned}\Sigma_{12}^R(t_1) &= \frac{i\hbar}{2} \sum_{3,4} [G_{34}^>(t_1) + G_{34}^<(t_1)] W_{1423}^R(t_1) \\ &= \begin{cases} \frac{1}{2} \sum_3 \{ [1 - 2 f_3(t_1)] W_{1323}^R(t_1) - V_{1323} \} & \lambda_1 = \lambda_2 \\ - \sum_{3,4} \psi_{34}(t_1) W_{1423}^R(t_1) & \lambda_1 = c, \lambda_2 = v \end{cases}.\end{aligned}\quad (4.18)$$

In the last line intra-band transition amplitudes are neglected and the analysis is restricted to interband transitions and populations. For the unexcited system the screened interaction reduces to the bare one (see Eq. (4.15b)) and hence to recover the Fock selfenergy (4.9) a correction, $-\frac{1}{2} V_{1323}$, is introduced. Usually the contributions are separated into the screened-exchange (SX) and the Coulomb-hole (CH) part,

$$\Sigma_{12}^{\text{SX}}(t) = \begin{cases} -\sum_3 W_{1323}^R(t) f_3(t) & \lambda_1 = \lambda_2 \\ -\sum_{3,4} W_{1423}^R(t) \psi_{34}(t) & \lambda_1 = c, \lambda_2 = v \end{cases}, \quad (4.19)$$

$$\Sigma_{12}^{\text{CH}}(t) = \begin{cases} \frac{1}{2} \sum_3 [W_{1323}^R(t) - V_{1323}] & \lambda_1 = \lambda_2 \\ 0 & \lambda_1 = c, \lambda_2 = v \end{cases}. \quad (4.20)$$

2nd order Born selfenergy

To describe carrier scattering due to Coulomb interaction higher order diagrams have to be included. Here, the 2nd order Born approximation (SBA) is used, where all processes up to second order in the screened Coulomb interaction $W_e^{\text{R/A}}$ are taken into account. For the first vertex correction beyond the RPA diagram by means of the first step of a ladder approximation we find the selfenergy

$$\begin{aligned} \Sigma^{\text{SBA}}(\underline{1}, \underline{2}) &= i\hbar n_1 G(\underline{1}, \underline{2}) W_e(\underline{2}, \underline{1}) \\ &- (i\hbar)^2 n_1 n_3 \iint d\underline{3} d\underline{4} G(\underline{1}, \underline{3}) W_e(\underline{2}, \underline{3}) G(\underline{3}, \underline{4}) G(\underline{4}, \underline{2}) W_e(\underline{4}, \underline{1}). \end{aligned} \quad (4.21)$$

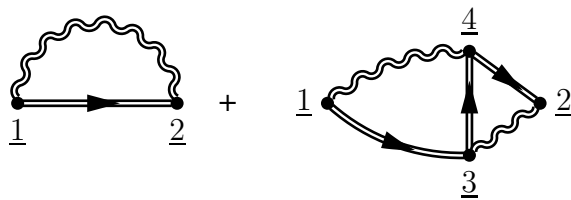


Fig. 4.4: Self consistent 2nd order Born selfenergy for the Coulomb interaction.

The SBA selfenergy is depicted in Fig. 4.4. When decomposing the Keldysh contour and considering that W_e^{\gtrless} is at least of second order in the Coulomb interaction $W_e^{\text{R/A}}$, we find

that in second order we are left with

$$\begin{aligned} \Sigma^{\text{SBA},\gtrless}(1, 2) = \hbar^2 \iint d3d4 & \left[G^{\gtrless}(1, 2) W_e^R(2, 3) G^{\gtrless}(3, 4) G^{\lessgtr}(4, 3) W_e^A(4, 1) \right. \\ & \left. - G^{\gtrless}(1, 3) W_e^R(2, 3) G^{\lessgtr}(3, 4) G^{\gtrless}(4, 2) W_e^A(4, 1) \right]. \end{aligned} \quad (4.22)$$

In eigenfunction representation the SBA selfenergy reads

$$\begin{aligned} \Sigma_{12}^{\text{SBA},\gtrless}(t_1, t_2) = \hbar^2 \iint dt_3 dt_4 \sum_{3\dots8} & \\ & \times \left[G_{34}^{\gtrless}(t_1, t_2) W_{4672}^R(t_2, t_3) G_{78}^{\gtrless}(t_3, t_4) G_{56}^{\lessgtr}(t_4, t_3) W_{8135}^A(t_4, t_1) \right. \\ & \left. - G_{34}^{\gtrless}(t_1, t_3) W_{8452}^R(t_2, t_3) G_{56}^{\lessgtr}(t_3, t_4) G_{78}^{\gtrless}(t_4, t_2) W_{6137}^A(t_4, t_1) \right], \end{aligned} \quad (4.23)$$

which is diagrammatically depicted in Fig. 4.5. Note, that these diagrams are only intended to illustrate the index structure as no diagram rules that distinguish between the different GFs are involved. In contrast to the SX-CH selfenergy which replaces the HF selfenergy, the SBA selfenergy has to be added to the instantaneous HF part.

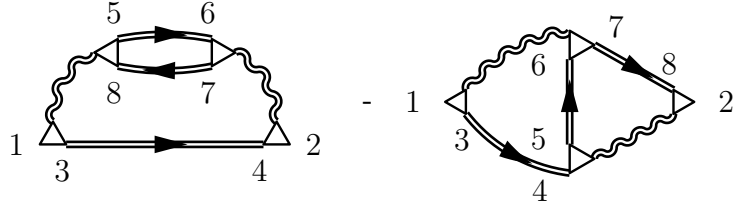


Fig. 4.5: Eigenfunction representation of the self-consistent 2nd Born self-energy for the Coulomb interaction.

4.2 Carrier-phonon interaction

The basic interaction vertex for the carrier-phonon interaction contains in eigenfunction representation the carrier scattering from state $|1\rangle$ to state $|2\rangle$ due to the interaction with the mode \mathbf{q} of the phonon system. This is depicted graphically in Fig. 4.6a. The interaction potential is given by the first order term $V_{e\text{-ph}}(\mathbf{r}) = \sum_l \mathbf{Q}_l \cdot \nabla V_{e\text{-i}}(\mathbf{r} - \mathbf{R}_l^0)$ in the expansion of the electron-ion interaction (3.44) around the equilibrium ion positions \mathbf{R}_l^0 with \mathbf{Q}_l being the lattice displacement. Using the Fourier representation of the interaction potential

$V_{\text{e-ph}}$ and the eigenmode expansion for the lattice displacements, we obtain the interaction matrix element [97]

$$M_{12}(\mathbf{q}) = \int d^3r \hat{\Psi}_1^\dagger(\mathbf{r}) M_{\mathbf{q}}(\mathbf{r}) \hat{\Psi}_2(\mathbf{r}) \quad (4.24)$$

with

$$M_{\mathbf{q}}(\mathbf{r}) = -\sqrt{\frac{\hbar}{2\omega_{\mathbf{q}}^j \varrho V}} e^{i\mathbf{qr}} V_{\text{e-i}}(\mathbf{q}) \mathbf{q} \cdot \boldsymbol{\xi}_{\mathbf{q}}. \quad (4.25)$$

The matrix element contains the unscreened electron-ion Coulomb potential $V_{\text{e-i}}$, the polarization vector $\boldsymbol{\xi}_{\mathbf{q}}$ and the dispersion $\omega_{\mathbf{q}}^j$ of the phonon mode j . Furthermore ϱ is the density of the material. From first sight we find that transversal phonons do not couple to the carrier system due to the scalar product $\mathbf{q} \cdot \boldsymbol{\xi}_{\mathbf{q}}$. Furthermore, several simplifying approximations are possible. Since for optical processes mainly the vicinity of the Γ point is of importance we can restrict ourselves to the long-wavelength limit $\mathbf{q} \rightarrow 0$.

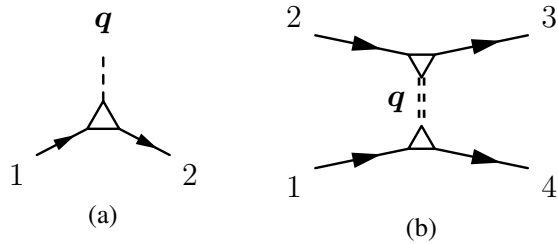


Fig. 4.6: Basic interaction vertex for the carrier-phonon interaction (a) and effective Coulomb-like carrier-phonon interaction (b).

The further evaluation of the coupling matrix element depends on the particular phonon mode considered. In principle two distinct types of lattice oscillations are found, acoustic and optical modes. Acoustic modes are characterized by density waves whereas optical modes are characterized by dipole oscillations in ionic crystals, leading to different coupling mechanisms. Density waves, i.e. acoustic phonons, build up a time dependent gradient of the ionic charge density. Their influence on the carrier system can be incorporated by a so-called deformation potential [97]. In contrast, dipole oscillations, i.e. optical phonons, set up an electric field which can be very large in ionic crystals. The coupling to the carrier system is described by the Fröhlich mechanism. According to Ref. [61] the corresponding effective interaction is given by

$$M_{12}^{\text{LO}}(\mathbf{q}) = \frac{1}{\sqrt{V}} \sqrt{4\pi\alpha} \frac{\hbar}{\sqrt{2\mu}} (\hbar\omega_{\text{LO}})^{3/2} \frac{1}{|\mathbf{q}|} \langle 1 | e^{i\mathbf{qr}} | 2 \rangle, \quad (4.26)$$

containing the dimensionless polar coupling constant

$$\alpha = \frac{e^2}{8\pi\varepsilon_0} \frac{1}{\hbar\omega_{\text{LO}}} \sqrt{\frac{2\mu\omega_{\text{LO}}}{\hbar}} \left(\frac{1}{\varepsilon_\infty} - \frac{1}{\varepsilon_B} \right). \quad (4.27)$$

In perturbation theory, the coupling constant α determines the polaron shift $\Delta E = -\alpha \hbar\omega_{\text{LO}}$ and the polaron mass renormalization $m^* = m/1-\frac{\alpha}{6}$ [62]. Whereas in principle the coupling is different for electrons and holes, we take into account an effective coupling for both via using the effective mass μ .

Effective Coulomb interaction

In Chap. 3.2 it is demonstrated that the carrier-phonon interaction enters the GF theory via a ionic density-density correlation function. This correlation function is evaluated in the following, using the Fröhlich coupling mechanism. For the phonon contribution to the screened interaction (3.59c) we make use of the electronic part of the dielectric function ε_e^{-1} and write

$$W_{\text{ph}}(\underline{1}, \underline{2}) = \iint d\underline{3} d\underline{4} \varepsilon_e^{-1}(\underline{1}, \underline{3}) U(\underline{3}, \underline{4}) \varepsilon_e^{-1}(\underline{4}, \underline{2}), \quad (4.28)$$

where we introduced the potential-fluctuation correlation function

$$i\hbar U(\underline{1}, \underline{2}) = \langle T [\Delta V(\underline{1}) \Delta V(\underline{2})] \rangle. \quad (4.29)$$

The ion-density fluctuations due to lattice vibrations can be associated with polarization charges according to Poisson's equation $\text{div } \mathbf{P} = -q \text{ div } \mathbf{Q} = \rho_{\text{pol}}^2$. Correspondingly, within the Born-Oppenheimer approximation and a harmonic expansion we find that the electrostatic potential ΔV due to the ion-density fluctuations can be expressed in terms of normal-mode phonon operators according to

$$\Delta V(\underline{1}) = -\frac{e^2}{4\pi\varepsilon_0} \int d^3R \frac{\Delta \hat{N}(\mathbf{R}, t)}{|\mathbf{r} - \mathbf{R}|} = \sum_{\mathbf{q}} M_{\mathbf{q}}(\mathbf{r}_1) \left(\hat{b}_{\mathbf{q}}(\underline{t}_1) + \hat{b}_{-\mathbf{q}}^\dagger(\underline{t}_1) \right). \quad (4.30)$$

Thus, we find the correlation function $U(\underline{1}, \underline{2})$ given in terms of phonon GFs $D_{\mathbf{q}_1 \mathbf{q}_2}$,

$$i\hbar U(\underline{1}, \underline{2}) = \sum_{\mathbf{q}_1, \mathbf{q}_2} M_{\mathbf{q}_1}(\mathbf{r}_1) D_{\mathbf{q}_1 \mathbf{q}_2}(\underline{t}_1, \underline{t}_2) M_{\mathbf{q}_2}^*(\mathbf{r}_2). \quad (4.31)$$

Neglecting screening effects, we obtain in eigenfunction expansion the carrier-phonon interaction vertex

²In the globally neutral system with the ions in their equilibrium positions and the homogeneous negatively charged background provided by the electron gas, lattice displacements correspond to the creation of dipole charges.

$$W_{1234}^{\text{ph}}(\underline{t}_1, \underline{t}_2) = \sum_{\mathbf{q}_1, \mathbf{q}_2} M_{14}(\mathbf{q}_1) D_{\mathbf{q}_1 \mathbf{q}_2}(\underline{t}_1, \underline{t}_2) M_{23}^*(\mathbf{q}_2), \quad (4.32)$$

that contains two basic carrier-phonon interaction vertices $M_{12}(\mathbf{q})$ connected by a phonon GF $D_{\mathbf{q}_1 \mathbf{q}_2}$ which is discussed below. Diagrammatically this is depicted in Fig. 4.6b. The effective carrier-phonon interaction is mediated by the phonon system and, in contrast to the Coulomb case, not instantaneous.

Phonon Green's function

The phonon GF can be introduced similar to the carrier GF, describing the time dependent correlation of lattice displacements,

$$i\hbar D_{\mathbf{q}_1 \mathbf{q}_2}(\underline{t}_1, \underline{t}_2) = \left\langle \hat{b}_{\mathbf{q}_1, j}(\underline{t}_1) \hat{b}_{\mathbf{q}_2, j}^\dagger(\underline{t}_2) + \hat{b}_{\mathbf{q}_1, j}^\dagger(\underline{t}_1) \hat{b}_{\mathbf{q}_2, j}(\underline{t}_2) \right\rangle. \quad (4.33)$$

A Dyson equation for the phonon GF is obtained by using Heisenberg's equation of motion for the displacement operators and successively applying the functional derivative with respect to the perturbation J_{ext} . A detailed derivation considering the Fröhlich Hamiltonian (3.2) is given in Ref. [80]. The structure $D = d + d G G \tilde{\Gamma} D$ of the Dyson equation with the “bubble” $G G \tilde{\Gamma}$ is similar to the screening of the Coulomb interaction (3.59b). Therefore, the techniques discussed in the previous chapter can be applied. The functional derivative approach to the equation of motion for the single-phonon GF of harmonic solids was first introduced by Baym [98]. An extension to anharmonic solids which includes phonon-phonon interaction is presented for example in Refs. [99, 100], where basically the effective potential for the electron-ion and ion-ion interaction is expanded beyond the second order in the lattice displacement.

Considering the non-interacting case, the phonon GF can be obtained directly from Eq. (4.33) by using the equilibrium phonon eigenmodes

$$\hat{b}_{\mathbf{q}}^{(\dagger)}(\underline{t}) = \hat{b}_{\mathbf{q}}^{(\dagger)} e^{\mp i\omega_{\mathbf{q}}^j \underline{t}}. \quad (4.34)$$

The phonon GF (4.33) on the Keldysh contour is decomposed similarly to the carrier GF. For the propagators we find

$$i\hbar d_j^{\gtrless}(\mathbf{q}, t_1, t_2) = N_{\mathbf{q}}^j e^{\pm i\omega_{\mathbf{q}}^j(t_1 - t_2)} + (N_{\mathbf{q}}^j + 1) e^{\mp i\omega_{\mathbf{q}}^j(t_1 - t_2)}, \quad (4.35)$$

where the equilibrium phonon population at the lattice temperature is given by a Bose distribution function

$$N_{\mathbf{q}}^j = \frac{1}{e^{\beta \hbar \omega_{\mathbf{q}}^j} - 1}. \quad (4.36)$$

In the following the effective Coulomb interaction (4.32) together with the equilibrium phonon propagator (4.35) will be denoted as

$$i\hbar D_{1234}^{\gtrless}(t_1, t_2) = i\hbar \sum_{\mathbf{q}} M_{14}(\mathbf{q}) M_{23}^*(\mathbf{q}) d_j^{\gtrless}(t_1, t_2). \quad (4.37)$$

Note, that for the carrier-LO-phonon interaction the index ordering is the same as in the Coulomb case (4.1), $V_{1234}(\mathbf{q}) \propto M_{14}(\mathbf{q}) M_{23}^*(\mathbf{q})$.

A few comments on the interpretation of the effective interaction vertex (4.32) are appropriate. The corresponding diagram is shown in Fig. 4.6b and describes the interaction with the phonon system rather than the emission and re-absorption of a single phonon. In this sense, the equilibrium phonon GF used in our approach describes a phonon bath held at a given temperature. Energy dissipation and absorption for the carrier system is included due to fluctuations of the phonon number. However, the influence of the carriers on the phonon system is not considered. This would require a self-consistent solution of the corresponding Dyson equation for the phonon GF together with the Dyson equation (3.59a) for carriers.

Carrier-phonon self-energies

The RPA and Hartree selfenergy diagrams for the carrier-phonon interaction are shown in Fig. 4.7. On the Keldysh contour, they read

$$\Sigma^{\text{RPA}}(\underline{1}, \underline{2}) = i\hbar n_1 G(\underline{1}, \underline{2}) W_{\text{ph}}(\underline{2}, \underline{1}), \quad (4.38)$$

$$\Sigma^{\text{PH}}(\underline{1}, \underline{1}) = -i\hbar \int d\underline{3} W_{\text{ph},0}^{\text{R}}(\underline{1}, \underline{3}) G(\underline{3}, \underline{3}^+). \quad (4.39)$$

Here, W_{ph} denotes the carrier-phonon contribution to the interaction (3.59c). Similar to the Coulomb case, the RPA and Hartree diagrams presented in Fig. 4.7 arise from Eq. (3.59d) and (3.48). Correspondingly, the phonon-Hartree term (4.39) contains the „bare” carrier-phonon interaction whereas the RPA diagram contains the screened one.

Unfolding the Keldysh contour we find for the RPA diagram

$$\Sigma^{\text{RPA}, \gtrless}(1, 2) = i\hbar G^{\gtrless}(1, 2) W_{\text{ph}}^{\lessgtr}(2, 1), \quad (4.40)$$

$$\Sigma^{\text{RPA}, \text{R}}(1, 2) = i\hbar [G^{\text{R}}(1, 2) W_{\text{ph}}^{\gtrless}(2, 1) - G^{\gtrless}(1, 2) W_{\text{ph}}^{\text{R}}(2, 1)]. \quad (4.41)$$

Expanding into an eigenfunction basis and using the effective interaction matrix element (4.32) with the free phonon propagator (4.35) the selfenergy reads

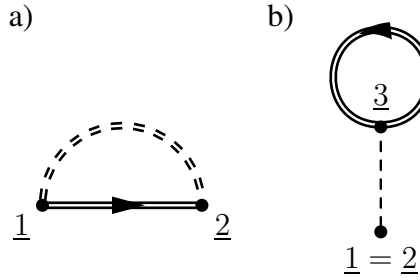


Fig. 4.7: RPA (a) and phonon Hartree (b) selfenergy for the carrier-phonon interaction. The diagrams for the corresponding eigenfunction representation are similar to the Coulomb case shown in Fig. 4.3.

$$\Sigma_{12}^{\text{F},\gtrless}(t_1, t_2) = i\hbar \sum_{34} \sum_{\mathbf{q}} M_{13}(\mathbf{q}) M_{24}^*(\mathbf{q}) G_{34}^{\gtrless}(t_1, t_2) d_{\mathbf{q}}^{\gtrless}(t_2, t_1), \quad (4.42)$$

$$\begin{aligned} \Sigma_{12}^{\text{F,R}}(t_1, t_2) = i\hbar \sum_{34} \sum_{\mathbf{q}} M_{13}(\mathbf{q}) M_{24}^*(\mathbf{q}) \\ \times [G_{34}^{\text{R}}(t_1, t_2) d_{\mathbf{q}}^<(t_2, t_1) - G_{34}^<(t_1, t_2) d_{\mathbf{q}}^{\text{R}}(t_2, t_1)]. \end{aligned} \quad (4.43)$$

For the Hartree diagram we have to consider that by definition $G(\underline{2}, \underline{2}^+) = G^<(\underline{2}, \underline{2})$. We find

$$\Sigma^{\text{PH,R}}(1, 1^+) = -i\hbar D^{\text{R}}(1, 2) G^<(2, 2^+), \quad (4.44)$$

which in eigenfunction expansion reads

$$\Sigma_{12}^{\text{PH,R}}(t_1) = -i\hbar \sum_{34} \sum_{\mathbf{q}} M_{12}(\mathbf{q}) M_{43}^*(\mathbf{q}) \int_{-\infty}^{t_1} dt_2 G_{\gamma\delta}^<(t_2) d_{\mathbf{q}}^{\text{R}}(t_1, t_2). \quad (4.45)$$

That the Hartree diagram also for the carrier-phonon interaction arises from Eq. (3.48) is less obvious than in the Coulomb case. From the total ion density $\hat{N} = \hat{N}_0 + \Delta\hat{N}$ only the fluctuation part contributes, as the equilibrium one provides the lattice-periodic potential which enters the band structure. Similar to Eq. (4.30) we may express the charge fluctuations in terms of phonon operators and obtain for the effective potential

$$U_{\text{eff}}(\underline{1}) = \int d\underline{3} V(\underline{1}, \underline{3}) \langle \Delta\hat{N}(\underline{3}) \rangle = -\sqrt{\frac{2\omega_q}{\hbar}} \int d\underline{3} \sum_{\mathbf{q}} M_{\mathbf{q}}(\mathbf{r}_3) \langle \hat{Q}_{\mathbf{q}}(\underline{t}_3) \rangle. \quad (4.46)$$

Note, that for the discussion we follow the notation from van Leeuwen [80] and introduce the displacement operator $\hat{Q}_{\mathbf{q}} = \sqrt{\frac{\hbar}{2\omega_q}} (\hat{b}_{\mathbf{q}}(t) + \hat{b}_{-\mathbf{q}}^\dagger(t))$. Considering the Fröhlich

Hamiltonian, the equation of motion for the displacement operators reads [80]

$$\left(\frac{\partial^2}{\partial t^2} + \omega_{\mathbf{q}}^2 \right) \hat{Q}_{\mathbf{q}}(t) = -\sqrt{\frac{2\omega_{\mathbf{q}}}{\hbar}} \int d^3r M_{\mathbf{q}}(\mathbf{r}) \hat{n}(\mathbf{r}, t), \quad (4.47)$$

whose solution for the average value in Fourier space yields

$$\sqrt{\frac{2\omega_{\mathbf{q}}}{\hbar}} \langle \hat{Q}_{\mathbf{q}}(\omega) \rangle = -\frac{1}{\hbar} \frac{2\omega_{\mathbf{q}}}{\omega^2 - \omega_{\mathbf{q}}^2} \int d^3r M_{\mathbf{q}}(\mathbf{r}) \langle \hat{n}(\mathbf{r}, \omega) \rangle. \quad (4.48)$$

We identify the Fourier transform of the free retarded phonon GF $d^R(\omega) = \frac{1}{\hbar} \frac{2\omega_{\mathbf{q}}}{\omega^2 - \omega_{\mathbf{q}}^2}$ as well as the lesser GF $-i\hbar G^<(1) = \langle \hat{n}(1) \rangle$. Then, transforming back into the time domain indeed yields in eigenfunction expansion the Hartree contribution (4.45).

4.3 Light-matter interaction

The interaction with a classical optical light field is considered by means of the minimal coupling $\mathbf{p} \rightarrow \mathbf{p} - e\mathbf{A}$ in the Hamiltonian $\hat{H} = \frac{(\mathbf{p}-e\mathbf{A})^2}{2m}$. In dipole approximation a unitary transformation yields the dipole interaction Hamiltonian $\hat{H} = \mathbf{d}\mathbf{E}$, where the dipole interaction matrix elements in 2nd quantization and eigenfunction representation are given by [61, 64]

$$\mathbf{d}_{12} = \int d^3r \hat{\Psi}_1^\dagger(\mathbf{r}) e\mathbf{r} \hat{\Psi}_2(\mathbf{r}). \quad (4.49)$$

Note, that the index 1 contains state and band index. Due to the symmetry properties of the wave-functions involved, d_{12} represents the selection rules for dipole-allowed transitions. More details on dipole selection rules and the evaluation of matrix elements in the framework of a envelope wave function approximation as well as a tight-binding approach are presented in Chap. A.3.

The corresponding selfenergy for the dipole interaction reads

$$\Sigma_{12}^R(t_1, t_2) = -\mathbf{d}_{12} \cdot \mathbf{E}(t_1) \delta(t_1, t_2). \quad (4.50)$$

Considering the excitation with a laser pulse, the electric component of the electro-magnetic field

$$\mathbf{E}(t, \mathbf{r}) = E_0(t) e^{i\omega_0 t} \mathbf{p}_0 e^{i\mathbf{k}_0 \cdot \mathbf{r}} \quad (4.51)$$

can be described by an envelope part $E_0(t)$, e.g. of Gaussian shape, the oscillation with the carrier frequency ω_0 , the polarization vector \mathbf{p}_0 , and the propagation wave-vector \mathbf{k}_0 . Usually a Gaussian shape $E_0(t) = E_0 e^{-\left(\frac{t-t_0}{\tau}\right)^2}$ of the pulse is used.

Part III

Application

5 Carrier-phonon scattering

Non-equilibrium processes and many-body effects have always received broad interest in semiconductor physics, as they are strongly involved in the typical experimental situation of perturbing the system and measuring its response. Common perturbations in semiconductor physics are the optical excitation with a laser pulse and the application of a bias voltage, both driving the system into non-equilibrium conditions. For the description of such situations the framework of non-equilibrium GFs (cf. Chap. 3.2) turned out to be a powerful tool. After their development for nuclear and plasma physics [53–55, 101], these methods were also applied to solid-state physics [98–100, 102] to include for example phonons in the description of neutron scattering. The kinetics of optically excited carriers was already considered in first applications to the semiconductor system [57, 58, 103–110]. Rapid progress was made and many non-equilibrium phenomena were studied using GFs. Among them are transport phenomena [59, 60], the build-up of screening [93–95, 111–114] and coherent effects like biexciton formation [73, 74] or four-wave-mixing experiments [113, 115, 116].

One important advantage of non-equilibrium GFs is the consistent treatment of spectral and kinetic properties. In this chapter we focus on the carrier-LO-phonon interaction and study the interplay of quasi-particle renormalizations and carrier scattering. First approaches [117, 118] to describe carrier-phonon scattering using GFs considered non-interacting single-particle properties as they are known analytically and tremendously reduce the numerical effort. Improved spectral functions [119] as well as single-particle properties beyond a pole approximation have been presented for bulk semiconductors [120, 121].

In the following, these models are extended to study the carrier-LO-phonon interaction in self-assembled semiconductor QDs. This type of QDs has been introduced in Chap. 2 and interesting physical effects arise from the fact that their energy spectrum contains discrete QD states as well as an energetically close continuum of 2D WL states. In a good approximation, the bulk LO phonon modes can be considered as dispersionless. For this model quasi-particle renormalizations are found, which can not be described using perturbation theory. Especially for the description of carrier relaxation processes these quasi-particle properties are of central importance. Therefore a consistent treatment of the spectral and kinetic properties of QD carriers within the framework of non-equilibrium GFs is presented.

We first discuss the so-called polaron problem for QD systems and introduce the quasi-

particle renormalizations that arise from the interaction of a carrier with a surrounding cloud of lattice distortions. In a second step, these quasi-particle properties are included in kinetic calculations and the carrier scattering is studied on various levels of sophistication. A discussion about carrier scattering naturally leads to the question if the temporal evolution leads in the long-time limit to a steady-state carrier distribution and if this steady-state corresponds to a thermal distribution. For the interacting system a generalization of the Fermi-Dirac distribution which includes the quasi-particle properties has to be considered. The carrier scattering is studied for the room-temperature as well as for the low-temperature regime. Finally, a theory-experiment comparison is presented, which shows the agreement of recent experiments with our theoretical findings. Note, that the focus of this chapter is on the particle scattering. In contrast to this, Chap. 6 deals with the polarization dynamics and dephasing in the context of optical experiments.

5.1 The polaron problem

The combined excitation of an electron interacting with a surrounding cloud of lattice distortions can be described as a quasi-particle called polaron. In the literature, the polaron picture was first introduced by Fröhlich [122] for the calculation of the electronic ground state energy for homogeneous polar crystals using perturbation theory. The surrounding cloud of lattice distortions causes a drag for the free carrier motion and the relocation of the polar surrounding yields a reduction of the electrostatic energy. Using perturbation theory, the resulting energy shift ΔE and the renormalized mass m^* can be related to the polar coupling constant α [62, 122],

$$\Delta E = -\alpha \cdot \hbar\omega_{\text{LO}} , \quad m^* = \frac{m}{1 - \frac{\alpha}{6}} . \quad (5.1)$$

Besides the fundamental interest in the bandstructure of solids, a rapidly increasing scientific interest emerged for the polaron problem. It enabled to apply quantum-field theoretical methods [123, 124] that have been newly developed at that time. Nowadays the polaron picture is more generally used and is also applied to molecules for the interaction of valence electrons with discrete vibrational excitations [6]. Even in quantum optics polaron effects are studied by trapping ultra-cold atoms in an optical lattice [125–127]. In the context of superconductors and spin physics similar methods are applied to the interaction of carriers with spin waves (carrier-magnon interaction), giving rise to the formation of so called magnetic polarons [128, 129].

Focusing on the semiconductor system and lattice vibrations, elaborated models for optical polarons [130–132], acoustic polarons [133], and the formation of bipolarons [134, 135] are discussed in the literature. In case of QD systems where bound states are well separated and considered as decoupled from any continuum, numerically exact calculations

for the electron-LO-phonon interaction [130, 131, 136, 137] as well as for the electron-LA-phonon interaction [133, 138, 139] are available. For self-assembled semiconductor QDs especially the coupling between the discrete QD states and the energetically close WL continuum is of interest. In the following we consider an unexcited semiconductor to study the polaronic properties. For a general non-equilibrium situation in principle also population effects contribute. However, for low carrier densities these corrections turn out to be small (cf. Chap. 5.1.5) and for high carrier densities additionally Coulomb-scattering effects have to be taken into account which completely change the picture (cf. Chap. 6.1).

Throughout this chapter we consider for the calculation weak polar coupling ($\alpha = 0.06$) self-assembled InGaAs QDs. Their energy spectrum shows with two confined shells, a s-shell and a two-fold degenerate p-shell, below a continuum of WL states, both for electrons and holes. It is schematically depicted in Fig. 2.2b. For the electrons a level spacing of $1.1 \hbar\omega_{\text{LO}}$ between s- and p-shell as well as between p-shell and WL is considered. Similarly for holes a level spacing of $0.4 \hbar\omega_{\text{LO}}$ is used. The QD density on the WL we consider amounts to $1 \times 10^{10} \text{ cm}^{-2}$. Further material parameters are summarized in Tab. B.1 and the interaction matrix elements are evaluated using the envelope wave-function model discussed in App. A.1. Deviations from these parameters are stated explicitly.

5.1.1 The polaron Green's function

In the framework of non-equilibrium GFs spectral properties are contained in the retarded GF, which via the spectral function (see next chapter) is connected to the density of states. The corresponding Dyson equation is solved in the time domain, which is more convenient in view of kinetic calculations (see Chap. 5.2.1). The polaronic retarded GF $G_{\alpha}^{\text{R}}(t)$ obeys the Dyson equation

$$\left(i\hbar\frac{\partial}{\partial t} - \epsilon_{\alpha}\right) G_{\alpha}^{\text{R}}(t) = \delta(t) + \int_0^t dt' \Sigma_{\alpha}^{\text{R}}(t-t') G_{\alpha}^{\text{R}}(t') , \quad (5.2)$$

for which we use the selfenergy

$$\Sigma_{\alpha}^{\text{R}}(t) = i\hbar \sum_{\beta} D_{\alpha\beta\alpha\beta}^{>}(t) G_{\beta}^{\text{R}}(t) , \quad (5.3)$$

calculated in the self-consistent RPA. A detailed discussion of the selfenergy is given in Chap. 4.2 and $D^{>}$ is defined according to Eq. (4.37). Eqs. (5.2)–(5.3) together with the initial condition $G_{\alpha}^{\text{R}}(0) = 1/i\hbar$ completely define the polaron problem for electrons. In the electron-hole picture, identical equations are obtained for holes. To illustrate the interpretation of the retarded GF, we consider non-interacting carriers whose GF follows from (5.2) for $\Sigma = 0$ and reads

$$G_{\alpha}^{\text{R},0}(\tau) = -\frac{i}{\hbar} \Theta(\tau) e^{-\frac{i}{\hbar}\epsilon_{\alpha}\tau} . \quad (5.4)$$

A renormalization of the form $\Sigma_\alpha(\tau) = (\Delta_\alpha + i\gamma_\alpha) \delta(\tau)$ gives rise to a shift Δ_α of the free-particle energy and a damping of the oscillation, reflecting a finite quasi-particle lifetime \hbar/γ_α . For the polaron problem, we solve the Dyson equation (5.2) together with Eq. (5.3) by introducing a renormalization function \mathcal{G} according to $G^R(\tau) = G^{R,0}(\tau) \mathcal{G}(\tau)$ and numerically solve the resulting equation for \mathcal{G} . Results are shown in Fig. 5.1, where the modulus of the electron and hole retarded GF is presented for the room temperature (300K) as well as for the low-temperature (10K) regime.

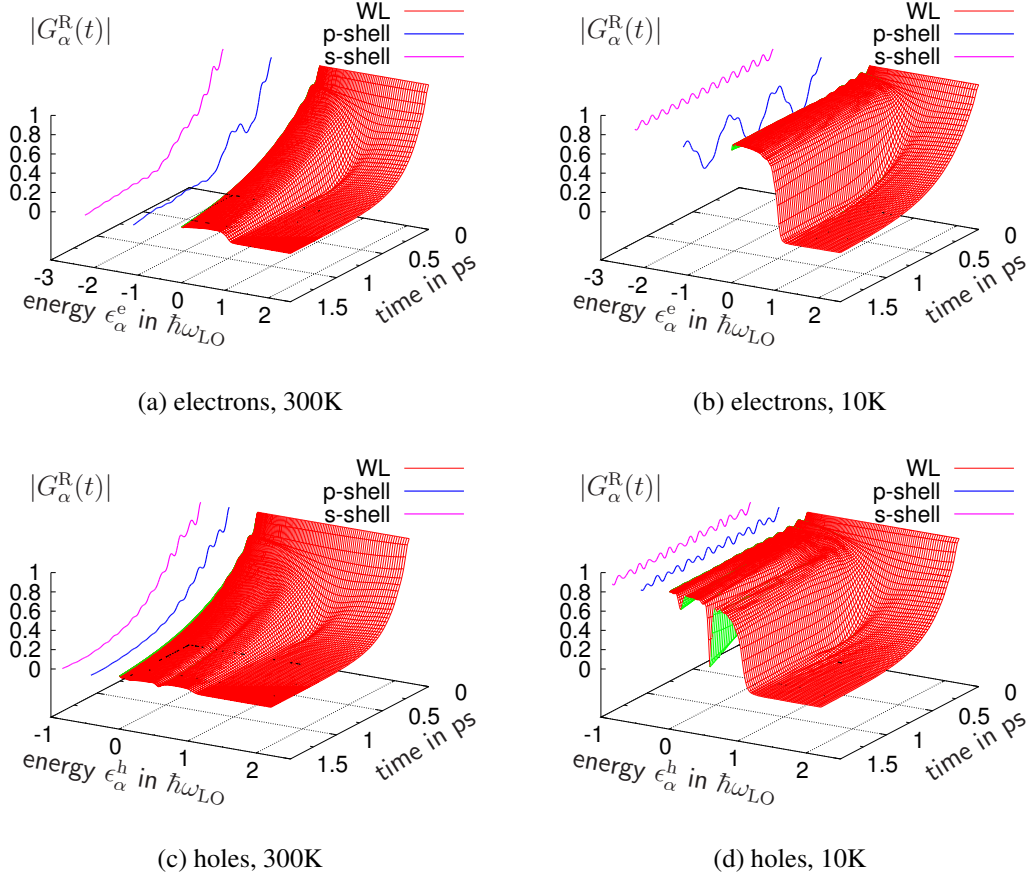


Fig. 5.1: Modulus of the electron and hole retarded GF for InGaAs QDs in the room- and low-temperature regime.

In Fig. 5.1 the modulus of the retarded GFs for QD and WL states is given as a function of the free-particle energy and time. The decay reflects the polaron lifetime and for both temperature regimes a *phonon threshold* is observed where the polaron lifetime is enhanced for WL states whose energies obey the condition $\epsilon_k < 1 \hbar\omega_{LO}$. For these states phonon emission processes are suppressed due to lacking final states and only phonon absorption processes contribute. The presence of QDs additionally leads to a reduced po-

laron lifetime for states below the phonon threshold that are connected to the QD states by multiple phonon processes. In the low temperature regime, the phonon threshold is more pronounced since phonon absorption processes are less likely than in the room temperature case and thus the polaron lifetime is enhanced further.

For WL states around the band edge $\mathbf{k} = 0$, the decay is superimposed by oscillations whose period of approximately 115 fs points towards phonon satellites. In case of QD states a plenty of superimposed oscillations are observed, indicating a complex sideband structure. A more detailed analysis of the polaron retarded GF is given in the following chapter by means of the spectral function.

5.1.2 The spectral function

A convenient way to discuss quasi-particle properties is to analyze the spectral function which is defined as

$$\widehat{G}_\alpha(\omega) = \frac{i}{2\pi} [G_\alpha^R(\omega) - G_\alpha^A(\omega)] = -\frac{1}{\pi} \text{Im } G_\alpha^R(\omega). \quad (5.5)$$

Here, the frequency dependence arises from a Fourier-transform with respect to the relative time.¹ The spectral function reflects the density of states by its properties

$$D(\hbar\omega) = \sum_\alpha \widehat{G}_\alpha(\hbar\omega), \quad \int d(\hbar\omega) \widehat{G}_\alpha(\hbar\omega) = 1. \quad (5.6)$$

In this sense \widehat{G}_α is the contribution of a state α to the density of states. To illustrate the interpretation, we consider non-interacting carriers whose spectral function

$$\widehat{G}_\alpha^0(\omega) = \frac{1}{\pi} \frac{\gamma_\alpha}{(\hbar\omega - \epsilon_\alpha)^2 + \gamma_\alpha^2} \quad (5.7)$$

is obtained from the Fourier-transform of (5.4) and shows in the limit $\gamma_\alpha \rightarrow +0$ δ -peaks at the free-particle energies. For WL states these peaks follow the energy dispersion $\epsilon_{\mathbf{k}} = \hbar^2 k^2 / 2m$. A renormalization of the form $\Sigma_\alpha = (\Delta_\alpha + i\gamma_\alpha)$ gives rise to Lorentzian-shaped resonances that are peaked at the shifted energies $\epsilon_\alpha^0 + \Delta_\alpha$. The line-width γ_α is connected to the quasi-particle lifetime. By a non-uniform energy shift Δ_α also a mass renormalization is included.

Results for the polaron spectral function for electrons, corresponding to Fig. 5.1, are shown in Fig. 5.2. We first focus on the room-temperature results. For the WL band-edge we find, compared to the free-particle spectral function, a polaron shift Δ and a broadening

¹Considering the two-time retarded GF $G^R(t, \tau)$ and performing a Fourier transformation with respect to the relative time results in a spectral function $\widehat{G}(\omega, t)$ also depending on the center time t .

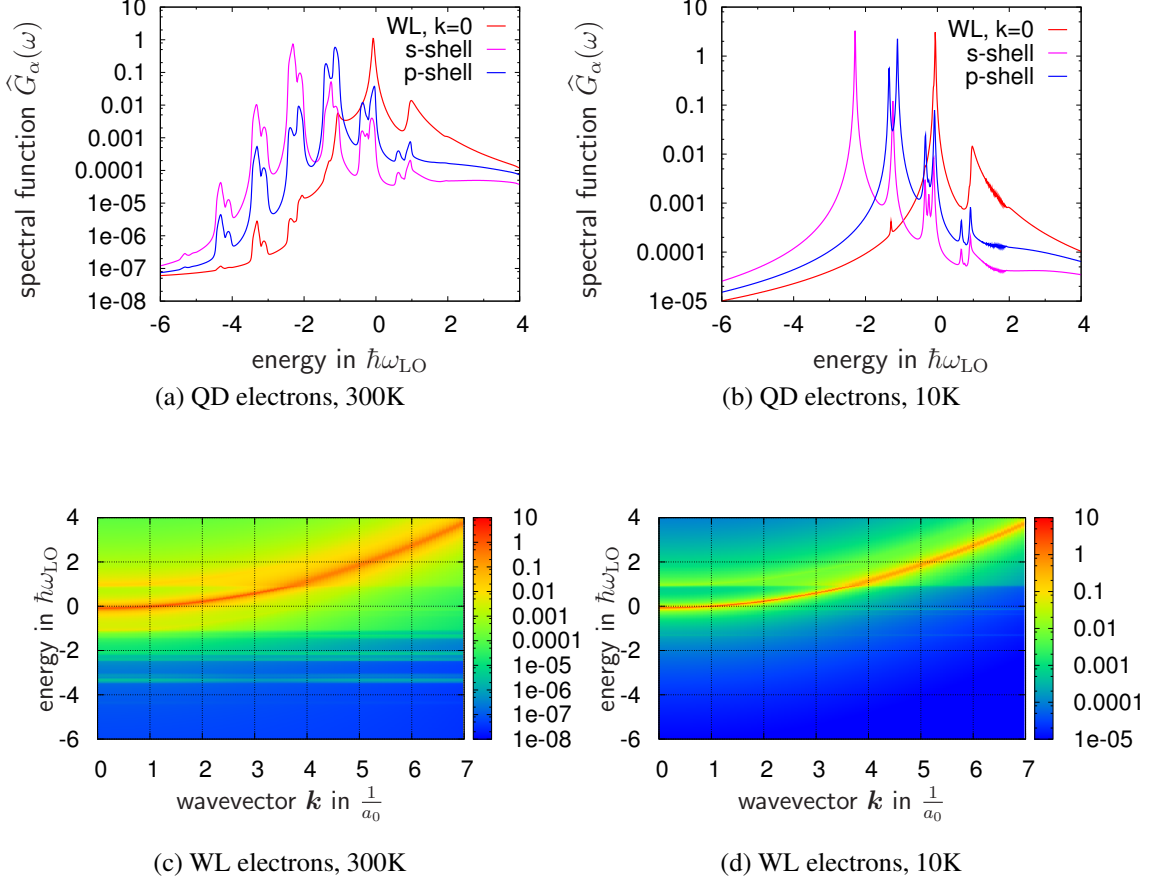


Fig. 5.2: Spectral function for QD and WL states of InGaAs QDs in the room- and low-temperature regime.

Γ of the main resonance. Furthermore, satellites due to phonon emission and absorption processes are found on the low and high energy side. These satellites give rise to the beating in the time domain with a frequency that corresponds to one LO-phonon energy. The main resonance as well as the phonon satellites follow a nearly parabolic dispersion as seen in Fig. 5.2c. For energies larger than the phonon threshold, the broadening of the main resonance drastically increases due to phonon emission processes which start to contribute. This feature can also be understood analytically in case of bulk semiconductors [121]. From the dispersion around $k \approx 0$ a polaron mass m^* can be extracted, that is in good agreement with the prediction from perturbation theory. A summary of the extracted polaron renormalizations is given in Tab. 5.1. Furthermore, dispersionless features due to the interaction with QD states are observed energetically below the band-edge. For the QD states the spectral function shown in Fig. 5.2a exhibits a sideband structure. One observes satellites spaced $1 \hbar\omega_{\text{LO}}$ apart, each splitted into two peaks. This hybridization

arises from the fact that the spectral position of the phonon satellites from the s-shell are close to those of the p-shell. For example, the spectral position of the first phonon-emission satellite of the s-shell is almost at the p-shell resonance. A more detailed analysis of the hybridization is given in the following chapter. For the low temperature regime the spectral function is shown in Fig. 5.2b,d. To numerically perform the Fourier transform an artificial broadening of $0.01\hbar\omega_{\text{LO}}$ meV is included. In the low temperature case phonon absorption processes are strongly suppressed because of the low phonon population. Therefore one observes in the spectral function only phonon replicas on the high energy side of the main pole, which correspond to phonon emission processes. Similar to the room-temperature case polaron renormalizations can be extracted. For the low-temperature case they are also summarized in Tab. 5.1.

		Δ in meV	Γ in meV	m^*/m_{eff}
300K	electrons	-2.79	1.11	1.03
	holes	-3.68	1.30	1.0
10 K	electrons	-2.11	0.13	1.03
	holes	-2.77	0.008	1.02

Tab. 5.1: Polaron renormalizations of the main WL resonance.

Via Eq. (5.6), the spectral function is connected to the density of states. In Fig. 5.3 corresponding results are presented for the room- and the low-temperature regime. The contribution from QD and WL states is given separately and the weight of the QD contribution is determined by the QD density of $1 \times 10^{10} \text{ cm}^{-2}$. Comparing the result with the Θ -like band-edge known from non-interacting carriers in quantum-well systems (cf. Fig. 2.1), we also find a constant polaron DOS above the band-edge. Below the band-edge, the δ -like free-particle DOS for QDs is strongly modified and the hybridized satellite structure of the polaron as well as the broadening due to the finite particle lifetime dominates.

The carrier-LO-phonon interaction contributes even in the case of an unexcited semiconductor where Coulomb effects are not present. Therefore Fig. 5.3 represents the *true DOS*, deviating from the free DOS often considered for discussions. In experiments usually an excited semiconductor is present whose DOS also contains Coulomb effects. For example, in case of coherent excitations the Coulomb interaction leads to the formation of a WL exciton [64] and for incoherent excitations multi-exciton resonances for the QD states appear [20, 140], depending on the number of confined carriers.

In summary, we find that the carrier-LO-phonon interaction strongly modifies the spectral properties. For WL states the spectral function shows a dominating main resonance. In this case the renormalizations are close to those obtained from perturbation theory. For QD states perturbation theory clearly fails. The satellite structure and hybridization effects

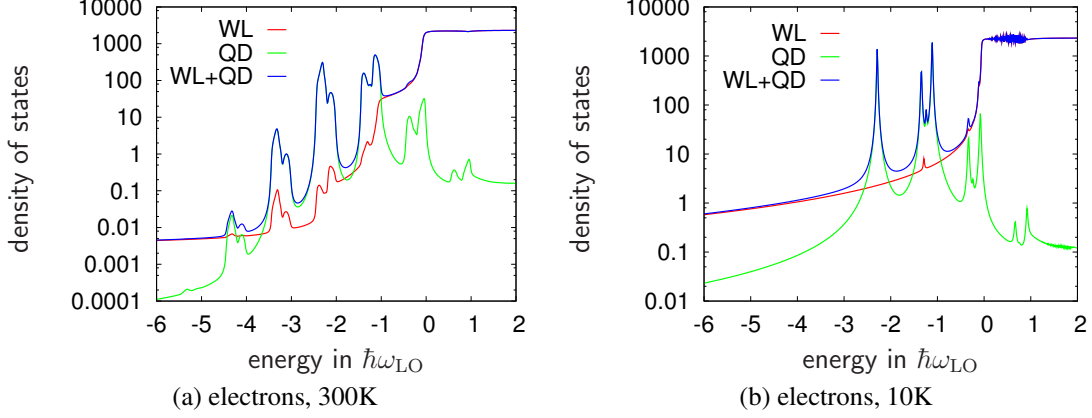


Fig. 5.3: Electronic density of states of unexcited self-assembled InGaAs QDs, including the carrier-LO-phonon interaction.

indicate an enhanced effective coupling even for the weak polar coupling GaAs material system.

5.1.3 Strong-coupling effects

For a better understanding of the hybridization effects observed in the QD polaron spectral function (Fig. 5.2) we consider in the following a simplified two-level system. This model enables us to analyze separately the diagonal and off-diagonal contributions to the interaction. As limiting cases the so-called independent-boson model and the Jaynes-Cummings model are obtained. From their spectral functions the satellite structure of the RPA result can be understood in detail.

The corresponding model Hamiltonian for the two-level system reads

$$\hat{H} = \epsilon_\alpha \hat{\alpha}^\dagger \hat{\alpha} + \epsilon_\beta \hat{\beta}^\dagger \hat{\beta} + \hbar\omega_{\text{LO}} \hat{b}^\dagger \hat{b} + \sum_{i,j \in \{\alpha,\beta\}} M_{i,j} \hat{i}^\dagger \hat{j} (\hat{b}^\dagger + \hat{b}), \quad (5.8)$$

where the lower state $|\alpha\rangle$ and the upper state $|\beta\rangle$ are coupled by the carrier-LO-phonon interaction. We restrict ourselves to the interaction with one single phonon mode, which by means of a Wannier representation $\hat{b}_q = \frac{1}{\sqrt{N}} \sum_{\mathbf{R}} e^{i\mathbf{q}\cdot\mathbf{R}} \hat{b}_{\mathbf{R}}$ for the creation/annihilation operators for phonons, corresponds to phonons localized at the QD position $\mathbf{R} = 0$. In this case the interaction matrix elements are given by $M_{i,j} = \frac{1}{\sqrt{N}} \sum_{\mathbf{q}} M_{i,j}(\mathbf{q})$. A more sophisticated treatment of this model, including coupling to different LO-phonon modes, is presented by Stauber et al. [130, 131].

Independent-boson and Jaynes-Cummings model

Considering only diagonal coupling $M = M_{i,i}$ and restricting to a single state, we recover the independent-boson model (IBM)

$$\hat{H}^{\text{IBM}} = \epsilon_\alpha \hat{a}^\dagger \hat{a} + \hbar\omega_{\text{LO}} \hat{b}^\dagger \hat{b} + M \hat{a}^\dagger \hat{a} [\hat{b}^\dagger + \hat{b}] . \quad (5.9)$$

A diagonalization is obtained easily by a canonical transformation and introducing the new operators $\hat{B}^{(\dagger)} = \hat{b}^{(\dagger)} - M/\hbar\omega_{\text{LO}} \hat{c}^\dagger \hat{c}$ [97]. The corresponding eigenenergies form a phonon ladder that is renormalized by the polaron shift $\Delta = M^2/\hbar\omega_{\text{LO}}$.

On the contrary, when considering only resonant off-diagonal coupling $\widetilde{M} = M_{i,j}$ with $i \neq j$ we recover the Jaynes-Cummings model (JCM)

$$\hat{H}^{\text{JCM}} = \epsilon_\alpha \hat{a}^\dagger \hat{a} + \epsilon_\beta \hat{b}^\dagger \hat{b} + \hbar\omega_{\text{LO}} \hat{b}^\dagger \hat{b} + \widetilde{M} [\hat{a}^\dagger \hat{b} \hat{b}^\dagger + \hat{b}^\dagger \hat{a} \hat{b}] . \quad (5.10)$$

In this case the interaction couples the states $|0, 1, n_{\text{LO}}\rangle$ and $|1, 0, n_{\text{LO}} + 1\rangle$.² Depending on the detuning $\delta = \epsilon_\beta - \epsilon_\alpha$, these states are (nearly) degenerate and the interaction introduces a level repulsion. For the eigenenergies the Jaynes-Cummings ladder

$$\epsilon_{n,\pm} = \frac{1}{2} (\epsilon_\alpha + \epsilon_\beta + (2n_{\text{LO}} + 1) \hbar\omega_{\text{LO}}) \pm \sqrt{\delta^2 + 4\widetilde{M}^2 (n_{\text{LO}} + 1)} \quad (5.11)$$

is found, where the level splitting increases with increasing number of phonons.

Spectral function for the independent-boson model

The equilibrium retarded GF is given by [129]

$$G_\alpha^R(t) = \frac{1}{i\hbar} \Theta(t) \langle \hat{a}_\alpha(t) \hat{a}_\alpha^\dagger(0) \rangle , \quad (5.12)$$

where the average is evaluated with respect to the particle vacuum, i.e. the corresponding diagrams contain no closed loops. For simplicity, state indices are omitted in the following since only one single state and diagonal coupling is considered.

In the diagrammatic representation of the GF for the IBM, shown in Fig. 5.4, we find that in any diagram the internal vertex of the first interaction line is connected to the rest of the diagram by two free GFs. Note, that the second term on the right-hand side in Fig. 5.4 schematically represents all possible diagrams that contain at least one interaction line. As the free GFs for the same state obey the semigroup property $G_\alpha^0(t_2, t') G_\alpha^0(t', t_3) = 1/i\hbar G_\alpha^0(t_2, t_3)$ and the internal interaction vertex is state diagonal, we find the internal end

²The notation for the Fock representation is $|n_\alpha, n_\beta, n_{\text{LO}}\rangle$.

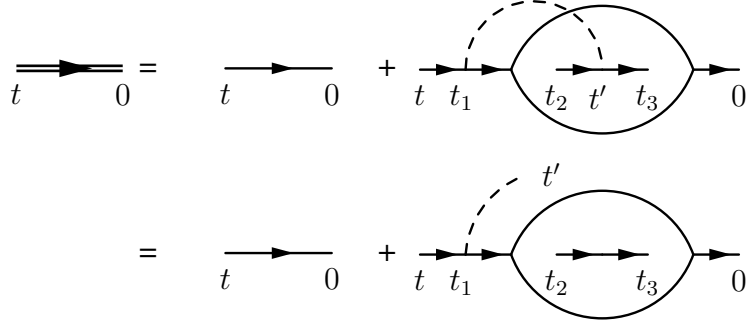


Fig. 5.4: Diagrammatic representation of the Green's function for the IBM.

t' of the interaction line disconnected. For the corresponding diagram we may take the time derivative and obtain for $t > 0$ the differential equation

$$\left(i\hbar \frac{\partial}{\partial t} - \epsilon \right) G^R(t) = \frac{1}{i\hbar} \int_0^t dt' D(t-t') G^R(t) \quad (5.13)$$

with the initial condition $G(0) = 1/i\hbar$ and $D(t-t')$ containing the interaction matrix elements and the phonon propagator according to Eq. 4.37. Note, that as all possible diagrams have to be considered the full GF is reconstructed. Integration of Eq. 5.13 yields

$$G^R(t) = \frac{1}{i\hbar} \exp \left[-\frac{i}{\hbar} \epsilon t - \frac{1}{\hbar^2} \underbrace{\int_0^t dt' \int_0^{t'} dt'' i\hbar D(t'')}_{\phi(t)} \right]. \quad (5.14)$$

with $\phi(t)$ defined by the conditions $\phi(0) = 0$ and $\dot{\phi}(0) = 0$. Denoting

$$R(t) = \sum_{\mathbf{q}} \frac{M_{\mathbf{q}}^2}{\omega_{\text{LO}}^2} [(N_{\text{LO}} + 1) e^{-i\omega_{\text{LO}} t} + N_{\text{LO}} e^{i\omega_{\text{LO}} t}] \quad (5.15)$$

we find the second derivative $\ddot{R}(t) = -i\hbar D(t)$ and $\phi(t) = R(t) - t\dot{R}(0) - R(0)$. Here $\dot{R}(0) = -i \sum_{\mathbf{q}} \frac{M^2}{\hbar\omega_{\text{LO}}} \equiv -i\Delta$ denotes the polaron shift and $R(0) = \sum_{\mathbf{q}} \frac{M^2}{\hbar\omega_{\text{LO}}} (1+2N_{\text{LO}}) \equiv \lambda$ is the Huang-Rhys factor [97]. From an expansion of the GF,

$$G^R(t) = \frac{1}{i\hbar} e^{-\lambda} e^{-i(\epsilon-\Delta)t} \times \sum_n \frac{1}{n!} \left[\left(\frac{M^2 (N_{\text{LO}} + 1)}{(\hbar\omega_{\text{LO}})^2} \right)^n e^{-in\omega_{\text{LO}} t} + \left(\frac{M^2 N_{\text{LO}}}{(\hbar\omega_{\text{LO}})^2} \right)^n e^{in\omega_{\text{LO}} t} \right], \quad (5.16)$$

it is found that the spectral function in Fourier space consists of δ peaks spaced one $\hbar\omega_{\text{LO}}$ apart.

Spectral function for the Jaynes-Cummings model

Starting from the expression (5.12) for the retarded GF we can directly evaluate the expectation value according to $\langle \dots \rangle = \frac{1}{Z} \sum_n e^{-\frac{\omega_{\text{LO}} n}{k_B T}} \langle 0, 0, n | \dots | 0, 0, n \rangle$ with $Z^{-1} = 1 - e^{-\frac{\omega_{\text{LO}}}{k_B T}}$ [129]. For the carrier creation/annihilation operator we use the Heisenberg representation $\hat{a}^{(\dagger)}(t) = e^{\pm \frac{i}{\hbar} \hat{H} t} \hat{a}^{(\dagger)} e^{\mp \frac{i}{\hbar} \hat{H} t}$ and find together with Eq. (5.12)

$$G_\alpha^R(t) = \frac{\Theta(t)}{i\hbar} \frac{1}{Z} \sum_{n \geq 0} e^{-\frac{\hbar\omega_{\text{LO}} n}{k_B T}} e^{in\omega_{\text{LO}} t} \langle 1, 0, n | e^{-\frac{i}{\hbar} \hat{H} t} | 1, 0, n \rangle . \quad (5.17)$$

Transforming into Fourier space and inserting the JCM Hamiltonian (5.10) yields

$$G_\alpha^R(\omega) = \frac{1}{Z} \sum_{n \geq 0} e^{-\frac{\hbar\omega_{\text{LO}} n}{k_B T}} \langle 1, 0, n | \begin{pmatrix} \hbar\omega - \epsilon_\alpha & -\sqrt{n} \widetilde{M}^* \\ -\sqrt{n} \widetilde{M} & \hbar\omega + \hbar\omega_{\text{LO}} - \epsilon_\beta \end{pmatrix}^{-1} | 1, 0, n \rangle , \quad (5.18)$$

and after evaluating the inverse we finally obtain the GFs

$$G_\alpha^R(\omega) = \frac{1}{Z} \sum_{n \geq 0} e^{-\frac{\hbar\omega_{\text{LO}} n}{k_B T}} \frac{1}{\hbar\omega - \epsilon_\alpha - \frac{\widetilde{M}^2 n}{\hbar(\omega + \omega_{\text{LO}}) - \epsilon_\beta}} , \quad (5.19)$$

$$G_\beta^R(\omega) = \frac{1}{Z} \sum_{n \geq 0} e^{-\frac{\hbar\omega_{\text{LO}} n}{k_B T}} \frac{1}{\hbar\omega - \epsilon_\beta - \frac{\widetilde{M}^2(n+1)}{\hbar(\omega - \omega_{\text{LO}}) - \epsilon_\alpha}} . \quad (5.20)$$

For each state two series of sidebands occur with δ -peaks at

$$\epsilon_{\alpha,n} = \frac{1}{2} \left\{ (\epsilon_\alpha + \epsilon_\beta - \hbar\omega_{\text{LO}}) \pm \sqrt{\frac{1}{4} (\epsilon_\alpha - \epsilon_\beta + \hbar\omega_{\text{LO}})^2 + \widetilde{M}^2 n} \right\} , \quad (5.21)$$

$$\epsilon_{\beta,n} = \frac{1}{2} \left\{ (\epsilon_\alpha + \epsilon_\beta + \hbar\omega_{\text{LO}}) \pm \sqrt{\frac{1}{4} (\epsilon_\alpha - \epsilon_\beta + \hbar\omega_{\text{LO}})^2 + \widetilde{M}^2 (n+1)} \right\} . \quad (5.22)$$

In case of resonance, the sideband contribution reduces to $[\widetilde{M}^2 n]^{1/2}$ for the ground state and to $[\widetilde{M}^2 (n+1)]^{1/2}$ for the excited state. For the ground state a zero phonon line is observed, whereas for the excited state phonon emission is always possible, resulting in a splitting even for the zero-phonon contribution.

Validity of the random-phase approximation

So far, we introduced a simplified two-level model for the QD states and presented exact solutions for the polaron GF arising from the independent-boson and the Jaynes-Cummings

model. This enables us to investigate the validity of the RPA, which we utilized in the calculations presented in Chap. 5.1.1–5.1.2, for these systems.

Using the RPA selfenergy (4.42), the corresponding GF for the two-level system is given by

$$G_{\lambda}^R(\omega) = \frac{1}{\hbar\omega - \epsilon_{\lambda} - \sum_{\gamma} M_{\lambda\gamma}^2 \left[N_{\text{LO}} G_{\gamma}^R(\hbar(\omega + \omega_{\text{LO}})) + (N_{\text{LO}} + 1) G_{\gamma}^R(\hbar(\omega - \omega_{\text{LO}})) \right]} , \quad (5.23)$$

where $\lambda, \gamma \in \{\alpha, \beta\}$. Here, diagonal as well as off-diagonal coupling is included. Restricting to resonant off-diagonal coupling only, corresponding to the JCM, the GFs for ground and excited state are

$$G_{\alpha}^R(\omega) = \frac{1}{\hbar\omega - \epsilon_{\alpha} - \widetilde{M}^2 N_{\text{LO}} G_{\beta}^R(\hbar(\omega + \omega_{\text{LO}}))} , \quad (5.24)$$

$$G_{\beta}^R(\omega) = \frac{1}{\hbar\omega - \epsilon_{\beta} - \widetilde{M}^2 (N_{\text{LO}} + 1) G_{\alpha}^R(\hbar(\omega - \omega_{\text{LO}}))} . \quad (5.25)$$

In comparison with the JCM (5.19), we find that the RPA result contains the average phonon number N_{LO} whereas in the JCM explicitly the average is taken over all phonon numbers n . Correspondingly, the splittings observed in the RPA result are $[\widetilde{M}^2 N_{\text{LO}}]^{1/2}$ and $[\widetilde{M}^2 (N_{\text{LO}} + 1)]^{1/2}$, respectively. This can be seen by an iterative solution of Eqs. 5.24–5.25, starting with free retarded GFs.

A comparison of the RPA result with the exact solution of the JCM is presented in Fig. 5.5a. For the calculation we consider a level spacing of $1.1 \hbar\omega_{\text{LO}}$, a temperature of 300 K and a diagonal and off-diagonal coupling of $M^2 = 0.05 \hbar\omega_{\text{LO}}$ and $\widetilde{M}^2 = 0.02 \hbar\omega_{\text{LO}}$, respectively. The exact solution shows the side-band structure according to the JCM (Eqs. (5.21) and (5.22)) as well as a zero-phonon line for the ground state. For the excited state no zero-phonon line is observed since the possibility of phonon emission already gives rise to hybridization, even when no phonons are in the system. Both results, the RPA and the exact solution, show good agreement especially when introducing a small broadening which due to a finite phonon lifetime is always present in the system.

Considering diagonal as well as off-diagonal coupling, also a numerical diagonalization of the full Hamiltonian (5.8) can be performed for a finite number of phonons. The spectral function is evaluated similar to Eq. (5.18). A comparison of the full diagonalization and the corresponding RPA calculation is presented in Fig. 5.5b and 5.5c for the s-shell and the p-shell, respectively. Due to the off-diagonal coupling (JCM) the inclusion of diagonal coupling (IBM) contributions results in multiple phonon satellites, in addition to the hybridization. Also in this case a good agreement is obtained when introducing a small broadening, especially for the main peaks.

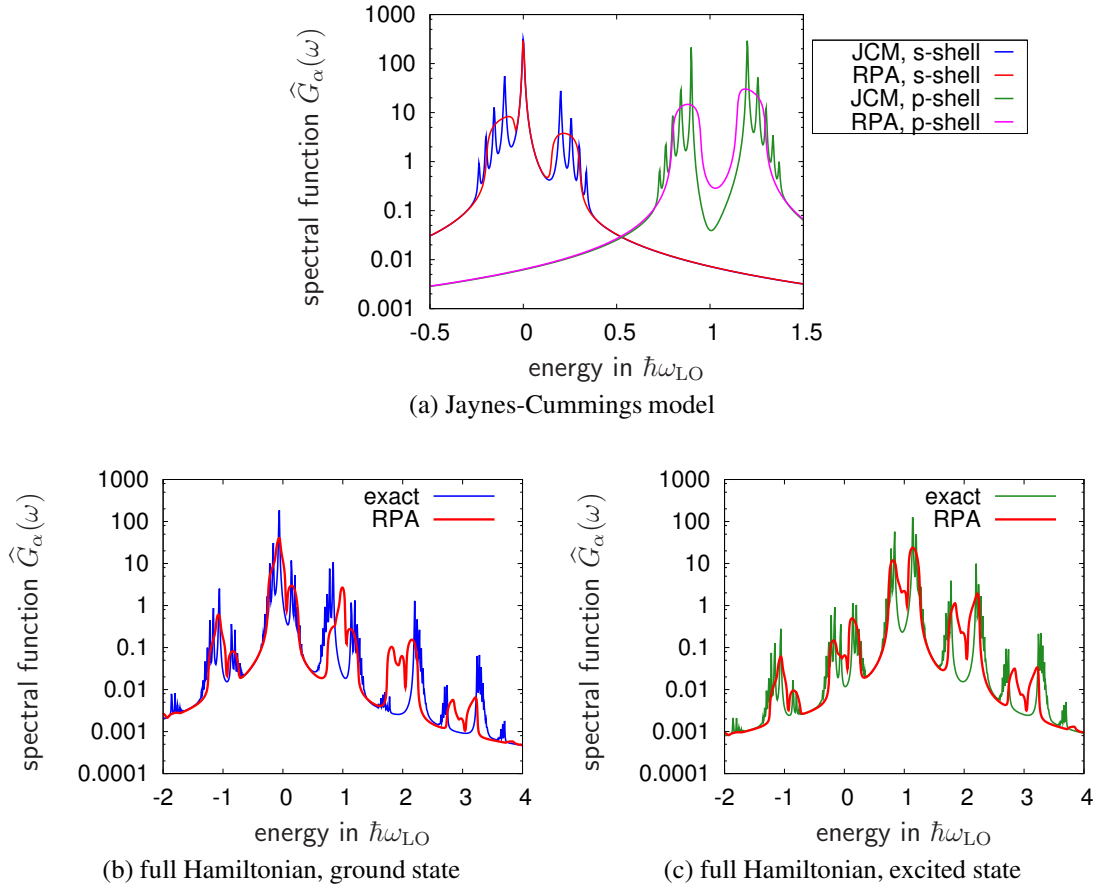


Fig. 5.5: The Spectral functions for a two-level system obtained from RPA and diagonalization method are compared for the JCM (a) and the full Hamiltonian (b,c).

In conclusion, the rather technical analysis of the hybridization effects observed in the spectral function yields two important results. First, the hybridized satellite peaks in the spectral function can be understood in detail. Whereas the phonon-satellite structure occurs due to the diagonal coupling (IBM), the hybridization effects can be assigned to the off-diagonal coupling (JCM). Furthermore the shape of the single peaks in the RPA result can be traced back to the contribution of different phonon numbers. Second, as the RPA was originally developed for the description of plasmas, their validity for discrete QD systems might be questioned. Our results show that the differences between a numerically exact model and a RPA calculation become small when considering a small broadening due to a finite phonon lifetime. Therefore, the RPA can be regarded as a good approximation. Its verification for QD systems states an important result. Consistent calculations of the carrier scattering (cf. Chap. 5.2.1) and polarization dephasing (cf. Chap. 6.1) are directly possible when using the RPA. A kinetic calculation in the basis states of an exact

diagonalization would be much more difficult, especially when including the energetically nearby continuum of WL states. Thus the RPA calculations are also suitable to study the interplay of discrete QD and continuous WL states.

5.1.4 Variation of the level-spacing

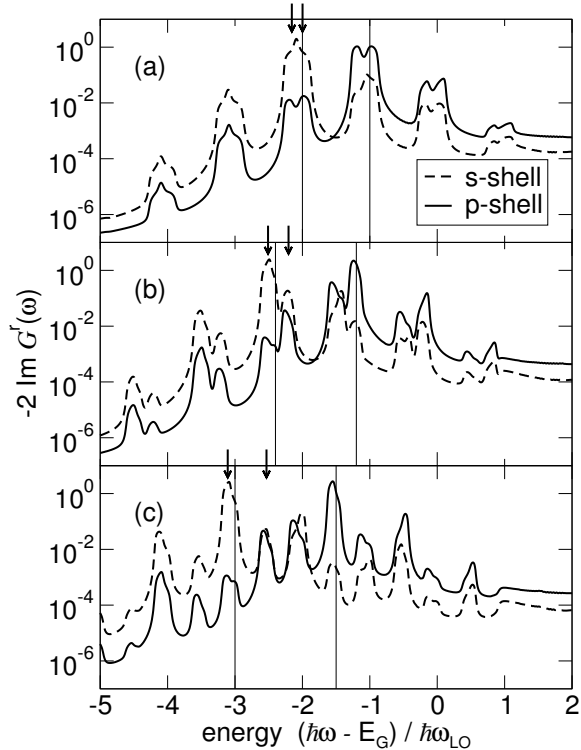


Fig. 5.6: QD polaron spectral function for electrons and various detunings at room temperature.

After analyzing the satellite structure of the QD polaron spectral function we return to the QD-WL system with the retarded GF given by the Dyson equation (5.2). An important parameter for the QD polaron is the level spacing. So far in all calculations a level spacing of $1.1 \hbar\omega_{\text{LO}}$ was considered. To study its influence on the spectral function, in Fig. 5.6 results for various detunings from the LO-phonon energy are presented, ranging from resonance to a mismatch of 40%. The calculations include QD and WL states, but for better visibility only the curves for the s- and p-shell are displayed. For the WL states the the spectral function is only weakly influenced by the coupling to the QDs as can be seen in Fig. 5.2. For the QD states one observes in all three cases (Fig. 5.6) a multi-peak-structure which contains a series of phonon satellites spaced by the LO-phonon energy and their hybridization.

From top to bottom the peak splitting increases with the detuning, as indicated by arrows. However, for larger detunings the assignment of the different peaks is not obvious at first glance, but can be performed according to the analysis presented in the previous chapter. Thus also for different detunings the structure of the spectral function can be understood and traced back to contributions from the diagonal and off-diagonal coupling.

5.1.5 Finite-density polaron

So far the original polaron problem was investigated, describing the quasi-particle renormalizations due to the carrier-LO-phonon interaction in an unexcited system. This case can be referred to as the zero-density polaron. In the following we consider a finite carrier density in the system, leading to the finite-density polaron. The influence of population effects is studied for the situation where, after optical excitation, all coherences are dephased and incoherent carriers form a quasi-equilibrium distribution.

In the context of a two-time calculation, cf. Eq. (3.68)–(3.71), which consistently treats polaron properties and carrier kinetics, Gartner et al. [83] have shown that the retarded GF for the zero-density polaron completely defines the history of the system prior to excitation. The two-time approach also describes the transient regime which includes carrier excitation and redistribution. This results in a time-dependent spectral function $\hat{G}(t, \omega)$. For the following discussion we restrict ourselves to the limiting case $t \rightarrow \infty$ and neglect effects of the transient regime. We assume that after optical excitation the carrier distribution reached its steady-state value (cf. Chap. 5.3) and consider timescales where carrier recombination is negligible. In this situation the polaron problem decouples from the kinetic problem, as in the zero-density case, and only a constant carrier distribution enters the theory.

For the finite-density polaron, the second term in the polaron selfenergy (4.42) has to be included. The two-time propagator involved can be mapped onto the time-diagonal by means of the GKBA (3.74). Furthermore restricting to state-diagonal retarded GFs and propagators we obtain the selfenergy

$$\begin{aligned} \Sigma_{12}^R(t_1, t_2) = i\hbar \sum_3 & M_{13}(\mathbf{q}) M_{32}^*(\mathbf{q}) \\ & \times G_{33}^R(t_1, t_2) [d^<(t_2, t_1) + i\hbar G_{33}^<(t_2) d^R(t_2, t_1)] . \end{aligned} \quad (5.26)$$

That indeed the transient regime does not contribute in the limit $t \rightarrow \infty$ is seen in the Dyson equation (5.2). We find that the retarded GF contained in the selfenergy (5.26) runs backwards in time under an integral. Therefore, the GFs themselves limit the memory depth if they decay sufficiently fast. Especially for the room-temperature regime this verifies our assumption of constant populations $G^<$ for late times. In addition to the RPA selfenergy (4.42), also the instantaneous selfenergies contribute to the retarded problem.

Namely the Coulomb Hartree and Fock terms (4.8)–(4.9) as well as the phonon Hartree selfenergy (4.45) have to be considered. As these self-energies are real quantities which simply give rise to energy shifts, they are not included in the following. Furthermore, also effects due to Coulomb scattering (cf. Eq. 4.23) are not taken into account. They are discussed in Chap. 6.1.

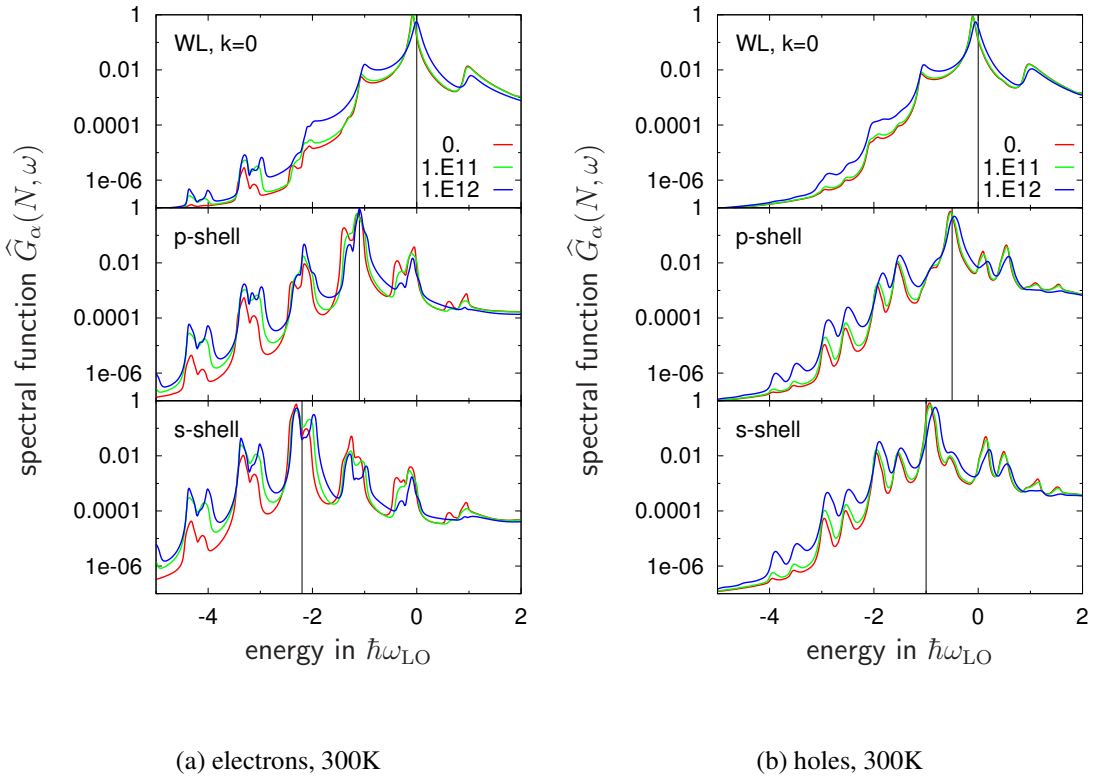


Fig. 5.7: Spectral function of the finite-density polaron for electrons and holes at room temperature and for various carrier densities in cm^{-2} .

The numerical solution of the Dyson equation and the calculation of the spectral function is performed similar to the approach presented in Chap. 5.1.1–5.1.2. Corresponding results for the finite-density polaron spectral function at room temperature are compared with the zero-density polaron in Fig. 5.7. For the calculation we considered steady-state carrier densities of $1 \times 10^{11} \text{ cm}^{-2}$ and $1 \times 10^{12} \text{ cm}^{-2}$. Up to carrier densities of $1 \times 10^{10} \text{ cm}^{-2}$ almost no difference to the zero-density polaron can be observed. For higher carrier densities the weight of the phonon absorption satellites increases whereas the weight of the phonon emission satellites decreases. Furthermore, for high carrier densities a small shift and an additional broadening can be observed.

We find that considerable corrections to the zero density polaron are obtained only for carrier densities where Coulomb scattering becomes important. Therefore, the zero-density polaron is a good approximation and population effects will not be included in the following discussions for the low carrier-density regime.

5.2 The phonon-bottleneck controversy

In the previous chapter, the quasi-particles of the carrier-LO-phonon interaction is discussed. This chapter focuses on their influence on carrier-scattering processes. A successful application of QDs in light-emitting devices requires fast carrier scattering towards the energetically lowest states. For low carrier densities one assumes that the contribution of Coulomb scattering to carrier relaxation processes can be neglected. In this case the most efficient relaxation channel is provided by the collision with LO phonons. As elaborated in Chap. 2, the LO phonons exhibit an almost flat dispersion. Because of the flat phonon dispersion and the discrete energy spectrum of QDs, the scattering efficiency of LO phonons was questioned in these systems.

Considering two states α and β , the corresponding transition rate in terms of time dependent perturbation theory [141] is given by Fermi's golden rule,

$$W_{\alpha\beta} = \frac{2\pi}{\hbar} \sum_{\mathbf{q}} |M_{\alpha\beta}(\mathbf{q})|^2 \left[(N_{\mathbf{q}} + 1) \delta(\epsilon_{\alpha} - \epsilon_{\beta} - \hbar\omega_{\mathbf{q}}) + N_{\mathbf{q}} \delta(\epsilon_{\alpha} - \epsilon_{\beta} + \hbar\omega_{\mathbf{q}}) \right]. \quad (5.27)$$

For a phonon bath in thermal equilibrium, $N_{\mathbf{q}}$ is a Bose-Einstein distribution with the lattice temperature and the δ -functions ensure strict energy conservation in the $\alpha \rightarrow \beta$ transition process assisted by either the emission ($\propto N_{\mathbf{q}} + 1$) or the absorption ($\propto N_{\mathbf{q}}$) of a phonon. Including Pauli-blocking effects, the temporal evolution of the population of state α can be described by the Boltzmann kinetic equation

$$\frac{\partial f_{\alpha}}{\partial t} = \sum_{\beta} \left\{ W_{\beta\alpha}(1 - f_{\alpha})f_{\beta} - W_{\alpha\beta}(1 - f_{\beta})f_{\alpha} \right\} \quad (5.28)$$

which contains in-scattering ($\propto 1 - f_{\alpha}$) and out-scattering ($\propto f_{\alpha}$) terms that are weighted with the corresponding transition rates. The relaxation properties of the Boltzmann kinetics are well understood and the following properties can be proven analytically:

1. The number of carriers $\sum_{\alpha} f_{\alpha}$ is conserved.
2. Positivity is preserved, i.e., if at $t = 0$ one has $f_{\alpha} \geq 0$ then this remains true at any later time.
3. The Fermi distribution $f_{\alpha} = [e^{-(\epsilon_{\alpha} - \mu)/k_B T} + 1]^{-1}$ is a steady-state solution by means of detailed balance scattering.

4. This steady state is the large time limit of the solution $f_\alpha(t)$ for any positive initial condition *provided* a certain connectivity property holds.

The connectivity property is fulfilled if any state of the carrier system can be reached from any other state through a chain of transitions having non-zero rates. The temperature of the stationary Fermi distribution is the lattice temperature and the chemical potential is fixed by the total number of carriers. If the set of carrier states is not connected in the above sense, any connected component behaves like a separate fluid and reaches equilibrium with its own chemical potential.

As satisfying as this picture looks, several problems arise here. The carrier-phonon interaction is essential as a relaxation mechanism but the carrier energies themselves are taken as if unaffected by it. In the energy conserving δ -functions and in the final Fermi distribution these energies appear as unperturbed. This corresponds to a low-coupling regime, which may not be valid in practical situations. Even in weakly polar semiconductors like GaAs, the confined nature of the states in quantum wells and even more so in quantum dots, gives rise to an enhanced effective interaction [132]. For higher coupling constants one expects departures from the simple picture discussed above. Moreover, in the case of a strong coupling and with the inclusion of memory effects, neglected in the Markovian limit, the energy conservation is not expected to hold. Finally, and specifically for LO phonons, their dispersionless spectrum associated with strict energy conservation turns a real QD system into a disconnected one, barring the level-spacing accidentally matches exactly the LO-phonon energy. Indeed, each carrier can move only up and down a ladder with fixed steps of size $\hbar\omega_{\text{LO}}$ but cannot jump on states outside this ladder. A *phonon bottleneck* effect in QDs was predicted on these grounds [142].

The phonon-bottleneck problem still receives considerable interest and in the literature experiments in favor [40, 41] as well as against [42, 43] it are presented. Theoretical investigations of this subject include several mechanisms whose main effect is the broadening of the spectral function due to for example the inclusion of a small LO-phonon dispersion [142] or a finite LO-phonon lifetime [143, 144]. Also second order processes have been investigated [145], where an energy mismatch is circumvented by the help of LA phonons. However, these inclusions allow for LO-phonon scattering only in a small spectral range around the exact energy conservation condition.

In this chapter a more fundamental insight into the carrier-phonon scattering mechanism is presented. The picture includes the influence of the polaron properties that have been discussed in Chap. 5.1. Especially the satellite structure and the hybridization effects turn out to be important for the scattering between QD states. In a quantum-kinetic treatment, the influence of these renormalizations on carrier scattering as well as non-Markovian effects are investigated. With this treatment one overcomes the limitations of the above discussed approaches which are restricted to perturbation theory. As will be shown, fundamental different results are obtained. The discussion starts with the fundamental scattering mechanism and the long-time limit of the kinetics for room temperature. In further in-

vestigations also low temperatures are considered and a theory-experiment comparison is presented.

5.2.1 Polaron scattering

For a deeper understanding of the carrier-phonon scattering mechanism we employ the framework of non-equilibrium GFs (cf. Chap. 3.2). The resulting quantum-kinetic equations consistently contain the influence of the polaron properties discussed in Chap. 5.1. We can proceed quickly as the Kadanoff-Baym equations and the selfenergies are discussed extensively in Chap. 3.3–4. The quantum kinetic description of carrier scattering is obtained from the collision term (3.72) where we use the RPA phonon selfenergy (4.42) and apply the GKBA (3.74). For homogeneous systems only diagonal GFs $G_{\mathbf{k},\mathbf{k}}$ contribute due to momentum conservation, which can be seen from the selfenergy (4.42). In general this is not the case for non-homogeneous systems. However, the so-called diagonal approximation, where only diagonal GFs are considered, has been shown to be reasonable for QD systems [146, 147]. Formally, this amounts to neglecting GFs which are off-diagonal in the state index, but still keeping off-diagonal terms with respect to the band index.

For the discussion of the carrier-phonon scattering mechanism we restrict the following analysis to the particle scattering. Considering the contributions discussed above, we finally obtain for each band a the quantum kinetic scattering term

$$\begin{aligned} \frac{d}{dt} f_\alpha^a &= 2\text{Re} \int_{-\infty}^t dt_2 \sum_\beta G_\beta^{\text{R},a}(t, t_2) [G_\alpha^{\text{R},a}(t, t_2)]^* \\ &\quad \times \left\{ -f_\alpha^a(t_2) [1 - f_\beta^a(t_2)] D_{\alpha\beta\alpha\beta}^{>,aa}(t, t_2) \right. \\ &\quad \left. + [1 - f_\alpha^a(t_2)] f_\beta^a(t_2) D_{\alpha\beta\alpha\beta}^{<,aa}(t, t_2) \right\}. \end{aligned} \quad (5.29)$$

In- and out-scattering contributions are found, similar to the Boltzmann kinetic equation (5.28). Additionally, memory effects are included and the energy conservation condition is expressed in terms of polaronic GFs. At this point the polaron properties discussed in Chap. 5.1 enter the kinetic calculation. Due to the memory integral, Eq. (5.29) includes a complex interplay between the time-dependent energy conservation condition and memory effects. Nevertheless, a clear picture how the polarons influence the energy conservation condition can be obtained when considering the Markovian limit $f_\alpha(t_2) \approx f_\alpha(t)$. In this case the quantum kinetic equation (5.29) reduces to

$$\frac{\partial f_\alpha}{\partial t} = \sum_\beta \left[\Lambda_{\alpha\beta}^{<,a}(t) [1 - f_\alpha^a(t)] f_\beta^a(t) - \Lambda_{\beta\alpha}^{>,a}(t) f_\alpha^a(t) [1 - f_\beta^a(t)] \right] \quad (5.30)$$

with the scattering kernel

$$\Lambda_{\alpha\beta}^{\gtrless,a} = 2\text{Re} \int_0^t dt_2 i\hbar D_{\alpha\beta\alpha\beta}^{\gtrless,aa}(t, t_2) G_\alpha^{\text{R},a}(t, t_2) [G_\beta^{\text{R},a}(t, t_2)]^*. \quad (5.31)$$

In a strict sense, this limit is only valid for steady-state situations. The product of retarded GFs in the time domain corresponds in the frequency domain to an overlap integral between the spectral functions of the two states involved in the scattering event. Due to the phonon propagator contained in D^{\gtrless} (cf. Eq. 4.37) a shift of a phonon frequency is introduced and we find the scattering kernel

$$\Lambda_{\alpha\beta}^{\gtrless,a} = \sum_{\mathbf{q}} |M_{\alpha\beta}(\mathbf{q})|^2 \int \frac{d\omega}{2\pi} \widehat{G}_{\alpha}^a(\omega) \left\{ (1 + N_{\text{LO}}) \widehat{G}_{\beta}^a(\omega + \omega_{\text{LO}}) + N_{\text{LO}} \widehat{G}_{\beta}^a(\omega - \omega_{\text{LO}}) \right\}. \quad (5.32)$$

Thus, an intuitive picture for the scattering of polarons is obtained. The transition rate is simply given by the interaction matrix element and the overlap of the polaron spectral functions for the corresponding states.

For non-interacting carriers the retarded GF is given by Eqs. (5.4) and (5.7), respectively. Due to the infinite lifetime of free carriers and the corresponding δ -like character of their spectral functions the Boltzmann case is recovered in the scattering kernels, describing exact energy conservation. Introducing a finite carrier lifetime according to $\epsilon \rightarrow \epsilon - i\gamma$ immediately results in a weakening of the strict energy conservation condition. Intuitively this is seen at the overlap integral (5.32) together with the corresponding Lorentzian line-shape of the spectral function. In case of the polaronic spectral function for QD states (cf. Fig. 5.2), the satellite structure as well as the interaction-induced finite polaron lifetime gives rise to a considerable overlap and hence fast scattering is expected. This results in open scattering channels even though the level spacing of the free carrier states does not match the LO-phonon energy.

To demonstrate the influence of quantum-kinetic effects due to QD polarons, we first study the relaxation of carriers in a QD with two confined shells. For convenience we choose the same parameters as in the discussion of the QD polaron and the room-temperature regime. The level spacing of $1.1 \hbar\omega_{\text{LO}}$ does not match the LO-phonon energy such that both, Fermi's golden rule and the kinetic equation (5.28) predict the absence of transitions. A direct numerical solution of the polaron GFs from Eq. (5.2)–(5.3) together with Eq. (5.29) is performed in the time domain. As initial population we assume $f_s(t_0) = 0$, $f_p(t_0) = 0.3$ and start the calculation at time t_0 . While this example addresses the relaxation process itself, more advanced calculations also include the carrier generation via optical excitation (cf. Chap. 5.2.2) and carrier capture from the WL into the QDs (discussed below). Furthermore, the inclusion of the optical excitation of carriers avoids ambiguities due to initial conditions. In this case the population prior to the pump process is zero, naturally providing the lower limit of the time integral in Eq. (5.29). However, in practice we find that within the GKBA results weakly depend on the details of the initial conditions.

The evaluation of the quantum-kinetic theory (solid lines in Fig. 5.8a) yields a fast population increase of the initially empty QD s-shell accompanied by oscillations which reflect in the time domain the hybridization of coupled carrier and phonon states. The analogy

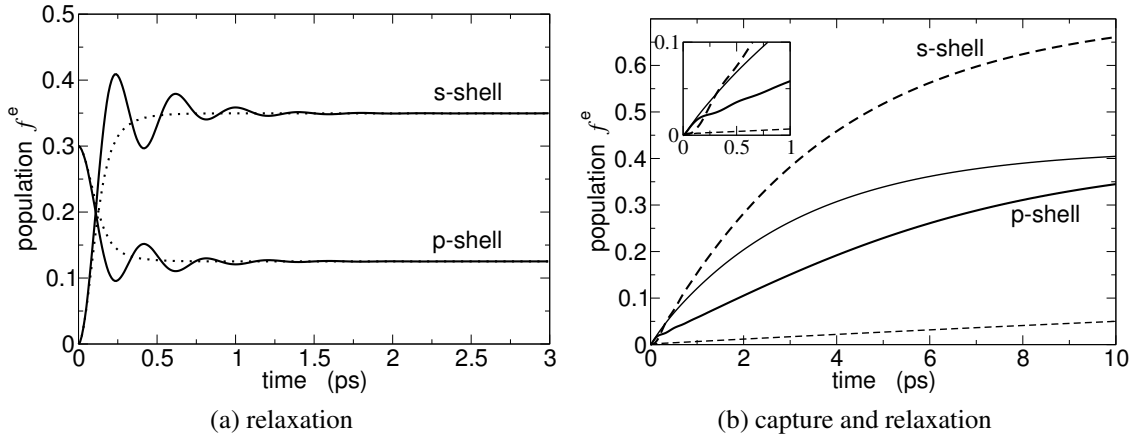


Fig. 5.8: Temporal evolution of the electron QD population due to carrier-phonon scattering at 300 K for a QD level spacing of $1.1 \hbar\omega_{\text{LO}}$.

to Rabi oscillations stemming from the interaction with the monochromatic phonon field has been pointed out by Inoshita and Sakaki [132]. If one uses the Markov approximation together with polaronic retarded GFs and solves Eq. (5.30), quasi-particle renormalizations are still included but the transient oscillations disappear (dotted lines in Fig. 5.8a). In both cases the same steady-state solution is obtained which corresponds to a thermal population at the renormalized energies. The equilibrium solution agrees with the Kubo-Martin-Schwinger (KMS) relation which is discussed in detail in Chap. 5.3. Note that particle number conservation is obeyed in Fig. 5.8a since the degeneracy of the p-shell is twice that of the s-shell.

Another important process is the capture of carriers from the delocalized WL states into the localized QD states. For the QDs also a level spacing of $1.1 \hbar\omega_{\text{LO}}$ between the p-shell and the lowest WL state is chosen, exceeding the LO-Phonon energy, so that again Fermi's golden rule and Eq. (5.28) predict the absence of electronic transitions. For the numerical solution of Eq. (5.29) we use now as initial condition empty QD states and a thermal population of carriers in the polaronic WL states (obtained from the KMS relation) corresponding to a carrier density of 10^{11} cm^{-2} at a temperature of 300 K. The thin-dashed and solid lines in Fig. 5.8b show the increase of the p- and s-shell population, respectively, when only direct capture processes are considered that contain scattering from a WL-polaron to a QD-polaron state due to emission of LO phonons. Also in this situation the quantum-kinetic theory predicts a fast population of the initially empty p-shell. In spite of the large detuning, exceeding two LO-phonon energies, the direct capture into the s-shell is still possible but considerably slower. When both, direct capture of carriers as well as relaxation of carriers between the QD states are included in the calculation, the thick-solid (dashed) line is obtained for the p-shell (s-shell) population. While faster capture to the p-shell states leads at early times to a p-shell population exceeding the s-shell populations (see inset of

Fig. 5.8b), the subsequent relaxation efficiently populates the s-states. Since the WL states form a quasi-continuum, beatings at early times are strongly suppressed. With the results in Fig. 5.8 we have demonstrated the ultra-fast (sub-picosecond) carrier relaxation and fast (picosecond) carrier capture for a material with weak polar coupling and 10% detuning between the transition energies and the LO-phonon energy. This detuning is sufficiently large for the alternative LO+LA mechanism proposed by Inoshita and Sakaki [145] to fail.

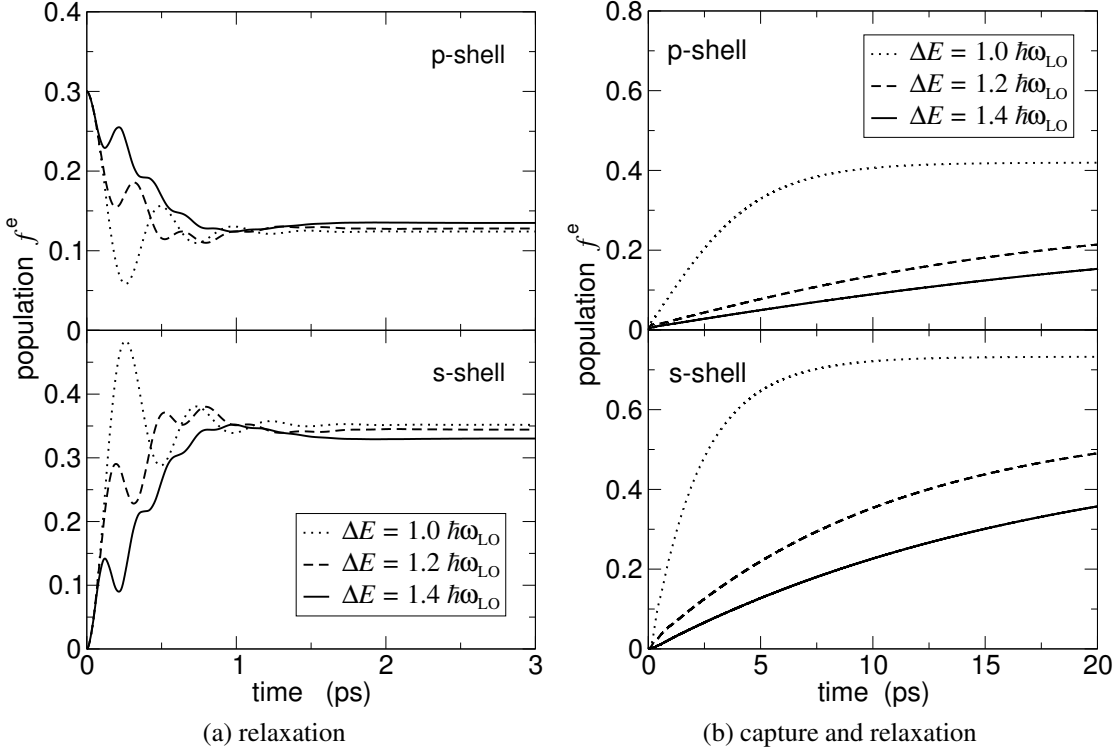


Fig. 5.9: Temporal evolution of QD p-shell (top) and s-shell (bottom) electron population for different energy spacings ΔE and a temperature of 300K.

We find that the fast scattering is not related to the near resonance condition and in fact relatively insensitive to the detuning between transition energies and LO-phonon energy. Spectral functions of the coupled QD-WL system for various detunings have been discussed in Chap. 5.1.4 and corresponding results for the carrier relaxation, as in Fig. 5.8a but for different detunings ΔE , are shown in Fig. 5.9a. The fast carrier relaxation towards an equilibrium situation is retained in all three cases and the main difference is in the oscillation period, which is reduced for larger detuning due to the increased splitting in Fig. 5.6. A stronger influence of the detuning between transition energies and the LO-phonon energy is found for the capture of carriers from the WL into the QD states. As can be seen in Fig. 5.9b, from the resonance situation to a detuning of 40% the capture efficiency is strongly reduced. Nevertheless, a significant occupancy can be reached within several ten

picoseconds. The reduced capture efficiency is related to a reduced overlap between the WL and QD spectral functions for increasing detuning, which is mainly because for the low QD density we consider the WL spectral function is only weakly influenced by the QD states (cf. Fig. 5.2) and therefore almost independent of the detuning. In comparison to this, the strong interaction between s- and p-states maintains a strong overlap between their spectral functions. As a consequence the relaxation time is less sensitive to the detuning.

5.2.2 Pulse excitation

In the previous chapter carrier capture and relaxation have been studied, starting from an initial carrier distribution. Within a quantum kinetic treatment and including polaron effects fast scattering channels are found. Subject of the following chapter is the extension of this model and include the optical excitation of carriers with a laser pulse. This way, the typical experimental condition for example in pump-probe experiments is simulated. Beside carrier generation the laser pulse also induces optical polarizations. Their dephasing can also be studied within our extended model and will be done in Chap. 6. For the one-time kinetics the optical carrier generation provides another technical advantage. Since prior to the optical pulse the system is in its ground state, which is the electron-hole vacuum, a natural cutoff for the memory integrals is present.

For the derivation of the quantum-kinetic equations including the optical excitation, again we refer to the extended technical discussion in Chap. 3.3–4 and proceed quickly. The one-time kinetic equation without collision terms, but considering optical excitation, is obtained from Eq. (3.68). In the instantaneous selfenergy we include Hartree and Fock contributions from the Coulomb interaction, Eq. (4.8) and (4.9), as well as the dipole coupling (4.50). From the commutator in Eq. (3.68) we obtain the so-called semiconductor Bloch equations (SBE) which in the electron-hole picture ($a \in \{e, h\}$) read

$$\frac{\partial}{\partial t} f_\alpha^a(t) = \frac{2}{\hbar} \operatorname{Im} \Omega_\alpha(t) \psi_\alpha^*(t) , \quad (5.33a)$$

$$\frac{\partial}{\partial t} \psi_\alpha(t) = \frac{i}{\hbar} \left[(\tilde{\epsilon}_\alpha^e + \tilde{\epsilon}_\alpha^h) \psi_\alpha(t) - [1 - f_\alpha^e(t) - f_\alpha^h(t)] \Omega_\alpha(t) \right] . \quad (5.33b)$$

The Coulomb correlations on Hartree-Fock level give rise to a renormalized Rabi energy $\Omega_\alpha(t)$ and the renormalized single particle energies $\tilde{\epsilon}_\alpha^a$,

$$\Omega_\alpha(t) = \mathbf{d}_\alpha \mathbf{E}(t) + \sum_\beta V_{\alpha\beta\alpha\beta}^{\text{eh}} \psi_\beta(t) , \quad (5.33c)$$

$$\tilde{\epsilon}_\alpha^a(t) = \epsilon_\alpha^a + \sum_\beta [V_{\alpha\beta\beta\alpha}^{aa} - V_{\alpha\beta\alpha\beta}^{aa}] f_\beta^a(t) . \quad (5.33d)$$

The renormalized Rabi energy represents an effective coupling to the optical field and gives rise to excitonic resonances, whereas the renormalized energies incorporate a red shift due

to the exchange interaction and a blue shift due to the Hartree interaction. For the description of scattering and dephasing processes, Coulomb correlations beyond the Hartree-Fock level or carrier-phonon correlations have to be taken into account. Considering the RPA selfenergy (4.42) for the carrier-phonon interaction and applying the GKBA, the one-time collision terms (3.72) for the carrier scattering are given by

$$\frac{\partial}{\partial t} f_\alpha^a(t) \Big|_{\text{coll}} = S_\alpha^{\text{f},a}(t) + S_\alpha^{\text{p},a}(t) \quad (5.34\text{a})$$

with

$$\begin{aligned} S_\alpha^{\text{f},a}(t) &= 2\text{Re} \int_{-\infty}^t dt_2 \sum_\beta G_\beta^{\text{R},a}(tt_2) [G_\alpha^{\text{R},a}(tt_2)]^* \\ &\times \left[-f_\alpha^a(t_2)(1-f_\beta^a(t_2))D_{\alpha\beta\alpha\beta}^{>,aa}(tt_2) \right. \\ &\left. + (1-f_\alpha^a(t_2))f_\beta^a(t_2)D_{\alpha\beta\alpha\beta}^{<,aa}(tt_2) \right] \} , \end{aligned} \quad (5.34\text{b})$$

$$\begin{aligned} S_\alpha^{\text{p},a}(t) &= 2\text{Re} \int_{-\infty}^t dt_2 \sum_\beta G_\beta^{\text{R},a}(tt_2) [G_\alpha^{\text{R},a}(tt_2)]^* \\ &\times \psi_\beta(t_2) \psi_\alpha^*(t_2) [D_{\alpha\beta\alpha\beta}^{>,aa}(tt_2) - D_{\alpha\beta\alpha\beta}^{<,aa}(tt_2)] \} . \end{aligned} \quad (5.34\text{c})$$

The term $S_\alpha^{\text{f},a}$ represents the population scattering which was discussed in detail in Chap. 5.2.1. In contrast, the polarization scattering term $S_\alpha^{\text{p},a}$ describes population changes induced by coherent polarizations which are negligibly small for weak excitations. Similar terms are obtained for the dephasing due to carrier-phonon interaction. They can be divided into a diagonal dephasing term (DD) and an off-diagonal dephasing term (OD) according to

$$\frac{\partial}{\partial t} \psi_\alpha(t) \Big|_{\text{coll}} = S_\alpha^{\text{DD}}(t) + S_\alpha^{\text{OD}}(t) \quad (5.35\text{a})$$

with

$$\begin{aligned} S_\alpha^{\text{DD}}(t) &= \int_{-\infty}^t dt_2 \sum_{\beta,a \neq b} \psi_\alpha(t_2) \left\{ G_\beta^{\text{R},a}(tt_2) G_\alpha^{\text{R},b}(tt_2) \right. \\ &\times \left. \left[(1-f_\beta^a(t_2)) D_{\alpha\beta\alpha\beta}^{>,ab}(tt_2) + f_\beta^a(t_2) D_{\alpha\beta\alpha\beta}^{<,ab}(tt_2) \right] \right\} , \end{aligned} \quad (5.35\text{b})$$

$$\begin{aligned} S_\alpha^{\text{OD}}(t) &= - \int_{-\infty}^t dt_2 \sum_{\beta,a \neq b} \psi_\beta(t_2) \left\{ G_\alpha^{\text{R},a}(tt_2) G_\beta^{\text{R},b}(tt_2) \right. \\ &\times \left. \left[(1-f_\alpha^a(t_2)) D_{\alpha\beta\alpha\beta}^{>,ab}(tt_2) + f_\alpha^a(t_2) D_{\alpha\beta\alpha\beta}^{<,ab}(tt_2) \right] \right\} . \end{aligned} \quad (5.35\text{c})$$

Whereas the DD term resembles the structure of a T_2 time, $\frac{d}{dt} \psi_\alpha \propto \Gamma_\alpha^{\text{DD}} \psi_\alpha$, the OD term does not. Since diagonal and off-diagonal dephasing partly compensate, it is important to

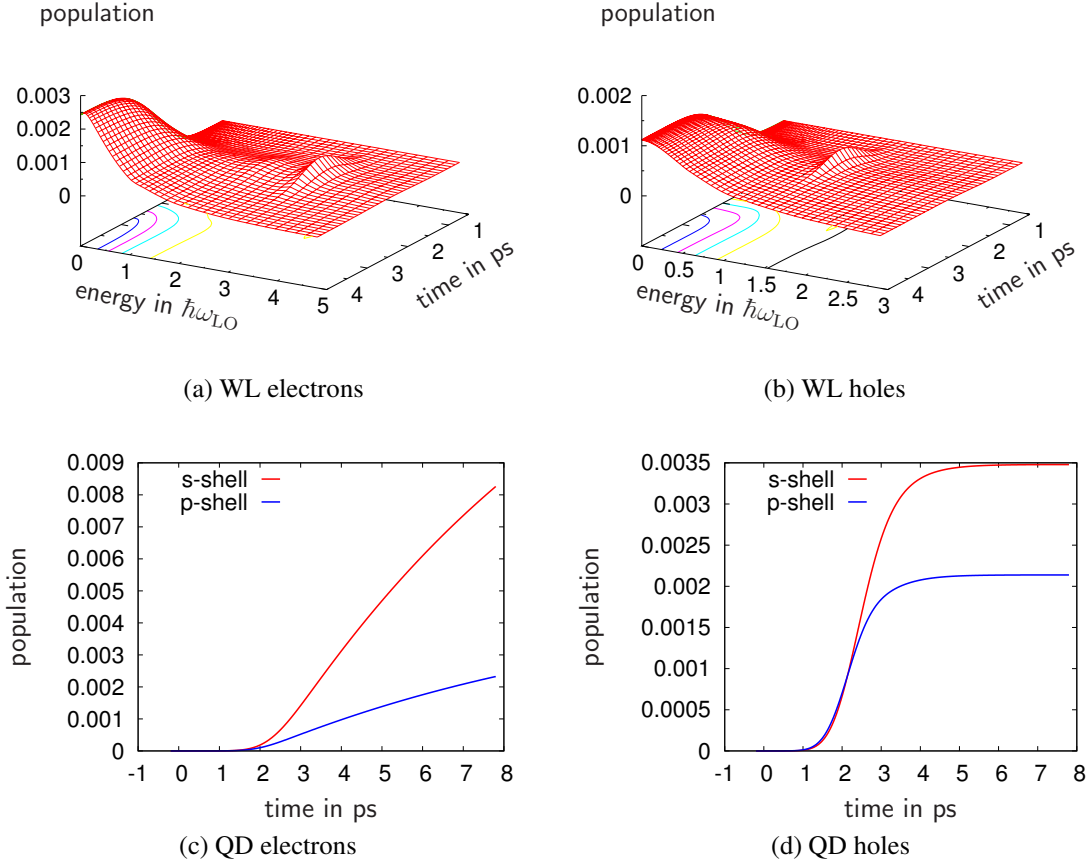


Fig. 5.10: Temporal evolution of the QD and WL carrier distribution after optical pulse excitation into the WL at a lattice temperature of 300 K.

include both in the calculation. A more detailed discussion of dephasing processes, in the context of optical absorption experiments, is given in Chap. 6.

To demonstrate the temporal evolution of a carrier distribution after optical pulse excitation we consider the InGaAs/GaAs QD-WL system introduced in Chap. 5.2.1. For the QD shells we choose a level spacing of $1.1 \hbar\omega_{LO}$ for electrons and $0.4 \hbar\omega_{LO}$ for holes. Results for the excitation with a 1 ps pulse into the WL ($\hbar\omega - E_G = 160$ meV) are shown in Fig. 5.10 where the temporal evolution of the WL and QD population for electrons and holes is presented.

In the WL, we find a fast relaxation of carriers towards the band edge. The electrons show a two-step cascade where a broadening of the replicas is observed. This indicates the weakening of the energy conservation condition due to polaron and non-Markovian effects. For the Boltzmann kinetics, in contrast, the strict energy conservation condition would result

in exact phonon replicas of the initial carrier distribution [148, 149]. The carrier distribution evolves towards a quasi steady-state that slowly decays due to carrier-capture into QD states, but retains its shape. Similar features are observed for holes, where the excitation condition allows only for a one-step process towards the band edge. Furthermore, the quantum kinetics shows the relaxation of WL carriers below the phonon threshold. This is due to multi-phonon emission and absorption processes in combination with the blurred energy conservation condition and has also been observed in QW systems [150].

Carrier capture and relaxation processes in QDs are discussed extensively in Chap. 5.2.1. Comparing electrons and holes in Fig. 5.10, we find the holes to be faster. Whereas after 2 ps for holes almost a steady-state carrier distribution is reached, the QD population for electrons is still increasing. In this case this is due to the fact that the level spacing for holes allows for direct capture processes from the WL into both, s- and p-shell. For the QD hole population and the carrier distribution in the WL a steady-state value is reached 6 ps after the optical excitation. At this point the question arises whether this steady-state corresponds to a thermal distribution. This discussion is subject of the following chapter.

5.3 The steady-state discussion

For the optically excited QD-WL system we find strong signatures of quantum-kinetic effects in the carrier relaxation. The broadening of phonon replicas as well as the sub-threshold relaxation in the WL indicate the weakening of the energy conservation condition due to memory effects and the inclusion of polaron properties. Due to the same reason a fast relaxation of QD carriers is observed. A steady-state carrier distribution evolves on a ps time scale. Subject of this chapter is an analysis of the steady-state distribution and the long-time properties of the quantum-kinetic equations.

In the Boltzmann kinetic equation (5.28) carriers are treated as being unaffected by the interaction and only the free-particle properties enter the theory. It can be shown that, provided all states are connected by scattering events, the steady-state distribution of the Boltzmann kinetics coincides with the Fermi-Dirac distribution. Also a non-thermal steady-state can be observed in the Boltzmann kinetics if the connectivity property does not hold. For example, in QW systems the relaxation of carriers below the phonon threshold is suppressed [148, 149].

Within a quantum-kinetic approach, the quasi-particle properties as well as memory effects prohibit to analyze the steady-state properties analytically. Therefore corresponding numerical results are presented in the following. First, the generalization of the Fermi-Dirac distribution to interacting systems is discussed, considering the spectral properties of the quasi-particles. This serves as a test if the steady-state distribution obtained in a quantum-kinetic calculation corresponds to a thermal one. The analysis of the thermal-

ization properties is performed for the one- and two-time version of the quantum kinetics. Furthermore, different temperature regimes are compared.

5.3.1 The Kubo-Martin-Schwinger relation

For a fermionic system in thermal equilibrium, the lesser and the spectral GF are connected by the relation

$$G_\alpha^<(\omega) = 2\pi i F(\omega) \widehat{G}_\alpha(\omega), \quad (5.36)$$

with $F(\omega) = [e^{(\hbar\omega - \mu)/k_B T} + 1]^{-1}$ being the Fermi-Dirac distribution [79]. In thermodynamic equilibrium, the GFs depend only on the relative time and Eq. (5.36) involves their Fourier transform with respect to this time. The relationship is known as the Kubo-Martin-Schwinger (KMS) condition or as the fluctuation-dissipation theorem. Using the polaronic retarded GF (5.2), the occupancy of a state α in thermal equilibrium is given by

$$f_\alpha = \int d\hbar\omega F(\omega) \widehat{G}_\alpha(\omega). \quad (5.37)$$

For non-interacting particles, the thermal population simply corresponds to the value of the Fermi-Dirac distribution at the free-particle energy $F(\epsilon_\alpha)$ due to the δ -like spectral function $\widehat{G}_\alpha(\omega) = \delta(\hbar\omega - \epsilon_\alpha)$. In the interacting case, a more complex spectral (cf. Chap. 5.1 in case of the carrier-phonon interaction) has to be considered. In this sense, the KMS relation is a generalization of the Fermi-Dirac distribution to interacting systems and therefore serves as a test to study the thermalization of carriers. Note, that for practical purposes the KMS relation (5.37) is evaluated in the time domain as outlined in App. B.3.

5.3.2 Steady-state analysis of the one-time kinetics

For the one-time kinetics, the long-time limit of the particle scattering term (5.34b) can be obtained directly. In the long-time limit, complete dephasing of the optical polarization has taken place and the population distribution has reached its limit value. Considering the regime of sufficiently low excitation, so that the occupation numbers f_α are much smaller than unity, one obtains for the steady state population a linear equation

$$\frac{\partial}{\partial t} f_\alpha = \sum_\beta \left[\sum_\gamma \Lambda_{\alpha\gamma}^> \delta_{\alpha\beta} - \Lambda_{\beta\alpha}^< \right] f_\beta = \sum_\beta K_{\alpha\beta} f_\beta = 0 \quad (5.38)$$

with the scattering kernel $\Lambda_{\alpha\beta}^>$ given by Eq. (5.31), where the in- and out-scattering terms are compensating each other. Note, that for the discussion the band index is omitted. Several comments are in order. First, since the spectral functions are positive, Eq. (5.32) shows

that the scattering kernels $\Lambda_{\alpha\beta}^{\gtrless}$ are positive too. This is to be expected, given their interpretation as transition rates. Secondly, Eq. (5.38) identifies the steady state solution as the right eigenvector of K corresponding to the eigenvalue $\lambda = 0$. The existence of this eigenvalue is guaranteed by the sum rule $\sum_\alpha K_{\alpha\beta} = 0$, which in turn is related to the particle number conservation $\sum_\alpha \partial/\partial t f_\alpha = 0$. Furthermore, the physical interpretation of the right eigenvector as population distribution requires that it has only positive components. That indeed this is the case is a consequence of the structure of the operator K , as given by Eq. (5.38). The positivity of its off-diagonal elements together with the particle conservation ensures the existence of a left eigenvector with constant components and a right eigenvector having only positive elements (Frobenius-Perron theorem [151]). This structure also implies that all the other eigenvalues have negative real parts (Gershgorin's circle theorem [152]). In an eigenvector expansion of the population this describes components which decay in time.

For elevated temperatures the integrals (5.31) rapidly converge due to the decaying polaron GFs. In case of low temperatures the validity of the long-time limiting procedure which leads to Eq. (5.38) may be questioned on the ground that the integrals in (5.31) converge slowly. Indeed, as explained in Chap. 5.1, the polaron retarded GFs may contain stable, non-decaying oscillating parts. These stable oscillations, which in the spectral function correspond to the presence of δ -like peaks, can be separated according to

$$G_\alpha^R(t) = -\frac{i}{\hbar} \Theta(t) \left[\sum_j e^{-\frac{i}{\hbar}(\epsilon_\alpha - \Delta_{\alpha,j})t} + \tilde{G}_\alpha(t) \right], \quad (5.39)$$

with $\tilde{G}(t) \rightarrow 0$ for $t \rightarrow \infty$. Thus, an analytical treatment of the δ part and a numerical one for the residual part \tilde{G} is possible.

For the scattering integrals $\Lambda_{\alpha\beta}^{\gtrless}$ in the frequency domain, given by Eq. (5.32), it is obvious that the δ -like terms in the two spectral GFs do not contribute unless they are separated by exactly one LO-phonon energy. This is reminiscent of the strict energy conserving condition of the Boltzmann approach. Of course the residual parts of the GFs do contribute, as well as the cross terms $\delta \cdot \mathcal{G}$. In this way one sees that the states remain connected by transition rates which are small but nonzero. It is clear that the elimination of the non-resonant δ -terms takes place only in the long-time limit when the time integral of Eq. (5.31) is complete. For the evaluation of the scattering integrals several situations may appear. In the case when both states α and β correspond to extended WL states, the higher state β is above the phonon threshold and does not contain δ -peaks. When both states are localized, barring accident the perfect resonance between the δ -peaks does not occur and they do not contribute to the transition rates. Nevertheless, the residual part in the retarded GFs (cf. Eq. (5.39)) gives rise to a non-zero transition rate. The remaining case with α localized and having a spectral peak one $\hbar\omega_{\text{LO}}$ below a peak belonging to a state β in the continuum, indeed gives rise to singular δ -terms in the transition rates. But these rates appear in the kinetic equation (5.38) with the index β running over a continuum, so that such δ -terms

are well defined, leading in the end to a finite contribution.

With the operator K defined as discussed above, the eigenvalues are found and the steady-state solution identified. The steady-state limit distributions of the kinetics obtained by numerical integration of the quantum-kinetic equation (cf. Chap. 5.2.2) can then be checked against those found by diagonalization of the transition rate matrix.

5.3.3 Steady-state analysis for the room-temperature regime

With the KMS condition (5.37) and the diagonalization procedure (5.38) for the long-time limit of the quantum-kinetic equation we can proceed with the analysis of the steady-state carrier distribution presented in Chap. 5.2.2. A comparison of the results obtained from all three approaches is presented in Fig. 5.11. The population of QD and WL states is depicted for electrons as well as for holes. We find that the one-time kinetics in the long time limit approaches the result of the diagonalization procedure. Whereas 8 ps after the optical pulse the holes reached a steady-state distribution, the electrons are not fully relaxed. A mono-exponential fit $f(t) = f_\infty [1 - \exp(-\frac{t-t_0}{\tau})]$ for the temporal evolution of the QD population in Fig. 5.10 indicates that also the electrons evolve towards the distribution obtained from the diagonalization procedure. Compared to the KMS distribution, we find that for this particular QD the WL distribution is close to the KMS condition whereas the QD populations do not fully reach their thermal values. This behavior of the one-time kinetics in QD systems has also been observed in other works [153, 154].

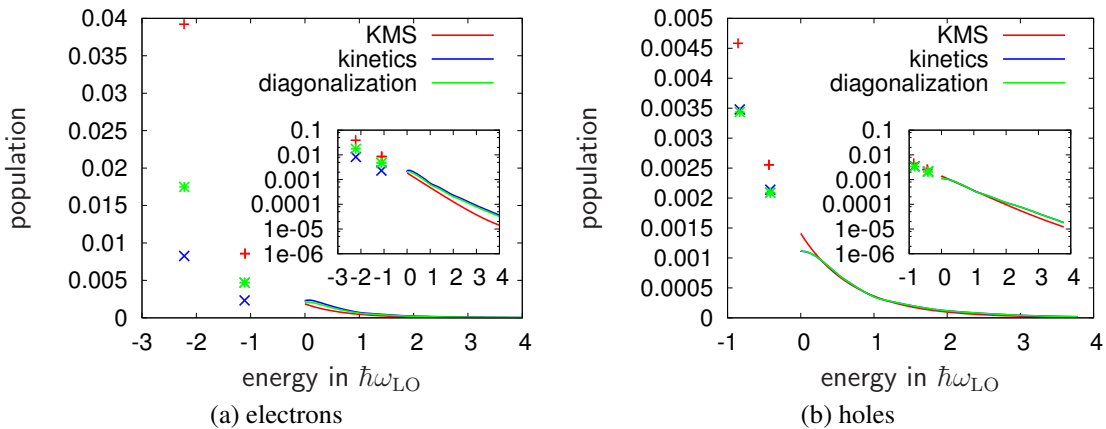


Fig. 5.11: Steady-state analysis of the one-time kinetics for the room-temperature regime.

The reason for the one-time kinetics not completely reaching the KMS distribution might be an artifact of the GKBA involved in the one-time calculations. For bulk semiconductors

Gartner et al. [83] compared one- and two-time calculations and observed that for weak polar coupling materials the GKBA is a good approximation whereas for intermediate polar couplings the deviations are more severe. However, in QD systems this statement might be questioned. Similar to the polaron problem discussed in Chap. 5.1, the enhancement of the carrier confinement might lead to an enhancement of the effective polar coupling.

To facilitate the steady-state analysis of the kinetics and to provide a verification of the GKBA involved in the one-time calculations, we also performed two-time calculations for the QD-WL system. The two-time calculations, which we show for comparison, have been obtained by Dr. Paul Gartner. Considering the combined QD-WL system for the weak polar coupling InGaAs material, unfortunately in the two-time calculations no steady-state could be obtained within the numerically available early-time regime. Instead, we consider a quantum-well (QW) system and compare the InGaAs material system ($\alpha = 0.069$) with the intermediate polar coupling CdTe material ($\alpha = 0.31$). The corresponding test of the steady-state solutions obtained from kinetic calculations against the KMS condition is seen in Fig. 5.12. Whereas for the CdTe QW the two-time calculation is in good agreement with the KMS curve, the one-time evolution is not. We find that the one-time kinetics produces a steady state with a temperature considerably exceeding that of the phonon bath. It is to be expected, however, that for a weaker coupling the discrepancy between the full two-time procedure and the GKBA is less severe. This is indeed the case, as shown in Fig. 5.12b where results for a GaAs QW are given. The wiggles seen in the two-time curve are traces of the phonon cascade, which are still present. This is due to the much longer relaxation time in low-coupling materials. Nevertheless the trend is clear, the steady-state solutions of both approaches are in good agreement with the KMS condition.

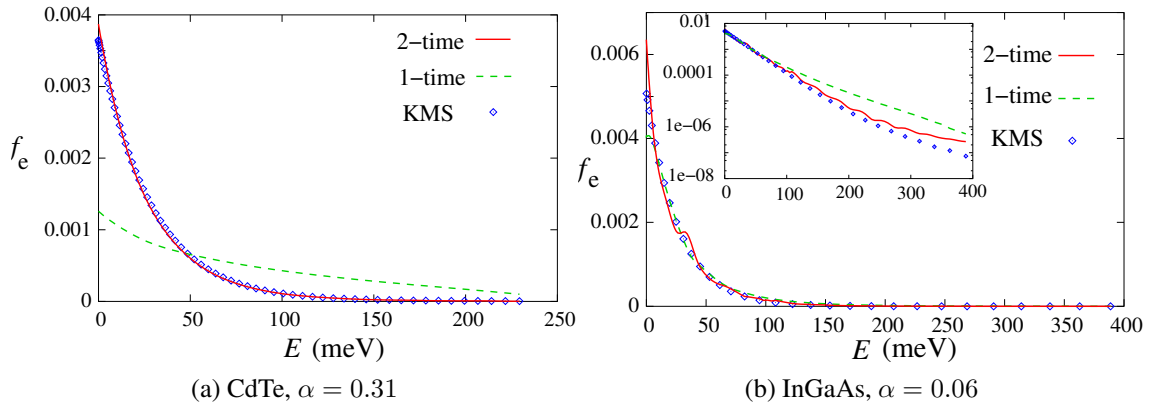


Fig. 5.12: Steady state QW electron population after optical excitation with a 100 fs laser pulse, compared to the KMS result. The inset in (b) shows the same on semi-logarithmic scale.

As example for a QD-WL system we consider CdTe lens-shaped self-assembled QDs, hav-

ing both for electrons and for holes two discrete levels below the WL continuum. Similar to previous calculations, these states are labeled s and p , according to their z -projection angular momentum. An equidistant energy spacing is considered, for electrons amounting to $2.4 \hbar\omega_{\text{LO}}$ between the WL continuum edge as well as between the p -level and the s -level. For the holes a similar spectrum with an energy spacing of $0.27 \hbar\omega_{\text{LO}}$ is assumed. Our calculations for this example include both, localized QD and delocalized WL states. Interaction matrix elements are calculated within the envelope wave function approximation which is discussed in App. A.1. In Fig. 5.13, the time evolution of the population of electrons is shown. The system is pumped close to the renormalized p -shell energy with a 100 fs laser pulse at time $t = 0$. Therefore the majority of the carriers is initially found in the p -states. Nevertheless, efficient carrier relaxation takes place and a steady state is reached, even if the level spacing does not match the LO-phonon energy. The two-time results (Fig. 5.13a) are again in agreement with the KMS condition, shown by open circles. In contrast, the one-time evolution (Fig. 5.13b) shows a small non-physical intermediate negative value for the WL population, strong scattering of carriers into energetically higher WL states, and converges to a state in strong disagreement with the KMS result. Note, that in both figures an identical ordinate axis is used to facilitate the comparison. These results indicate that the reason for the deviations from the KMS condition in Fig. 5.11 are an artifact due to the GKBA.

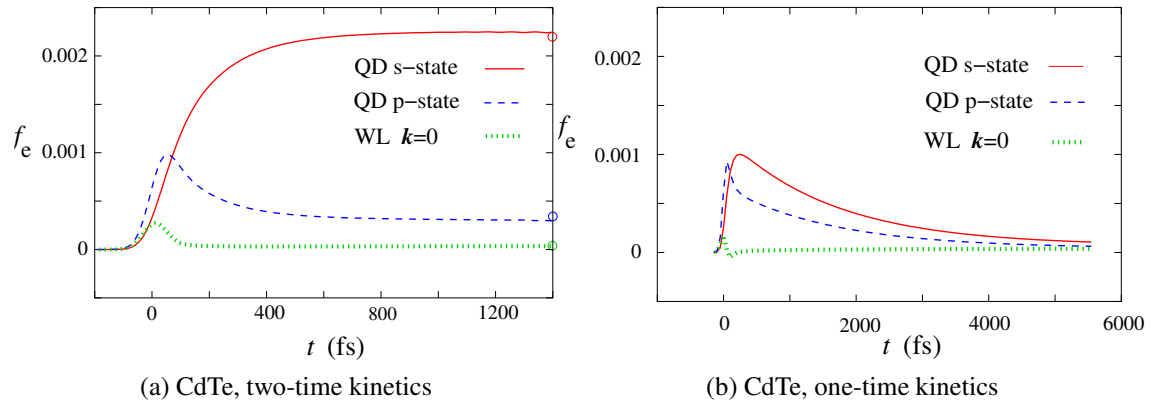


Fig. 5.13: Electron populations in the localized s and p states of a CdTe QD and in the extended $k = 0$ WL state after optical excitation with a 100 fs laser pulse at $t = 0$. Open circles represent the equilibrium values according to the KMS condition.

5.3.4 Steady-state analysis for the low-temperature regime

As a result of the steady-state analysis for the room-temperature regime we found that in the long-time limit a thermal carrier distribution is obtained, even though this corresponds

to a temperature somewhat higher than the lattice temperature. For the low-temperature regime, the polaron spectral function exhibits strong narrowing of the resonances as discussed in Chap. 5.1. Furthermore, in the low temperature regime phonon absorption processes are strongly suppressed. These properties of the low-temperature spectral function suggest relaxation properties that tend towards the Boltzmann limit, exhibiting strict energy conservation, when considering the scattering kernels (5.32). Based on these considerations, the question arises whether a thermalization is also observed for low temperatures. Thus, in the following the carrier kinetics and the steady-state properties are studied for this regime.

The two-time formalism is numerically much more demanding than the one-time one and cannot be carried out to long times. Therefore a direct comparison of the steady-state distributions from one- and two-time calculations, as presented in the previous chapter, is unfortunately not possible for the low-temperature regime. At low temperatures the limitation to the early time regime is more severe, as the polaronic retarded GF has non-decaying components. For room temperature and low polar coupling materials, the results of the previous chapter show that the one- and two-time kinetics are in good agreement. One expects this to be even more true for low temperatures. In this case, the enhancement of the effective coupling constant is reduced because the phonon population is smaller than for room temperature. Thus, in the following a comparison of numerical results for the early stage of the kinetics from one- and two-time calculations is given for the low-temperature regime. Again, the two-time calculations presented for comparison have been performed by Dr. Paul Gartner.

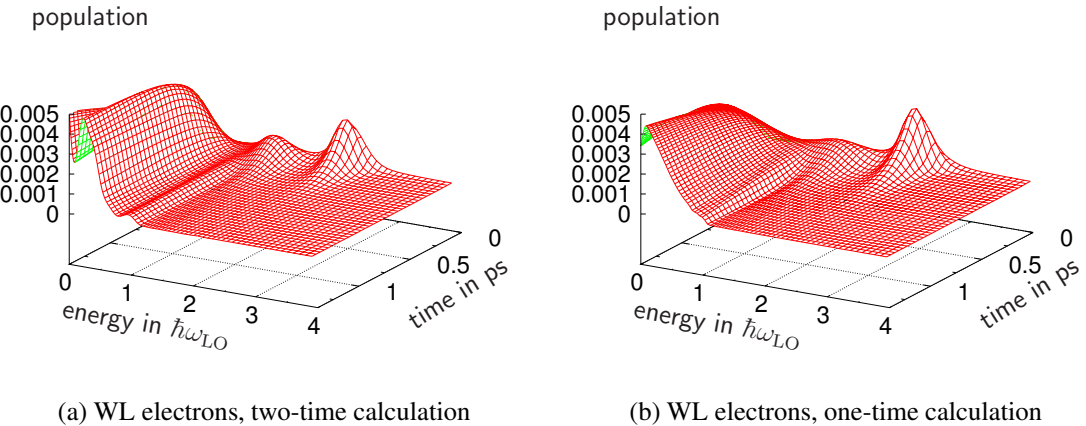


Fig. 5.14: Phonon cascade of electron relaxation in the WL after optical pulse excitation for (a) 2-time kinetics and (b) 1-time kinetics in the early time regime. The pulse energy is 110 meV above the continuum edge.

In Fig. 5.14 the WL population evolution up to 1.4 ps is shown for a carrier distribution gen-

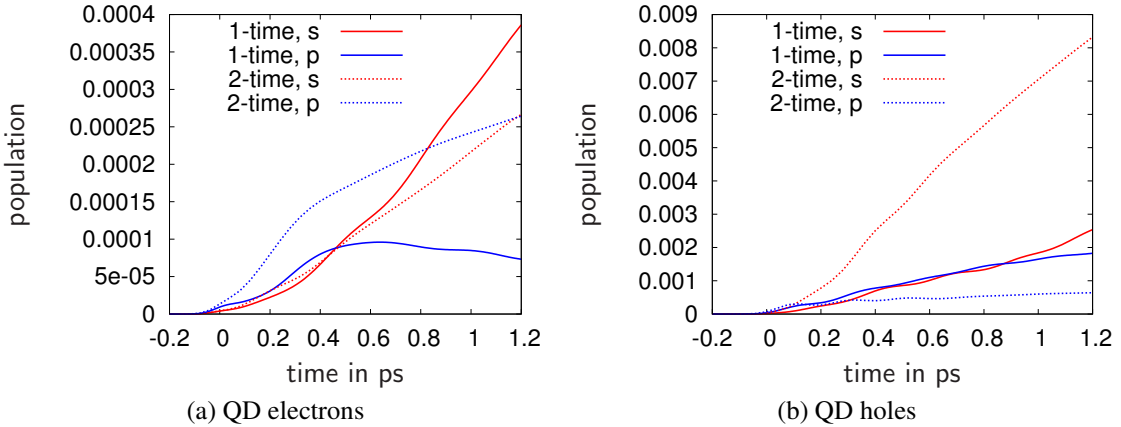


Fig. 5.15: Temporal evolution of the QD population in the early time regime after optical excitation for one-time and two-time kinetics.

erated by a 100 fs optical pulse around $t = 0$ with an excess energy of 110 meV above the continuum band edge. In the conduction band, where there is room for a phonon cascade, one observes two successive peaks being formed with increasing time below the initial, pump-generated one. They are broader in the one-time case, suggesting that the energy conservation in the scattering process is somewhat stricter in the two-time approach. Differences of the same kind can be seen also in the QD-state populations, shown in Fig. 5.15. They are especially evident in the s -state hole population, which is significantly higher in the two-time calculation. This is due to the near-resonance condition of the s -level energy for holes which is very close to two LO-phonon energies below the pulse energy. However, the estimation of the long-time behavior from the early time regime is difficult.

For the one-time kinetics, the long-time results for the QD and WL population are shown in Fig. 5.16. One observes an efficient redistribution of the carriers from the continuum into the bound states, both for electrons and for holes. The hole population of the QD is almost stable after 24 ps, while the electronic occupancies continue to grow. This difference is due to the closer energy spacing in the hole spectrum. The increase of the QD populations takes place at the expense of those in the WL, also shown in Fig. 5.16 as a function of time and momentum. One sees for the WL that after 24 ps the electron distribution continues to decrease, while the hole population has almost reached its steady state value. For both bands, the shape of the steady-state distribution is reached but does not seem thermalized, especially since it increases with energy near the band edge.

The comparison of the steady-state distribution obtained from the one-time kinetics and from a steady-state analysis (cf. Chap. 5.3.2) is made in Fig. 5.17. Especially for holes there is a very good agreement between the two, confirming that the $t \rightarrow \infty$ asymptotic is

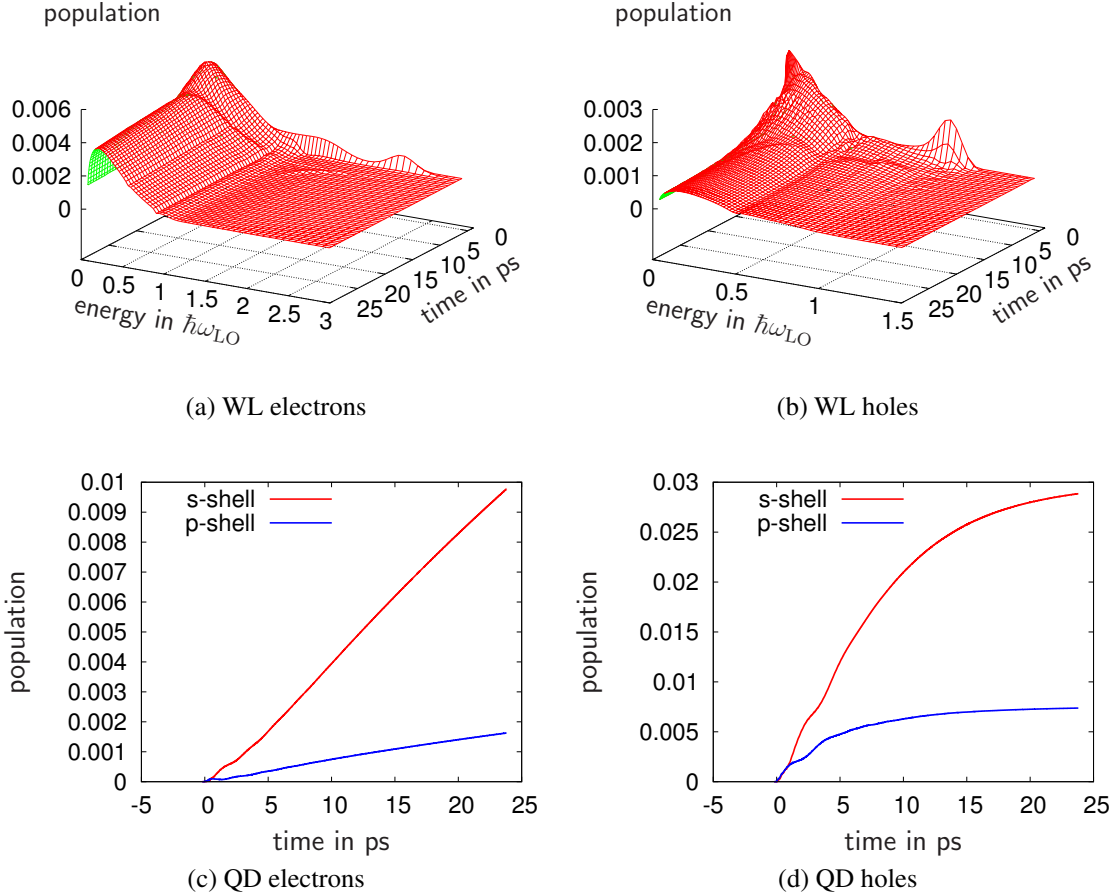


Fig. 5.16: Temporal evolution of the carrier distribution after optical pulse excitation in the WL at 10 K.

indeed reached. The WL distribution is shown at the last calculated time (24 ps) and it is clear that it has already the correct shape, even if it is still somewhat above the limit value. The fact that the WL population distributions are not monotonously decreasing in energy is an indication that the system does not evolve into a steady state that corresponds to thermal equilibrium. We check this more precisely by comparison with the KMS distribution, also shown in Fig. 5.17. The departure of the steady state from the KMS values shows that the kinetics does not ensure thermalization, even though providing a strong relaxation of carriers towards lower energies. Instead, too many carriers are found at higher energies, at the expense of a weaker occupancy of the s-shell. This freezing of the kinetics in the long time regime, without reaching thermal equilibrium, can be interpreted as an *asymptotic bottleneck* and is specific to low temperatures.

For the QD-WL system in the room-temperature regime it is found that due to the GKBA a

heating effect in the steady-state population is observed, which we also expect to be present in the low-temperature regime. However, for the interpretation of the asymptotic phonon bottleneck we think this is less severe due to several reasons. In the room-temperature regime a thermal distribution is observed, even though this distribution corresponds to a temperature somewhat higher than the lattice temperature. In contrast, for the low-temperature regime an accumulation of carriers below the phonon threshold without further relaxation is observed, obviously not corresponding to a thermal distribution. Second, the most convincing argument is the experimental observation of long-lived populations in higher QD states at low temperatures. The discussion and analysis of the corresponding experiments is the subject of the following chapter.

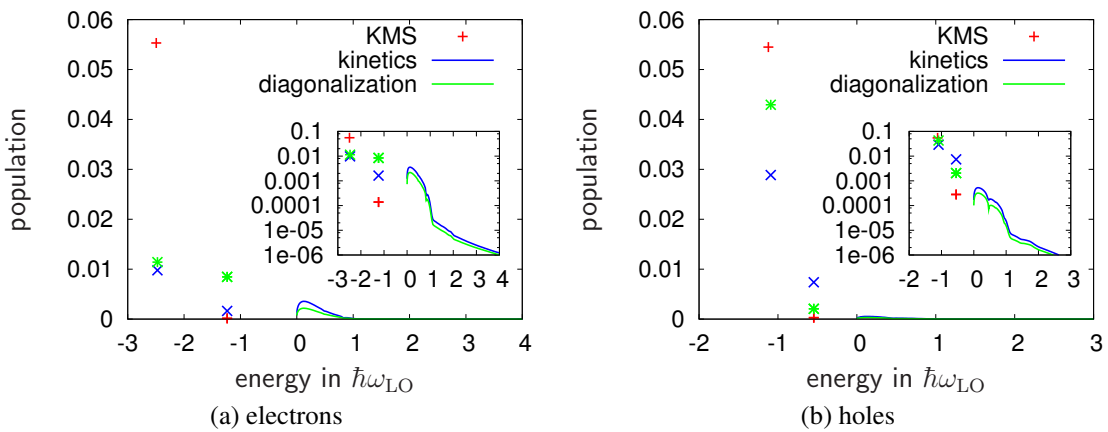


Fig. 5.17: The steady-state populations from a kinetic calculation are compared to the steady state obtained from a diagonalization procedure and to the thermal (KMS) population.

Even though a two-time analysis of the steady-state properties in the low-temperature regime is currently out of reach, we can identify some principal differences of one- and two-time calculations. The two-time calculation takes into account individual kinetics for the satellites of the polaron spectral function. This is due to the non-local correlations in time, as the two-time lesser GF $G_\alpha^<(t, \tau)$ after Fourier-transforming with respect to the relative time represents the energy resolved temporal evolution of the population $G_\alpha^<(t, \omega)$. Especially the scattering of carriers between satellites of the spectral function for the same state α is implicitly included. In contrast, the one-time calculation attributes the population of a state α to the whole spectral function, giving equal weight to all satellites. Due to this reason the weight of the population of the high-energy tail might be overestimated and that of the low-energy tail might be underestimated, leading to the heating effect observed in the one-time calculation. Therefore, in the low-temperature regime where the spectral function exhibits sharp resonances, the two-time calculation is expected to show

more strict energy conserving scattering processes. Indeed, this interpretation is in agreement with the more strict resonance condition in the two-time calculation in comparison to the one-time kinetics, cf. Fig. 5.14 and the s-shell population in Fig. 5.15b.

5.4 Theory-experiment comparison for the low-temperature regime

In previous chapters theoretical studies of the carrier-LO-phonon scattering mechanism have been presented. For self-assembled semiconductor QDs, the importance of polaron renormalizations was demonstrated and non-Markovian effects as well as the long-time properties of the kinetics were studied for different temperatures. In the low-temperature regime, we found that after fast initial carrier redistribution a phonon bottleneck emerged for later times, resulting in an incomplete thermalization. Subject of the following chapter is to show that these seemingly contradictory findings are indeed in agreement with recent experiments.

Various experimental techniques have been developed to monitor the temporal evolution of carrier distributions that are excited by an optical pulse. From the rise time of time-resolved photoluminescence signal one can estimate relaxation times [155]. Much more precise temporal resolution is obtained from pump-probe experiments. Beside common four-wave-mixing and photon-echo experiments, that yield information on the dephasing [34], a two-color pump-probe setup allows to excite carriers and probe the transmission changes at different spectral positions. Temporal information is obtained via the time-delay between pump and probe pulse and in recent experiments a resolution of 1 ps is achieved.

In the following, results of a theory-experiment comparison will be presented. The experiments have been performed in the group of Prof. Manfred Bayer at the TU Dortmund by Hannes Kurtze. Their sample contained 10 layers of undoped InGaAs/GaAs QDs and corresponding results are presented in Fig. 5.18. The top part of Fig. 5.18a displays the PL spectrum for 77 K and clearly shows the QD transition energies. A confinement energy of 90 meV and an approximately equidistant interband splitting of 22 meV between the QD shells is observed. The pump excitation intensity I_0 amounts to 40 W/cm² and the pulse duration of 1.5 ps, for the pump as well as for the probe pulse, corresponds to a spectral line-width below 3 meV. For a low pump intensity only emission from the ground and the first excited state is seen, whereas at high pump intensities also emission from higher QD shells is observed due to state filling effects.

The lower part of 5.18a shows the differential-transmission signal (DTS) as a function of the spectral position of the probe pulse and delay time. Pump excitation was into the GaAs barrier at 1.55 eV. The DTS signal itself reflects the change of the transmittivity due

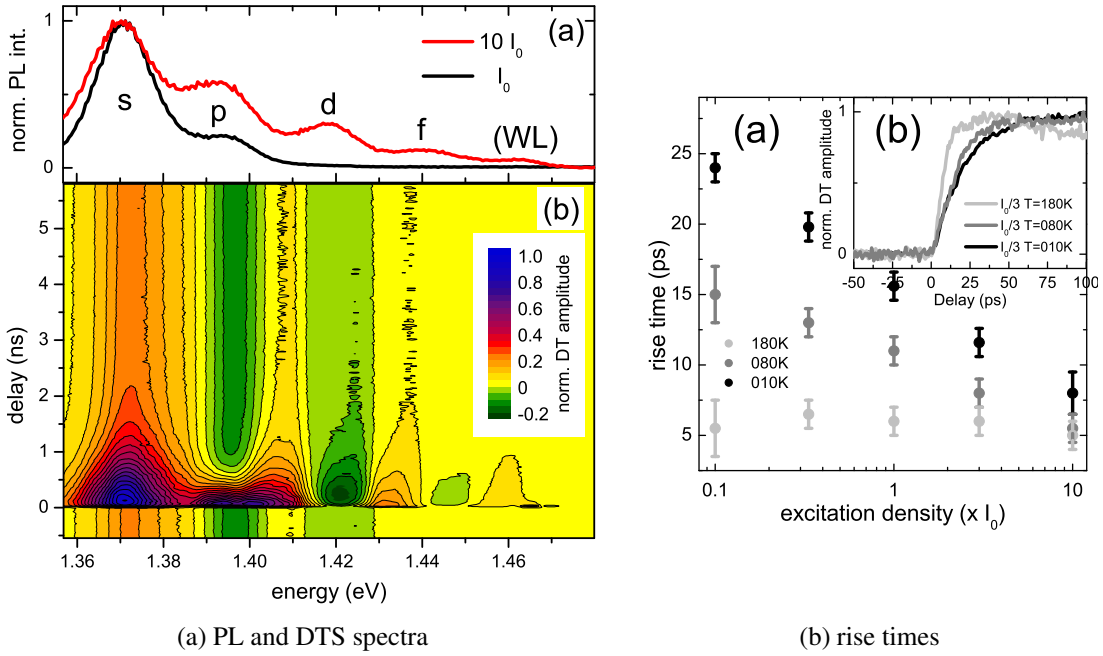


Fig. 5.18: DTS and PL spectra of an ensemble of InGaAs QDs at a temperature of 10 K (left panel) as well as the corresponding excitation density dependent rise time for various temperatures (right panel). Pictures courtesy of H. Kurtze and Prof. Dr. M. Bayer, University Dortmund.

to the action of the pump pulse, $I_{\text{DTS}} = \frac{T-T_0}{T_0}$. Even though the DTS does not directly map the carrier distribution but is also influenced by coherent polarization effects, it serves as a good indicator, especially for later times when coherent polarizations are dephased. An introduction into the theoretical description of pump-probe experiments is given in for example in Ref. [34, 96]. Around the spectral position of the QD resonances an enhanced transmission due to pump pulse action is seen. For all QD resonances a fast rise time is observed, indicating fast carrier relaxation from the GaAs barrier into the QD states. The intermediate time regime (< 2 ns) shows a complicated time dependent dynamics. Here, the population QD states leads to Coulomb renormalizations, mainly resulting in an blue shift of the resonances due to charging of the QDs described by the Hartree interaction (cf. Chap. 4.1). For later times (> 2 ns), exceeding the recombination time of about 1 ns, the carrier distribution seems to be frozen and an enhanced transmission even in higher QD shells is observed.

Temperature and excitation density dependent measurements provide additional information about the carrier-density regime in the experiment. In Fig. 5.18b the rise time of the ground-state DTS signal, obtained from a mono-exponential fit, is presented. For low tem-

peratures the strong dependence of the rise-time on the excitation density indicates the importance of Coulomb scattering processes. The elevated temperature regime above 180 K dominated by phonon scattering processes as it shows almost no density dependence.

In previous discussions about the phonon-bottleneck problem, Urayama et al. [40, 41] considered the Coulomb scattering mechanism for the interpretation of their low-temperature pump-probe measurements. Their conclusion was that due to Auger processes rapid carrier relaxation in QDs occurs only if electron and hole are captured into the same dot. This process has been named “geminate capture” in these references. In the opposite case of “non-geminate capture” where electron and hole are captured into different dots, the observation of a phonon bottleneck was explained due to the lack of scattering partners. However, the discussion for QDs did not include the presence of WL states. Even though the DTS data shown in Fig. 5.18 seem to support their findings for low temperatures, their argument contradicts with the observation of fast rise times for elevated temperatures, which are almost independent of the excitation density (cf. Fig. 5.18b). Thus, to understand the experimental observations including both temperature regimes, two major questions are addressed in the following:

- (i) What is the relative importance of carrier-carrier and carrier-phonon scattering processes in the low carrier-density regime?
- (ii) Can the long-lasting features in the DTS spectra be attributed to long-lived populations of QD states?

(i) Efficiency of different scattering processes

Even in the low carrier density regime a variety of scattering processes due to carrier-phonon and Coulomb interaction is expected to contribute. However, a comparison of the carrier-phonon interaction with the electron-electron and electron-hole scattering channels provided by the Coulomb interaction is still missing. Being interested in the relative strength of the various relaxation channels, we present a case study considering different carrier distributions that mimic snapshots of the temporal evolution of the populations after the pulse excitation and allows us to compare the corresponding scattering rates.

For the following investigations we consider an ensemble of InGaAs QDs, randomly distributed on the WL plane, each containing two confined shells for electrons as well as for holes. We refer to the ground state as s-shell and to the two-fold degenerate excited state as p-shell. The level spacings are chosen to be 40 meV and 15 meV for electrons and holes, respectively. Furthermore a temperature of 10K and a QD density of $10^{10}/\text{cm}^2$ is considered. In the weak polar coupling InGaAs material ($\alpha = 0.06$) the LO-phonon energy is 36 meV.

The calculation of the temporal evolution of a carrier distribution, excited by an optical pulse, and including both carrier-carrier and carrier-phonon scattering on a quantum-

kinetic basis, as discussed in Chap. 5.2.2, is not feasible due to numerical complexity. Instead an estimate for the relative importance of different processes is obtained by considering scattering rates for various carrier distributions. To be able to uniquely define in- and out-scattering rates, we employ the Markov approximation so that the kinetic equation for the carrier populations can be written in terms of scattering rates as

$$\frac{d}{dt} f_\alpha(t) = (1 - f_\alpha(t)) S_\alpha^{\text{in}}(t) - f_\alpha(t) S_\alpha^{\text{out}}(t). \quad (5.40)$$

Here, α denotes some state of the QD-WL system being either a QD state ν or a WL state k . For this chapter our focus is on the relaxation of carriers towards the ground state, and therefore we are interested in the in-scattering rate of the s-shell for electrons.

First, a brief review of our treatment of the Coulomb and the carrier-LO-phonon interaction is given. For the Coulomb interaction the in-scattering rate for electrons in second-order Born approximation (SBA, cf. Chap. 4.1) is given by

$$S_\alpha^{e,\text{in}} = \frac{2\pi}{\hbar} \sum_{\lambda=e,h} \sum_{\delta\beta\gamma} W_{\alpha\beta\gamma\delta}^* [2W_{\alpha\beta\gamma\delta}^* - \delta_{e,\lambda} W_{\alpha\beta\delta\gamma}^*] \times \delta(\epsilon_\alpha^e - \epsilon_\delta^e + \epsilon_\beta^\lambda - \epsilon_\gamma^\lambda) \left[(1 - f_\beta^\lambda) f_\gamma^\lambda f_\delta^e \right], \quad (5.41)$$

where λ specifies the band index and β, γ, δ run over all states in a given band (QD and WL states). f_α^λ describes the population of a state α in the band λ , and ϵ_α^λ its single-particle energy. The scattering rates contain direct and exchange contributions as well as Pauli blocking of the initial and final states. For the Coulomb matrix elements $W_{\alpha\beta\gamma\delta}$ a static screening provided by the Lindhard formula is used. Details on the treatment of Coulomb scattering are given in [91, 156]. In the scattering rate (5.41) electron-electron scattering ($\lambda = e$) as well as electron-holes scattering ($\lambda = h$) is included. One of the goals in this section of this work is a comparison of the relative strength of these processes.

The scattering rates for the carrier-LO-phonon interaction are evaluated in the random phase approximation (RPA) where the phonons are treated as a bath in thermal equilibrium held at a given temperature,

$$S_\alpha^{e,\text{in}} = 2\text{Re} \sum_{\beta \neq \alpha} M_{\alpha\beta} f_\beta \int_0^t d\tau G_\alpha^{e,\text{R}*}(\tau) G_\beta^{e,\text{R}}(\tau) \times [N_{\text{LO}} e^{-i\omega_{\text{LO}}\tau} + (1 + N_{\text{LO}}) e^{i\omega_{\text{LO}}\tau}] . \quad (5.42)$$

Here, $M_{\alpha\beta}$ denotes the carrier-LO-phonon interaction matrix elements, $\hbar\omega_{\text{LO}}$ the phonon energy, and N_{LO} the phonon population. For QDs it was shown in Chap. 5.2.1 that it is essential to include polaron effects, i.e. renormalizations of the single particle properties due to the carrier-phonon interaction, which enter the theory as retarded GFs $G_\alpha^{e,\text{R}}(\tau)$.

The interaction matrix elements for the Coulomb interaction, $W_{\alpha\beta\gamma\delta}$, as well as for the carrier-LO-phonon interaction, $M_{\alpha\beta}$, are determined using the envelope function approximation. For details on the wavefunction model used, we refer to Chap. A.1.

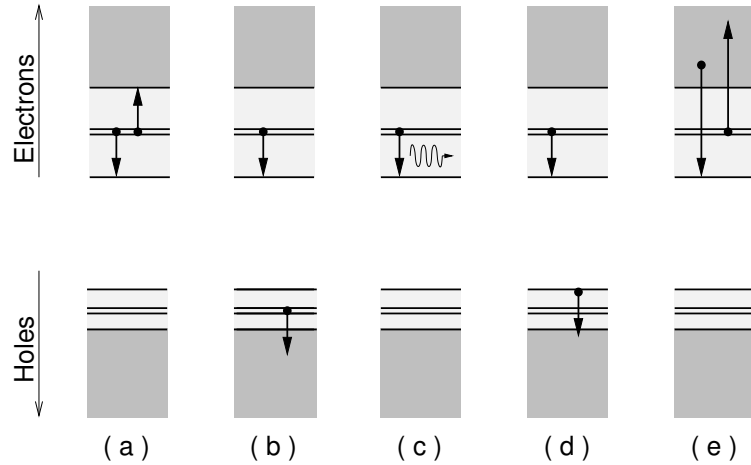


Fig. 5.19: Scattering processes contributing to the relaxation of an distribution where initially only the p-shell is filled (a)-(c) and intermediate situations where also the s-shell and WL states are populated (d)-(e).

After optical excitation of the p-shell, the time evolution of the populations towards a steady state distribution is governed by several scattering processes that are schematically shown in Fig. 5.19. For the initial situation, where only the p-shell is populated, the following processes contribute: Relaxation of an electron into the QD ground state assisted by the scattering of an electron from the QD into delocalized WL states (Fig. 5.19a), the same mechanism assisted by a hole (Fig. 5.19b), and the relaxation by means of LO-phonon emission (Fig. 5.19c). For later stages of the kinetics more processes come into play, like relaxation assisted by a hole in the QD s-shell (Fig. 5.19d) and other scattering processes that lead to a net relaxation of electrons (Fig. 5.19e).

In Fig. 5.20 the in-scattering rates for the electron s-shell are presented as a function of the carrier density excited by the optical pulse. The scattering rates due to Coulomb interaction have been calculated by Michael Lörke. The different cases considered correspond to stages of the temporal evolution of the carrier distribution after optical excitation. Whereas the fully populated p-shell mimics the initial excitation (Fig. 5.20a), scattering processes result in weakly populated s-shell and WL states (Fig. 5.20b). For long times after the pulse most carriers are expected to be in the ground state (Fig. 5.20c).

As expected, we find that for very low carrier densities the carrier-phonon scattering dominates. With increasing carrier density the electron-hole scattering becomes the most relevant relaxation mechanism, independent of the carrier distribution. For the situation under

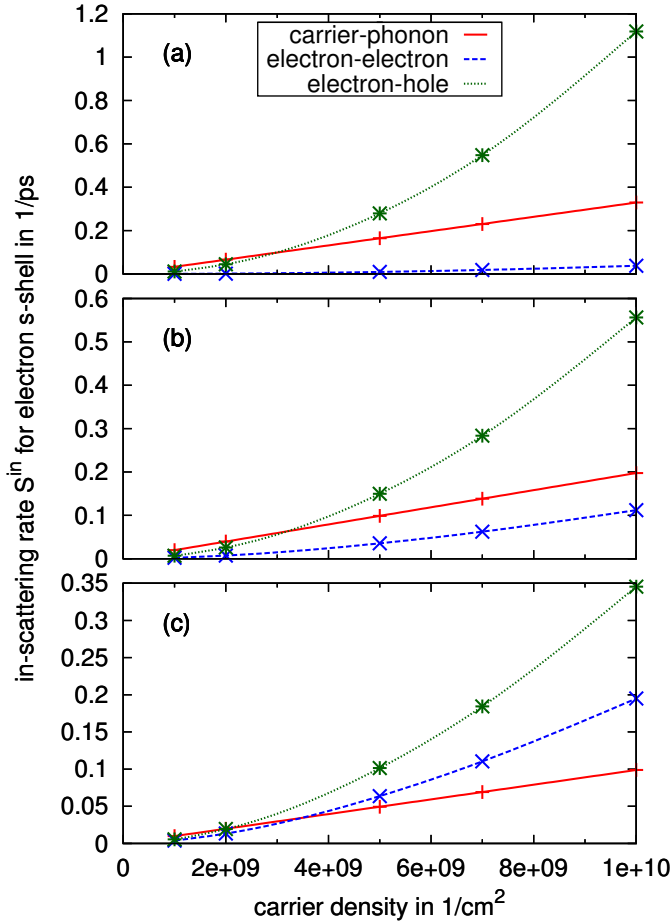


Fig. 5.20: Total in-scattering rate into the s-shell for electrons, considering a carrier distribution where only the p-shell is filled (a), 60% of the carrier density is in the p-shell, 30% in the s-shell, 10% in the WL (b) and 60% in the s-shell, 30% in the p-shell and 10% in the WL (c).

investigation, all scattering rates decrease when the populations evolve towards a steady state distribution. However, the relative strength of electron-electron and carrier-phonon scattering rates increase at later stages of the temporal evolution. While in the early stage of the evolution carrier-phonon scattering is more efficient than electron-electron scattering, both contributions are comparable for later stages.

For an ensemble of self-assembled QDs under resonant excitation of the p-shell, electron-hole pairs are always excited within the same QD. On the contrary, when electron-hole pairs are excited in the WL, electrons and holes might be captured into different QDs,

resulting in QDs that are only populated either by electrons or by holes. In that situation the electron-hole scattering channel is blocked. However, even in case of p-shell excitation carriers can be scattered into the WL, for example by the processes depicted in Fig. 5.19a-b, and subsequently captured into a different QDs. This also results in QDs that are only populated either by electrons or by holes. Additionally, for later stages of the kinetics also WL assisted processes contribute, independent of the excitation condition. Furthermore, our procedure also includes configurations with QDs populated by more than one electron-hole pair even if the total carrier density is less than the QD density. An important point is that this is also the case in typical experimental situations. A weak pump pulse, that on average generates one electron-hole pair per QD, can in fact generate two electron-hole pairs in one QD and no electron-hole pair in another QD. This opens relaxation processes where for example two QD electrons or two QD holes are scattered. As an example the electron-electron scattering is depicted in Fig. 5.19a.

Our results show that for the low-temperature regime all scattering processes are important, even though electron-hole scattering dominates for early stages of the kinetics after optical pulse excitation. Due to polaron renormalizations, the carrier-LO-phonon interaction gives rise to scattering rates comparable to Coulomb scattering, even though the polaron spectral function exhibits narrow resonances at low temperatures.

(ii) Experimental analysis

The DTS signal shown in Fig. 5.18a contains additional contributions beyond the carrier-carrier and carrier-phonon scattering processes discussed above. Coulomb interaction of confined carriers leads to so-called multi-exciton states [20, 140]. Also the carrier spin was not considered so far. Therefore a more detailed analysis is necessary to understand the experimental data.

A significant contribution to the long-lived DTS signal might be due to so-called dark-exciton configurations rather than Pauli-blocking effects. Dark excitons consist of an electron and a hole, both having identical spin. For this configuration optical transitions are forbidden and a carrier recombination requires a preceding spin-flip process which is very unlikely on a ns timescale. Due to the optical selection rules, conventional pump-probe setups are only sensitive to bright-exciton transitions. Using linearly polarized probe pulses it can be detected for example if the QD s-shell is populated with one or two bright excitons. In contrast, a single dark exciton blocks both bright transitions. Thus, a level that is populated by two bright excitons cannot be distinguished from a dark exciton. As a consequence, in the DTS data shown in Fig. 5.18 the number of carriers detected in higher states might be overestimated.

To gain more insight into the population of the QD, additional measurements have been performed, where a magnetic field is applied perpendicular to the incident pump and probe

beams (Voigt configuration). In a classical interpretation, the carriers react to this perturbation with a precession of the carrier spins around the field. The magnetic field breaks the cylindrical symmetry of the system, and as a consequence the angular momentum is no longer a good quantum number. However, the resulting states can be described as a superposition of the unperturbed angular momentum states [18]. As a consequence the bright- and dark-exciton states mix, resulting in an optical observability of all spin configurations. This experimental setup allows a more adequate detection of the carrier populations as no optical transitions are blocked due to dark-exciton configurations.

The corresponding experimental results obtained in Voigt configuration are presented in Fig. 5.21a. The dominating dark-exciton contribution to the ground state vanishes and an overall reduction of the DTS signal is observed. Also in Voigt configuration long-lived traces are observed, especially for the excited states. As in this case no dark excitons contribute, Fig. 5.21a represents more accurately the QD population. Thus, the long-lived features for the excited states can be clearly assigned to resident carriers.

For additional information about the origin of the DTS traces an external magnetic field in Faraday configuration was applied, with the magnetic field parallel to incident pump/probe beam in z-direction. The Zeeman splitting observed in the TRDT signal is depicted in Fig. 5.21b. Clearly an s-like, p-like and d-like splitting of the resonances is seen, confirming their interpretation as QD resonances.

Conclusion

The experimental results show fast carrier scattering for elevated temperatures and at low temperatures the emergence of a phonon bottleneck after fast initial relaxation. Within the quantum-kinetic description of carrier-scattering due to the interaction with LO phonons the experimental findings for both temperature regimes can be understood.

For elevated temperatures, the absence of a phonon-bottleneck is clearly verified by the fast rise time of the TRDT signal for the ground state, which does not depend on the excited carrier density as shown in Fig. 5.18b. It has been discussed in detail in Chap. 5.2.1 that this is due to polaron effects. In case of low temperatures, Fig. 5.18b shows a much slower relaxation times and a clear dependence on the excitation density. Furthermore, an incomplete thermalization is observed in Fig. 5.21a, which is seen in the population of energetically higher QD states for late times. Slow relaxation times can be understood by the much sharper resonances of the polaron spectral function in this temperature regime. Additionally, the quantum-kinetic calculation shows an incomplete thermalization of carriers in the long-time limit as depicted in Fig. 5.17.

Even though the experimental findings for both temperature regimes can be understood within our quantum-kinetic model for the carrier-LO-phonon interaction, in addition Coulomb effects might contribute in the experiment. For the particular experimental situation

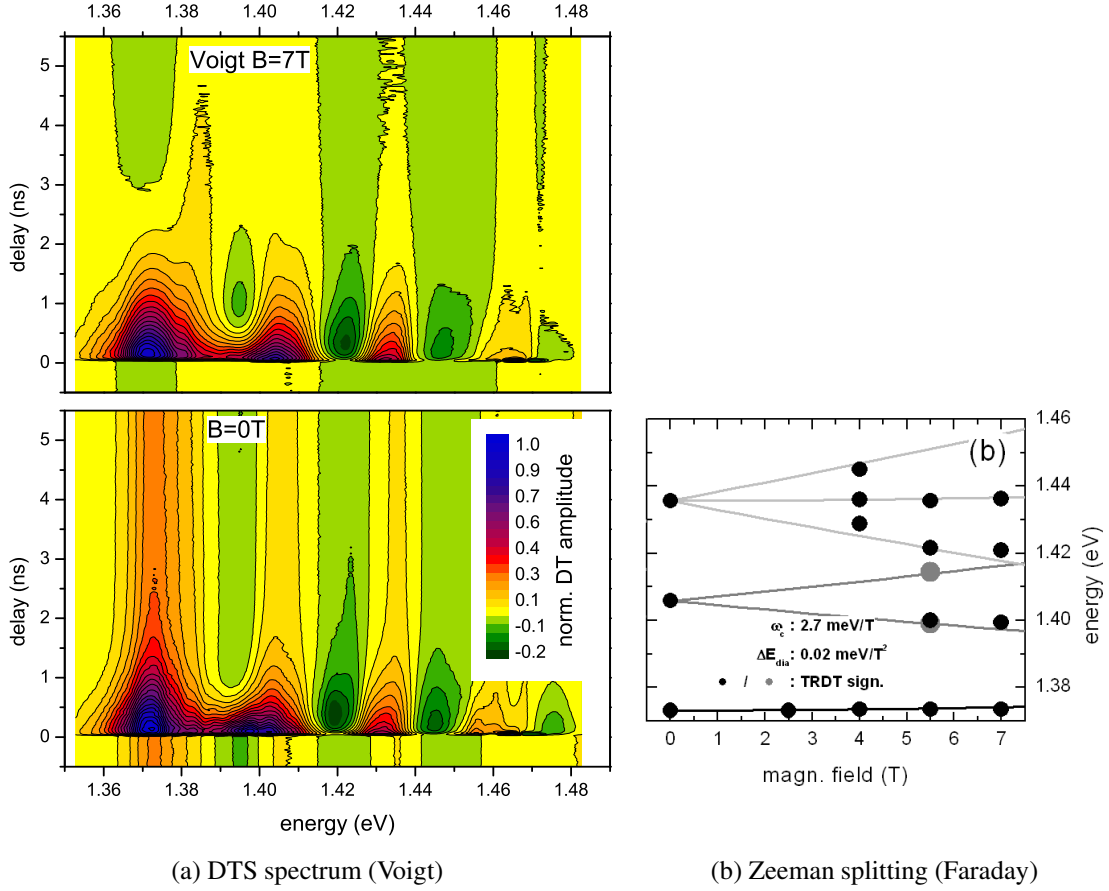


Fig. 5.21: DTS spectrum on an ensemble of InGaAs QDs with an magnetic field (7 T) applied in Voigt configuration (a) and Zeeman splitting of the QD traces in the DTS spectrum due to magnetic field in Faraday configuration (b). Pictures courtesy of H. Kurtze and Prof. Dr. M. Bayer, University Dortmund.

it is difficult to analyze the relative strength of carrier-carrier and carrier-LO-phonon scattering processes. Both mechanisms are competing, depending on the population configuration and temperature. As experimentally shown in Fig. 5.18b and theoretically confirmed in Fig. 5.20, even in the low-carrier-density regime Coulomb scattering plays an important role in the relaxation of carriers towards the ground state. However, the non-thermal carrier distribution observed in the experiment is a signature of the interaction with LO-phonons. For carrier-carrier scattering processes one expects a Fermi-Dirac distribution in the long-time limit, as any energy can be transferred to the scattering partner. Therefore, we can conclude that in Fig. 5.21a the kinetics is not dominated by Coulomb processes but by the interaction with LO phonons, even though both mechanisms contribute to the fast carrier relaxation.

6 Optical experiments

In contrast to Chap. 5 where the focus is on carrier scattering, this chapter is dedicated to optical effects like coherent polarization dynamics and photoluminescence. Their importance for the application of QDs in LED and laser devices has been already elaborated in Chap. 2. Semiconductor optics is a wide field that ranges from wave-guide structures for light confinement to quantum optics, light-matter coupling, and ultrafast carrier kinetics [18, 34]. In the following chapter we focus on the optical response and the photoluminescence properties of semiconductor QDs.

To experimentally study the optical response of a semiconductor, nowadays well-established pump-probe experiments are available, using for example photon-echo or four-wave-mixing (FWM) configurations [34]. For the discussion of the optical response basically two pictures are employed, depending on the excitation density regime. Whereas for high carrier densities results are discussed by means of the many-body interaction of an electron-hole plasma, in the low-carrier-density regime the exciton picture is adequate, taking into account few-particle interactions. An example for a few-particle system are QDs in the low-temperature and low-excitation regime, where most of the carriers are in the ground state. This so-called multi-exciton regime is successfully described using the configuration-interaction (CI) method in order to calculate the corresponding absorption spectra [20, 140, 157]. For high carrier densities, the coherent polarization dynamics can be described using the framework of NGFs, which follows similar lines as discussed for the carrier scattering in Chap. 5. Already early publications on the carrier kinetics included coherent polarization effects [57, 107]. Absorption spectra [158, 159] as well as ultra-fast phenomena in pump-probe experiments have been studied using this method [34, 58, 96]. An alternative approach is the dynamics-controlled truncation (DCT) developed by Axt and Stahl [69, 70], which was successfully used to study exciton and biexciton resonances in FWM experiments and can also be formulated using NGFs [71, 73, 74]. Besides Coulomb effects like exciton and biexciton formation, mainly the dephasing due to the interaction with LA phonons has been investigated. For example the influence of dephasing on Rabi oscillations in QDs [160, 161], which are considered for application as optical switch. It has been pointed out that for the low-temperature regime LA phonons provide the dominant contribution, whereas at elevated temperatures also LO phonons play an important role [44–46].

Our focus in Chap. 6.1 is on laser applications where elevated temperatures and high carrier-densities are present and hence the combined influence of Coulomb and phonon

effects is important. For the optical properties especially the influence of many-body renormalizations like polaron effects, as well as the importance of different scattering channels is of interest.

The coherent optical response is governed by dephasing processes on a femto-second time scale. In contrast, photoluminescence experiments incorporating carrier recombination processes take place on a much longer timescale of nano seconds. For laser applications the carrier recombination dynamics is of central importance. The spontaneous and stimulated emission of photons provides the basic mechanism for laser operation, together with the optical feedback of the cavity. Interesting subjects of current research are for example single-photon sources [18], which can be used for quantum cryptography. These devices involve only a single QD as light emitter. Therefore, the light-matter interaction of the QD with the cavity mode is of special interest and is currently intensively investigated in the field of the so-called cavity QED [18, 23, 26, 162]. Furthermore, single-photon sources show almost no threshold behavior in the input-output curve. However, the transition from spontaneous to stimulated emission can be seen in the photon statistics of the emitted light, which is investigated using corresponding correlation measurements [18, 163, 164].

For the theoretical description of such single-emitter devices, bridging the timescales for carrier scattering and recombination processes is one of the main problems. Optical coherences dephase rapidly but carrier scattering processes on a fs timescale strongly influence the recombination dynamics. They determine the population of the QD ground state as well as renormalizations of the single-particle states. The development of a model for the recombination dynamics and its incorporation in a laser model is a challenging task on its own. Detailed studies on this subject are presented for example in Refs. [67, 68, 165]. In this thesis, the focus of Chap. 6.2 is on bridging the different timescales and including carrier-scattering and quasi-particle renormalizations in the emitter model.

6.1 Linear absorption and optical gain

The goal of this chapter is to determine the optical properties of a QD system by means of an optical absorption experiment. For laser applications at room temperature, high carrier densities are necessary to obtain population inversion. In this chapter we focus on the situation where the optical excitation/injection of carriers and successive scattering processes due to carrier-carrier and carrier-phonon interaction leads to a quasi-equilibrium carrier distribution. After a quasi-equilibrium situation is reached, the carrier distribution is influenced by recombination processes only. For this situation we consider an experiment where the sample is excited by a weak optical probe pulse and the transmitted field is detected. The probe-induced polarization as the response to the optical excitation is given

via the non-linear optical susceptibility χ according to

$$\mathbf{P}(\mathbf{r}, t) = \int d\mathbf{r}' \int dt' \chi(\mathbf{r}, \mathbf{r}', t, t') \mathbf{E}(\mathbf{r}', t') \quad (6.1)$$

$$= \chi^{(1)} \mathbf{E} + \chi^{(3)} \mathbf{E} \mathbf{E}^* \mathbf{E} + \dots \quad (6.2)$$

Note, that the optical susceptibility contains only odd powers of the optical field as even powers correspond to coherent populations¹. In general the susceptibility has tensorial character, but for simplification usually the response function is classified into terms of n-th order in the optical field, the so called $\chi^{(n)}$ regimes. While propagating through the sample, the electric field of the pulse satisfies, according to Maxwell's equations, the propagation equation

$$\left(\frac{1}{c^2} \frac{\partial^2}{\partial t^2} - \Delta \right) \mathbf{E}(\mathbf{r}, t) = -\mu_0 \frac{\partial^2}{\partial t^2} \mathbf{P}(\mathbf{r}, t). \quad (6.3)$$

These propagation effects, describing the interplay of modified electric fields and polarization, in principle have to be taken into account. However, in thin samples we assume these effects to be negligible and for details on their inclusion we refer the reader to Refs. [71, 77]. For the description of the optical properties, the knowledge of χ is sufficient since it directly reflects the dielectric function

$$\epsilon_{\mathbf{q}}(\omega) = 1 + \chi_{\mathbf{q}}(\omega), \quad (6.4)$$

which contains both the refractive index and the absorption coefficient in its real and imaginary parts. The macroscopic polarization can be determined in terms of lesser GFs, which in second quantization and expanded into an eigenfunction basis is given by

$$\mathbf{P}_{\mathbf{q}}(t) = \sum_{12} \mathbf{d}_{12}(\mathbf{q}) G_{12}^<(t) \quad 1 \neq 2. \quad (6.5)$$

The dipole coupling matrix element $\mathbf{d}_{12}(\mathbf{q})$ incorporates the optical selection rules (cf. Chap. 4.3). In this notation $G_{12}^<$ contains all inter-band and intra-band polarizations, but in the following we restrict ourselves only to inter-band contributions $\lambda_1 \neq \lambda_2$. From the macroscopic polarization the response function can then be determined by means of a functional derivative

$$\chi_{\mathbf{q}}(t, t') = \frac{\delta \mathbf{P}_{\mathbf{q}}(t)}{\delta \mathbf{E}_{\mathbf{q}}(t')} = \sum_{\alpha\beta,\gamma\delta} \mathbf{d}_{\alpha\beta}(\mathbf{q}) \mathbf{d}_{\gamma\delta}(\mathbf{q}) G_{\alpha\beta\gamma\delta}^R(tt, t't'), \quad (6.6)$$

where we find the susceptibility given in terms of a two-particle GF. For the derivation a Fourier expansion of \mathbf{E} and \mathbf{P} was performed. Details of the calculation of the two-particle GF by means of a T -matrix formalism can be found for example in Ref. [166].

¹Cf. for example the discussion of the optical Bloch equations in Ref. [34]

However, in this thesis a different approach is used. For weak probe pulses, i.e. in the $\chi^{(1)}$ regime, the susceptibility depends only on the time difference for equilibrium situations. In this case a Fourier transform with respect to the relative time can be performed and the optical response is simply given by

$$\chi(\omega) = \frac{P(\omega)}{E(\omega)}. \quad (6.7)$$

Note, that due to the steep photon dispersion $\omega = c \cdot |\mathbf{q}|$ we restrict the discussion in the following to the $\mathbf{q} = 0$ contribution and hence the corresponding index is dropped. For the high carrier densities considered in the following, the inclusion of both carrier-phonon and carrier-carrier scattering processes is important. However, a time-dependent treatment consistently including both contributions as discussed in Chap. 5 is not necessary in our case. For a fixed quasi-equilibrium carrier population and restricting to the $\chi^{(1)}$ regime, the problem simplifies considerably in the frequency domain. The derivation of the corresponding quantum-kinetic equations follows the same lines as discussed in Chap. 5 for the carrier scattering, but results can then be obtained from a numerically less demanding matrix diagonalization procedure. Note, that the following results were obtained in close collaboration with Michael Lorke who performed the calculations that include the Coulomb scattering terms.

Quantum kinetic equations

Considering a weak probe pulse, i.e. restricting to the $\chi^{(1)}$ regime, means that probe-induced population changes are neglected as they correspond to at least $\chi^{(2)}$ processes. For the selfenergy contributions discussed in Chap. 5.2.2 and considering a fixed quasi-equilibrium carrier distribution, we obtain for the frequency representation of the SBE (5.33)

$$\begin{aligned} (\epsilon_\alpha^e + \epsilon_\alpha^h - \hbar\omega) \psi_\alpha(\omega) - (1 - f_\alpha^e - f_\alpha^h) \Omega_\alpha(\omega) \\ = -i\hbar \left(-\Gamma_{\alpha\alpha}^{\text{DD}}(\omega) \psi_\alpha(\omega) + \sum_\beta \Gamma_{\alpha\beta}^{\text{OD}}(\omega) \psi_\beta(\omega) \right). \end{aligned} \quad (6.8)$$

Due to the Hartree and Fock contributions of the Coulomb interaction we find renormalized single-particle energies $\epsilon_\alpha^a = \epsilon_{0,\alpha}^a + \sum_\beta (V_{\alpha\beta\alpha\beta} - V_{\alpha\beta\beta\alpha}) f_\beta^a$ and a renormalized Rabi energy $\Omega_\alpha(\omega) = \mathbf{d}_\alpha \mathbf{E}(\omega) + \sum_\beta V_{\alpha\beta\alpha\beta} \psi_\beta(\omega)$ which gives rise to excitonic resonances. Furthermore, Pauli-blocking factors $1 - f_\alpha^e - f_\alpha^h$ determine whether the system is in the absorption or in the gain regime. For a detailed analysis of the exciton problem and the corresponding absorption spectra we refer the reader to Ref. [149]. Similar to the discussion of the carrier-phonon scattering in Chap. 5.2.2, the collision terms give rise to a diagonal (DD) and an off-diagonal (OD) contribution to the dephasing. The terms due to

the carrier-phonon interaction (frequency representation of (5.35)) read

$$\begin{aligned} \Gamma_{\alpha}^{\text{DD}}(\hbar\omega) = i & \sum_{\substack{a,b=e,h \\ b \neq a}} \sum_{\beta,\mathbf{q}} M_{\alpha\beta}^a(\mathbf{q}) M_{\alpha\beta}^{*,b}(\mathbf{q}) \\ & \times \left\{ (1 - f_{\beta}^a) \left[(1 + N_{\text{LO}}) \tilde{G}_{\beta,\alpha}^{a,b}(\hbar\omega - \hbar\omega_{\text{LO}}) + N_{\text{LO}} \tilde{G}_{\beta,\alpha}^{a,b}(\hbar\omega + \hbar\omega_{\text{LO}}) \right] \right. \\ & \left. + f_{\beta}^a \left[(1 + N_{\text{LO}}) \tilde{G}_{\beta,\alpha}^{a,b}(\hbar\omega + \hbar\omega_{\text{LO}}) + N_{\text{LO}} \tilde{G}_{\beta,\alpha}^{a,b}(\hbar\omega - \hbar\omega_{\text{LO}}) \right] \right\} \end{aligned} \quad (6.9)$$

and

$$\begin{aligned} \Gamma_{\alpha\beta}^{\text{OD}}(\hbar\omega) = i & \sum_{\substack{a,b=e,h \\ b \neq a}} \sum_{\mathbf{q}} M_{\alpha\beta}^a(\mathbf{q}) M_{\alpha\beta}^{*,b}(\mathbf{q}) \\ & \times \left\{ (1 - f_{\alpha}^a) \left[(1 + N_{\text{LO}}) \tilde{G}_{\beta,\alpha}^{b,a}(\hbar\omega - \hbar\omega_{\text{LO}}) + N_{\text{LO}} \tilde{G}_{\beta,\alpha}^{b,a}(\hbar\omega + \hbar\omega_{\text{LO}}) \right] \right. \\ & \left. + f_{\alpha}^a \left[(1 + N_{\text{LO}}) \tilde{G}_{\beta,\alpha}^{b,a}(\hbar\omega + \hbar\omega_{\text{LO}}) + N_{\text{LO}} \tilde{G}_{\beta,\alpha}^{b,a}(\hbar\omega - \hbar\omega_{\text{LO}}) \right] \right\} \end{aligned} \quad (6.10)$$

with the scattering kernel

$$\tilde{G}_{\alpha\beta}^{a,b}(\omega) = \int_0^t d\tau e^{i\omega\tau} G_{\beta}^{\text{R},a}(\tau) G_{\alpha}^{\text{R},b}(\tau). \quad (6.11)$$

These contributions to the dephasing arise from carrier scattering due to phonon emission ($\propto 1 + N_{\text{LO}}$) and absorption ($\propto N_{\text{LO}}$) processes, weighted by the corresponding scattering kernel that contains the overlap of electron and hole retarded GFs. The frequency dependence of the diagonal and the off-diagonal terms reflects the non-Markovian nature of the dephasing processes, as the product $\Gamma(\omega) \cdot \Psi(\omega)$ in Eqs. (6.9)–(6.10) amounts in the time domain to a convolution integral that describes memory effects. Even though only non-Markovian calculations are presented below, some comments on the Markovian limit of the dephasing terms (6.9)–(6.11) are appropriate. The Markovian limit is obtained when applying the reverse GKBA (3.75) in the derivation. In this case the polarizations in the collision terms depend only on the external time t as no memory effects are included, resulting in scattering kernels that do not depend on frequency ω . Hence, in the Markovian limit the dephasing becomes frequency independent. Note, that in this case the scattering kernel (6.11) is band diagonal due to the reverse GKBA, i.e. $a = b$, in contrast to the non-Markovian treatment.

The evaluation of the corresponding collision terms for the carrier-carrier interaction follows the same lines as discussed above for the phonons. A diagonal approximation for the GFs is used and the GKBA is applied. Details on the evaluation of the collision are presented for example in Refs. [92, 156, 167, 168]. For the diagonal and off-diagonal

dephasing we find

$$\begin{aligned} \Gamma_{\alpha}^{\text{DD}}(\hbar\omega) = i & \sum_{\substack{a,b=e,h \\ b \neq a}} \sum_{\alpha_1\alpha_2\alpha_3} \\ & \times \left\{ W_{\alpha\alpha_2\alpha_3\alpha_1} [2W_{\alpha\alpha_2\alpha_3\alpha_1}^* - W_{\alpha\alpha_2\alpha_1\alpha_3}^*] \right. \\ & g(\hbar\omega - \tilde{\varepsilon}_{\alpha}^b - \tilde{\varepsilon}_{\alpha_1}^a + (\tilde{\varepsilon}_{\alpha_2}^a)^* - \tilde{\varepsilon}_{\alpha_3}^a) \left[(1 - f_{\alpha_2}^a) f_{\alpha_3}^a f_{\alpha_1}^a + (f \rightarrow 1 - f) \right] \\ & + 2W_{\alpha\alpha_2\alpha_3\alpha_1}^* W_{\alpha\alpha_2\alpha_3\alpha_1} \\ & \left. g(\hbar\omega - \tilde{\varepsilon}_{\alpha}^b - \tilde{\varepsilon}_{\alpha_1}^a - \tilde{\varepsilon}_{\alpha_2}^b + (\tilde{\varepsilon}_{\alpha_3}^b)^*) \left[f_{\alpha_2}^b (1 - f_{\alpha_3}^b) f_{\alpha_1}^a + (f \rightarrow 1 - f) \right] \right\}, \end{aligned} \quad (6.12)$$

and

$$\begin{aligned} \Gamma_{\alpha\alpha_1}^{\text{OD}}(\hbar\omega) = i & \sum_{\substack{a,b=e,h \\ b \neq a}} \sum_{\alpha_2\alpha_3} \\ & \times \left\{ W_{\alpha\alpha_2\alpha_3\alpha_1} [2W_{\alpha\alpha_2\alpha_3\alpha_1}^* - W_{\alpha\alpha_2\alpha_1\alpha_3}^*] \right. \\ & g(\hbar\omega - \tilde{\varepsilon}_{\alpha}^a - \tilde{\varepsilon}_{\alpha_1}^b - \tilde{\varepsilon}_{\alpha_2}^a + (\tilde{\varepsilon}_{\alpha_3}^a)^*) \left[(1 - f_{\alpha_3}^a) f_{\alpha_2}^a f_{\alpha}^a + (f \rightarrow 1 - f) \right] \\ & + 2W_{\alpha\alpha_2\alpha_3\alpha_1}^* W_{\alpha\alpha_2\alpha_3\alpha_1} \\ & \left. g(\hbar\omega - \tilde{\varepsilon}_{\alpha}^a - \tilde{\varepsilon}_{\alpha_1}^b + (\tilde{\varepsilon}_{\alpha_2}^b)^* - \tilde{\varepsilon}_{\alpha_3}^b) \left[f_{\alpha_3}^b (1 - f_{\alpha_2}^b) f_{\alpha}^a + (f \rightarrow 1 - f) \right] \right\} \end{aligned} \quad (6.13)$$

with the scattering kernels $g(\dots)$ discussed below. Both equations contain direct terms $\propto 2|W_{\alpha_1\alpha_2\alpha_3\alpha_4}|^2$ and exchange terms $\propto W_{\alpha_1\alpha_2\alpha_3\alpha_4} W_{\alpha_1\alpha_2\alpha_4\alpha_3}$. The contributions to the dephasing due to carrier-carrier scattering can be classified into different scattering channels. Interaction matrix elements which contain three WL indices and one QD index, for example $W_{k_1 k_2 k_3 \nu}$, represent the capture of a WL carrier into the QD while another WL carrier is scattered to an energetically higher quasi-continuum state. These processes are therefore denoted as WL-assisted capture. Similarly WL-assisted relaxation ($2 \times k$, $2 \times \nu$), QD-assisted relaxation ($1 \times k$, $3 \times \nu$), and intra-QD processes ($4 \times \nu$) are introduced. A detailed analysis of these processes is beyond the scope of this thesis. For their relative importance in the context of carrier scattering rates we refer the reader to Refs. [92, 156], whereas the contributions of the different scattering channels to the dephasing is discussed in Refs. [167, 168]. It turns out, that the dominating contributions are the intra-QD and WL-assisted relaxation processes, as they also contain the so-called pure-dephasing processes that leave the population unchanged.

In analogy to the carrier-phonon case, the scattering kernel is determined by the retarded GFs of the involved states. The corresponding scattering kernel contains four GFs as the

Coulomb scattering is a two-particle process, in contrast to the carrier-phonon interaction where only two GFs are involved. Within a single-pole approximation for the GFs, the scattering kernel can be evaluated analytically according to

$$\begin{aligned} g(\hbar\omega - \tilde{\epsilon}_\alpha - \tilde{\epsilon}_\beta - \tilde{\epsilon}_\gamma + \tilde{\epsilon}_\delta^*) &= \int_0^t d\tau e^{i\omega\tau} G_\alpha^R(\tau) G_\beta^R(\tau) G_\gamma^R(\tau) G_\delta^A(\tau) \\ &= \frac{1}{\hbar\omega - \tilde{\epsilon}_\alpha - \tilde{\epsilon}_\beta - \tilde{\epsilon}_\gamma + \tilde{\epsilon}_\delta^*}. \end{aligned} \quad (6.14)$$

In this case the energy shifts and carrier lifetimes are included via a complex single-particle energy $\tilde{\epsilon} = \epsilon_0 + \Delta - i\Gamma$. Hence, the single-particle energies contained in the dephasing terms (6.12)–(6.13) as well as in the scattering kernel (6.14) are complex too. At this point one has to be careful since a self-consistency problem arises. The selfenergy contributions from carrier-carrier and carrier-phonon interaction that lead to the many-body renormalizations of the transition amplitudes both also give rise to renormalizations of the single-particle properties reflected in the retarded GFs. This subject is discussed in more detail in the next section. In the Markovian limit, the dephasing becomes frequency independent due to the same reasons discussed above for the carrier-phonon interaction. The reader who is interested in details of the calculation for the carrier-carrier interaction is referred to Refs. [167, 168].

Self-consistent retarded Green's functions

To illustrate the self-consistent treatment of the carrier-carrier and carrier-phonon interaction, we note that in the kinetic equation (6.8) the selfenergy $\Sigma = \Sigma^{\text{HF}} + \Sigma^{\text{SBA}} + \Sigma^{\text{e-ph}}$ gives rise to the dephasing contributions discussed above. According to the Kadanoff-Baym equations (3.64), a self-consistent treatment requires the consideration of the same contributions in the retarded GF, which in frequency representation is given by

$$G_\alpha^R(\omega) = \frac{1}{\hbar\omega - [\epsilon_\alpha + \Sigma_\alpha^R(\omega)]}. \quad (6.15)$$

This GF is evaluated in a single-pole approximation, similar to the collision terms. In a first step only the Hartree and Fock as well as the SBA Coulomb contributions

$$\Sigma_\alpha^{a,R}(\hbar\omega) = -i \sum_{\substack{b=e,h \\ b \neq a}} \sum_{\alpha_1 \alpha_2 \alpha_3} \quad (6.16)$$

$$\begin{aligned} &\times \left\{ W_{\alpha \alpha_2 \alpha_3 \alpha_1}^* [2W_{\alpha \alpha_2 \alpha_3 \alpha_1}^* - W_{\alpha \alpha_2 \alpha_1 \alpha_3}^*] \right. \\ &g (\hbar\omega - \tilde{\epsilon}_{\alpha_1}^a + (\tilde{\epsilon}_{\alpha_2}^a)^* - \tilde{\epsilon}_{\alpha_3}^a) \left[(1 - f_{\alpha_2}^a) f_{\alpha_3}^a f_{\alpha_1}^a + (f \rightarrow 1 - f) \right] \\ &+ 2W_{\alpha \alpha_2 \alpha_3 \alpha_1}^* W_{\alpha \alpha_2 \alpha_3 \alpha_1} \\ &\left. g \left(\hbar\omega - \tilde{\epsilon}_{\alpha_1}^a - \tilde{\epsilon}_{\alpha_2}^b + (\tilde{\epsilon}_{\alpha_3}^b)^* \right) \left[f_{\alpha_2}^b (1 - f_{\alpha_3}^b) f_{\alpha_1}^a + (f \rightarrow 1 - f) \right] \right\} \end{aligned} \quad (6.17)$$

are used. To self-consistently combine carrier-carrier and carrier-phonon contributions, in a second step the full retarded GF is calculated from the Dyson equation (5.2), where the Coulomb-renormalized single-particle energies $\tilde{\epsilon} = \epsilon + \Sigma^R$ are dressed by the carrier-phonon interaction. The corresponding retarded GF reads

$$G^R(t) = -\frac{i}{\hbar} \Theta(t) \mathcal{G}_\alpha(t) e^{-\frac{i}{\hbar} \tilde{\epsilon}_\alpha t}. \quad (6.18)$$

Since the Coulomb scattering provides a large damping, also the polaron GF can be treated in single-pole approximation. By iteration the renormalized single-particle energies for the combined carrier-Coulomb and carrier-phonon interaction are calculated self-consistently. Usually convergence is obtained after a few iterations. This approach is equivalent to the one discussed for the finite-density polaron in Chap. 5.1.5, as any selfenergy that simply shifts the poles of the retarded GF can be incorporated by means of a renormalized single-particle energy.

Results for the self-consistently calculated spectral function are shown in Fig. 6.1. The calculations are performed for a InGaAs QD-WL system where the QDs contain an s- and a two-fold degenerate p-shell with a level spacing of 40 meV for electrons and 15 meV for holes. Further material parameters are summarized in Tab. B.1. Polaronic structures are strongly broadened in the spectral function as a result of the dominant role of damping due to Coulomb scattering. Furthermore, large interaction-induced energy shifts are observed. In the time domain, the exponential decay $\exp -\frac{\gamma_\alpha^a}{\hbar} t$ of the retarded GF (6.18) due to Coulomb interaction is superimposed on the polaronic renormalizations $\mathcal{G}_\alpha^a(t)$. Thus, at low carrier densities the broadening of the resonances in the spectral function might be overestimated. In this regime excitonic effects dominate and the treatment of the carriers as a plasma is not expected to be a good approximation. Nevertheless, for the following calculations of the optical gain we are interested in high carrier densities ($> 1 \times 10^{10} \text{ cm}^{-2}$). In this situation a strong broadening of the polaron satellites is observed, resulting in a single-peak structure and verifying the pole approximation for the retarded GF. Due to the dominating influence of Coulomb renormalizations also small corrections due to population effects in the polaron selfenergy (cf. Chap. 5.1.5) can be neglected and are not considered in the following.

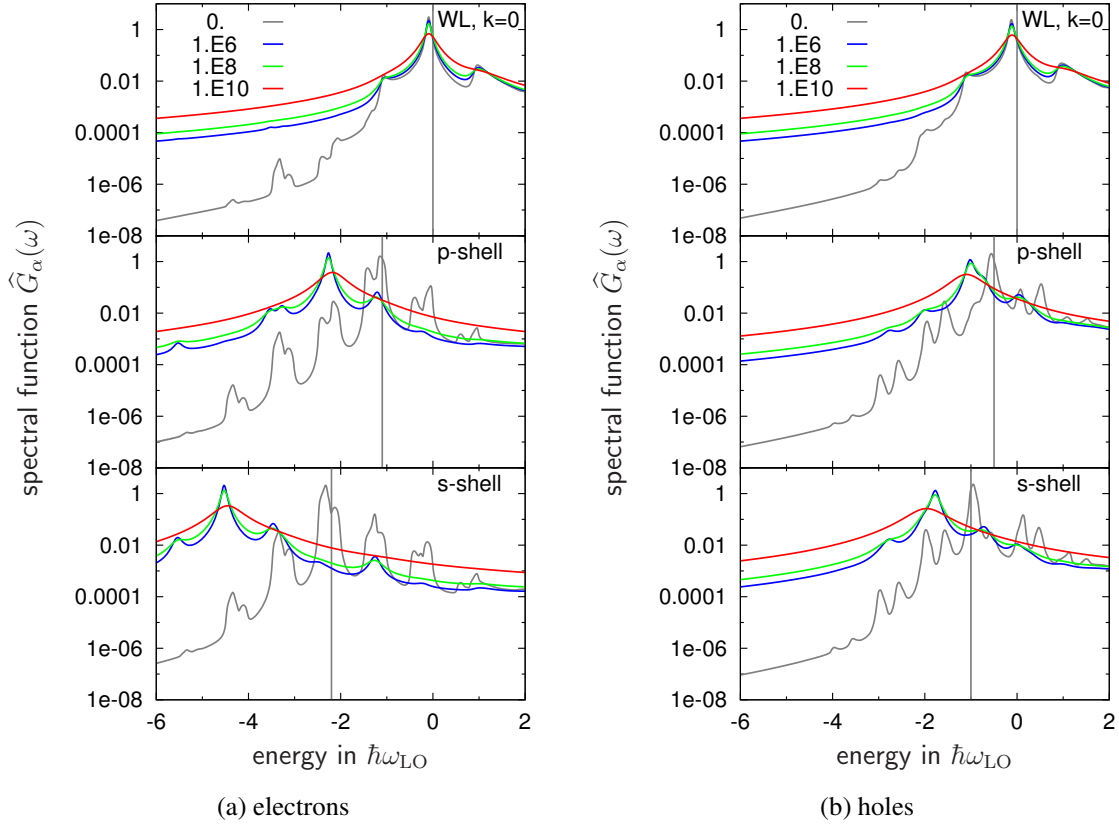


Fig. 6.1: Spectral function of the $k=0$ WL state and the QD p- and s-shell states including the interaction with LO phonons and Coulomb interaction of carriers for various carrier densities in $1/\text{cm}^2$.

Absorption spectra and gain

Using the selfconsistently calculated retarded GFs in the collision terms, now we are able to calculate the corresponding absorption spectra. Absorption spectra that are obtained from the SBE (6.8) without collision terms exhibit only three resonances, namely s-shell, p-shell, and the excitonic resonance of the WL. Considering correlation contributions due to the interaction of carriers with LO phonons, we find the absorption spectra shown in Fig. 6.2a. Energetically above the resonances of the s-shell and the p-shell several peaks due to polaron effects can be observed. Whereas the non-Lorentzian character of the line shapes is very pronounced, their broadening is not affected by the carrier density.

Polaronic renormalizations of the single-particle states lead to a more complicated resonance structure for the interband transitions. From the inset in logarithmic scale one can identify phonon replicas and hybridization effects of the polaron GF which is discussed

6 Optical experiments

in Chap. 5.1.2. For example, the s-shell resonance has a shoulder on the lower energetic side due to hybridization of the corresponding electron state. The influence of the polaron GF on the absorption spectra is contained in the dephasing kernel (6.11), whose interpretation is similar to the scattering kernel (5.31) discussed in Chap. 5.2.1. In this case the interband-overlap of electron and hole GF determines the transition strength, together with the corresponding interaction matrix elements.

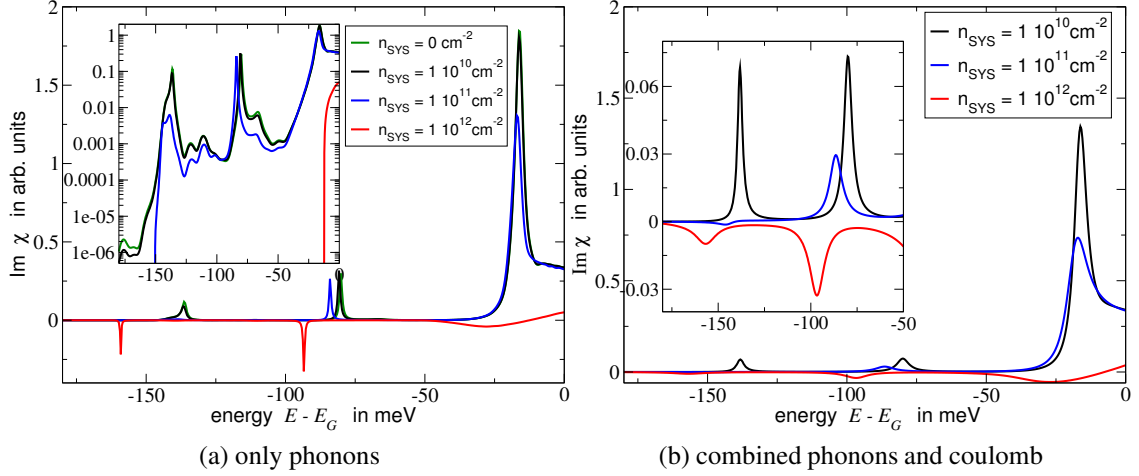


Fig. 6.2: Room-temperature absorption spectra including only carrier-LO-phonon collisions in panel (a) and both carrier-LO-phonon as well as carrier-carrier collisions on a self-consistent footing in panel (b).

Considering correlations due to carrier-LO-phonon interaction (6.9)–(6.10) as well as carrier-carrier scattering (6.12)–(6.13), both evaluated with self-consistently renormalized single-particle energies (6.15), the absorption spectra shown in Fig. 6.2b are found. Due to many-body interactions a bleaching and red-shift of the resonances as well as saturation of the s-shell gain is observed. Although we find that the Coulomb interaction is clearly the dominant dephasing mechanism at high carrier densities, we also infer from a comparison of both contributions, presented in Fig. 6.3, that even in the gain regime the carrier-phonon interaction considerably contributes to the dephasing. Nevertheless, polaronic features are absent in the spectra since the complicated multi-peak structure of the spectral function is completely damped out due to Coulomb effects (cf. Fig. 6.1).

For intermediate carrier densities around $5 \times 10^{10} \text{ cm}^{-2}$, both types of interaction processes are equally important. Comparing the results in Fig. 6.3a we find for our situation that taking into account only the Coulomb dephasing mechanism underestimates the dephasing of the ground state transition by roughly a factor of two, while on the contrary the broadening of the WL is dominated by carrier-phonon interaction. For higher carrier densities, however, this picture changes as can be seen in Fig. 6.3b. At a carrier density of $2 \times 10^{11} \text{ cm}^{-2}$,

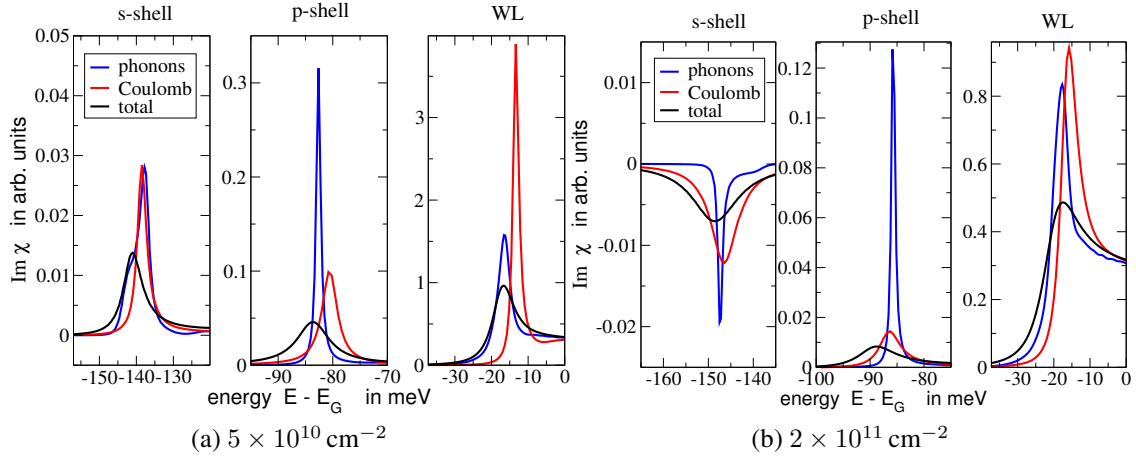


Fig. 6.3: Comparison of carrier-carrier and carrier-phonon contributions to the dephasing in room-temperature absorption spectra for QD systems.

the Coulomb interaction is the dominant dephasing mechanism for the QD resonances. For the excitonic resonance of the WL, the two mechanisms are equally important at this rather high carrier density, where the s-shell transition is already in the gain regime.

These results indicate the importance of including both, carrier-carrier and carrier-phonon interaction, on a self-consistent footing in the calculation of optical absorption spectra. Artifacts that arise from using non-self-consistently calculated single-particle energies as well as a detailed analysis on the relative importance of diagonal and off-diagonal contributions to the dephasing and various scattering channels is presented by Lorke [167], Lorke et al. [168]. Furthermore, this model for the optical absorption of QD systems predicts new physical effects like a reduction of the optical gain with increasing carrier density [169], which can not be observed in QWs and is unique to QD systems. Another application of this model is the calculation of technologically relevant quantities like the line-width-enhancement factor that is important for laser application [170].

6.2 Time-resolved photoluminescence

The carrier scattering and dephasing processes which are discussed in previous chapters take place on a ps timescale. In this chapter we focus on time-resolved photoluminescence experiments (TRPL) where the carrier recombination processes takes place on a much slower timescale (ns). The main goal is to bridge the different timescales and combine a quantum-kinetic calculation for the scattering with a model that describes the photoluminescence.

In TRPL experiments a pump pulse is used to optically excite carriers into the energetically higher WL or bulk states. Scattering processes due to carrier-carrier and carrier-phonon interaction lead to a relaxation towards the energetically lowest states, resulting in a quasi-equilibrium carrier distribution. From the optically active states carrier recombination processes takes place. For the theoretical description of the corresponding TRPL signal we treat the light-matter interaction quantum-mechanically. The Hamiltonian we consider in the following is given by (3.2), where the dipole interaction with a classical light field is replaced by the quantized light-matter interaction

$$\hat{H}_{\text{LM}} = -i \sum_{\xi,12} \left(g_{12}^{\xi} \hat{a}_1^\dagger \hat{a}_2 \hat{b}_\xi - \text{h.c.} \right) \quad 1 \neq 2 \quad (6.19)$$

with $1 \in \{\alpha_1, \lambda_1\}$ containing state index α and band index λ . Carrier creation and annihilation operators are denoted by $\hat{a}_i^{(\dagger)}$ and photon operators by $\hat{b}_\xi^{(\dagger)}$. The coupling matrix element

$$g_{12}^{\xi} = E^{\xi} \langle 1 | e \mathbf{r} \cdot \mathbf{U}^{\xi}(\mathbf{r}) | 2 \rangle \approx \tilde{E}_{\xi} \mathbf{d}_{\lambda_1 \lambda_2} \mathbf{U}_x i \delta_{\alpha_1 \alpha_2} = g^{\xi} \delta_{\alpha_1 \alpha_2}. \quad (6.20)$$

contains the overlap of the local dipoles $e \mathbf{r}$ with the optical mode $\mathbf{U}^{\xi}(\mathbf{r})$ which is classified by the index $\xi \in \{\mathbf{q}, \mathbf{e}\}$ denoting the mode \mathbf{q} and the polarization e . This can be simplified when considering equal envelope wavefunctions and the dipole approximation (second term). A detailed discussion of the light-matter interaction Hamiltonian is presented for example in Refs. [67, 68, 140, 149]. The interaction vertices of the light-matter interaction are similar to those of the carrier-phonon interaction. A carrier scatters from state $|1\rangle$ to state $|2\rangle$ by emission or absorption of a photon in mode ξ . The main difference is that the light-matter interaction describes inter-band processes, whereas in the carrier-phonon interaction only intra-band processes are involved. In this notation the Hamiltonian (6.19) contains resonant $\hat{c}^\dagger \hat{v} \hat{b}$ as well as non-resonant $\hat{v}^\dagger \hat{c} \hat{b}$ terms. A common approximation at this point is the so-called rotating-wave approximation (RWA) where one restricts to resonant terms only, as the non-resonant terms describe elementary processes that are not energy-conserving.

The quantities of interest for the calculation of the PL are the carrier-populations f_α and the photon number $N_\xi = \langle \hat{b}_\xi^\dagger \hat{b}_\xi \rangle$. The PL spectrum itself is obtained from the total number of emitted photons,

$$I(\omega) = \sum_{\xi} \frac{d}{dt} N_{\xi} \Big|_{\omega=c|\mathbf{q}|}. \quad (6.21)$$

To derive the corresponding equations of motion we use the cluster expansion method of Fricke [65, 66], which is introduced briefly in Chap. 3.1. In principle, here one could also introduce a photon Green's function and solve the corresponding Dyson equation. From the cluster expansion, the resulting equations of motion for the carrier populations and the

photon number are the semiconductor-luminescence equations (SLE)

$$\frac{d}{dt}N_\xi = |g_\xi|^2 \operatorname{Re} \sum_\alpha \langle \hat{b}_\xi^\dagger \hat{v}_\alpha^\dagger \hat{c}_\alpha \rangle \quad (6.22)$$

$$\frac{d}{dt}f_\alpha \Big|_{\text{LM}} = -\operatorname{Re} \sum_\xi |g_\xi|^2 \langle \hat{b}_\xi^\dagger \hat{v}_\alpha^\dagger \hat{c}_\alpha \rangle + \frac{d}{dt}f_\alpha \Big|_{\text{coll}}. \quad (6.23)$$

The number of photons emitted into the mode ξ is determined by the photon-assisted inter-band transition amplitude, i.e. the recombination of carriers. Correspondingly, the population of the involved states is reduced by the emission into all modes ξ . The photon assisted polarization obeys its own equation of motion

$$\begin{aligned} \left[i\hbar \frac{d}{dt} - (\tilde{\epsilon}^c - \tilde{\epsilon}^v - \hbar\omega_\xi - i\Gamma) \right] \langle \hat{b}_\xi^\dagger \hat{v}_\alpha^\dagger \hat{c}_\alpha \rangle &= ig_\xi f_\alpha^c (1 - f_\alpha^v) + N_\xi (f_\alpha^c - f_\alpha^v) \\ &\quad + (f_\alpha^c - f_\alpha^v) \sum_\beta V_{\alpha\beta\alpha\beta} \langle \hat{b}_\xi^\dagger \hat{v}_\beta^\dagger \hat{c}_\beta \rangle \\ &\quad + ig_\xi \sum_\beta C_{\beta\alpha\alpha\beta}^x \end{aligned} \quad (6.24)$$

containing spontaneous emission (first term RHS), stimulated emission which is important in cavities (second term RHS), and correlation terms. Similar to the SBE, the single-particle energies $\tilde{\epsilon}$ are renormalized due to Hartree and Fock contributions of the Coulomb interaction and excitonic resonances in the photoluminescence are found (third term RHS). The fourth term contains electron-hole correlations.

The electron-hole correlations C^x are two-particle contributions (doublet level) due to the Coulomb interaction. In contrast, the stimulated emission and the excitonic renormalization arise from a factorization of higher order correlations like $\langle \hat{b}^\dagger \hat{b} \hat{c}^\dagger \hat{c} \rangle$. Note, that the creation or emission of a photon corresponds to a inter-band carrier-transition and correspondingly expectation values like $\langle \hat{b}^\dagger \hat{v}^\dagger \hat{c} \rangle$ represent two-particle processes. The analysis of correlations due to light-matter and Coulomb interaction as well as photon-photon correlations is not subject of this thesis. For details we refer the reader to Refs. [67, 68, 140]. Considering additionally the carrier-phonon interaction, the corresponding correlations give rise to a dephasing of the photon-assisted polarization and other correlations. For the calculations presented below we consider at this point a phenomenological dephasing Γ . A more sophisticated approach to include dephasing processes due to carrier-phonon interaction within a microscopic approach is presented in Refs. [171, 172] for QW systems.

Within this thesis the focus is on carrier-LO-phonon collisions providing an efficient mechanism to populate the QD states. The main difficulty in combining the quantum kinetics for carrier scattering and the luminescence dynamics lies in the different timescales on which the underlying processes take place. Carrier scattering processes typically occur on a ps timescale, whereas recombination processes are in the order of 1 ns. Hence, some

6 Optical experiments

approximation for the carrier-scattering processes in the luminescence model is affordable and we might employ the relaxation time approximation

$$\frac{d}{dt} f_\alpha \Big|_{\text{coll}} = -\frac{f_\alpha - F_\alpha}{\tau_\alpha}. \quad (6.25)$$

Close to the quasi-equilibrium/steady-state population F_α , the Markov approximation is valid. In a first step, we extract the relaxation times τ_α from a quantum-kinetic calculation for an initially empty QD-WL system where carriers are excited optically into the WL. Using these relaxation times, in a second step Christopher Gies performed the calculation of the time-resolved PL signal from the SLE including correlations as outlined above. Specifically, we considered an unstructured sample where stimulated emission is absent. The corresponding results are shown in Fig. 6.4, including a comparison with experiments performed by Gareth Beirne in the group of Prof. Peter Michler at the University of Stuttgart.

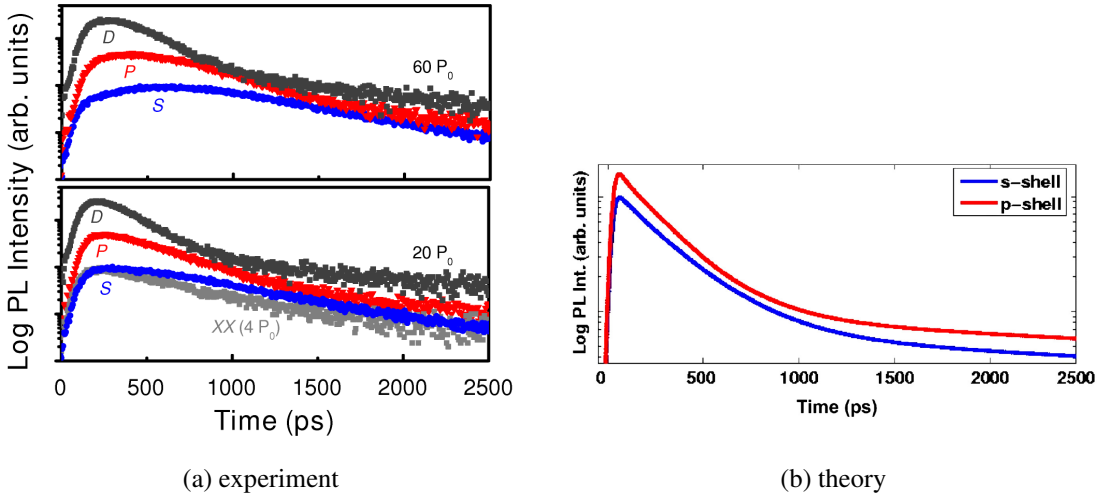


Fig. 6.4: Time-dependent PL signal of a single InP/InGa_{0.51}P_{0.49} semiconductor QD obtained from experiment and theory [173].

The experimental results for the s-, p- and d-shell emission lines of a single InP QD at 4 K are presented in Fig. 6.4a. In general, all of the transients show a fast rising time and a non-exponential decay. Furthermore an increasingly delayed PL intensity maximum with increasing power density and a larger width of this maximum for the s-shell than for higher shells is observed. The behavior of the PL maximum originates from the filling of lower-lying levels from occupied higher levels. Due to successive relaxation, the d-shell reaches its PL maximum earlier than the s-shell. Even for late times the s-shell population is still feeded by higher shells, resulting in the broader PL maximum.

For the microscopic analysis we restrict ourselves to a InP/InGaP QD system with two confined shells, s- and p-shell, for electrons and holes. The level spacing is chosen in such

a way that for low-density excitation conditions a phonon bottleneck for the scattering to the lowest confined electron state is predicted by perturbation theory. It turns out that the results from the microscopic analysis, depend only weakly on the exact values used for the level spacing. In the example shown in Fig. 6.4b, we chose a level spacing of 34.4 meV for electrons and 9.6 meV for holes, whereas the LO-phonon energy is 46 meV. Other material parameters are summarized in Tab. B.1.

In a first step we consider the optical excitation in the WL and neglect carrier recombination. From the quantum kinetic calculation (cf. Chap. 5.2.2 for InGaAs QDs) we find efficient carrier relaxation for the present low-temperature conditions (10 K). The evolution towards a steady-state population can be approximately described by a relaxation time of $\tau_e=3.5$ ps for electrons and $\tau_h=1.5$ ps for holes. These relaxation times are effective values, considering all of the possible inward and outward scattering processes. Note, that for elevated excitation densities also carrier-carrier interaction contributes to fast scattering processes, while at low carrier densities the effects due to carrier-phonon interaction discussed above are expected to dominate.

The luminescence dynamics calculated according to the theory outlined above are shown in Fig. 6.4b. To mimic the finite temporal resolution of the experimental setup of about 35 ps, we convoluted the results with a corresponding Gaussian-shaped apparatus function. First, due to fast carrier relaxation, a rapid rise of the PL intensity is observed. From our quantum kinetic calculation we find practically the same relaxation time for the s- and the p-shell. Therefore, similar rise times are expected in the PL signal, which is also observed in the experiment. The initial decay of the PL signal from the p-shell is faster, because, in addition to recombination, carrier relaxation to the s-shell further reduces the p-shell population. At later times when the QD is populated, the PL intensity decays as spontaneous recombination processes reduce the population. The decay of the PL signal reveals a non-exponential signature. This is due to the fact that in semiconductor QDs electrons and holes are not fully correlated, in contrast to atomic systems where an electron in the excited state implies that there is a hole in the lower state.

The non-exponential decay can be understood analytically. Neglecting Coulomb correlations and adiabatically solving Eq. 6.24, we find from Eq. 6.22 that for example the loss of conduction-band carriers due to spontaneous recombination is given by $\frac{d}{dt}f_\alpha^c = -\frac{f_\alpha^c(1-f_\alpha^v)}{\tau_\alpha}$. Hence, as long as the valence-band population is not fixed, for example by background doping, a non-exponential behavior is observed due to the fact that the temporal evolution of conduction-band and valence-band states might be different.

7 Nitride semiconductors

In recent years an increasing interest in nitride-based semiconductor nanostructures evolved. For practical applications they have several advantages in comparison to GaAs materials or II-VI compounds. As can be inferred from Fig. 7.1, this material system allows for light sources with emission frequencies ranging from amber to the UV. A famous example is the first blue GaN-based laser diode demonstrated by Nakamura [174]. Nowadays, blue and green nitride LEDs are widely used in full-color LED displays and traffic lights. Nitride laser diodes emitting at 405 nm are for example implemented in the upcoming Blu-ray players. More applications and a detailed introduction into nitride semiconductors are presented in Refs. [175–178].

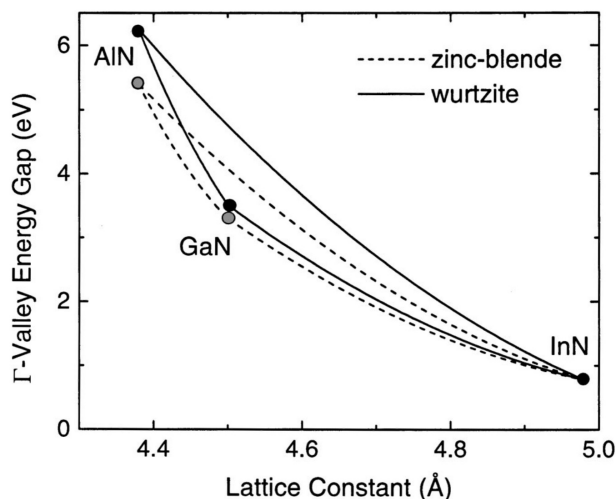


Fig. 7.1: Bandgap vs. lattice constant. Picture taken from Ref. [179] (Reprinted with permission, Copyright 2003, American Institute of Physics).

Nitrides are a challenging material system, in the experiment as well as for the theoretical description. Their compounds crystallize either in a meta-stable zincblende phase [180] or in the stable wurtzite structure, depending on growth conditions and the substrate. For optoelectronic devices usually the wurtzite structure is used and therefore we restrict the following discussion to this phase. The crystal growth is accompanied by various types of defects, dislocations, and segregation [175, 176], which complicate the fabrication of

nanostructures like quantum dots or Bragg-reflectors in good crystalline quality. For the theoretical description most challenges arise from the wurtzite crystal structure. The crystal structure is of central importance for the understanding of the electronic and optical properties as it implies the symmetry properties of the wave-functions. Additionally, one has to account for example for a non-parabolic dispersion, a pronounced mass anisotropy, and built-in electrostatic fields [179, 181]. As a consequence, many of the approximations working well for zincblende GaAs materials are not applicable to the nitride system.

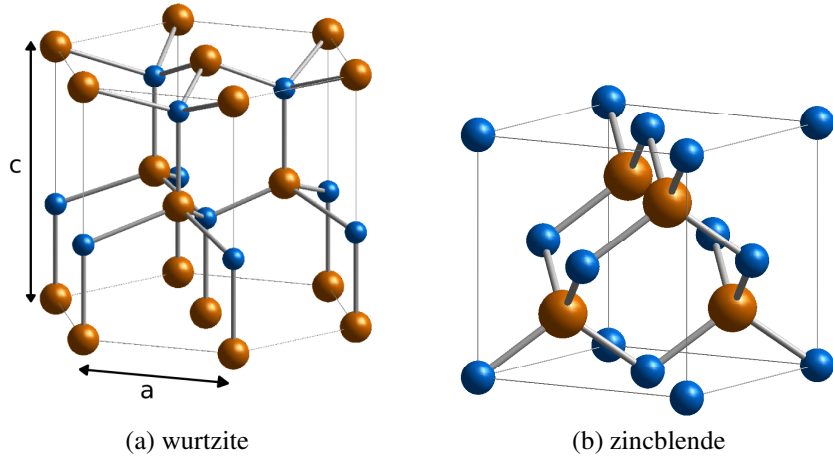


Fig. 7.2: Conventional unit cell of GaN in zincblende and wurtzite phase (picture courtesy of N. Baer [140]).

One important consequence of the crystal symmetry are intrinsic electrostatic fields due to spontaneous and strain-induced polarization. The unstrained zincblende structure shown in Fig. 7.2b is non-polar. Its inversion symmetry ensures that polarizations due to different bond lengths are compensated, see for example Ref. [178]. In contrast, even the unstrained wurtzite lattice shown in Fig. B.1a exhibits a polar axis in c -direction. The geometry of the conventional unit cell usually deviates from the ideal ratio of $\frac{c}{a} = \sqrt{8/3}$ [182], resulting in a so-called spontaneous polarization in c -direction. Beside the spontaneous polarization, large strain-induced piezoelectric fields (1-10 MV/cm) are observed [179, 183, 184], especially in heterostructures like QDs and QWs. In a QW, the resulting electrostatic fields give rise to a separation of electron and hole wavefunction, also known as the quantum-confined Stark effect (QCSE) [185]. As the charge separation implies a reduction of dipole transitions, many investigations for QWs [48, 186] and QDs [47, 49] were devoted to this effect. For device application, several approaches have been developed to circumvent these internal fields. Among them are for example the growth on the non-polar a - and m -planes [187, 188] or strain-engineering by using lattice-matched quaternary alloys [189].

Much work has been devoted to study the electronic properties of group-III nitrides [179]. Basically three approaches are available: continuum $\mathbf{k} \cdot \mathbf{p}$ models, atomistic tight-binding

(TB) models, and density-functional theory (DFT) calculations. Even on nowadays supercomputers DFT calculations are restricted to a few hundred atoms, and hence this method is not appropriate to study QDs. In the following, basically TB calculations are used. A comparison of the TB approach with a $\mathbf{k} \cdot \mathbf{p}$ model is subject of current research [190].

In previous chapters of this thesis weak polar coupling InGaAs QDs have been investigated. Polaron renormalizations and their influence on carrier scattering and optical absorption spectra were studied. For this discussion, the nitride material system provides new interesting aspects. Stronger polaron effects are expected due to the intermediate polar coupling. Furthermore, the influence of material properties like piezo-fields and strong band-mixing effects on polaron renormalizations, carrier scattering, and optical properties is of particular interest.

To study the influence of a stronger polar coupling and specific material properties, two approaches are followed in this chapter. In a first step the influence of the built-in electrostatic fields and the intermediate polar coupling is estimated within an effective-mass model. In a second step a much more detailed study is presented. We start from an atomistic empirical TB approach for the single-particle states. This is combined with the GF theory for the carrier kinetics and the influence of polaron renormalizations on optical spectra is studied as a first application of this method.

7.1 Envelope wave function model

The most striking differences between GaN and GaAs QDs are a larger polar coupling and the presence of intrinsic electrostatic fields. In the following chapter, their influence on the polaron renormalizations and the carrier scattering is investigated. In a first approach we restrict the analysis to an effective mass approximation and use the envelope wave-function model discussed in Chap. A.1. The calculation of the energy dispersion for the WL states is more involved. Especially for holes, a strong band-mixing of the heavy-hole and the light-hole band occurs, resulting in non-parabolic bands and a strong mass anisotropy [179, 181]. However, the inclusion of such effects is the subject of Chap. 7.2–7.4. Here, they are not considered.

Very controversial values have been reported for the spontaneous polarization as well as for the elastic constants that determine the strain-induced contribution. For InGaN nanostructures that are embedded compressively strained in GaN, the resulting intrinsic electrostatic fields amount to a few MV/cm [179, 183, 184]. Therefore, we consider typical values of +2.0 MV/cm inside the QD-WL region and -0.5 MV/cm in the surrounding GaN. A detailed summary of the material parameters for the $\text{In}_{0.2}\text{Ga}_{0.8}\text{N}$ alloy we consider is presented in Tab. B.2.

Quantum-confined Stark effect

The carrier confinement together with the built-in electrostatic fields gives rise to the so-called quantum-confined Stark effect (QCSE). Using the separation of the envelope wave function (A.1), the electrostatic fields only influence the component in growth direction. The corresponding one-dimensional Schrödinger equation is given by

$$\left[-\frac{\hbar^2}{2m} \frac{\partial^2}{\partial z^2} + U(z) \right] \xi(z) = E(z) \xi(z) , \quad (7.1)$$

where the potential

$$U(z) = U_0(z) + U_p(z) + U_{scr} \quad (7.2)$$

contains the confinement potential $U_0(z)$, the potential due to the electric field U_p , and the potential of the screening field U_{scr} due to the spatial separation of electrons and holes. The screening potential

$$U_{scr}(z) = \frac{e^2 N}{2\varepsilon_0 \varepsilon_b} \int dz' [|\xi^e(z')|^2 - |\xi^h(z')|^2] |z - z'| \quad (7.3)$$

is calculated by solving Poisson's equation for a set of uniformly charged sheets.

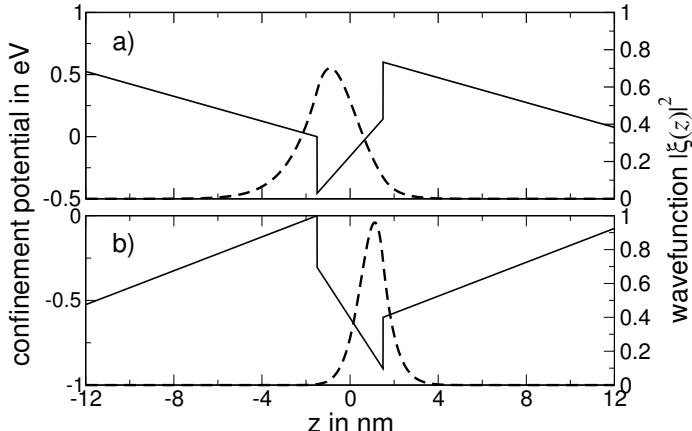


Fig. 7.3: Quantum confined stark effect due to intrinsic electrostatic fields in growth direction for electrons (a) and holes (b).

The spontaneous polarization of the GaN matrix and of the strain-induced polarization of InGaN QD have different magnitude and opposite sign. This gives rise to a consequence, a sawtooth profile of the band structure in z -direction, similar to a set of capacitors with non-equal surface charges [183, 191]. Corresponding results from a self-consistent solution of the Schrödinger-Poisson equation (7.1)–(7.3) are shown in Fig. 7.3. Due to the tilted confinement potential a spatial separation of charges is observed. This has several

consequences. Less effective interband processes are expected due to the reduced overlap of electron and hole wave functions in the corresponding matrix elements. On the other hand, intra-band interaction matrix elements remain almost unchanged.

Nitride polaron

In comparison to InGaAs QDs, stronger polaron effects are expected in GaN QDs due to the larger polar coupling. The polaron renormalizations for nitride QDs are calculated similar to the InGaAs material. As discussed in detail in Chap. 5.1, the corresponding Dyson equation for the retarded GF is solved in the time domain and the spectral function is obtained by Fourier transformation.

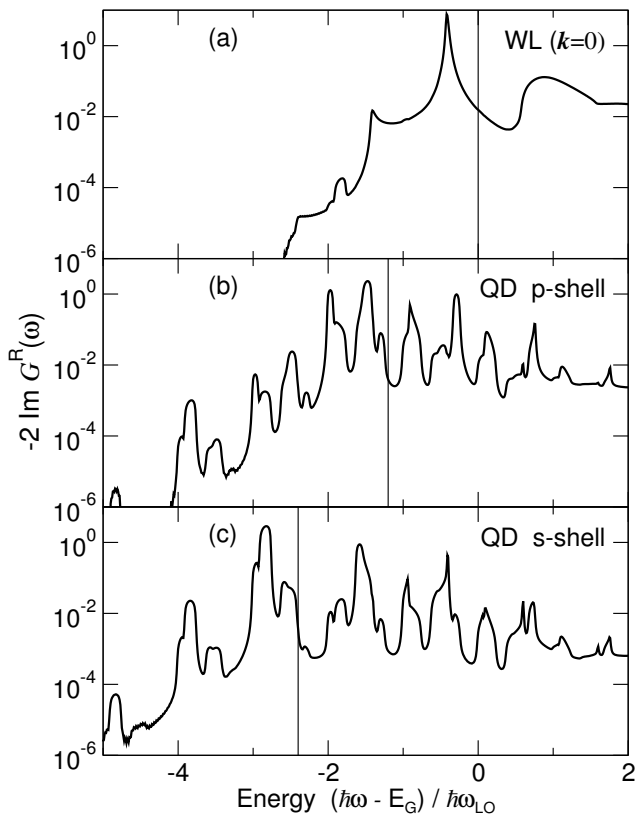


Fig. 7.4: Polaron spectral function for InGaN QDs at 300K.

For the discrete QD states, the spectral function in Fig. 7.4 shows that the free-particle picture is strongly modified. On this level, a direct comparison between the weak-polar coupling material system InGaAs (Fig. 5.2) and the InGaN system with intermediate polar coupling is possible. In the first case, one can clearly distinguish between phonon

replicas of the QD states which are spaced by the LO-phonon energy $\hbar\omega_{\text{LO}}$ around the central peak, and the hybridization effect which leads to a splitting of these peaks that is smaller than the LO-phonon energy (when the detuning between the QD level spacing and the LO-phonon energy is small). In the InGaN material system, the hybridization is much stronger and one can no longer distinguish between phonon replicas and their splitting. Moreover, the obtained rich multi-peak structure provides a stronger overlap between the spectral functions which increases the scattering efficiency discussed below. Broadening of the resonances is provided by the coupling to the WL states and the finite LO-phonon lifetime (assumed to be 5 ps).

Consequences for carrier-LO-phonon scattering

The scattering mechanism including polarons is discussed extensively in Chap. 5.2.2 for the weak polar coupling InGaAs material. In QD systems, the spectral functions are of central importance, since their overlap basically determines the scattering efficiency between two particular states. As shown above, large polaron renormalizations are found in the intermediate polar coupling regime. Their influence on the carrier scattering in nitride QDs, together with the intrinsic electrostatic fields, is subject of the following discussion

In a first example, we study the capture of WL carriers into QD states and the relaxation of QD carriers for a given WL population. The time evolution of the occupation function for s- and p-shell is shown in Fig. 7.5a. As initial condition we use empty QD states and a thermal population of the WL states that corresponds to a carrier density 10^{10} cm^{-2} . For a situation where for electrons the level-spacing is $1.2 \hbar\omega_{\text{LO}}$, fast scattering processes are observed which lead to capture times of 1.07 ps and 1.02 ps for s- and p-shell, respectively. As discussed in Chap. 5.2.1 for the InGaAs material, the fast carrier scattering is due to quasi-particle renormalizations which strongly modify the picture of scattering between free-carrier states as well as due to memory effects. Our finding of a weak dependence of the ultrafast redistribution of carriers on the detuning between level spacing and LO-phonon energy in weak polar coupling materials (cf. Chap. 5.2.1) remains true for intermediate polar coupling nitride materials. The influence of the built-in electrostatic field on the carrier dynamics turns out to be weak, since the charge separation only weakly modifies the matrix elements for intra-band scattering processes.

Another example is the carrier scattering after optical excitation in the p-shell. In Fig. 7.5b corresponding results are presented for a QD with a level-spacing of $1.2 \hbar\omega_{\text{LO}}$ for electrons and $0.4 \hbar\omega_{\text{LO}}$ for holes. Due to pulse excitation, first the p-shell is populated. The carrier relaxation is so fast that already during the optical pulse a strong redistribution from the p-shell to the s-shell takes place. As the ultrafast scattering processes are connected with strong dephasing of the coherent interband polarization, which is included on the same quantum-kinetic level as the carrier scattering, the time evolution of the interband polarization practically follows the optical pulse (not shown). Correspondingly, the coherent

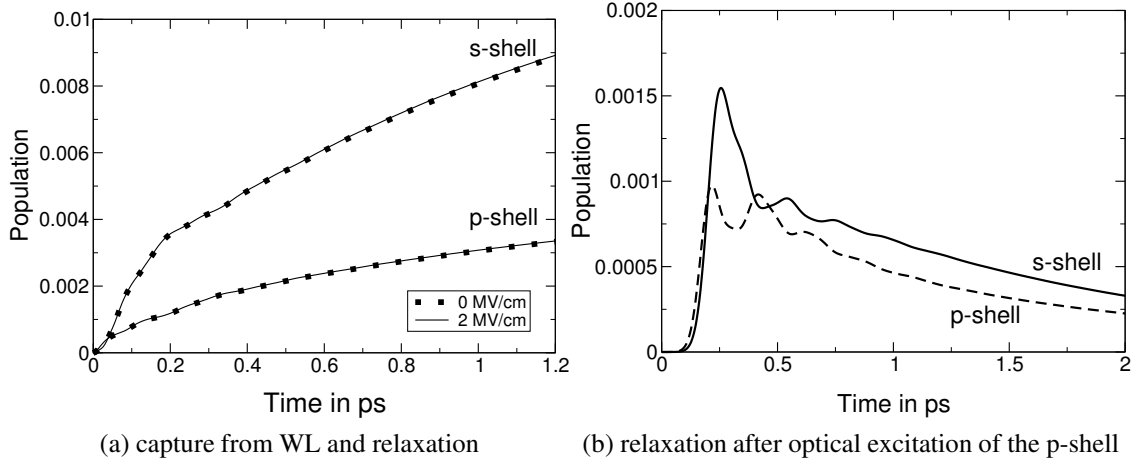


Fig. 7.5: Influence of the QCSE on the temporal evolution of the QD population which is initially empty due to (a) capture and relaxation of WL carriers and (b) optical excitation of carriers in the p-shell.

regime is limited to the duration of the 100 fs pump pulse. During the coherent regime a transient strong increase of the total carrier density is obtained. While relaxation, the time-domain oscillations in Fig. 7.5b indicate the strong coupling between carriers and phonons and the oscillation frequency is connected to the hybridization in the DOS as discussed in Chap. 5.2.1. Note that the oscillations appear after the optical pump pulse in the incoherent regime and hence they are not connected to optical coherence. At larger times, the possibility of carrier transitions between QD and WL states leads to a redistribution of carriers from the QD states into the WL. Of course, the total carrier density remains constant after the pulse.

The ultrafast scattering and dephasing processes are the direct result of the polaronic renormalizations. Only within a non-Markovian calculation the above mentioned oscillations in connection with the strong-coupling regime for the carrier-phonon interaction can be obtained. In this respect, there is no qualitative difference between the InGaAs and InGaN material systems. But in the latter case, the larger polar coupling increases the scattering efficiency, while the electron and hole charge separation induced by the built-in fields reduces only inter-band but not intra-band processes. We restricted the analysis to low carrier densities and the interaction with LO phonons. At elevated excitation densities, carrier-carrier scattering additionally contributes. A detailed discussion of this topic is beyond the scope of this thesis. Nevertheless, corresponding studies are presented by Nielsen et al. [91, 92, 192].

7.2 Tight-binding wave-function model

In the previous discussion of polaron effects in nitride QDs, the influence of the larger polar coupling and intrinsic electrostatic fields was studied using an effective-mass approach. Effects originating from the wurtzite crystal structure and strong band-mixing have been considered neither in the QD wave functions nor in the energy dispersion of WL carriers. The inclusion of such effects within an empirical tight-binding (TB) approach is subject to this chapter.

In the following, the basic idea of the empirical TB approach is presented, as well as a procedure to incorporate the corresponding results in a many-body theory. For the description of QD properties, the inclusion of the WL plays a crucial role [146, 168]. Therefore, some comments on the inclusion of the WL in our calculations are in order. As discussed below, the localized QD wave functions are calculated in a finite supercell. Were we to directly model the combined QD-WL system within a supercell, we would have to use periodic boundary conditions that could lead to numerical artifacts due to coupling between the QDs in different instances of the supercell. Moreover, such a procedure would imply an unrealistic periodic array of QDs. Therefore, we include the WL along similar lines as discussed Chap. A.1 using the envelope function-approximation. In a first step, independent calculations for QD and QW states are performed and in a second step the OPW orthogonalization procedure is applied for the combined QD-WL system. This approach on the one hand has the advantage of reducing numerical complexity and on the other hand accounts for the random distribution of QDs of the WL plane. Incorporating the random QD distribution is of central importance, as in this case the in-plane momentum is conserved on average (cf. Chap. A.1).

The results presented in the following have been obtained in close collaboration with Michael Lorke and Stefan Schulz. Stefan Schulz provided the TB wavefunctions and the dipole interaction matrix elements, whereas the calculation of Coulomb interaction matrix elements, polaron renormalizations, and absorption spectra was performed together with Michael Lorke.

7.2.1 Empirical tight-binding model for bulk semiconductors

The basic assumption of the TB approach is that electrons are tightly bound to their ions. Therefore one chooses as basis states the eigenfunctions to the atomic problem, which are the atomic orbitals. Correspondingly, the Schrödinger equation for an electron in a crystal,

$$[H^{\text{atom}} + \Delta V(\mathbf{R})] \psi(\mathbf{r}) = E \psi(\mathbf{r}), \quad (7.4)$$

is separated into the atomic problem and the Coulomb potential originating from all other electrons. The wavefunction for the solid then can be expanded in terms of atomic orbitals

$\phi_{\mathbf{R},\sigma}$ localized at the various lattice sites \mathbf{R} ,

$$\psi(\mathbf{r}) = \sum_{\mathbf{R},\sigma} c_\sigma(\mathbf{R}) \phi_{\mathbf{R},\sigma}(\mathbf{r}) . \quad (7.5)$$

The index $\sigma \in \{\alpha, \nu, s\}$ denotes the atomic orbital type α (e.g. sp^3 basis), the atom type ν and the spin s . In case of bulk semiconductors, Bloch's theorem might be employed due to translational invariance and from an expansion into plane waves we find

$$|\mathbf{k}\rangle = \sqrt{\frac{V_0}{V}} \sum_{\alpha,\nu,s} \sum_{\mathbf{R}} e^{i\mathbf{k}\cdot\mathbf{R}} c_{\alpha,\nu,\sigma}(\mathbf{k}) |\mathbf{R}, \alpha, \nu, \sigma\rangle . \quad (7.6)$$

Here, the spatial dependence of the TB coefficients $c_\sigma(\mathbf{R})$ is reduced to a single unit-cell by means of Bloch's theorem. Using this expansion then yields a Schrödinger equation for the TB coefficients,

$$\sum_{\mathbf{R}',\sigma'} \langle \sigma, \mathbf{R} | \hat{H}^{\text{TB}} | \sigma', \mathbf{R}' \rangle c_{\sigma'}^\alpha(\mathbf{R}') = E^\alpha c_\sigma^\alpha(\mathbf{R}) . \quad (7.7)$$

The atomic orbitals from different lattice sites are in general not orthogonal. In this situation a transformation to orthogonalized Löwdin orbitals can be employed, which preserves the localization and symmetry properties of the atomic orbitals [33].

In Eq. 7.7, the dominant contributions arise from nearest-neighbor coupling because of the strong localization of the atomic orbitals. One observes that for bulk semiconductors the TB matrix can be reduced to a small number of TB parameters. A detailed evaluation of the TB overlaps is beyond the scope of this introduction and can be found for example in Ref. [33]. Thus, from a physical point of view the TB approach is quite intuitive, as the wave function is basically determined from the overlap of neighboring atomic orbitals.

Extensions of the basic TB model include spin-orbit coupling, crystal-field splitting, intrinsic piezoelectric fields, and strain fields. Technical details can be found in Ref. [33]. For nitride semiconductors, especially the inclusion of spontaneous and strain-induced electric fields is of central importance [193]. The spontaneous polarization for various alloys is known from the literature [179]. On the other hand, the inclusion of the strain-induced part of the piezo-electric polarization is more involved. In this case the strain field for the particular situation, elastic moduli, and piezoelectric constants have to be considered [194]. The corresponding electrostatic potential is obtained from the solution of Poisson's equation. Within the TB model the resulting electrostatic fields can be included as site-diagonal contributions $V_p(\mathbf{r}) = -e\phi_p(\mathbf{r})$ to the Hamiltonian. This approach is also successfully applied to QW [195] and QD [196] structures.

7.2.2 The QD model

For the calculation of QD wave functions within the TB approach, the utilization of Bloch's theorem is not possible due to the lack of translational invariance. Instead, a finite supercell with zero boundary conditions is introduced. Such a supercell including a lens-shaped QD is schematically shown in Fig. 7.6. Additionally the corresponding spatial dimensions are given. The particular QD that we consider in the following consists of pure InN and is located on top of an InN WL, grown in the (0001)-direction. QD and WL are embedded in a GaN matrix.

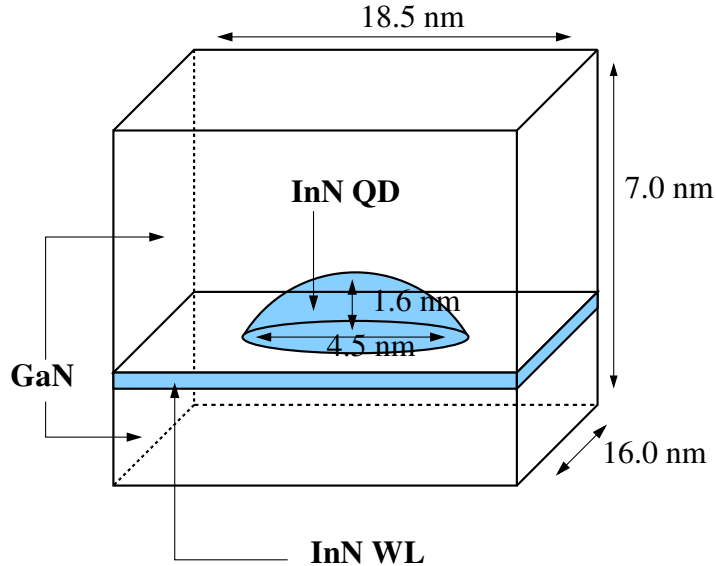


Fig. 7.6: Super cell and QD geometry for the calculation of QD states. Picture courtesy of Stefan Schulz, [33].

The QD wave functions are calculated from a numerical diagonalization of the TB Schrödinger equation (7.7). As an approximation, the corresponding TB parameters known from bulk semiconductors are used $\langle \sigma, \mathbf{R} | H | \sigma', \mathbf{R}' \rangle \approx \langle \sigma, \mathbf{R} | H^{\text{bulk}} | \sigma', \mathbf{R}' \rangle$. For the TB matrix, at each lattice site of the supercell the corresponding TB parameters are chosen according to the species of the occupying atom (In, Ga or N). At the InN/GaN interfaces of the nanostructure the assignment of the N atoms is ambiguous. In this case an averaging between InN and GaN parameters is employed [33, 197]. The band gap of GaN and InN as well as the band offsets for valence and conduction band are chosen according to recommendations in the literature [32, 179]. For the valence band, an offset of 0.5 eV is included as an energy shift in the site-diagonal TB matrix elements for the bulk material [32]. Additionally, also the intrinsic electrostatic fields are considered as site-diagonal energy shifts. Spin-orbit coupling and crystal-field splitting is neglected, as they only give rise to minor corrections. For a detailed investigation see Ref. [33, 197].

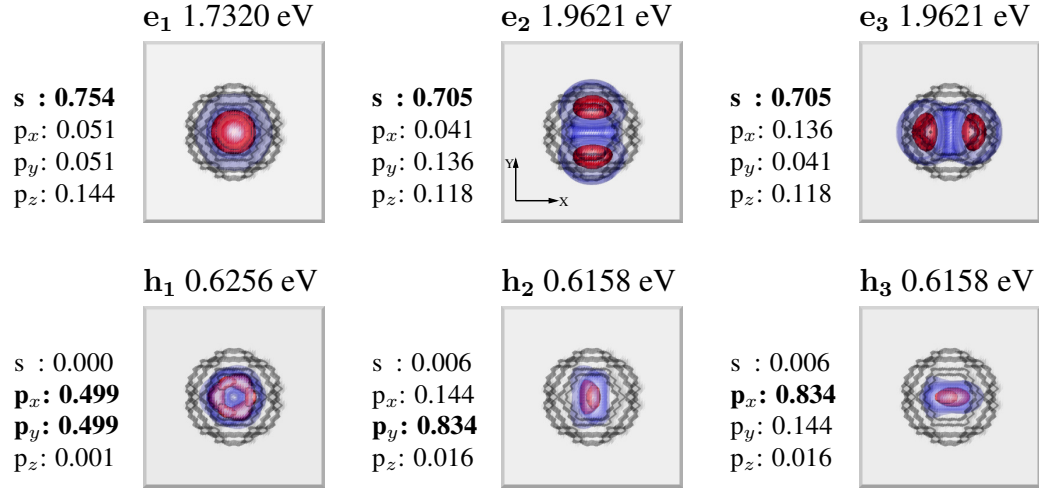


Fig. 7.7: Modulus squared of the QD wavefunctions in top view. The QD structure is depicted in gray whereas the iso-surfaces of the charge density are shown for 10% (blue) and 50% (red) of the maximum value. Furthermore the orbital composition is given and the dominant contribution is highlighted. Pictures courtesy of Stefan Schulz, [33, 157].

The TB wave functions were calculated by Stefan Schulz, [32, 33, 197, 198]. Fig. 7.7 shows results for the three energetically lowest confined states of the QD geometry depicted in Fig. 7.6. The ground state both for electrons and holes shows no degeneracy, apart from spin degeneracy. In contrast, the first excited states are two-fold degenerate, which is due to the fact that spin-orbit coupling and crystal-field splitting are not considered. Including these contributions lifts the degeneracy [33, 197].

For the classification of the electronic states some symmetry considerations are of paramount importance. A detailed analysis in this respect is beyond the scope of the present thesis and we refer the reader to the excellent discussions in Refs. [33, 140]. Nevertheless, we want to summarize the basic results of those considerations. In the following, a function that is invariant under discrete rotations around the z-axis is called “s-state”. Correspondingly, if the state transforms like an atomic p-function under these rotations it is called “p-state”. From the nodal structure of the wave functions shown in Fig. 7.7, a classification into s- and p-like states is directly evident for the electron states, but it is much less obvious for the hole states. However, in fact such a classification is possible by analyzing the behavior of the hole states under symmetry operations of the underlying group C_{3v} . The total symmetry of a wave function in TB representation is determined by the symmetry of the atomic orbitals and that of the TB coefficients. Comparing the TB representation Eq. (7.5) with the envelope-function approximation Eq. A.1, we find that the atomic orbitals translate into the Bloch functions and the TB coefficients are the discretized analog to the envelope function. The weight of the different orbitals is given

in Fig. 7.7. As expected, we find that the electron states are mainly composed of s-type orbitals, while in the hole states mainly p-type orbitals contribute. Furthermore, we can infer from the modulus of the wave functions shown in Fig. 7.7 that the symmetry of the TB coefficients is s-like for the ground state and p-like for the two excited states. These symmetries of the orbital composition and the TB coefficients in total result in an s-like symmetry for the ground state and a p_x - and p_y -like symmetry of the two excited states, both for electron and hole states.

7.2.3 The WL model

For the description of the combined QD-WL system we start from separate calculations for a QD and a QW, where in a second step the resulting QW states are orthogonalized to the QD states. The calculation of the localized QD states and their symmetry properties are discussed in the previous chapter. In this chapter corresponding calculation for a QW is presented, which additionally yields the energy dispersion of the delocalized WL states.

In contrast to the QD case, the TB calculation for a QW can be considerably simplified. Due to translational invariance Bloch's theorem can be employed in the WL plane and one can restrict the calculation to a column of unit cells along the growth direction, as shown in Fig. 7.8. Additional details on TB calculations for QW systems can be found for example in Refs. [199, 200]. As the alert reader might notice, the application of Bloch's theorem in this system is not straightforward due to the existence of two layers within the unit cell (cf. Figs. B.1 and 7.8). For convenience, we split \mathbf{R} into an in-plane part and a z-part according to

$$\mathbf{R} = (\mathbf{R}_{||} + \mathbf{f}_l) + \mathbf{R}_z , \quad (7.8)$$

where $\mathbf{R}_{||}$ is the in-plane position of the unit cell and \mathbf{f}_l denotes the in-plane position of layer l within the unit cell. By this procedure we assure that $\mathbf{R}_{||}$ is always a lattice vector and Bloch's theorem for the double layer structure reads

$$c_{\sigma}^k(\mathbf{R}) = c_{\sigma}^k(\mathbf{f}_l + \mathbf{R}_z) \exp(i\mathbf{k}\mathbf{R}_{||}) . \quad (7.9)$$

A further advantage of this approach is that a direct classification of WL states using the in-plane crystal momentum $\hbar\mathbf{k}$ is achieved. This is also desirable from a physical point of view, as the in-plane translational invariance being present in the QW system, also holds in the QD-WL system, at least on average.

For the diagonalization of the Schrödinger equation (7.7) for the TB coefficients, again at each lattice site of the unit-cell column the bulk TB parameters according to the species of the occupying atom (In, Ga or N) are used and at the interfaces an averaging between InN and GaN parameters is employed. The calculation of the QW states has also been performed by Stefan Schulz. For the lowest conduction band (CB) and the two highest valence bands (VB), the resulting in-plane energy dispersion for the QW is shown in Fig. 7.9

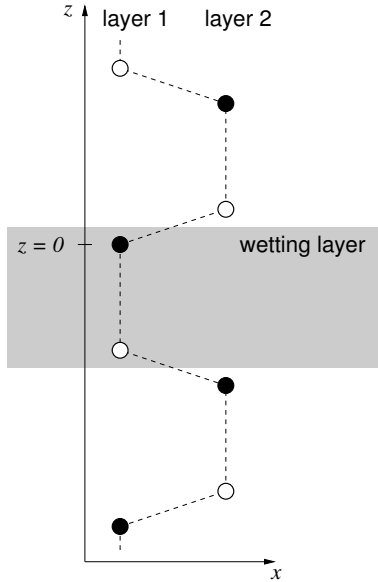


Fig. 7.8: Column of unit cells for the calculation of QW states, showing the double-layer structure of the wurtzite lattice.

Around the Γ point, for the conduction band as well as for the two highest valence bands, the dispersion is to a good approximation rotational invariant. For larger \mathbf{k} first the hexagonal structure of the real space lattice and later, rotated by 30° , the hexagonal structure of the Brillouin zone is reflected in the energy dispersion. Furthermore, strong band-mixing effects are observed, giving rise to the “oscillations” seen in the iso-surface lines.

Note, that due to the fact that the two highest VBs are energetically nearly degenerate at the Γ -point, a restriction to only one VB, as we typically use it in the GaAs material system is not applicable. Thus, for the calculation of optical properties we need to take both VBs into account. For further calculations, we are only interested in the bandstructure in the vicinity of the Γ -point. Therefore, in a good approximation we might use the angle-averaged band structure, which is shown in Fig. 7.10. Even though the dispersion shows a clear non-parabolic behavior, an estimate for the effective masses can be given from a fit in the vicinity of the Γ -point. For the CB we find a mass of $0.18 m_0$, whereas for the upper and lower VB $-2.84 m_0$ and $-0.19 m_0$ are found.

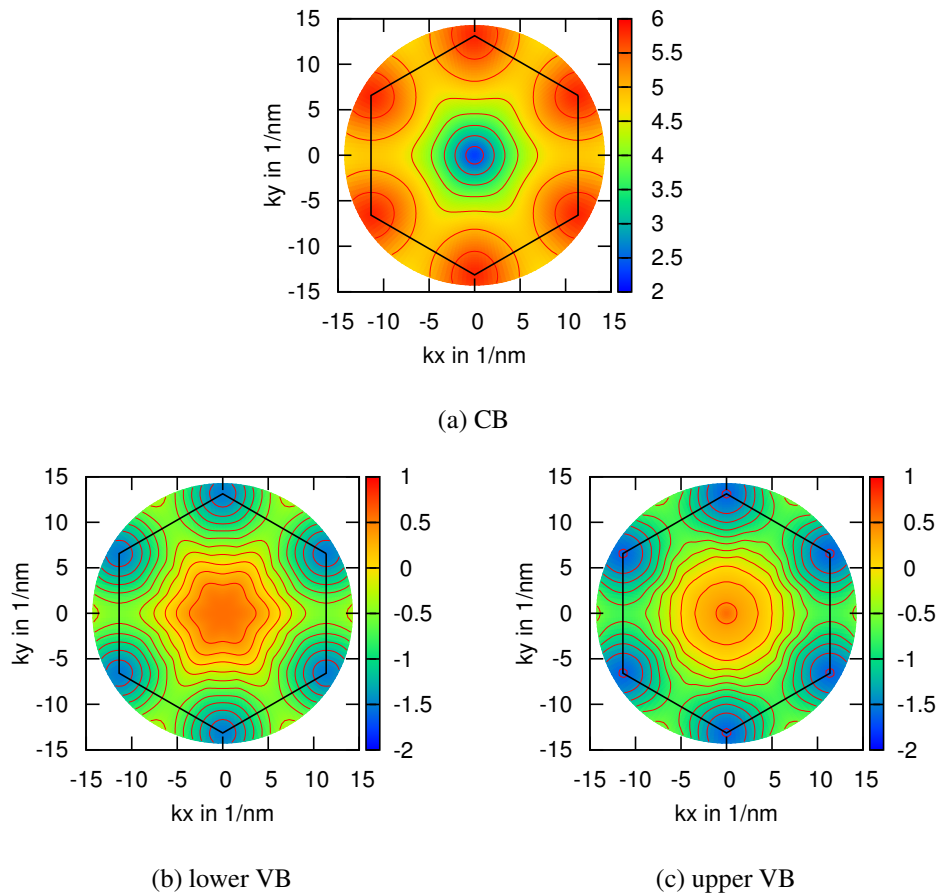


Fig. 7.9: Energy dispersion as a function of the 2D in-plane wavevector k_{\parallel} for the conduction and valence band. The hexagonally shaped border of the Brillouin zone is marked in black.

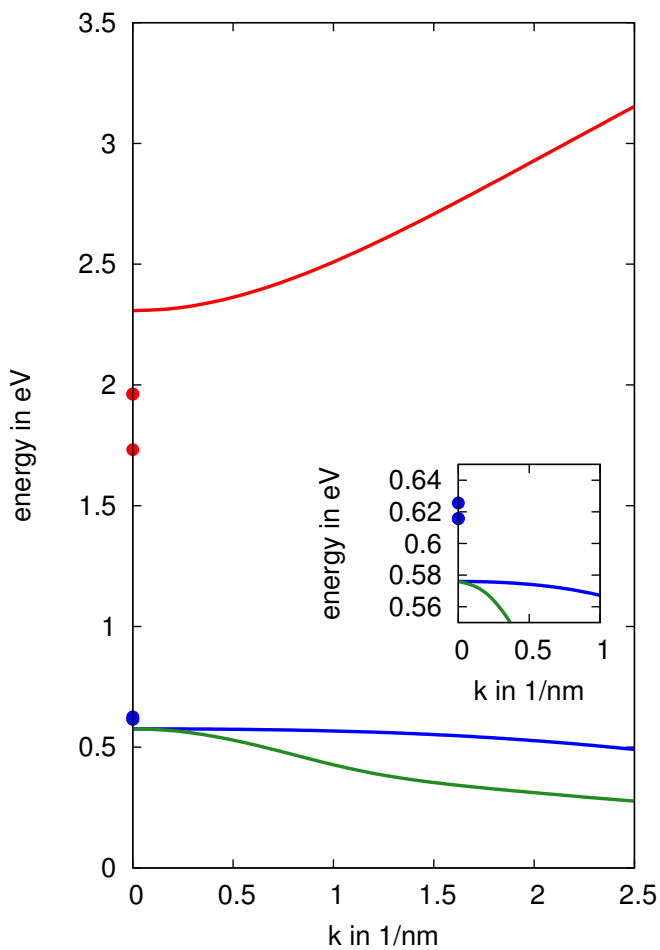


Fig. 7.10: Angle-averaged in-plane energy dispersion. The dots mark the energies of the QD states obtained from their respective TB calculation.

7.2.4 Evaluation of Coulomb matrix elements

An atomistic approach like a tight-binding calculation allows to account for symmetry properties of the wurtzite crystal structure. The wavefunction is expressed as a linear combination of atomic orbitals $\phi_{\mathbf{R},\sigma}$ localized at the lattice site \mathbf{R} ,

$$\psi(\mathbf{r}) = \sum_{\mathbf{R},\sigma} c_\sigma(\mathbf{R}) \phi_{\mathbf{R},\sigma}(\mathbf{r}), \quad (7.10)$$

with the index σ denoting the orbital types (sp^3 basis) at each lattice site. For the calculation of single-particle energies, the explicit knowledge of the localized orbital functions is not needed within a TB approach. To calculate Coulomb matrix elements, in principle they are required. However, the dominant contributions to the Coulomb matrix elements stem from its long-ranged part and therefore the localized orbitals in good approximation act as point charges. The explicit structure of the localized orbitals enters only in the short-ranged contributions. Therefore, the real space integration of wavefunctions in Eq. (4.1) might be approximated by a sum over TB coefficients at their lattice sites,

$$V_{\alpha\beta\gamma\delta} \approx \frac{e^2}{4\pi\varepsilon_0\varepsilon_B} \sum_{\mathbf{R}\mathbf{R}'} \sum_{\sigma\tau} c_\sigma^{\alpha*}(\mathbf{R}) c_\tau^{\beta*}(\mathbf{R}') \frac{1}{|\mathbf{R} - \mathbf{R}'|} c_\tau^\gamma(\mathbf{R}') c_\sigma^\delta(\mathbf{R}). \quad (7.11)$$

This scheme can be easily used when the analysis is restricted to the localized states. It has been successfully used to determine Coulomb matrix elements for InN/GaN QDs in combination with configuration-interaction (CI) calculations to describe multi-exciton spectra and the influence of symmetry properties on allowed optical transitions [33, 140, 157, 201]

For our purpose of calculating optical properties of nitride QDs, including both localized and delocalized states, it is more convenient to determine the Coulomb matrix elements from Eq. (4.1), involving the Fourier transform of the Coulomb potential. Using the same approximation for the real-space integration as above, the appearing overlap integrals can be written as

$$\langle \alpha | e^{i\mathbf{q}\mathbf{r}} | \beta \rangle = \int d^3r \psi_\alpha^*(\mathbf{r}) e^{+i\mathbf{q}\mathbf{r}} \psi_\beta(\mathbf{r}) \approx \sum_{\mathbf{R},\sigma} c_\sigma^{\alpha*}(\mathbf{R}) e^{+i\mathbf{q}\mathbf{R}} c_\sigma^\beta(\mathbf{R}). \quad (7.12)$$

As the plane wave $\exp(i\mathbf{q}\mathbf{r})$ does not decay for large distances, the argument used to derive Eq. (7.11) also holds in this case. Note, that in Eq. 7.12 also the orthogonality of the atomic orbitals was used, giving rise to the fact that both coefficients carry the same orbital index.

Calculation of overlaps

The overlaps for two QD states can easily be calculated using Eq. (7.12). Using Bloch's theorem we also can evaluate the QD-WL overlaps directly

$$\langle \nu | e^{i\mathbf{q}\mathbf{r}} | \mathbf{k}_0 \rangle = \sum_{\mathbf{R}, \sigma} c_\sigma^*(\mathbf{R}) e^{+i\mathbf{q}\mathbf{R}} c_\sigma^{\mathbf{k}}(\mathbf{f} + \mathbf{R}_z) e^{i\mathbf{k}\mathbf{R}_{||}} . \quad (7.13)$$

Note, that for the numerical evaluation one eventually has to account for a different normalization of the TB coefficients for QD and QW states.¹ The WL-WL overlaps require a little more attention. However, we again can employ Bloch's theorem and the fact, that the unit cell has a double layer structure. This allows us to write

$$\begin{aligned} \langle \mathbf{k}_0 | e^{i\mathbf{q}\mathbf{R}} | \mathbf{k}'_0 \rangle &= \frac{1}{N} \sum_{\sigma, \mathbf{R}} c_{\mathbf{k}, \sigma}^*(\mathbf{R}) e^{i\mathbf{q}\mathbf{R}} c_{\mathbf{k}', \sigma}(\mathbf{R}) \\ &= \frac{1}{N} \sum_{l=1}^2 \sum_{\mathbf{R}_{||}} \sum_{\sigma \mathbf{R}_z} c_{\mathbf{k}, \sigma}^*(\mathbf{R}) e^{i\mathbf{q}_z \mathbf{R}_z} e^{i\mathbf{q}_{||} \mathbf{R}_{||}} e^{i\mathbf{q}_{||} \mathbf{f}_l} c_{\mathbf{k}', \sigma}(\mathbf{R}) \\ &= \frac{1}{N} \sum_{l=1}^2 \sum_{\mathbf{R}_{||}} \left(\sum_{\sigma \mathbf{R}_z} e^{i\mathbf{q}_z \mathbf{R}_z} c_{\mathbf{k}, \sigma}^*(\mathbf{f}_l + \mathbf{R}_z) c_{\mathbf{k}', \sigma}(\mathbf{f}_l + \mathbf{R}_z) \right) e^{i(\mathbf{q}_{||} + \mathbf{k}' - \mathbf{k}) \mathbf{R}_{||}} e^{i\mathbf{q}_{||} \mathbf{f}_l} \\ &= \sum_{l=1}^2 e^{i\mathbf{q}_{||} \mathbf{f}_l} F_l(\mathbf{k}, \mathbf{k}', q_z) \frac{1}{N} \sum_{\mathbf{R}_{||}} e^{i(\mathbf{q}_{||} + \mathbf{k}' - \mathbf{k}) \mathbf{R}_{||}} \\ &= \delta_{\mathbf{q}_{||}, \mathbf{k} - \mathbf{k}'} \sum_{l=1}^2 e^{i\mathbf{q}_{||} \mathbf{f}_l} F_l(\mathbf{k}, \mathbf{k}', q_z) . \end{aligned} \quad (7.14)$$

For the two layers of the unit cell $l = (1, 2)$, separately a formfactor can be defined,

$$F_l(\mathbf{k}, \mathbf{k}', q_z) = \sum_{\sigma \mathbf{R}_z} e^{i\mathbf{q}_z \mathbf{R}_z} c_{\mathbf{k}, \sigma}^*(\mathbf{f}_l + \mathbf{R}_z) c_{\mathbf{k}', \sigma}(\mathbf{f}_l + \mathbf{R}_z) .$$

Even though the definition of two separate formfactors is not necessary, it is of practical advantage as it allows to save computer memory. For the evaluation of the interaction matrix elements, the QW states $|\mathbf{k}_0\rangle$ are then orthogonalized by means of the OPW procedure discussed in Chap. A.1.

¹Usually in the QD calculation the TB coefficients are normalized to the supercell and those of the QW calculation are normalized to the unit-cell column. In wurtzite crystals one lattice point in the hexagon plane is associated with the area of $S = a^2 \sqrt{3}/2$, cf. the crystal structure in App. B.2.

7.2.5 Dipole interaction matrix elements

The dipole matrix elements for the QD-QD transitions can be directly obtained from the TB calculation of the QD. Details on the calculation are presented in Refs. [33, 201] and we summarize the numerical values in Tab. 7.1. For the particular QD geometry under consideration we find that direct transitions, i.e. s→s and p→p transitions, only weakly couple to the electro-magnetic field in comparison to the off-diagonal transitions s→p and p→s. These selection rules deviate from the ones known for zincblende GaAs QD, where one observes only direct transitions due to the Bloch functions. These “skew” selection rules for nitride QDs are related to the underlying symmetry of the wurtzite lattice. As e.g. for the ground-state transition the wave function for electrons as well as for holes exhibits an s-like symmetry, the corresponding dipole transition is zero. In contrast, for the GaAs the wave function in envelope function approximation obeys an s-like symmetry for electrons and an p-like symmetry for holes, cf. Chap. A.3, yielding non-zero dipole transitions. Whereas the ground-state transition exactly vanishes, the excited-state transitions are non-zero but small due to the C_{6v} symmetry of the wurtzite lattice. In case of an $C_{\infty v}$ symmetry, e.g. considered in $\mathbf{k} \cdot \mathbf{p}$ calculations, also the excited-state transitions would vanish. For a detailed discussion of the symmetry properties we refer the reader to Refs. [33, 140, 157].

d^{cv}/e	1	2	3
1	0.000	1.538	1.538
2	1.196	0.011	0.011
3	1.196	0.011	0.011

Tab. 7.1: QD dipole matrix elements in nm from a TB approach with spontaneous and strain-induced electric fields included [33].

As in this thesis our focus is on QD transitions, a simpler treatment of the WL-WL dipole matrix elements is affordable. We employ the results of a $\mathbf{k} \cdot \mathbf{p}$ model for a QW presented in Ref. [181], utilizing the parameters recommended in Ref. [179]. However, for completeness a scheme for calculating the corresponding dipole matrix element from an TB approach is outlined in App. A.3. Furthermore QD-WL matrix elements are neglected for computational reasons, though they could be included along the lines discussed in Ref. [33, 201] using Bloch’s theorem.

7.3 Nitride polarons

The calculation of interaction matrix elements using TB wave functions for a nitride QD-WL system is presented in the previous chapter. With these matrix elements we are able to combine the microscopic calculation for the single-particle states with a quantum-kinetic description of the carrier kinetics. As a first application, the polaron renormalizations for InN QDs are studied.

For InGaAs QDs, the importance of polaron renormalizations and their influence on carrier scattering and dephasing processes is discussed in Chap. 5–6. In comparison to these investigations where the effective mass approximation is employed, interesting new features expected from the TB model. The corresponding energy spectrum of the particular QD presented in Chap. 7.2 shows two striking features. First, for electrons a large level spacing of $2.55 \hbar\omega_{\text{LO}}$ is observed and second, for the WL two valence bands have to be included where the upper one exhibits a rather flat dispersion. In the following the influence of these features is investigated and a comparison with previous results for the InGaAs case (cf. Chap. 5.1.2) and for the GaN case (cf. Chap. 7.1) is made.

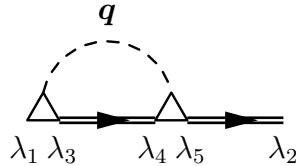


Fig. 7.11: Schematic diagram for the $\Sigma \cdot G$ term of the Dyson equation for the polaron, considering the RPA selfenergy.

The polaron retarded GF for nitrides obeys the Dyson equation (5.2), where we consider the RPA selfenergy (5.3). In comparison to the InGaAs QDs discussed in Chap. 5.1, the model for nitride QDs additionally includes a second valence band of the WL. This has several consequences and some comments are appropriate. The corresponding diagram that represents the Dyson equation for the polaron containing the RPA selfenergy is depicted in Fig. 7.11, where only the band indices are given explicitly. From this diagram we can infer, that different subbands are coupled either by off-diagonal GFs $G^{\lambda\lambda'}$ or by off-diagonal interaction vertices $M_{\alpha\beta}^{\lambda\lambda'}(\mathbf{q})$. Both possibilities are not included in our calculation. Due to the same assumptions discussed for the Coulomb case (Chap. 4.1), also for the basic carrier-phonon interaction vertices only band-diagonal overlaps are considered. Furthermore, off-diagonal GFs are only driven by an optical field [83]. This is not considered and therefore we restrict our analysis to band-diagonal retarded GFs. Note, that the two VBs are still connected indirectly via the QD states, even though only band-diagonal GFs and interaction vertices are considered.

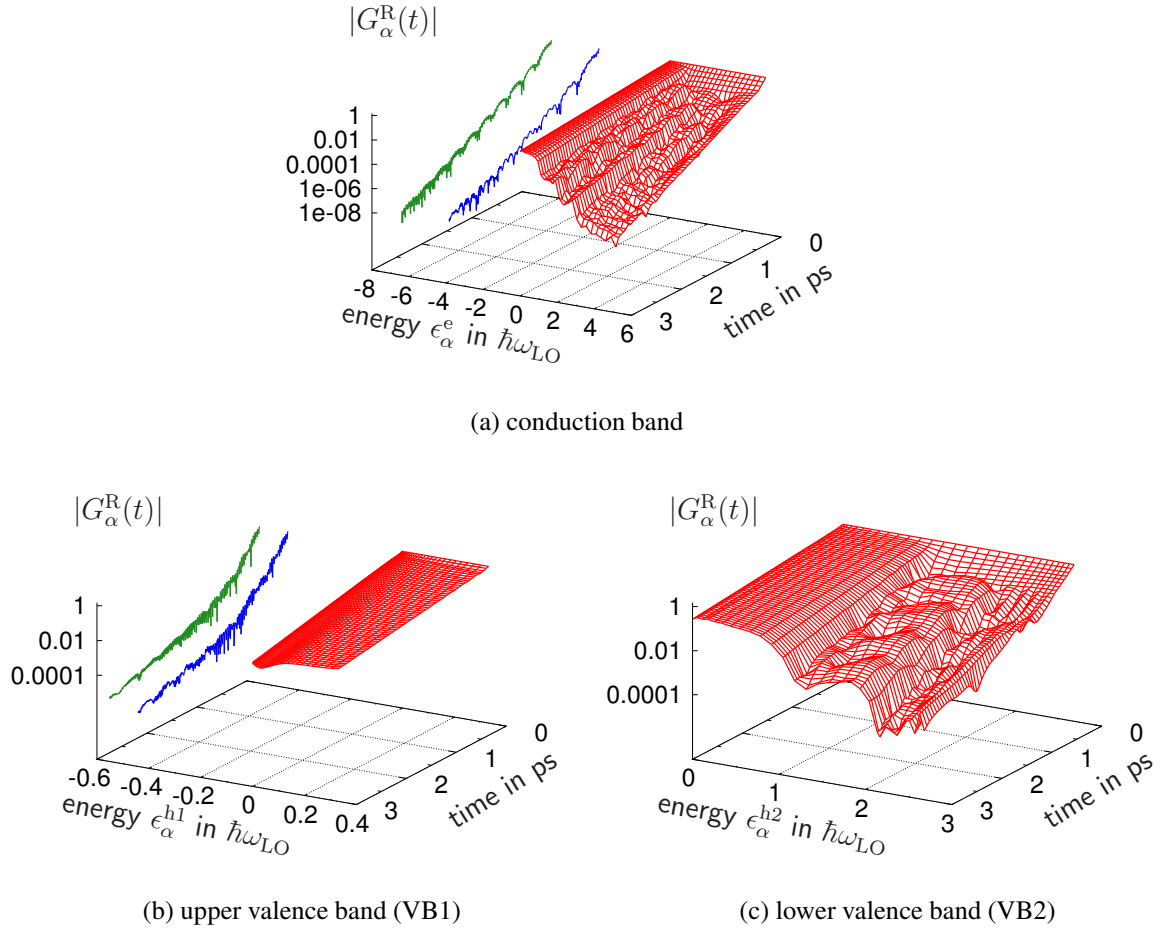


Fig. 7.12: Modulus of the polaron retarded GF for the conduction band as well as for the upper and lower valence band.

In Fig. 7.12 the modulus of the retarded GF in the time domain, following from a numerical solution of the corresponding Dyson equation, is depicted as a function of time and energy, both for QD and WL states. The energy dispersion taken into account is depicted in Fig. 7.10, whereas other material parameters are summarized in Tab. B.1. For the discussion note, that GaN is an intermediate polar coupling material, $\alpha = 0.5$, and the LO phonon energy amounts to $\hbar\omega_{LO} = 90$ meV.² As discussed in detail in Chap. 5.1.1, the modulus of the retarded GF reflects the quasi-particle lifetime, whereas its phase describes the quasi-particle energy. Remarkably, despite the large level spacing of approximately $2.55 \hbar\omega_{LO}$ for the conduction-band QD states, we find a considerable decay that corresponds to a short quasi-particle lifetime. The oscillatory character points towards a side-

²cf. the discussion on the phonon dispersion for nitrides in Chap. B.1.

band structure in the spectral function, which is discussed below. For the conduction-band (CB) WL states a phonon threshold is observed around $1 \hbar\omega_{\text{LO}}$. Below the threshold the decay is significantly slower due to reduced phonon emission processes. For the lower valence-band (VB2) WL states a similar behavior is observed. In contrast, for the upper valence band (VB1) WL states no phonon threshold is present, as the energy dispersion is rather flat. To observe a phonon threshold for a flat dispersion large momentum transfer is necessary, but the corresponding matrix elements are negligible. Note, that especially for higher WL states the calculation contains numerical artifacts as a finer discretization of the WL continuum exceeds our computational capacities.

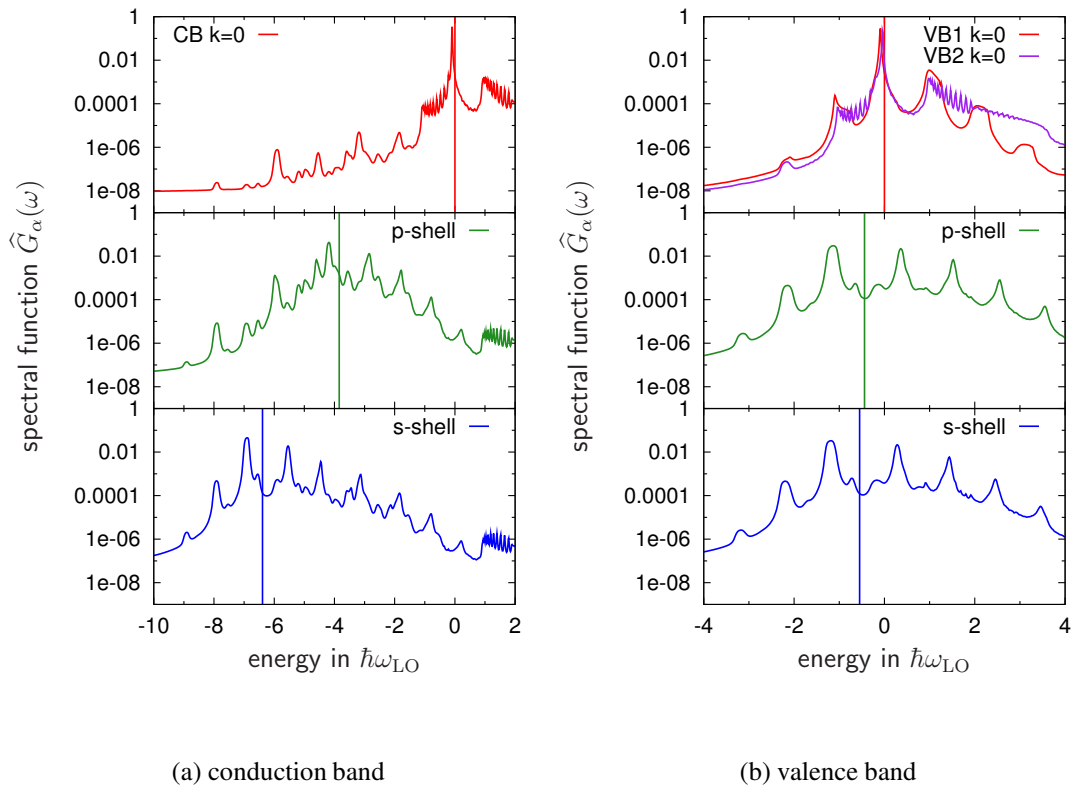


Fig. 7.13: Spectral function for QD and WL $k = 0$ states of the conduction band and the valence band.

The corresponding spectral functions are presented in Fig. 7.13. For the CB QD states a broad structure, containing multiple phonon satellites as well as hybridization effects (cf. the discussion in Chap. 5.1.2), is observed. Even though the level spacing is approximately $2.55 \hbar\omega_{\text{LO}}$ for CB QD states, the QD states strongly interact via multiple-phonon processes, whereas the interaction between QD and WL states (level spacing exceeds $3.8 \hbar\omega_{\text{LO}}$) is

considerably smaller. In the CB WL spectral function we observe a main peak exhibiting a polaron shift and a broad satellite $1 \hbar\omega_{\text{LO}}$ energetically above. For the VB states the picture is more involved due to the presence of several subbands. Whereas the VB2 WL spectral function resembles the effects discussed for the CB, the VB1 WL spectral function as well as the VB QD states show a qualitatively different behavior. In contrast to the CB we observe mainly satellites spaced $1 \hbar\omega_{\text{LO}}$ apart. Since the same physics as in the CB case, i.e. diagonal and off-diagonal coupling of QD states, is involved, one would expect hybridization effects. Note, that also in the spectral function numerical artifacts due to the coarse discretization of the WL continuum are observed.

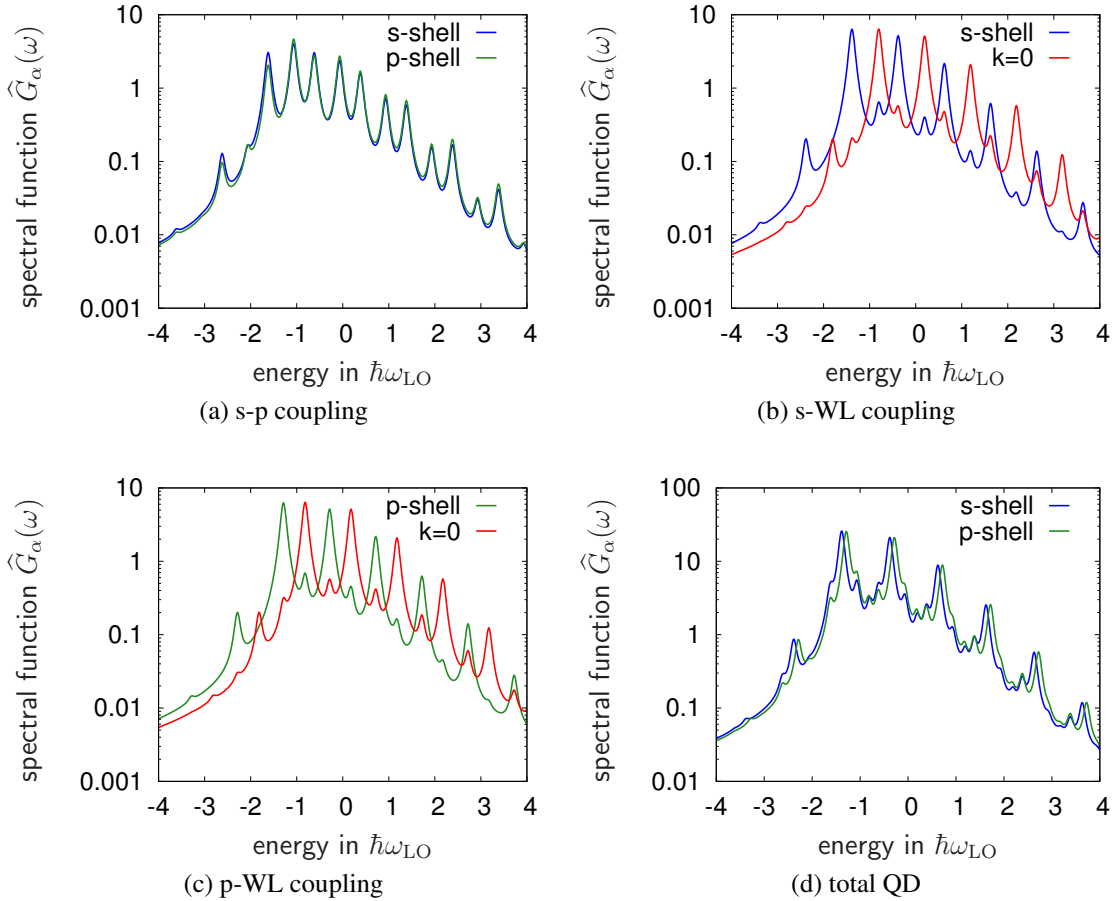


Fig. 7.14: Contributions to the model spectral function of QD states that interact with a dispersionless WL.

To analyze the situation, we consider a two-level model that can be diagonalized numerically, cf. Chap. 5.1.3, where a phenomenological broadening was chosen to resemble the broadening in Fig. 7.13b. The two levels either describe the two QD states or one

QD state and the $\mathbf{k} = 0$ WL state. Considering only the QD states whose level spacing is about $0.1 \hbar\omega_{\text{LO}}$ we find the spectral function shown in Fig. 7.14a, showing a series of satellites spaced $\approx 0.5 \hbar\omega_{\text{LO}}$ apart. In contrast, for the QD-WL coupling the level splitting is $0.56 \hbar\omega_{\text{LO}}$ for the s-shell and $0.44 \hbar\omega_{\text{LO}}$ for the p-shell, we find the spectral function shown in Fig. 7.14b and Fig. 7.14c, showing dominant satellites spaced $\approx 1 \hbar\omega_{\text{LO}}$ apart. In addition to the level splitting, important differences are in the ratio of diagonal and off-diagonal coupling. From the coupling matrix elements we infer that the QD-WL coupling is approximately a factor of ten smaller, compared to the off-diagonal QD-QD coupling. In this sense the QD-WL coupling resembles the independent-boson model, cf. Chap. 5.1.3. However, for the total spectral function the weight of the QD-WL spectral function dominates as an integration over the nearly dispersionless VB1 continuum is involved. An approximate superposition of both contributions to the spectral functions of the QD states is presented in Fig. 7.14d. We find that this model reproduces the main features of the RPA calculation shown in Fig. 7.13b. For the VB1 spectral function the contributions of QD-WL coupling are negligible. Because of the $\frac{1}{q^2}$ dependency of the WL-WL interaction matrix elements the diagonal couplings dominate and hence also the main features of the independent-boson model are found.

Consequences for carrier scattering

From the structure of the spectral function, several consequences for carrier scattering can be estimated by the scattering kernel in Markov approximation,

$$\Lambda_{\alpha\beta}^{\gtrless} \propto \int d\omega \widehat{G}_\alpha(\omega) \widehat{G}_\beta(\omega \pm \omega_{\text{LO}}). \quad (7.15)$$

For details see Chap. 5.2.1. As for the CB QD states multiple phonon satellites contribute, from the overlap between the two QD spectral functions fast scattering processes are expected. In contrast, capture processes are expected to be much slower, because of the larger energetic separation of the WL band edge from the QD states. For the VB states both, capture and relaxation processes are expected to be fast because of the small level spacing. However, the picture is more complicated if considering inter-subband scattering between WL states of VB1 and VB2. As can be inferred from Fig. 7.11, the assumption of band-diagonal interaction vertices only allows for polarization scattering between the sub-bands. Particle scattering of the form $f^{v_1} (1 - f^{v_2})$ is not possible within our approach and would require the inclusion of off-diagonal vertices. However, scattering between both WL VBs is still possible via capture from one WL VB into the QD and subsequent scattering into the other WL VB.

7.4 Optical properties

In this chapter we return to the optical response of semiconductor QDs. The particular InN QD introduced in Chap. 7.2 shows several differences, compared to the InGaN QDs discussed in Chap. 5–6. The most striking feature is the off-diagonal dipole coupling of QD states, which can be traced back to the symmetry properties of the QD states (cf. Chap. 7.2.5). To investigate the influence of the off-diagonal dipole coupling we calculate optical absorption spectra. The model for the optical polarization presented in Chap. 5.2.2 is extended correspondingly.

The free-particle absorption spectrum is determined by the dipole selection rules together with single-particle energy spectrum. Wave functions obtained from a TB calculation are used to calculate the dipole matrix element. Thus, the oscillator strength of the optical transitions and the influence of intrinsic electrostatic fields are included on a microscopic footing. Beside the single-particle properties, the optical absorption is strongly influenced by excitation-induced many-body effect. Coulomb renormalizations are included within the screened-exchange and Coulomb-hole approximation. In a second step, we make use of the polaron renormalizations we calculated in the previous chapter and additionally include carrier-LO-phonon scattering as dephasing mechanism. At this point the atomistic TB theory for the single-particle properties is combined with a quantum-kinetic many-body theory.

7.4.1 Kinetic equation

The interband transition amplitudes are described by the off-diagonal elements of the single-particle density matrix, which corresponds to the time-diagonal lesser GF in the framework of non-equilibrium GFs. Their equation of motion arises from the Kadanoff-Baym equations (3.64) and is given by

$$i\hbar \frac{d}{dt} G^<(t) = [\Sigma^\delta(t), G^<(t)] + \left. \frac{d}{dt} G^<(t) \right|_{\text{coll}} . \quad (7.16)$$

A detailed derivation is presented in Chap. 3.3–3.5. In this notation, the lesser GF $G^<$ and the selfenergy Σ are to be understood in matrix notation with respect to the state and subband indices. To clarify the structure of diagonal and off-diagonal couplings, the

commutator in Eq. 7.16, which includes the instantaneous selfenergy contributions, reads

$$i\hbar \frac{d}{dt} G^{<,cc}(t) = [\Sigma^{\delta,cc} G^{<,cc} - G^{<,cc} \Sigma^{\delta,cc}] + [\Sigma^{\delta,cv} G^{<,cv} - G^{<,cv} \Sigma^{\delta,cv}] \quad (7.17a)$$

$$i\hbar \frac{d}{dt} G^{<,vv}(t) = [\Sigma^{\delta,cv} G^{<,cv} - G^{<,cv} \Sigma^{\delta,cv}] + [\Sigma^{\delta,vv} G^{<,vv} - G^{<,vv} \Sigma^{\delta,vv}] \quad (7.17b)$$

$$i\hbar \frac{d}{dt} G^{<,cv}(t) = [\Sigma^{\delta,cc} G^{<,cv} - G^{<,cc} \Sigma^{\delta,cv}] + [\Sigma^{\delta,cv} G^{<,vv} - G^{<,cv} \Sigma^{\delta,vv}] \quad (7.17c)$$

$$i\hbar \frac{d}{dt} G^{<,vc}(t) = i\hbar \frac{d}{dt} [G^{<,cv}(t)]^\dagger \quad (7.17d)$$

with the band indices given explicitly. The lesser GFs $G^{<,cv}$ represent inter-band transition amplitudes that are diagonal and off-diagonal in the state index, i.e. direct and indirect inter-band transitions. On the other hand the intra-band quantities are given by $G_{\alpha\beta}^{<,cc}$ and $G_{\alpha\beta}^{<,vv}$, describing the population for $\alpha = \beta$ and intra-band transition amplitudes for $\alpha \neq \beta$. In Eq. (7.17), state and subband indices are still to be understood in matrix notation according to

$$A^{cc} = \begin{bmatrix} \nu^c \nu^c & \nu^c \mathbf{k}^c \\ \hline \mathbf{k}^c \nu^c & \mathbf{k}^c \mathbf{k}^c \end{bmatrix}, \quad A^{cv} = \begin{bmatrix} \nu^c \nu^v & \nu^c \mathbf{k}_1^v & \nu^c \mathbf{k}_2^v \\ \hline \nu^c \mathbf{k}_1^c & \mathbf{k}_1^c \mathbf{k}_1^v & \mathbf{k}_2^c \mathbf{k}_2^v \end{bmatrix},$$

$$A^{vc} = [A^{cv}]^\dagger, \quad A^{vv} = \begin{bmatrix} \nu^v \nu^v & \nu^v \mathbf{k}_1^v & \nu^v \mathbf{k}_2^v \\ \hline \nu^v \mathbf{k}_1^v & \mathbf{k}_1^v \mathbf{k}_1^v & \mathbf{k}_2^v \mathbf{k}_1^v \\ \hline \nu^v \mathbf{k}_2^v & \mathbf{k}_1^v \mathbf{k}_2^v & \mathbf{k}_2^v \mathbf{k}_2^v \end{bmatrix}. \quad (7.18)$$

Here, ν^λ indicates a QD state and \mathbf{k}_n^λ a WL state of the n -th subband, with λ representing the corresponding band. In this example one conduction band and two subbands of the valence band are considered. Please note, that the QD states occur only once, even though the valence band contains two subbands. Furthermore the matrix notation implies a "sum" over all states in the system. Depending on the sub-blocks of the matrices that are multiplied with each other in Eq. 7.17, this "sum" is to be understood either as an integration $\frac{1}{(2\pi)^2} \int d^2k$ over a continuum of WL states or a summation $\sum_{R,\nu}$ over QD states and positions.

Instantaneous selfenergy contributions

As instantaneous selfenergy contributions we consider in the following the free-particle energy dispersion, the optical pulse excitation, and Coulomb renormalizations in SX-CH approximation. A detailed discussion of the different selfenergy contributions is presented in Chap. 4. Consequently, only a short summary is given, where nitride-specific properties are discussed.

The energy dispersion $\varepsilon_\alpha^\lambda$ we consider for the calculation is depicted in Fig. 7.10 and included by means of the selfenergy

$$\Sigma_{\alpha\beta}^{\text{free},\lambda\lambda'} = \varepsilon_\alpha^\lambda \delta_{\alpha\beta} \delta_{\lambda\lambda'} . \quad (7.19)$$

Off-diagonal dipole transitions are driven by the optical pulse, which is included via the selfenergy (4.50). Only those transition amplitudes $G_{\alpha\beta}^{<,cv}$ are driven whose corresponding dipole matrix elements $d_{\alpha\beta}^{cv}$ are nonzero. For InGaAs QDs the selfenergy $\Sigma^\delta = \Sigma^{\text{free}} + \Sigma^{\text{pulse}}$ is diagonal in the state index. In this case no off-diagonal elements of $G_{\alpha\beta}^{<}$ are driven in the SBE (7.16), even in the presence of two valence bands. For InN QDs where also the off-diagonal dipole coupling for the QD states is taken into account, the corresponding interband transition amplitudes $G^{<,cv}$ are driven by the pulse directly. Other inter- and intra-band transition amplitudes can be driven indirectly, for example via the Coulomb interaction.

The Coulomb interaction is considered by means of the SX-CH selfenergy (4.19) and (4.20), as well as the Hartree contributions (4.12). To facilitate the discussion of off-diagonal contributions, let us first focus on the diagrammatic representation of the Hartree terms is depicted in Fig. 4.3b. As we are restricting ourselves to interaction vertices diagonal in the band index, only population functions³ appear in the Hartree terms. Were we to include all possible band-index combinations in the overlaps, also Hartree contributions containing interband transition amplitudes would appear. The corresponding diagrammatic representation for the SX-CH selfenergy is depicted in Fig. 4.3a. Due to the off-diagonal nature of the main QD transitions, cf. the dipole selection rules, the selfenergy for the WL states reads

$$\Sigma_{\mathbf{k}\mathbf{k}}^{\lambda\lambda'}(t) = i\hbar \sum_{\nu\mu} V_{\mathbf{k}\nu\mathbf{k}\mu}^{\lambda\lambda'} G_{\mu\nu}^{<,\lambda\lambda'}(t) + i\hbar \sum_{\mathbf{k}'} V_{\mathbf{k}\mathbf{k}'\mathbf{k}\mathbf{k}'}^{\lambda\lambda'} G_{\mathbf{k}'\mathbf{k}'}^{<,\lambda\lambda'}(t) , \quad (7.20)$$

where all GFs $G_{\delta\gamma}^{<,cv}$ involving two QD states are non-vanishing and hence all interaction matrix elements $V_{\mathbf{k}\gamma\mathbf{k}\delta}^{\lambda\lambda'}$ are required. As the WL-WL overlaps (7.14) contain the momentum conservation, we can restrict our analysis to diagonal WL GFs $G_{\mathbf{k}\mathbf{k}}^{\geq}$. Note, that in $V_{\mathbf{k}\mathbf{k}'\mathbf{k}\mathbf{k}'}^{\lambda\lambda'}$ we have to deal with the problem of lifting the Coulomb singularity. The procedure we

³In principle also intra-band transitions amplitudes.

use is discussed in Refs. [64] and an extension to the TB approach is outlined in App. B.4. Likewise we find for the QD states

$$\Sigma_{\nu\mu}^{\lambda\lambda'}(t) = i\hbar \sum_{\mathbf{k}} V_{\nu\mathbf{k}\mu\mathbf{k}}^{\lambda\lambda'} G_{\mathbf{kk}}^{<,\lambda\lambda'}(t) + i\hbar \sum_{\chi\xi} V_{\nu\chi\mu\xi}^{\lambda\lambda'} G_{\xi\chi}^{<,\lambda\lambda'}(t), \quad (7.21)$$

where all QD-QD couplings $V_{\nu\chi\mu\xi}^{\lambda\lambda'}$ are included.

The complicated interplay of all transition amplitudes via the Coulomb matrix elements poses the question, whether transition amplitudes that are not directly driven by the optical field via the dipole interaction can be driven indirectly via the Coulomb interaction. To investigate this, let us consider for example the dynamics of a interband transition amplitude connecting QD and WL states $G_{\nu k}^{<,cv}$. The corresponding equation of motion for this GF reads

$$i\hbar \frac{d}{dt} G_{\nu k}^{cv}(t) = i\hbar \left[+ \Sigma_{\nu k}^{cc} G_{kk}^{cv} + \Sigma_{\nu k}^{cv} G_{kk}^{vv} \right. \\ \left. + \Sigma_{\nu\nu}^{cc} G_{\nu k}^{cv} + \Sigma_{\nu\nu}^{cv} G_{\nu k}^{vv} \right. \\ \left. - G_{\nu k}^{cc} \Sigma_{kk}^{cv} - G_{\nu k}^{cv} \Sigma_{kk}^{vv} \right. \\ \left. - G_{\nu\nu}^{cc} \Sigma_{\nu k}^{cv} - G_{\nu\nu}^{cv} \Sigma_{\nu k}^{vv} \right], \quad (7.22)$$

where the indices k and ν are to be understood symbolically for the respective state belonging either to the WL or to a QD. Furthermore the \gtrless components are suppressed for simplicity. All contributions that drive this polarization are proportional to a polarization times a population. Therefore, in the linear regime, i.e. $\chi^{(1)}$, these terms are not driven in the limit of vanishing background carrier density. Considering finite background carrier densities, e.g. for gain calculations, these terms in principle have to be taken into account. However, all transition amplitudes not directly driven by the optical pulse, i.e. $d_{\alpha\beta} = 0$, do not directly contribute to the macroscopic polarization (6.5). Their influence is restricted to the back-action on directly driven polarizations. To simplify the numerical evaluation, we therefore neglect these transition amplitudes in the following. Similar to the discussion for the Hartree terms, the inclusion of band off-diagonal vertices implies additional terms.

7.4.2 Linear absorption

The linear absorption spectrum is calculated from the macroscopic polarization via $\chi(\omega) = \frac{P(\omega)}{E(\omega)} \propto \alpha(\omega)$ as discussed in Chap. 6.1. As the SX-CH and the Hartree selfenergies we consider for the calculation do not provide microscopic dephasing, in a first step we use a phenomenological value of $\gamma = 10$ meV. Calculations that additionally include microscopic dephasing due to carrier-LO-phonon collisions are presented below. In comparison to typical InGaAs QDs discussed in previous chapters, the InN QD under consideration exhibits deeply confined shells, especially for electrons, cf. Fig. 7.10. The confinement

energy for the lowest QD states with respect to the band edge is -575.4 meV and -345.3 meV for electrons, and -49.6 meV and -39.8 meV for holes. In conjunction with the "skew" dipole selection rules discussed in Chap. 7.2.5, this corresponds to free-carrier transition energies of -615.2 meV and -394.9 meV, relative to the WL bandgap of 1731 meV. As initial carrier distribution, we assume a quasi-equilibrium situation for the CB as well as a common one for the two VBs.

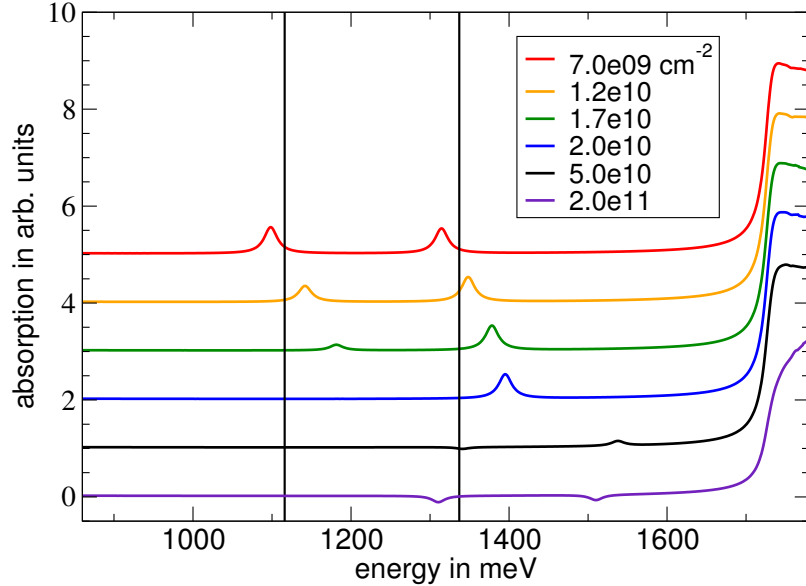


Fig. 7.15: Linear optical absorption spectra for InN QDs at 300 K and for various carrier densities, considering a phenomenological dephasing of 10 meV.

The corresponding absorption spectra for a temperature of 300 K and various carrier densities are shown in Fig. 7.15. With increasing carrier density, the transition energies exhibit a blue shift accompanied by bleaching of the absorption and transition to gain. For carrier densities exceeding $5 \times 10^{10} \text{ cm}^{-2}$ the blue shift is reduced. This complicated behavior is due to the interplay of Hartree, screened-exchange (SX) and Coulomb hole (CH) contributions. The corresponding numbers for three exemplary carrier densities are given in Tab. 7.2. As we can infer, the CH energy shifts are practically the same for CB and VB carriers and therefore only slightly influence the interband transition energies. In contrast, Hartree as well as SX terms give rise to a relative shift of CB and VB energies. Since for each band the Hartree term contains contributions from all bands (cf. Eq. (4.12) and Fig. 4.3b), the influence of the QD population on the Hartree shift is similar for CB and VB. The large difference between CB and VB shifts arises from the screened interaction matrix elements. The blue shift for small to intermediate carrier densities stems from the steep increase of the Hartree contributions. For larger carrier densities, the Hartree terms saturate due to filling of the QD states. Simultaneously the screening of the Coulomb

		$2 \times 10^{10} \text{ cm}^{-2}$	$5 \times 10^{10} \text{ cm}^{-2}$	$2 \times 10^{11} \text{ cm}^{-2}$
CB	SX 1	-73.7	-88.9	-64.5
	SX 2	-17.5	-58.3	-46.3
	CH 1	-14.1	-20.1	-36.5
	CH 2	-13.3	-18.6	-31.9
	H 1	149.0	285.5	189.4
	H 2	124.8	245.7	156.2
VB	SX 1	2.9	6.4	15.4
	SX 2	2.4	5.4	14.4
	CH 1	-13.9	-19.7	-35.6
	CH 2	-14.0	-19.9	-36.3
	H 1	-13.3	-29.1	-70.1
	H 2	-14.4	-31.7	-79.1

Tab. 7.2: Energy shift contributions from screened-exchange (SX), Coulomb hole (CH), and Hartree (H) selfenergies in meV.

interaction increases due to filling of WL states which leads to a strong reduction of the Hartree contributions. In contrast, saturation effects are smaller for the SX terms because of increasing contributions from WL carriers. This leads in total to a reduced blue shift for high carrier densities.

To employ a microscopic dephasing mechanism we consider the interaction with LO phonons, where, similar to the extended discussion in Chap. 5.2.2, we use the RPA selfenergy. Specifically, we consider the one-time collision terms (3.72) in the Markovian limit which is obtained by application of the reverse GKBA, cf. Chap. 3.5. This procedure

yields

$$\begin{aligned}
 \frac{d}{dt} G_{\alpha\beta}^{<,cv}(t) \Big|_{\text{coll}} = & \hbar^2 \sum_{\gamma\delta\xi} \sum_{\mathbf{q}} \int_{-\infty}^t dt_3 \left\{ \right. \\
 & + G_{\delta\xi}^{cc,>}(t) G_{\xi}^{c,R}(t, t_3) D_{\alpha\xi\gamma\delta,\mathbf{q}}^{cccc,<}(t_3, t) G_{\gamma}^{c,A}(t_3, t) G_{\gamma\beta}^{cv,<}(t) \\
 & - G_{\delta\xi}^{cc,<}(t) G_{\xi}^{c,R}(t, t_3) D_{\alpha\xi\gamma\delta,\mathbf{q}}^{cccc,>}(t_3, t) G_{\gamma}^{c,A}(t_3, t) G_{\gamma\beta}^{cv,>}(t) \\
 & + G_{\alpha\gamma}^{cc,<}(t) G_{\gamma}^{c,R}(t, t_3) G_{\delta}^{c,A}(t_3, t) G_{\delta\xi}^{cv,>}(t) D_{\gamma\xi\beta\delta,\mathbf{q}}^{cvvc,<}(t, t_3) \\
 & - G_{\alpha\gamma}^{cc,>}(t) G_{\gamma}^{c,R}(t, t_3) G_{\delta}^{c,A}(t_3, t) G_{\delta\xi}^{cv,<}(t) D_{\gamma\xi\beta\delta,\mathbf{q}}^{cvvc,>}(t, t_3) \\
 & + G_{\delta\xi}^{cv,>}(t) G_{\xi}^{v,R}(t, t_3) D_{\alpha\xi\gamma\delta,\mathbf{q}}^{cvvc,<}(t_3, t) G_{\gamma}^{v,A}(t_3, t) G_{\gamma\beta}^{vv,<}(t) \\
 & - G_{\delta\xi}^{cv,<}(t) G_{\xi}^{v,R}(t, t_3) D_{\alpha\xi\gamma\delta,\mathbf{q}}^{cvvc,>}(t_3, t) G_{\gamma}^{v,A}(t_3, t) G_{\gamma\beta}^{vv,>}(t) \\
 & + G_{\alpha\gamma}^{cv,<}(t) G_{\gamma}^{v,R}(t, t_3) G_{\delta}^{v,A}(t_3, t) G_{\delta\xi}^{vv,>}(t) D_{\gamma\xi\beta\delta,\mathbf{q}}^{vvvv,<}(t, t_3) \\
 & \left. - G_{\alpha\gamma}^{cv,>}(t) G_{\gamma}^{v,R}(t, t_3) G_{\delta}^{v,A}(t_3, t) G_{\delta\xi}^{vv,<}(t) D_{\gamma\xi\beta\delta,\mathbf{q}}^{vvvv,>}(t, t_3) \right\}. \tag{7.23}
 \end{aligned}$$

with $D_{\alpha\beta\gamma\delta}(t_1, t_2)$ containing the interaction matrix elements as well as the phonon propagator, cf. Eq. 4.32. Also in this case a separation into diagonal and off-diagonal dephasing is possible, even though the situation is more complicated due to the coupling of different off-diagonal GFs. Nevertheless, a compensation between the two contributions also holds in this case.

The corresponding optical absorption spectra including dephasing due to LO-phonon collisions are presented in Fig. 7.16. Energy shifts due to polaron effects are small in comparison to SX-CH and Hartree interaction which are identical as in the results shown above. The main influence of carrier-phonon scattering is dephasing of the optical polarization that corresponds to broadening of the resonances. An asymmetric line shape as well as a typical line width of 22 meV for the energetically lower and 18 meV for the energetically higher transition are found. The difference arises due to the fact that for the energetically lower transition the off-diagonal compensation is reduced due to the large energetic separation from the WL. It should be noted, that at the low energy side of the QD resonances a slightly negative absorption is observed. This artifact we attribute to the GKBA, since as shown in Chap. 5.3.3 the validity of the GKBA for intermediate to strong polar coupling materials is questioned.

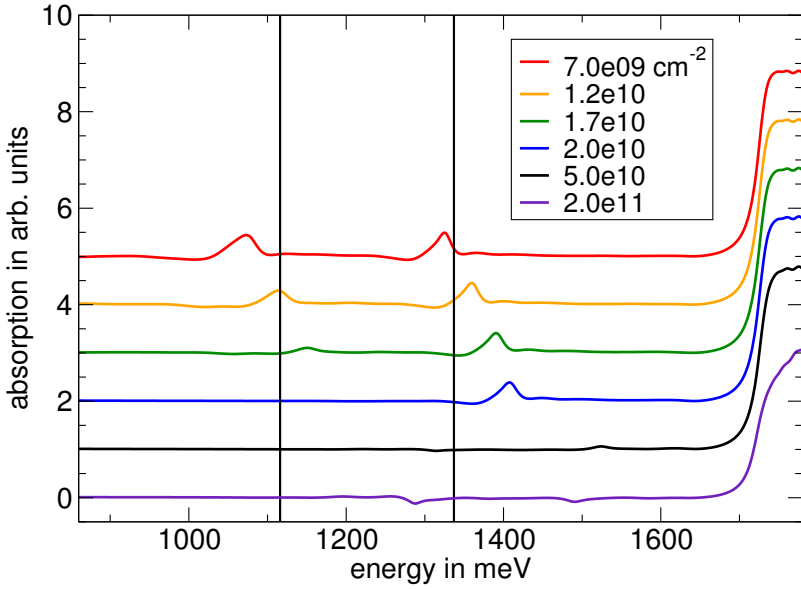


Fig. 7.16: Linear optical absorption spectra for InN QDs at 300 K and for various carrier densities. The dephasing is provided by carrier-LO-phonon collisions and included on a microscopic basis.

7.4.3 Dephasing due to Coulomb scattering

Absorption spectra for InGaAs QDs are presented in Chap. 6.1. To determine excitation-induced dephasing due to Coulomb interaction the second Born approximation (SBA) was employed, cf. Chap. 4.1. In contrast, for the nitride material system we use the SX-CH approximation. Therefore several comments on important differences between the two approaches are in order.

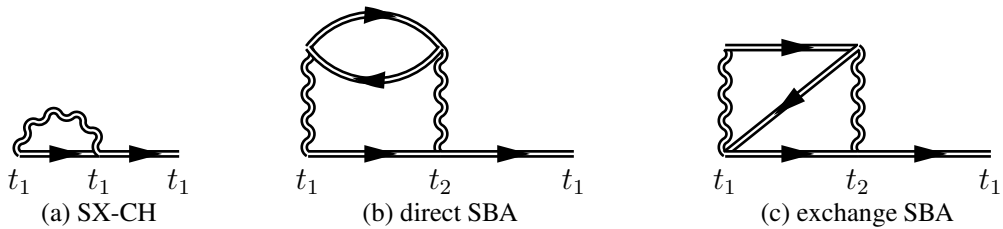


Fig. 7.17: Schematic representation of SX-CH diagrams SBA diagrams.

Schematically, the contributing diagrams in the Kadanoff-Baym equations (3.64) are depicted in Fig. 7.17. In contrast to the usual notation, the wiggly interaction line denotes the retarded/advanced plasmon GF $W^{R/A}$ and the carrier propagators G^{\geqslant} are represented by

straight lines. Therefore, these diagrams should not be confused with Feynman diagrams as no systematic perturbation expansion is implied. For the following discussion note, that $W^{R/A}$ is a real quantity under the assumption that the screening is instantaneous and does not contain retardation effect, cf. the discussion in Chap. A.2. Considering the homogeneous part of the equation of motion for the polarization, $i\hbar \frac{d\psi}{dt} = \Delta\psi$, the dephasing is identified as the imaginary part of Δ . In the SX-CH selfenergy diagram (cf. Fig. 7.17a) no retardation effects are included due to the instantaneous interaction and hence all internal times are fixed to the external ones. This implies the structure $\Delta \propto W^{R/A}f$, which is a real quantity and hence provides no dephasing. In contrast, in the SBA diagrams an internal time t_2 is involved (cf. Fig. 7.17b,c). Hence, retardation effects, that are included in the two-time propagators $G^{\gtrless}(t_1, t_2)$, contribute. This can be easily seen when representing the two-time propagator by means of the GKBA, which maps the two-time propagators onto the time-diagonal with the help of retarded/advanced GFs, cf. Chap. 3.5. For the equation of motion this implies the structure $\Delta = WW^* f f f G^R G^R G^R G^R$, which is complex in general, and hence provides dephasing. However, the inclusion of dephasing due to Coulomb scattering in our calculations for nitride semiconductors remains a challenging task as in addition to the calculations shown in Chap. 6.1 one has to account for off-diagonal GFs. Moreover, in the calculations for the InGaAs material using the harmonic-oscillator model (cf. Chap. A.1) the matrix elements to a large extend can be calculated analytically, which is not possible in the nitride case and thus by far enhancing the computational effort.

8 Conclusion

This thesis provides a deeper insight into carrier-LO-phonon scattering mechanism in semiconductor QDs. On the one hand the interaction gives rise to renormalizations of the single-particle states, and on the other hand it leads to carrier scattering and dephasing processes. The interplay of these two effects was studied using the framework of non-equilibrium Green's functions.

Most important for the understanding of scattering and dephasing mechanism are the renormalizations of the single-particle states. In case of the carrier-LO-phonon interaction, they are described by the formation of polarons. An intuitive approach for the discussion of polarons is the spectral function, which is connected to the density of states. For continuous systems like QWs, the spectral function is dominated by a single resonance. In this case results from perturbation theory are in good agreement with our non-perturbative approach, leading simply to a shift of the free-particle energies and introducing a finite carrier lifetime. In contrast, for QD systems perturbation theory clearly fails. The carrier confinement gives rise to an enhanced effective coupling, resulting in pronounced phonon satellites and their hybridization. Strong coupling effects are observed, even for weak polar coupling materials. Additionally, the interaction of QD states with the energetically close continuum of WL states leads to a further broadening of the polaron resonances at room temperature. In contrast, at low temperatures only a few phonons are present. As a consequence, phonon absorption processes are strongly suppressed and emission processes dominate. This leads to a much weaker interaction between QD and WL states, resulting in much narrower resonances of the spectral function.

These polaron properties determine to a large extent the efficiency of carrier-scattering processes, as the scattering kernel is given by the overlap of the spectral functions of the involved states. Thus, within the quasi-particle picture of carrier-scattering a deeper insight into the phonon-bottleneck controversy was achieved. Because of the controversial experimental findings regarding the phonon-bottleneck discussion, further investigations have been performed. For elevated temperatures we find that polaron effects give rise to fast scattering channels, whereas in the low-temperature regime an initial fast relaxation is followed by a freezing of the carrier distribution at later times, not reaching a thermal distribution. Thus, our analysis shows that the phonon bottleneck discussion in QDs should include the energy spectrum of the QD, the temperature regime, and the timescales involved. The question about the presence of a phonon bottleneck can not be answered by the energy mismatch argument alone. As applications of the developed quantum-kinetic

model we have presented an investigation of the influence of carrier-phonon scattering on the optical response by means of absorption spectra and the temporally resolved photoluminescence. The analysis of the optical response, including dephasing processes due to both, carrier-carrier and carrier-phonon interaction, showed that it is essential to consider quasi-particle renormalizations in a self-consistent way. Furthermore it was found that both contributions to the dephasing are important, even in the high carrier-density regime.

For the nitride material system it turned out that, besides many-body effects, a microscopic treatment of the electronic properties is of central importance, as intrinsic and strain-induced electric fields as well as the QD geometry and the underlying wurtzite crystal structure strongly influence the electronic properties. To study the interplay of the particular single-particle wave functions and many-body effects, a procedure to incorporate results from an atomistic tight-binding approach into our quantum-kinetic theory was developed. As a first application the properties of nitride polarons have been investigated. In a second step absorption spectra are presented where we considered Coulomb renormalizations as well as the dephasing due to carrier-phonon interaction including polaron effects. These results show large excitation-induced shifts of the QD resonances, which definitely have to be considered for practical applications like LEDs and laser diodes.

Future directions

The results presented in this thesis may serve as a starting point for further investigations in the field of quantum kinetics and semiconductor quantum dot systems. Whereas the one-time kinetics provides an intuitive way to incorporate memory effects and quasi-particle renormalizations, intrinsic shortcomings of the involved GKBA, in particular for intermediate to strong polar coupling materials, should be investigated further. Such investigations might for example include new quasi-particle concepts presented by Velický et al. [89], a more detailed analysis of the reconstruction scheme for two-time propagators, and a further analysis of the two-time equations including the kinetics of individual polaron satellites. For the carrier scattering a calculation of the temporal evolution of the population distribution including both, carrier-carrier and carrier-phonon interaction, would be interesting, especially since the relaxation times we computed indicate that in QD systems even at low carrier densities Coulomb scattering is not negligible. With the new generation of CPU clusters such calculations in a one-time version should be feasible. Another aspect for the optical response of semiconductor QDs is the exciton phonon interaction, represented by selfenergy diagrams that contain both carrier-carrier and carrier-phonon interaction lines. Such contributions, giving rise to phonon replica of the exciton resonances in the optical spectra, are clearly observed in experimental data. Furthermore, the procedure presented to incorporate wave functions obtained from atomistic tight-binding calculations opens a whole field of future investigations. For the nitride material system, especially the influence of specific material compositions, e.g. ternary alloys, concentration gradients due to

segregation effects and new QD geometries can be studied. For the far future one might imagine to use holographic information of a particular QD sample to extract atom positions, QD geometry and strain, obtained for example with a transmission-electron microscope. Using these data as input for a tight-binding calculation, immediately enables us to determine the optical response including many-body effects.

Part IV

Appendix

A Envelope wave function model and additional material

A.1 Envelope wave function model

Based on the symmetry properties of the QD-WL system, one assumes for the wave functions in Bloch representation a factorization of the envelope function into an 2D in-plane part $\varphi(\boldsymbol{\rho})$ and an 1D part $\xi(z)$ in growth direction,

$$\psi(\mathbf{r}) = \varphi(\boldsymbol{\rho}) \xi(z) u_{\mathbf{k} \approx 0}(\mathbf{r}), \quad (\text{A.1})$$

with the lattice periodic Bloch function $u_{\mathbf{k} \approx 0}(\mathbf{r})$. The envelope part in growth direction is described by a 1D quantum well (QW) wave function, where only the lowest subband is taken into account. The simplest approach would be to consider QW barriers of infinite height, where the eigenfunctions are known analytically, $\xi(z) = \sin(\frac{\pi}{L}z)$. Considering barriers of finite height or a more complicated potential to incorporate e.g. the Quantum confined Stark effect (see Chap. 7.1), the envelope part is evaluated numerically by discretization of the corresponding 1D Schrödinger equation in real space, see e.g. [202, 203]. In the absence of QDs, the delocalized states are described by 2D plane waves (PW)

$$\varphi_{\mathbf{k}}^0(\boldsymbol{\rho}) = \frac{1}{\sqrt{A}} e^{i\mathbf{k}\boldsymbol{\rho}}, \quad (\text{A.2})$$

with \mathbf{k} being the 2D in-plane momentum. Considering flat, lens-shaped quantum dots, the in-plane confinement potential was shown to be harmonic in good approximation [140, 204]. The corresponding 2D harmonic oscillator wave functions are well known [29] and classified by their angular momentum properties. Correspondingly they are referred to as

s-, p- and d-shell.

$$\varphi_{m=0}^s(\boldsymbol{\rho} - \mathbf{R}) = \frac{\beta}{\sqrt{\pi}} e^{-\frac{\beta^2 |\boldsymbol{\rho} - \mathbf{R}|^2}{2}}, \quad (\text{A.3a})$$

$$\varphi_{m=\pm 1}^p(\boldsymbol{\rho} - \mathbf{R}) = \frac{\beta}{\sqrt{\pi}} e^{-\frac{\beta^2 |\boldsymbol{\rho} - \mathbf{R}|^2}{2}} \cdot \beta |\boldsymbol{\rho} - \mathbf{R}| e^{\pm i\phi}, \quad (\text{A.3b})$$

$$\varphi_{m=\pm 2}^d(\boldsymbol{\rho} - \mathbf{R}) = \frac{\beta}{\sqrt{\pi}} e^{-\frac{\beta^2 |\boldsymbol{\rho} - \mathbf{R}|^2}{2}} \cdot (\beta |\boldsymbol{\rho} - \mathbf{R}|)^2 e^{\pm i2\phi}, \quad (\text{A.3c})$$

$$\varphi_{m=0}^d(\boldsymbol{\rho} - \mathbf{R}) = \frac{\beta}{\sqrt{\pi}} e^{-\frac{\beta^2 |\boldsymbol{\rho} - \mathbf{R}|^2}{2}} \cdot [(\beta |\boldsymbol{\rho} - \mathbf{R}|)^2 - 1] \quad (\text{A.3d})$$

In this notation \mathbf{R} is the position of the QD on the WL plane and $\beta = \frac{\sqrt{m\Delta E}}{\hbar}$ is the inverse oscillator length, determining the equidistant energy separation ΔE between the QD shells.

Interaction matrix elements

According to the separation ansatz (A.1), the z -dependence in the bare Coulomb interaction matrix elements (4.1) might be cast into a formfactor,

$$V_{1234} = \frac{e^2}{4\pi\varepsilon_0} \int d^2q \frac{1}{\mathbf{q}} F_{1234}(\mathbf{q}) \langle \phi_1 | e^{i\mathbf{q}\boldsymbol{\rho}} | \phi_4 \rangle \langle \phi_2 | e^{-i\mathbf{q}\boldsymbol{\rho}} | \phi_3 \rangle \quad (\text{A.4})$$

with

$$F_{1234}(\mathbf{q}) = \int dz \int dz' \xi(z) \xi(z') e^{iq_z(z-z')} \xi(z') \xi(z). \quad (\text{A.5})$$

The overlap integrals for the QD-WL system under consideration are discussed below. Note, that the Carrier-LO-phonon interaction matrix elements and the bare Coulomb interaction matrix elements are connected according to (4.37).

Orthogonalized plane waves

As for the in-plane part the harmonic oscillator states and the plane waves are orthogonal among themselves but not among each other, the orthogonalized-plane-waves (OPW) scheme is applied,

$$|\mathbf{k}\rangle = \frac{1}{N_{\mathbf{k}}} \left[|\mathbf{k}_0\rangle - \sum_{\nu, \mathbf{R}} |\nu, \mathbf{R}\rangle \langle \nu, \mathbf{R} | \mathbf{k}_0 \rangle \right], \quad (\text{A.6})$$

$$N_{\mathbf{k}} = \sqrt{1 - N \sum_{\nu} |\langle \mathbf{k}_0 | \nu \rangle|^2}. \quad (\text{A.7})$$

Here, explicitly the random distribution of QDs on the WL plane was used. Since the QD position only gives rise to a phase factor $\langle \nu, \mathbf{R} | \mathbf{k}_0 \rangle = \langle \nu | \mathbf{k}_0 \rangle e^{i\mathbf{k}\mathbf{R}}$, on average momentum conservation is restored, $\langle \mathbf{k} | \mathbf{k}' \rangle \propto \delta(\mathbf{k} - \mathbf{k}')$. Keeping in mind that $\langle \mathbf{k}_0 | \nu \rangle \propto \frac{1}{\sqrt{A}}$, effectively only the QD density $N_{\text{QD}} = \frac{N}{A}$ enters the theory.

In principle the OPW scheme also leads to a modification of the energies of the WL states. However, this change can be neglected if the QD density and the QD size are sufficiently small or, in other words, if the fraction of the WL plane that is covered with QDs is sufficiently small. Consider the expectation value of the total energy for the total Hamiltonian containing QD and WL states,

$$\begin{aligned} \langle \mathbf{k} | H | \mathbf{k} \rangle &= \langle \mathbf{k}_0 | H | \mathbf{k}_0 \rangle - N \sum_{\nu} \langle \mathbf{k}_0 | H | \nu \rangle \langle \nu | \mathbf{k}_0 \rangle - N \sum_{\nu} \langle \mathbf{k}_0 | \nu \rangle \langle \nu | H | \mathbf{k}_0 \rangle \\ &\quad + N \sum_{\nu, \mu} \langle \mathbf{k}_0 | \nu \rangle \langle \nu | H | \mu \rangle \langle \mu | \mathbf{k}_0 \rangle \\ &= \langle \mathbf{k}_0 | H | \mathbf{k}_0 \rangle - N \sum_{\nu} E_{\nu} | \langle \nu | \mathbf{k}_0 \rangle |^2. \end{aligned} \quad (\text{A.8})$$

Taking into account that the overlaps $| \langle \nu | \mathbf{k}_0 \rangle |^2$ contain factors of $\frac{1}{A}$, we find that in the last line the second term is proportional to the QD density N_{QD} . This shows that for sufficiently low QD densities (in the sense explained above), we can disregard the OPW corrections to the WL energies. As the WL energies in the presence of QDs are not known, we work in good approximation work with the PW energies $\langle \mathbf{k}_0 | H | \mathbf{k}_0 \rangle \approx E_{\mathbf{k}}^0$. However, as the matrix elements calculated from non-orthogonal states lead to clear deviations in the results, it is essential to include the OPW corrections to the wave-functions.

Overlap integrals

For the calculation of Coulomb and Fröhlich interaction matrix elements, see Chap. 4, overlap integrals of the form $\langle \alpha | e^{i\mathbf{q}\mathbf{r}} | \beta \rangle$ have to be evaluated. Using the OPW scheme and assuming identical QDs, we find for the QD-WL overlaps

$$\langle \nu | e^{i\mathbf{q}\mathbf{r}} | \mathbf{k} \rangle = \frac{1}{N_{\mathbf{k}}} \left[\langle \nu | e^{i\mathbf{q}\mathbf{r}} | \mathbf{k}_0 \rangle - \sum_{\nu'} \langle \nu | e^{i\mathbf{q}\mathbf{r}} | \nu' \rangle \langle \nu' | \mathbf{k}_0 \rangle \right], \quad (\text{A.9})$$

and for the WL-WL overlaps

$$\langle \mathbf{k} | e^{i\mathbf{q}\mathbf{r}} | \mathbf{k}' \rangle = \delta(\mathbf{q} + \mathbf{k}' - \mathbf{k}) D_{\text{OPW}}(\mathbf{k}, \mathbf{q}, \mathbf{k}'), \quad (\text{A.10})$$

$$\begin{aligned}
D_{\text{OPW}}(\mathbf{k}, \mathbf{q}, \mathbf{k}') = & \frac{1}{N_{\mathbf{k}}} \frac{1}{N_{\mathbf{k}'}} \left(1 - N_{\text{QD}} \sum_{\nu} \langle \mathbf{k}_0 | e^{i\mathbf{qr}} | \nu \rangle \langle \nu | \mathbf{k}'_0 \rangle \right. \\
& - N_{\text{QD}} \sum_{\nu} \langle \mathbf{k}_0 | \nu \rangle \langle \nu | e^{i\mathbf{qr}} | \mathbf{k}'_0 \rangle \\
& \left. + N_{\text{QD}} \sum_{\nu, \mu} \langle \mathbf{k}_0 | \nu \rangle \langle \nu | e^{i\mathbf{qr}} | \mu \rangle \langle \mu | \mathbf{k}'_0 \rangle \right). \quad (\text{A.11})
\end{aligned}$$

More details on the OPW scheme using harmonic oscillator states for the QD and PWs for the WL, as well as on the analytic evaluation of the OPW overlap integrals are presented in [91, 92, 156].

A.2 RPA screening for inhomogeneous systems

We consider the screening of the Coulomb interaction in the random phase approximation. The retarded component of the longitudinal polarization reads

$$P^{\text{R}}(1, 2) = -i\hbar [G^{\text{R}}(1, 2)G^<(2, 1) + G^<(1, 2)G^{\text{A}}(2, 1)]. \quad (\text{A.12})$$

Using the Fourier expansion

$$P^{\text{R}}(1, 2) = \sum_{\mathbf{q}_1, \mathbf{q}_2} e^{i\mathbf{q}_1 \mathbf{r}_1 - i\mathbf{q}_2 \mathbf{r}_2} P_{\mathbf{q}_1, \mathbf{q}_2}^{\text{R}}(t_1, t_2) \quad (\text{A.13})$$

for the polarization function and a general eigenfunction expansion

$$G(1, 2) = \sum_{\alpha\beta} G_{\alpha\beta}(t_1, t_2) \varphi_{\alpha}(\mathbf{r}_1) \varphi_{\beta}^*(\mathbf{r}_2) \quad (\text{A.14})$$

for the GFs, we find

$$\begin{aligned}
P_{\mathbf{q}_1, \mathbf{q}_2}^{\text{R}}(t_1, t_2) = & -i\hbar \sum_{\alpha\beta\gamma\delta} \langle \delta | e^{-i\mathbf{q}_1 \mathbf{r}} | \alpha \rangle \langle \beta | e^{i\mathbf{q}_2 \mathbf{r}} | \gamma \rangle \\
& \times [G_{\alpha\beta}^{\text{R}}(t_1, t_2) G_{\gamma\delta}^<(t_2, t_1) + G_{\alpha\beta}^<(t_1, t_2) G_{\gamma\delta}^{\text{A}}(t_2, t_1)]. \quad (\text{A.15})
\end{aligned}$$

Using the GKBA (3.74) and constricting ourselves to retarded functions diagonal in the state and band indices, we find for $t_1 > t_2$

$$\begin{aligned}
G_{\alpha\beta}^<(t_1, t_2) &= i\hbar G_{\alpha\alpha}^r(t_1, t_2) G_{\alpha\beta}^<(t_2) \\
G_{\alpha\beta}^<(t_2, t_1) &= -i\hbar G_{\alpha\beta}^<(t_2) G_{\beta\beta}^a(t_2, t_1),
\end{aligned} \quad (\text{A.16})$$

Alternatively, the reverse GKBA (3.75) might be applied. Using this in Eq. (A.15) we find

$$P_{\mathbf{q}_1, \mathbf{q}_2}^R(t_1, t_2) = (i\hbar)^2 \left\{ \sum_{\alpha\gamma\delta} \langle \delta | e^{-i\mathbf{q}_1 \cdot \mathbf{r}} | \alpha \rangle \langle \alpha | e^{i\mathbf{q}_2 \cdot \mathbf{r}} | \gamma \rangle G_{\alpha\alpha}^R(t_1, t_2) G_{\gamma\delta}^<(t_2) G_{\delta\delta}^A(t_2, t_1) \right. \\ \left. - \sum_{\alpha\beta\delta} \langle \delta | e^{-i\mathbf{q}_1 \cdot \mathbf{r}} | \alpha \rangle \langle \beta | e^{i\mathbf{q}_2 \cdot \mathbf{r}} | \delta \rangle G_{\alpha\alpha}^R(t_1, t_2) G_{\alpha\beta}^<(t_2) G_{\delta\delta}^A(t_2, t_1) \right\}. \quad (\text{A.17})$$

If we furthermore consider only overlaps from states of the same band $\langle \delta | e^{-i\mathbf{q} \cdot \mathbf{r}_1} | \alpha \rangle \propto \delta_{\lambda_\delta, \lambda_\alpha}$ and disregard intra-band polarization terms $G_{\alpha\beta}^{cc, <}$, this reduces to

$$P_{\mathbf{q}_1, \mathbf{q}_2}^R(t_1, t_2) = \hbar^2 \sum_{\alpha\beta} \langle \alpha | e^{i\mathbf{q}_2 \cdot \mathbf{r}} | \beta \rangle \langle \beta | e^{-i\mathbf{q}_1 \cdot \mathbf{r}} | \alpha \rangle \\ \times [G_{\alpha\alpha}^R(t_1, t_2) G_{\alpha\alpha}^<(t_2) G_{\beta\beta}^A(t_2, t_1) - G_{\alpha\alpha}^R(t_1, t_2) G_{\beta\beta}^<(t_2) G_{\beta\beta}^A(t_2, t_1)]. \quad (\text{A.18})$$

To get the frequency dependence of the polarization function, lets assume that it only depends on the difference of the time arguments, $P_{\mathbf{q}_1, \mathbf{q}_2}^R(t_1, t_2) = P_{\mathbf{q}_1, \mathbf{q}_2}^R(t_1 - t_2)$. If we choose the retarded/advanced GFs to be *free* ones, equation (A.18) only depends on the relative time and we can perform a Fourier transformation that leads to

$$P_{\mathbf{q}_1, \mathbf{q}_2}^R(\omega) = \sum_{\alpha\beta} \langle \alpha | e^{i\mathbf{q}_2 \cdot \mathbf{r}} | \beta \rangle \langle \beta | e^{-i\mathbf{q}_1 \cdot \mathbf{r}} | \alpha \rangle (G_{\alpha\alpha}^< - G_{\beta\beta}^<) \int_0^\infty d\tau e^{\frac{i}{\hbar}(\hbar\omega - \varepsilon_\alpha + \varepsilon_\beta)\tau} \\ = i\hbar \sum_{\alpha\beta} \langle \alpha | e^{i\mathbf{q}_2 \cdot \mathbf{r}} | \beta \rangle \langle \beta | e^{-i\mathbf{q}_1 \cdot \mathbf{r}} | \alpha \rangle \frac{G_{\alpha\alpha}^< - G_{\beta\beta}^<}{\hbar\omega - \varepsilon_\alpha + \varepsilon_\beta + i\delta} \\ P_{\mathbf{q}_1, \mathbf{q}_2}^R = \sum_{\alpha\beta} \langle \alpha | e^{i\mathbf{q}_2 \cdot \mathbf{r}} | \beta \rangle \langle \beta | e^{-i\mathbf{q}_1 \cdot \mathbf{r}} | \alpha \rangle \frac{f_\alpha - f_\beta}{\varepsilon_\alpha - \varepsilon_\beta}. \quad (\text{A.19})$$

Here we have assumed that the population like GFs $G^<$ follow the time evolution adiabatically and in the last line we applied the static limit $\omega \rightarrow 0$. The screened interaction follows from

$$W_{\mathbf{q}_1, \mathbf{q}_2} = V_{\mathbf{q}_1} + \sum_{\mathbf{q}_3} V_{\mathbf{q}_1} P_{\mathbf{q}_1, \mathbf{q}_3} W_{\mathbf{q}_3, \mathbf{q}_2} \quad (\text{A.20})$$

whose solution involves a matrix inversion. In analogy to the bare Coulomb matrix elements (4.1), the screened ones are given by

$$W_{\alpha\beta\gamma\delta}^R = \sum_{\mathbf{q}_1 \mathbf{q}_2} W_{\mathbf{q}_1 \mathbf{q}_2}^R \langle \alpha | e^{-i\mathbf{q}_1 \cdot \mathbf{r}} | \delta \rangle \langle \beta | e^{+i\mathbf{q}_2 \cdot \mathbf{r}} | \gamma \rangle. \quad (\text{A.21})$$

Quantum dot - wetting layer system

In QD systems momentum conservation does not hold and therefore a polarization function depending on \mathbf{q}_1 and \mathbf{q}_2 is necessary. Unfortunately, the numerical evaluation of (A.20) with (A.19) is beyond resource limits of nowadays supercomputers. However, in the limit of large carrier densities a restriction to WL contributions is possible.

As for the WL momentum conservation ($\mathbf{q}_1 = \mathbf{q}_2$) is fulfilled, in the presence of QDs at least on average, equation (A.22) reduces to

$$P_{\mathbf{q}}^R = \sum_{\alpha\beta} |\langle \alpha | e^{i\mathbf{q}_2 \cdot \mathbf{r}} | \beta \rangle|^2 \frac{f_\alpha - f_\beta}{\varepsilon_\alpha - \varepsilon_\beta}. \quad (\text{A.22})$$

Correspondingly the screened interaction and the matrix elements follow from

$$W_{\mathbf{q}} = \frac{V_{\mathbf{q}}}{1 - P_{\mathbf{q}}^R V_{\mathbf{q}}} \quad (\text{A.23})$$

and

$$W_{\alpha\beta\gamma\delta}^R = \sum_{\mathbf{q}} W_{\mathbf{q}}^R \langle \alpha | e^{-i\mathbf{q} \cdot \mathbf{r}} | \delta \rangle \langle \beta | e^{+i\mathbf{q} \cdot \mathbf{r}} | \gamma \rangle. \quad (\text{A.24})$$

A.3 Dipole matrix elements

Envelope wave-function approach

In envelope wave-function approximation $\Psi_1(\mathbf{r}) = \phi_1(\mathbf{r}) \cdot u_1(\mathbf{r})$ with $\phi_1(\mathbf{r})$ being the envelope function and $u_1(\mathbf{r})$ being the Bloch function, the matrix element for the dipole interaction is given by

$$\begin{aligned} \langle 1 | d\mathbf{E} | 2 \rangle &= \sum_{\mathbf{q}} \sum_j \phi_1^*(\mathbf{R}_j) e^{i\mathbf{q} \cdot \mathbf{R}_j} \phi_2^*(\mathbf{R}_j) \mathbf{E}_{\mathbf{q}} \\ &\times \left[\int d^3r u_1^*(\mathbf{r}) e\mathbf{r} u_2(\mathbf{r}) + e\mathbf{R}_j \int d^3r u_1^*(\mathbf{r}) u_2(\mathbf{r}) \right] \end{aligned} \quad (\text{A.25})$$

$$= \sum_{\mathbf{q}} \langle 1 | e^{i\mathbf{q} \cdot \mathbf{r}} | 2 \rangle \tilde{\mathbf{d}}_{12} \mathbf{E}_{\mathbf{q}} \quad (\text{A.26})$$

$$= \sum_{\mathbf{q}} \mathbf{d}_{12}(\mathbf{q}) \mathbf{E}_{\mathbf{q}}. \quad (\text{A.27})$$

Here we made use of the dipole approximation $\mathbf{E}(\mathbf{r}) = \mathbf{E}(\mathbf{R}_j)$ where we exploited the fact that the electric field is almost constant within a unit cell. Hence the total integration

is split into a sum of integrations over unit cells. Furthermore a Fourier expansion of the electric field is performed.

Whereas the 2nd term in Eq. A.25 represents an intra-band contribution which is not considered in the following, the inter-band term determines the selection rules via the symmetry of the Bloch functions. As the Bloch functions for the conduction band have a s-like symmetry and those of the valence band p-like symmetry, the inter-band transition is non-zero whereas the intra-band transitions vanish. The overlap of the envelope functions additionally modifies the oscillator strength. Note, that due to the photon dispersion $\omega = c \cdot |q|$ basically the $|q| = 0$ term contributes.

Tight-binding approach for WL-WL transitions

To obtain the dipole matrix elements for the QD-WL transition, a similar approach as for the QD-WL overlaps can be used, by means of Bloch's theorem.

For the WL-WL transitions we have

$$\begin{aligned} \mathbf{d}_{\mathbf{k}\mathbf{k}'}^{cv} &= e_0 \int d^3r \psi^*(\mathbf{r}) \mathbf{r} \psi(\mathbf{r}) \\ &= \frac{1}{N} e_0 \sum_{R,R',\sigma,\tau} c_{\mathbf{k},\sigma}^{c*}(\mathbf{R}) \left(\int d^3r \phi_{\sigma,\mathbf{R}}^*(\mathbf{r}) \mathbf{r} \phi_{\tau,\mathbf{R}'}(\mathbf{r}) \right) c_{\mathbf{k}',\tau}^v(\mathbf{R}') . \end{aligned} \quad (\text{A.28})$$

As the simplest approximation we keep only the $\mathbf{R} = \mathbf{R}'$ contributions, this is possible because the atomic orbitals are localized at the atomic positions and orbitals at different atomic positions don't overlap.

$$\mathbf{d}_{\mathbf{k}\mathbf{k}'}^{cv} = \frac{1}{N} e_0 \sum_{R,\sigma,\tau} c_{\mathbf{k},\sigma}^{c*}(\mathbf{R}) \left(\int d^3r \phi_{\sigma}^*(\mathbf{r} - \mathbf{R}) \mathbf{r} \phi_{\tau}(\mathbf{r} - \mathbf{R}) \right) c_{\mathbf{k}',\tau}^v(\mathbf{R}) ,$$

because the atomic orbitals are the same at every atom position. We can introduce $\mathbf{r}' = \mathbf{r} - \mathbf{R}$ and split the integral into two contributions

$$\begin{aligned} \mathbf{d}_{\mathbf{k}\mathbf{k}'}^{cv} &= \frac{1}{N} e_0 \sum_{R,\sigma,\tau} c_{\mathbf{k},\sigma}^{c*}(\mathbf{R}) c_{\mathbf{k}',\tau}^v(\mathbf{R}) \left(\underbrace{\int d^3r' \phi_{\sigma}^*(\mathbf{r}') \mathbf{r}' \phi_{\tau}(\mathbf{r}')}_{\mathbf{d}_{\sigma,\tau}} + \phi_{\sigma}^*(\mathbf{r}') \mathbf{R} \phi_{\tau}(\mathbf{r}') \right) \\ &= \frac{1}{N} e_0 \sum_{R,\sigma,\tau} c_{\mathbf{k},\sigma}^{c*}(\mathbf{R}) c_{\mathbf{k}',\tau}^v(\mathbf{R}) \left(\mathbf{d}_{\sigma,\tau} + \mathbf{R} \int d^3r' \phi_{\sigma}^*(\mathbf{r}') \phi_{\tau}(\mathbf{r}') \right) \\ &= \frac{1}{N} e_0 \sum_{R,\sigma,\tau} c_{\mathbf{k},\sigma}^{c*}(\mathbf{R}) c_{\mathbf{k}',\tau}^v(\mathbf{R}) (\mathbf{d}_{\sigma,\tau} + \mathbf{R} \delta_{\sigma,\tau}) \end{aligned}$$

In the last step we used the orthonormality of the atomic orbitals. As in the calculation of the overlaps we can pull the WL coefficients back to the unit column by means of Bloch's theorem, and we find

$$\begin{aligned}
d_{kk'}^{cv} &= \frac{1}{N} e_0 \sum_{l=1}^2 \sum_{R_{||}, R_z, \sigma, \tau} c_{k,\sigma}^{c*}(\mathbf{f}_l + \mathbf{R}_z) c_{k',\tau}^v(\mathbf{f}_l + \mathbf{R}_z) e^{i(\mathbf{k}' - \mathbf{k})R_{||}} (\mathbf{d}_{\sigma,\tau} + \mathbf{R}\delta_{\sigma,\tau}) \\
&= \frac{1}{N} e_0 \sum_{l=1}^2 \left(\sum_{R_{||}, R_z, \sigma, \tau} c_{k,\sigma}^{c*}(\mathbf{f}_l + \mathbf{R}_z) c_{k',\tau}^v(\mathbf{f}_l + \mathbf{R}_z) \mathbf{d}_{\sigma,\tau} \delta_{k,k'} \right. \\
&\quad \left. + \sum_{R_z, \sigma} c_{k,\sigma}^{c*}(\mathbf{f}_l + \mathbf{R}_z) c_{k',\sigma}^v(\mathbf{f}_l + \mathbf{R}_z) \sum_{R_{||}} \mathbf{R} e^{i(\mathbf{k}' - \mathbf{k})R_{||}} \right)
\end{aligned} \tag{A.29}$$

While the first part can readily be evaluated upon knowledge of $\mathbf{d}_{\sigma,\tau}$, the second part remains more tricky. First let us mention that the "prefactor" consisting of the coefficients of the same atomic orbital for conduction and valence band states is supposed to be rather small, as the conduction band states are mainly composed of s-like states, whereas the valence band states should consist mainly of p-like states. However, this argument is by no means sufficient to disregard the term, as the sum $\sum_{R_{||}}$ seems to be divergent.

So let's have a closer look at

$$\sum_{R_{||}} (\mathbf{R}_z + \mathbf{f}_l + \mathbf{R}_{||}) e^{i(\mathbf{k}' - \mathbf{k})R_{||}}.$$

The first two terms just give a delta-function $\delta_{k,k'}$ and we can include it in the first term of Eq. (A.29). The remaining contribution

$$\sum_{R_{||}} \mathbf{R}_{||} e^{i(\mathbf{k}' - \mathbf{k})R_{||}}$$

can be written as a derivative of a delta-function $\nabla_{\mathbf{k}} \delta_{k,k'}$. Now we have to keep in mind, we always use the dipole matrix elements for the WL in an integration, e.g. in the Rabi-energy or in the calculation of the macroscopic polarization. This means we can integrate by parts and use the delta-function to do the integration. Now that we are rid of the divergence, we can come back to the fact that the prefactor (in terms of TB coefficients) of this term is small, so that we actually can disregard it.

In conclusion we find for the WL-WL dipole matrix elements

$$d_{kk'}^{cv} = e_0 \delta_{k,k'} \sum_{l=1}^2 \sum_{R_z, \sigma, \tau} c_{k,\sigma}^{c*}(\mathbf{f}_l + \mathbf{R}_z) c_{k',\tau}^v(\mathbf{f}_l + \mathbf{R}_z) (\mathbf{d}_{\sigma,\tau} + (\mathbf{f}_l + \mathbf{R}_z)\delta_{\sigma,\tau}), \tag{A.30}$$

in addition we of course have to specify the polarization vector of the exciting light. This can lead to further simplifications as we are only interested in $d_{kk'}^{cv} = \mathbf{p}d_{kk'}^{cv}$ for the given light field polarization (with polarization vector \mathbf{p}).

The quantity $d_{\sigma\tau}$ that we need to calculate the matrix elements can be obtained as follows: Assume that the assumption given above holds, namely that the conduction band states are mainly composed of s-like states, whereas the valence band states consist mainly of p-like states. Then we expect only two matrix elements of $d_{\sigma\tau}$ to be relevant: d_{s,p_x} and d_{s,p_y} . As they should behave more or less like αx and αy the common factor α can be fitted in a way that the result is consistent with the Kane-parameter of kp -calculations, alternatively the 16 numbers $d_{\sigma\tau}$ for a given polarization can be obtained directly, using the orthogonalized Slater orbitals [157].

B Parameters and numerics

B.1 Material parameters

parameter	units	In _{0.2} Ga _{0.8} As	InGaP	CdTe	InN
E_{gap}	eV	1.52	1.90	1.55	1.73
ε		12.5	11.8	10.6	8.4
ε_∞		10.9	9.35	7.4	-
m_e	m_0	0.067	0.092	0.09	-
m_h	m_0	0.15	0.33	0.8	-
$\hbar\omega_{\text{LO}}$	meV	36.0	46.0	21.0	90.0
α		0.06	0.08	0.31	0.5

Tab. B.1: Parameters for various material systems.

parameter	units	GaN	InN	In _{0.2} Ga _{0.8} N
E_{gap}	eV	3.438	0.756	2.677
ΔE_e	eV	-	-	0.457 ^a
ΔE_h	eV	-	-	0.304 ^a
ε		8.9	15.3	10.2
m_e	m_0	0.2	0.07	0.174
m_h	m_0	-	-	-
E_{piezo}	MV/cm	-0.5	-	+2.0
$\hbar\omega_{\text{LO}}$	meV	90.0	-	-
α		0.5	-	-

Parameters chosen similar to Ref. [91]

Tab. B.2: Parameters for the InGaN/GaN material system and the calculations in envelope-wavefunction approximation.

B.2 Wurtzite crystal structure

The wurtzite crystal structure can be constructed from two interpenetrating sub-lattices, forming a hexagonally close packed lattice whose conventional unit cell is shown in Fig. B.1a. Choosing the origin in the center of the bottom hexagon, the basis vectors of the are given by

$$\mathbf{a}_1 = \left(\frac{\sqrt{3}}{2}a, -\frac{1}{2}a, 0 \right) \quad \mathbf{a}_2 = (0, a, 0) \quad \mathbf{a}_3 = (0, 0, c) \quad (\text{B.1})$$

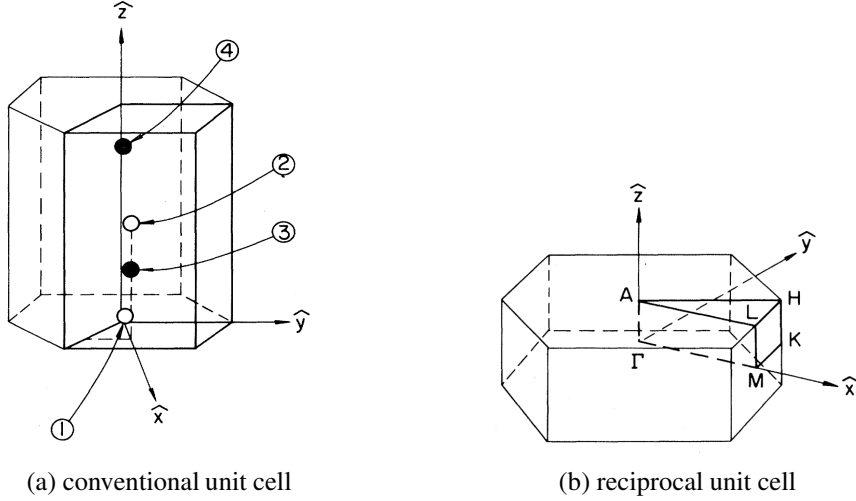


Fig. B.1: Conventional and reciprocal unit cell of the wurtzite lattice. Pictures taken from Ref. [205].

The unit cell of the wurtzite lattice contains four atoms located at

$$\mathbf{t}_1 = (0, 0, 0) \quad \mathbf{t}_2 = \left(\frac{a}{\sqrt{3}}, 0, \frac{c}{2} \right) \quad \mathbf{t}_3 = \left(\frac{a}{\sqrt{3}}, 0, \frac{c}{8} \right) \quad \mathbf{t}_4 = \left(0, 0, \frac{5c}{8} \right) \quad (\text{B.2})$$

where the anions are located at \mathbf{t}_1 , \mathbf{t}_2 and the cations are located at \mathbf{t}_3 , \mathbf{t}_4 . In z-direction, the lattice has a double-layer structure as shown in Fig. B.2b.

The reciprocal lattice also shows a hexagonal symmetry, rotated by 30 deg. with respect to the real space lattice, and is described by the basis

$$\mathbf{b}_1 = \frac{2\pi}{a} \left(\frac{2}{\sqrt{3}}, 0, 0 \right) \quad \mathbf{b}_2 = \frac{2\pi}{a} \left(\frac{1}{\sqrt{3}}, 1, 0 \right) \quad \mathbf{b}_3 = \frac{2\pi}{c} (0, 0, 1) . \quad (\text{B.3})$$

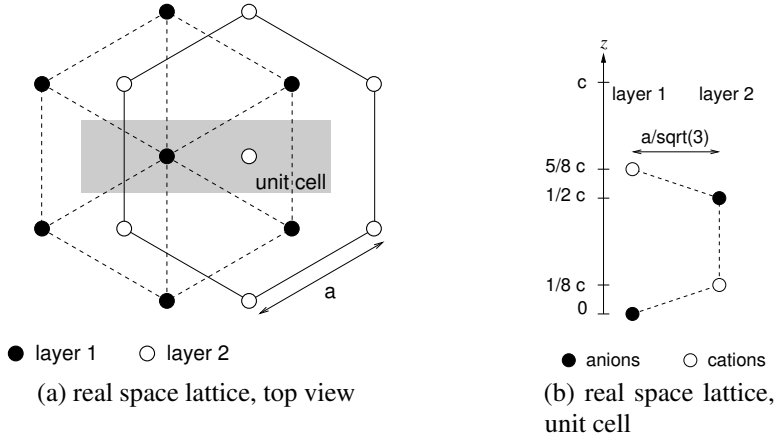


Fig. B.2: Hexagonal structure and unit cell of the real space wurtzite lattice.

The corresponding Brillouin zone (BZ) is shown in Fig. B.1b. The symmetry points in the plane of the middle hexagon of the BZ are given by

$$\Gamma = (0, 0, 0) \quad M = \frac{2\pi}{a} \left(\frac{1}{\sqrt{3}}, 0, 0 \right) \quad K = \frac{2\pi}{a} \left(\frac{1}{\sqrt{3}}, \frac{1}{3}, 0 \right) \quad (\text{B.4})$$

For the lattice constant $a=0.3189$ nm, the extension of the BZ in k_1 and k_2 direction is $|M|=11.38$ /nm and $|K|=13.14$ /nm. From the InGaAs material system, we can estimate that a cutoff at $k_{\max}=1.5$ /nm should be sufficient for convergent results.

B.3 KMS condition in the time domain

To evaluate the KMS relation (5.37) in the time domain we use Parseval's identity

$$f_\alpha = -2\pi \int_{-\infty}^{\infty} dt F(-t) \hat{G}_\alpha(t) . \quad (\text{B.5})$$

Since the Fourier transform of the Fermi-Dirac distribution $F(t)$ diverges we consider the Fourier transform of its derivative $h(w) = -\frac{\partial}{\partial \omega} F(\omega) e^{\eta\omega}$ with $\eta \rightarrow 0$. A direct evaluation of the Fourier integral on the one hand and partial integration on the other hand yields

$$h(t) = \frac{1}{2 \sinh(\pi \frac{t}{\hbar\beta})} = (it - \eta) e^{-i\frac{\mu}{\hbar}t} F(t) . \quad (\text{B.6})$$

Using Dirac's identity, the KMS condition in the time domain then reads

$$f_\alpha = \frac{1}{2} + 2 \operatorname{Im} \int_0^\infty \frac{h(t)}{t} G_\alpha^R(t) e^{\frac{i}{\hbar}\mu t} . \quad (\text{B.7})$$

The singularity at $t = 0$ is integrable and hence $\frac{h(t)}{t} G_\alpha^R(t) e^{\frac{i}{\hbar} ut} \Big|_{t=0} = -\frac{\epsilon_\alpha - \mu}{\pi\hbar}$.

B.4 Lifting the Coulomb singularity

The matrix elements $V_{\mathbf{k}\mathbf{k}'\mathbf{k}\mathbf{k}'}^{\lambda\lambda'}$ that are included in the Fock selfenergy contain the Coulomb singularity at $|\mathbf{q}| = 0$. To lift this singularity, we use a procedure that has been successfully implemented for the same problem in bulk materials and QWs for a long time [64]. Let us start by writing the integral that appears in the selfenergy as

$$\begin{aligned} \Sigma_k(t) &= i\hbar \int dk' d\varphi_k d\varphi_{k'} \\ &\times \sum_{\mathbf{q}} \frac{k'}{|\mathbf{q}_{||}|^2 + q_z^2} D_{\text{OPW}}(\mathbf{k}, \mathbf{q}, \mathbf{k}') \delta(\mathbf{q}_{||} + \mathbf{k}' - \mathbf{k}) \sum_{l=1}^2 e^{i\mathbf{q}_{||}\mathbf{f}_l} F_l(\mathbf{k}, \mathbf{k}', q_z) G_{k'}^<(t) \\ &= i\hbar \int dk' d\varphi_k d\varphi_{k'} V_{\mathbf{k},\mathbf{k}'} G_{k'}^<(t) \end{aligned} \quad (\text{B.8})$$

Now we add and subtract $G_k^<(t) \cdot \int dk' d\varphi_k d\varphi_{k'} V_{\mathbf{k},\mathbf{k}'} \alpha(k, k')$, with a convergence enforcing function $\alpha(k, k') = \frac{4k^4}{k^2 + k'^2}$. The result can be written as

$$\begin{aligned} \Sigma_k(t) &= i\hbar \left\{ \int dk' d\varphi_k d\varphi_{k'} V_{\mathbf{k},\mathbf{k}'} [G_{k'}^<(t) - \alpha(k, k') G_k^<(t)] \right. \\ &\quad \left. + G_k^<(t) \int dk' d\varphi_k d\varphi_{k'} V_{\mathbf{k},\mathbf{k}'} \alpha(k, k') \right\} \end{aligned} \quad (\text{B.9})$$

and upon discretization of the k' integral

$$\Sigma_k(t) = i\hbar \left[\sum_{j \neq i} \tilde{V}_{i,j} G_j^<(t) - G_i \sum_{j \neq i} \alpha_{i,j} \tilde{V}_{i,j} - \sum_m \alpha_{i,m} \tilde{V}_{i,m} \right], \quad (\text{B.10})$$

where we introduced $\tilde{V}_{k,k'} = \int d\varphi_k d\varphi_{k'} V_{\mathbf{k},\mathbf{k}'}$ and likewise for the discretized version.

B.5 Numerical methods

For the numerical implementation basically standard algorithms were utilized that are well documented e.g. in Refs. [202, 203]. In integrations either Gauss-Chebyshev (GTS) polynomials or the trapezian (TRAPEZ) rule are used. A summary of the utilized grids for discretization is given in Tab. B.3. In the calculations for nitride semiconductors involving

TB wave functions we had to restrict to much less grid points due to the available computer memory.

The kinetic equations for carrier scattering represent integro-differential equations and their numerical solution was performed using a multistep predictor-corrector method, namely the 3rd-order Adams-Bashforth-Moulton (ABM) algorithm. Convergent results were achieved using a discretization of the time axis of typically 1 fs. For matrix operations the LAPACK library [206] was used, especially the routine DGEEVX for the calculation of eigenvalues and eigenvectors was involved.

grid	interval	units	grid points	algorithm
envelope wave function approach				
$ \mathbf{k} $	$0 \dots a$	$1/\text{nm}$	128	TRAPEZ
ϕ_k	$0 \dots 2\pi$	-	60	GTS
$ \mathbf{q} $	$0 \dots 1.0$	$1/\text{nm}$	64	GTS
ϕ_q	$0 \dots 2\pi$	-	60	GTS
tight-binding wave function approach				
$ \mathbf{k} $	$0 \dots 1.5$	$1/\text{nm}$	31	TRAPEZ
ϕ_k	$0 \dots 2\pi$	-	25	TRAPEZ
$ \mathbf{q} $	$0 \dots 7.0$	$1/\text{nm}$	32	GTS
ϕ_q	$0 \dots 2\pi$	-	32	GTS
q_z	$-20 \dots +20$	$1/\text{nm}$	28	GTS

a corresponding to a pair energy of $\hbar^2 k_{\max}^2 / 2\mu = 12.25 \hbar\omega_{\text{LO}}$

Tab. B.3: Summary of discretization grids.

Bibliography

- [1] 45nm high-k+metal gate strain-enhanced transistors. *Intel Technology Journal*, **12**: 77, 2008.
- [2] N.S. Wingreen. Quantum many-body effects in a single-electron transistor. *Science*, **304**:1258, 2004.
- [3] L.P. Kouwenhoven, D.G. Austing, and S. Tarucha. Few-electron quantum dots. *Rep. Prog. Phys.*, **64**:701, 2001.
- [4] S. Kubatkin, A. Danilov, M. Hjort, J. Cornil, J.-L. Brédas, N. Stuhr-Hansen, P. Hedegårt, and T. Bjørnholm. Single-electron transistor of a single organic molecule with access to several redox states. *Nature*, **425**:698, 2003.
- [5] N.J. Tao. Electron transport in molecular junctions. *Nature Nanotechnology*, **1**:173, 2006.
- [6] A. Pecchia and A. Di Carlo. Atomistic theory of transport in organic and inorganic nanostructures. *Rep. Prog. Phys.*, **67**:1497, 2004.
- [7] R.M Westervelt. Graphene nanoelectronics. *Science*, **320**:324, 2008.
- [8] J. Wecker, R. Kinder, and R. Richter. Sandwiches mit riesigem Magnetwiderstand . *Physik in unserer Zeit*, **33**:210, 2002.
- [9] P. Bruno. Die Entdeckung des Riesen-Magnetowiderstandes. *Physik in unserer Zeit*, **38**:272, 2007.
- [10] S.A. Wolf, D.D. Awschalom, R.A. Buhrman, J.M. Daughton, S. von Molnár, M.L. Roukes, A.Y. Chtchelkova, and D.M. Treger. Spintronics: A spin-based electronics vision for the future. *Science*, **294**:1488, 2001.
- [11] P. Alivisatos. The use of nanocrystals in biological detection. *Nature Biotechnology*, **22**:47, 2004.
- [12] Energy savings estimates of light emitting diodes in niche lighting applications, 2008. URL http://www.netl.doe.gov/ssl/PDFs/nichefinalreport_october2008.pdf.

Bibliography

- [13] S.M. Reimann and M. Manninen. Electronic structure of quantum dots. *Rev. Mod. Phys.*, **74**:1283, 2002.
- [14] V.I. Klimov. Nanocrystal quantum dots - from fundamental photophysics to multi-color lasing. *Los Alamos Science*, **28**:214, 2003.
- [15] W. Seifert, N. Carlsson, M. Miller, M. Pistol, L. Samuelson, and L. Reine Wallenberg. In-situ growth of quantum dot structures by the Stranski-Krastanow growth mode. *Prog. Crystal Growth and Charact.*, **33**:423, 1996.
- [16] K. Jacobi. Atomic structure of InAs quantum dots on GaAs. *Progress in Surface Science*, **71**:185, 2003.
- [17] P.L. Gourley. Microstructured semiconductor lasers for high-speed information processing. *Nature*, **371**:571, 1994.
- [18] P. Michler, editor. *Single Quantum Dots - Fundamentals, Applications and New Concepts*. Springer-Verlag, Berlin, 2003.
- [19] J.J. Finley, P.W. Fry, A.D. Ashmore, A. Lemaître, A.I. Tartakovskii, R. Oulton, D.J. Mowbray, M.S. Skolnick, M. Hopkinson, P.D. Buckle, and P.A. Maksym. Observation of multicharged excitons and biexcitons in a single InGaAs quantum dot. *Phys. Rev. B*, **63**:161305, 2001.
- [20] N. Baer, P. Gartner, and F. Jahnke. Coulomb effects in semiconductor quantum dots. *Eur. Phys. J. B*, **42**:213, 2004.
- [21] G.J. Beirne, C. Hermannstädter, L. Wang, A. Rastelli, O.G. Schmidt, and P. Michler. Quantum light emission of two lateral tunnel-coupled (In,Ga)As/GaAs quantum dots controlled by a tunable static electric field. *Phys. Rev. Lett.*, **96**:137401, 2006.
- [22] G. Ortner, R. Oulton, H. Kurtze, M. Schwab, D. R. Yakovlev, M. Bayer, S. Fafard, Z. Wasilewski, and P. Hawrylak. Energy relaxation of electrons in InAs/GaAs quantum dot molecules. *Phys. Rev. B*, **72**:165353, 2005.
- [23] J.P. Reithmaier. Strong exciton-photon coupling in semiconductor quantum dot systems. *Semiconductor Science and Technology*, **23**:123001, 2008.
- [24] P. Michler, A. Kiraz, C. Becher, W.V. Schoenfeld, P.M. Petroff, Lidong Zhang, E. Hu, and A. Imamoğlu. A quantum dot single-photon turnstile device. *Science*, **290**:2282, 2000.
- [25] J.P. Reithmaier, E. Sèc, A. Löffler, C. Hofmann, S. Kuhn, S. Reitzenstein, L.V. Keldysh, V.D. Kulakovskii, T.L. Reinecke, and R. Forchel. Strong coupling in a single quantum-dot microcavity system. *Nature*, **432**:197, 2004.

- [26] P. Lodahl, A. Floris van Driel, A.S. Nikolaev, A. Irman, K. Overgaag, D. Vanmaekelbergh, and W.L. Vos. Controlling the dynamics of spontaneous emission from quantum dots by photonic crystals. *Nature*, **430**:654, 2004.
- [27] S. Anders, C.S. Kim, B. Klein, M.W. Keller, R.P. Mirin, and A.G. Norman. Bimodal size distribution of self-assembled $In_xGa_{1-x}As$ quantum dots. *Phys. Rev. B*, **66**:125309, 2002.
- [28] A. Wojs, P. Hawrylak, S. Fafard, and L. Jacak. Electronic structure and magneto-optics of self-assembled quantum dots. *Phys. Rev. B*, **54**:5604, 1996.
- [29] C. Cohen-Tannoudji, B. Diu, and F. Laloe. *Quantum mechanics - Volume One*. Wiley, Paris, 1977.
- [30] T.B. Bahder. Eight-band $\mathbf{k} \cdot \mathbf{p}$ model of strained zinc-blende crystals. *Phys. Rev. B*, **41**:11992, 1990.
- [31] C. Pryor, M.E. Pistol, and L. Samuelson. Electronic structure of strained InP/Ga_{0.51}In_{0.49}P quantum dots. *Phys. Rev. B*, **56**:10404, 1997.
- [32] S. Schulz, S. Schumacher, and G. Czycholl. Tight-binding model for semiconductor quantum dots with a wurtzite crystal structure: From one-particle properties to Coulomb correlations and optical spectra. *Phys. Rev. B*, **73**:245327, 2006.
- [33] S. Schulz. *Electronic and Optical Properties of Quantum Dots: A Tight-Binding Approach*. PhD thesis, Universität Bremen, 2007.
- [34] J. Shah. *Ultrafast Spectroscopy of Semiconductors and Semiconductor Nanostructures*. Springer-Verlag, Berlin, 1999.
- [35] S. Hayashi, H. Sanda, M. Agata, and K. Yamamoto. Resonant raman scattering from ZnTe microcrystals: Evidence for quantum size effects. *Phys. Rev. B*, **40**:5544, 1989.
- [36] Shang-Fen Ren, Deyu Lu, and G. Qin. Phonon modes in InAs quantum dots. *Phys. Rev. B*, **63**:195315, 2001.
- [37] V.A. Fonoferov and A.A. Balandin. Interface and confined optical phonons in wurtzite nanocrystals. *Phys. Rev. B*, **70**:233205, 2004.
- [38] P. Giannozzi, S. de Gironcoli, P. Pavone, and S. Baroni. Ab initio calculation of phonon dispersions in semiconductors. *Phys. Rev. B*, **43**:7231, 1991.
- [39] M. Betz, G. Göger, A. Leitenstorfer, K. Ortner, C.R. Becker, G. Böhm, and A. Laubereau. Ultrafast electron-phonon scattering in semiconductors studied by nondegenerate four-wave mixing. *Phys. Rev. B*, **60**:R11265, 1999.

Bibliography

- [40] J. Urayama, T.B. Norris, J. Singh, and P. Bhattacharya. Observation of phonon bottleneck in quantum dot electronic relaxation. *Phys. Rev. Lett.*, **86**:4930, 2001.
- [41] J. Urayama, T.B. Norris, H. Jiang, J. Singh, and P. Bhattacharya. Differential transmission measurement of phonon bottleneck in self-assembled quantum dot intersubband relaxation. *Physica B*, **316-317**:74, 2002.
- [42] T.S. Sosnowski, T.B. Norris, H. Jiang, J. Singh, K. Kamath, and P. Bhattacharya. Rapid carrier relaxation in $\text{In}_{0.4}\text{Ga}_{0.6}\text{As}/\text{GaAs}$ quantum dots characterized by differential transmission spectroscopy. *Phys. Rev. B*, **57**:R9423, 1998.
- [43] M. Wesseli, C. Ruppert, S. Trumm, H. J. Krenner, J.J. Finley, and M. Betz. Nonequilibrium carrier dynamics in self-assembled InGaAs quantum dots. *phys. stat. sol. (b)*, **243**:2217, 2006.
- [44] H. Htoon, D. Kulik, O. Baklenov, A.L. Holmes, T. Takagahara, and C. K. Shih. Carrier relaxation and quantum decoherence of excited states in self-assembled quantum dots. *Phys. Rev. B*, **63**:241303, 2001.
- [45] P. Borri, W. Langbein, S. Schneider, U. Woggon, R.L. Sellin, D. Ouyang, and D. Bimberg. Ultralong dephasing time in InGaAs quantum dots. *Phys. Rev. Lett.*, **87**:157401, 2001.
- [46] P. Borri, W. Langbein, S. Schneider, U. Woggon, R.L. Sellin, D. Ouyang, and D. Bimberg. Relaxation and dephasing of multiexcitons in semiconductor quantum dots. *Phys. Rev. Lett.*, **89**:187401, 2002.
- [47] F. Widmann, J. Simon, B. Daudin, G. Feuillet, J.L. Rouvière, N.T. Pelekanos, and G. Fishman. Blue-light emission from GaN self-assembled quantum dots due to giant piezoelectric effect. *Phys. Rev. B*, **58**:R15989, 1998.
- [48] R. Cingolani, A. Botchkarev, H. Tang, H. Morkoç, G. Traetta, G. Coli, M. Lomascolo, A. Di Carlo, F. Della Sala, and P. Lugli. Spontaneous polarization and piezoelectric field in $\text{GaN}/\text{Al}_{0.15}\text{Ga}_{0.85}\text{N}$ quantum wells: Impact on the optical spectra. *Phys. Rev. B*, **61**:2711, 2000.
- [49] V.A. Fonooberov and A.A. Balandin. Excitonic properties of strained wurtzite and zinc-blende $\text{GaN}/\text{Al}_x\text{Ga}_{1-x}\text{N}$ quantum dots. *J. Appl. Phys.*, **94**:7178, 2003.
- [50] R.P. Feynman. The theory of positrons. *Phys. Rev.*, **76**:749, 1949.
- [51] R.P. Feynman. Space-time approach to quantum electrodynamics. *Phys. Rev.*, **76**:769, 1949.
- [52] R.P. Feynman. Mathematical formulation of the quantum theory of electromagnetic interaction. *Phys. Rev.*, **80**:440, 1950.

- [53] L.V. Keldysh. Diagram technique for nonequilibrium processes. *Sov.Phys. JETP*, **20**:1018, 1965.
- [54] G. Baym and L.P. Kadanoff. Conservation laws and correlation functions. *Phys. Rev.*, **124**:287, 1961.
- [55] L. Hedin. New method for calculating the one-particle Green's function with application to the electron gas problem. *Phys. Rev.*, **139**:A796, 1965.
- [56] R. van Leeuwen, N.E. Dahlen, and A. Stan. Total energies from variational functionals of the Green function and the renormalized four-point vertex. *Phys. Rev. B*, **74**:195105, 2006.
- [57] H. Haug and S. Schmitt-Rink. Electron theory of the optical properties of laser-excited semiconductors. *Progress in Quant. Electron.*, **9**:3, 1984.
- [58] H. Haug. The 1984 electron theory of the optical properties of laser-excited semiconductors revisited. What happened since? *Progress in Quant. Electron.*, **29**:261, 2005.
- [59] Y. Meir and N.S. Wingreen. Landauer formula for the current through an interacting electron region. *Phys. Rev. Lett.*, **68**:2512, 1992.
- [60] A.-P. Jauho, N.S. Wingreen, and Y. Meir. Time-dependent transport in interacting an noninteracting resonant-tunneling systems. *Phys. Rev. B*, **50**:5528, 1994.
- [61] W. Schäfer and M. Wegener. *Semiconductor Optics and Transport Phenomena*. Springer-Verlag, Berlin, 1. edition, 2002.
- [62] G. Czycholl. *Theoretische Festkörperphysik*. Vieweg Verlag, Braunschweig, 2000.
- [63] G.C. Wick. The evaluation of the collision matrix. *Phys. Rev.*, **80**:268, 1950.
- [64] H. Haug and S.W. Koch. *Quantum Theory of the Optical and Electronic Properties of Semiconductors*. World Scientific Publ., Singapore, 3. edition, 1994.
- [65] J. Fricke. Transport equations including many-particle correlations for an arbitrary quantum system: A general formalism. *Ann. Phys.*, **252**:479, 1996.
- [66] J. Fricke. Improved transport equations including correlations for electron-phonon systems: Comparison with exact solutions in one dimension. *Ann. Phys.*, **253**:177, 1997.
- [67] N. Baer, C. Gies, J. Wiersig, and F. Jahnke. Luminescence of a semiconductor quantum dot system. *Eur. Phys. J. B*, **50**:411, 2006.

Bibliography

- [68] C. Gies. *Theory for Light-Matter Interaction in Semiconductor Quantum Dots*. PhD thesis, Universität Bremen, 2008.
- [69] V.M. Axt and A. Stahl. A dynamics-controlled truncation scheme for the hierarchy of density matrices in semiconductor optics. *Z. Phys. B*, **93**:195, 1994.
- [70] V.M. Axt and A. Stahl. The role of the biexciton in a dynamic density matrix theory of the semiconductor band edge. *Z. Phys. B*, **93**:205, 1994.
- [71] M. Buck. *Theoretische Beschreibung kohärenter optischer Nichtlinearitäten in Halbleiter-Quantenfilmen*. PhD thesis, Universität Bremen, 2004.
- [72] M. Buck, L. Wischmeier, S. Schumacher, G. Czycholl, F. Jahnke, T. Voss, I. Rückmann, and J. Gutowski. Light-polarization and intensity dependence of higher-order nonlinearities in excitonic FWM signals. *Eur. Phys. J. B*, **42**:175, 2004.
- [73] N.H. Kwong and R. Binder. Green's function approach to the dynamics-controlled truncation formalism: Derivation of the $\chi^{(3)}$ equations of motion. *Phys. Rev. B*, **61**:8341, 2000.
- [74] W. Schäfer, R. Löwenich, N. Fromer, and D.S. Chemla. Formation and decay of coherent four-particle correlations in semiconductors: A Green's function theory. *phys. stat. sol. (b)*, **221**:195, 2000.
- [75] P. Danielewicz. Quantum theory of nonequilibrium processes. *Ann. Phys.*, **152**:239, 1984.
- [76] D.F. DuBois. *Lectures in Theoretical Physics - Kinetic theory*, volume 9C, chapter „Nonequilibrium quantum statistical mechanics of plasmas and radiation“, pages 469–620. Gordon and Breach, New York, 1966.
- [77] R. Binder and S.W. Koch. Nonequilibrium semiconductor dynamics. *Progress in Quant. Electron.*, **19**(4/5), 1995.
- [78] J. Rammer and H. Smith. Quantum field-theoretical methods in transport theory of metals. *Rev. Mod. Phys.*, **58**:323, 1986.
- [79] H. Haug and A.-P. Jauho. *Quantum Kinetics in Transport & Optics of Semiconductors*. Springer-Verlag, Berlin, 1. edition, 1996.
- [80] R. van Leeuwen. First-principles approach to the electron-phonon interaction. *Phys. Rev. B*, **69**:115110, 2004.
- [81] D. Semkat, D. Kremp, and M. Bonitz. Kadanoff-Baym equations with initial correlations. *Phys. Rev. E*, **59**:1557, 1999.

- [82] D. Semkat, M. Bonitz, and D. Kremp. Relaxation of a quantum many-body system from a correlated initial state. a general and consistent approach. *Contrib. Plasma Phys.*, **43**:321, 2003.
- [83] P. Gartner, L. Bányai, and H. Haug. Two-time electron-LO-phonon quantum kinetics and the generalized Kadanoff-Baym approximation. *Phys. Rev. B*, **60**:14234, 1999.
- [84] P. Lipavský, V. Špička, and B. Velický. Generalized Kadanoff-Baym ansatz for deriving quantum transport equations. *Phys. Rev. B*, **34**:6933, 1986.
- [85] V. Špička, B. Velický, and A. Kalvová. Long and short time quantum dynamics: I. Between Green's functions and transport equations. *Physica E*, **29**:154, 2005.
- [86] V. Špička, B. Velický, and A. Kalvová. Long and short time quantum dynamics: II. Kinetic regime. *Physica E*, **29**:175, 2005.
- [87] V. Špička, B. Velický, and A. Kalvová. Long and short time quantum dynamics: III. Transients. *Physica E*, **29**:196, 2005.
- [88] B. Velický, A. Kalvová, and V. Špička. Between Green's functions and transport equations: Reconstruction theorems and the role of initial conditions. *J. Phys.: Conf. Series*, **35**:1, 2006.
- [89] B. Velický, A. Kalvová, and V. Špička. Quasiparticle states of electron systems out of equilibrium. *Phys. Rev. B*, **75**:195125, 2007.
- [90] P. Gartner, L. Bányai, and H. Haug. Coulomb screening in the two-time Keldysh-Green-function formalism. *Phys. Rev. B*, **62**:7116, 2000.
- [91] T.R. Nielsen, P. Gartner, M. Lorke, J. Seebbeck, and F. Jahnke. Coulomb scattering in nitride based self-assembled quantum-dot systems. *Phys. Rev. B*, **72**:235311, 2005.
- [92] T.R. Nielsen. *Carrier-carrier and carrier-phonon scattering in self-assembled quantum dots*. PhD thesis, Universitt Bremen, 2005.
- [93] K. El Sayed, S. Schuster, H. Haug, G. Herzl, and K. Henneberger. Subpicosecond plasmon response: Buildup of screening. *Phys. Rev. B*, **49**:7337, 1994.
- [94] Q.T. Vu and H. Haug. Time-dependent screening of the carrier-phonon and carrier-carrier interactions in nonequilibrium systems. *Phys. Rev. B*, **62**:7179, 2000.
- [95] H. Haug. Coulomb quantum kinetics for semiconductor femtosecond spectroscopy. *phys. stat. sol. (b)*, **221**:179, 2000.
- [96] H. Haug and A.-P. Jauho. *Quantum Kinetics in Transport & Optics of Semiconductors*. Springer-Verlag, Berlin, 2. edition, 2008.

Bibliography

- [97] G.D. Mahan. *Many-Particle Physics*. Plenum Press, New York, 1990.
- [98] G. Baym. Field-theoretic approach to the properties of the solid state. *Ann. Phys.*, **14**:1, 1961.
- [99] T. Högberg. Green's function formalism for an anharmonic metal. *phys. stat. sol. (b)*, **35**:659, 1969.
- [100] R.K. Wehner. Phonon Green functions by functional methods. *phys. stat. sol. (b)*, **22**:527, 1967.
- [101] G. Baym. Self-consistent approximations in many-body systems. *Phys. Rev.*, **127**:1391, 1962.
- [102] G. Baym. Thermodynamic Green's function methods in neutron scattering by crystals. *Phys. Rev.*, **121**:741, 1961.
- [103] K. Henneberger and V. May. Nonequilibrium Green's functions and kinetic equations for highly excited semiconductors: I. General considerations. *Physica A*, **138**:537, 1986.
- [104] K. Henneberger, G. Manzke, V. May, and R. Zimmermann. Nonequilibrium Green's functions and kinetic equations for highly excited semiconductors: II. Application to the study of nonlinear optical and transport properties of the many-exciton system. *Physica A*, **138**:557, 1986.
- [105] K. Henneberger. Resonant laser excitation and electron-hole kinetics of a semiconductor: I. Nonequilibrium Green's function treatment and fundamental equations. *Physica A*, **150**:419, 1988.
- [106] K. Henneberger and K.H. Kühn. Resonant laser excitation and electron-hole kinetics of a semiconductor: II. Nonlinear particle transport and field propagation. *Physica A*, **150**:439, 1988.
- [107] K. Henneberger and H. Haug. Nonlinear optics and transport in laser-excited semiconductors. *Phys. Rev. B*, **38**:9759, 1988.
- [108] H. Haug. Nonequilibrium many-body theory of optical nonlinearities of semiconductors. *J. Lumin.*, **30**:171, 1985.
- [109] W. Schäfer and J. Treusch. An approach to the nonequilibrium theory of highly excited semiconductors. *Z. Phys. B*, **63**:407, 1986.
- [110] W. Schäfer, R. Binder, and K. H. Schuldt. The influence of dynamical correlations in semiconductor plasmas on optical spectra. *Z. Phys. B*, **70**:145, 1988.

- [111] K. El Sayed, L. Bányai, and H. Haug. Coulomb quantum kinetics and optical dephasing on the femtosecond time scale. *Phys. Rev. B*, **50**:1541, 1994.
- [112] L. Bányai, Q.T. Vu, B. Mieck, and H. Haug. Ultrafast quantum kinetics of time-dependent RPA-screened Coulomb scattering. *Phys. Rev. Lett.*, **81**:882, 1998.
- [113] Q.T. Vu, L. Bányai, H. Haug, F.X. Camescasse, J.-P. Likforman, and A. Alexandrou. Screened Coulomb quantum kinetics for resonant femtosecond spectroscopy in semiconductors. *Phys. Rev. B*, **59**:2760, 1999.
- [114] Q.T. Vu, H. Haug, W.A. Hügel, S. Chatterjee, and M. Wegener. Signature of electron-plasmon quantum kinetics in GaAs. *Phys. Rev. Lett.*, **85**:3508, 2000.
- [115] L. Bányai, E. Reitsamer, D.B. Tran Thoai, and H. Haug. Quantum kinetics of femtosecond four-wave mixing in semiconductors. *J. Opt. Soc. Am. B*, **13**:1278, 1996.
- [116] L. Bányai, Q.T. Vu, and H. Haug. Excitation induced dephasing in four-wave mixing and Coulomb quantum kinetics. *Phys. Rev. B*, **58**:R13341, 1998.
- [117] H. Haug. Interband quantum kinetics with LO-phonon scattering in a laser-pulse-excited semiconductor: I. theory. *phys. stat. sol. (b)*, **173**:139, 1992.
- [118] L. Bányai, D.B. Tran Thoai, C. Remling, and H. Haug. Interband quantum kinetics with LO-phonon scattering in a laser-pulse-excited semiconductor: II. numerical studies. *phys. stat. sol. (b)*, **173**:149, 1992.
- [119] L. Bányai and H. Haug. Improved spectral functions for quantum kinetics. *Solid State Comm.*, **100**:303, 1996.
- [120] L. Bányai, P. Gartner, and H. Haug. Self-consistent RPA retarded polaron Green function for quantum kinetics. *Eur. Phys. J. B*, **1**:209, 1998.
- [121] P. Gartner, L. Bányai, and H. Haug. Self-consistent RPA for the intermediate-coupling polaron. *Phys. Rev. B*, **66**:75205, 2002.
- [122] H. Fröhlich. Electrons in lattice fields. *Adv. Phys.*, **3**:325, 1954.
- [123] R.P. Feynman. Slow electrons in a polar crystal. *Phys. Rev.*, **97**:660, 1955.
- [124] T.K. Mitra, A. Chatterjee, and S. Mukhopadhyay. Polarons. *Phys. Rep.*, **153**:91, 1987.
- [125] L. Mathey, D.W. Wang, W. Hofstetter, M.D. Lukin, and E. Demler. Luttinger liquid of polarons in one-dimensional boson-fermion mixtures. *Phys. Rev. Lett.*, **93**:120404, 2004.

Bibliography

- [126] M. Bruderer, A. Klein, S.R. Clark, and D. Jaksch. Polaron physics in optical lattices. *Phys. Rev. A*, **76**:11605, 2007.
- [127] M. Bruderer, A. Klein, S.R. Clark, and D. Jaksch. Transport of strong-coupling polarons in optical lattices. *New Journal of Physics*, **10**:33015, 2008.
- [128] F. Reininghaus, T. Korb, and H. Schoeller. Fingerprints of the magnetic polaron in nonequilibrium electron transport through a quantum wire coupled to a ferromagnetic spin chain. *Phys. Rev. Lett.*, **97**:26803, 2006.
- [129] W. Nolting. *Grundkurs Theoretische Physik 7: Viel-Teilchen-Theorie*. Springer-Verlag, Berlin, 5 edition, 2002.
- [130] T. Stauber, R. Zimmermann, and H. Castella. Electron-phonon interaction in quantum dots: A solvable model. *Phys. Rev. B*, **62**:7336, 2000.
- [131] T. Stauber and R. Zimmermann. Optical absorption in quantum dots: Coupling to longitudinal optical phonons treated exactly. *Phys. Rev. B*, **73**:115303, 2006.
- [132] T. Inoshita and H. Sakaki. Density of states and phonon-induced relaxation of electrons in semiconductor quantum dots. *Phys. Rev. B*, **56**:R4355, 1997.
- [133] E.A. Muljarov, T. Takagahara, and R. Zimmermann. Phonon-induced exciton dephasing in quantum dot molecules. *Phys. Rev. Lett.*, **95**:177405, 2005.
- [134] M. Hohenadler and P.B. Littlewood. Quantum monte carlo results for bipolaron stability in quantum dots. *Phys. Rev. Lett.*, **76**:155122, 2007.
- [135] Y. Wan, G. Ortiz, and P. Phillips. Origin of pair-tunneling states in semiconductor quantum dots. *Phys. Rev. B*, **55**:5313, 1997.
- [136] A.V. Uskov, A.-P. Jauho, B. Tromborg, J. Mørk, and R. Lang. Dephasing times in quantum dots due to elastic LO phonon-carrier collisions. *Phys. Rev. Lett.*, **85**:1516, 2000. see also comment by Muljarov/Zimmermann PRL **96**, 19703 (2006).
- [137] E.A. Muljarov and R. Zimmermann. Exciton dephasing in quantum dots due to LO-phonon coupling: An exactly solvable model. *Phys. Rev. Lett.*, **98**:187401, 2007.
- [138] E.A. Muljarov and R. Zimmermann. Dephasing in quantum dots: Quadratic coupling to acoustic phonons. *Phys. Rev. Lett.*, **93**:237401, 2004.
- [139] B. Krummheuer, V.M. Axt, T. Kuhn, I. D'Amico, and F. Rossi. Pure dephasing and phonon dynamics in GaAs- and GaN-based quantum dot structures: Interplay between material parameters and geometry. *Phys. Rev. B*, **71**:235329, 2005.
- [140] N. Baer. *Optical and electronic properties of InGaAs and nitride quantum dots*. PhD thesis, Universität Bremen, 2006.

- [141] W. Nolting. *Grundkurs Theoretische Physik 5: Quantenmechanik - Methoden und Anwendungen*. Vieweg Verlag, Braunschweig, 3 edition, 1997.
- [142] H. Benisty. Reduced electron-phonon relaxation rates in quantum-box systems: Theoretical analysis. *Phys. Rev. B*, **51**:13281, 1995.
- [143] Xin-Qi Li and Yasuhiko Arakawa. Anharmonic decay of confined optical phonons in quantum dots. *Phys. Rev. B*, **57**:12285, 1998.
- [144] Xin-Qi Li, Hajime Nakayama, and Yasuhiko Arakawa. Phonon bottleneck in quantum dots: Role of lifetime of the confined optical phonons. *Phys. Rev. B*, **59**:5069, 1999.
- [145] T. Inoshita and H. Sakaki. Electron relaxation in a quantum dot: Significance of multiphonon processes. *Phys. Rev. B*, **46**:7260, 1992.
- [146] J. Seebeck, T.R. Nielsen, P. Gartner, and F. Jahnke. Polarons in semiconductor quantum dots and their role in the quantum kinetics of carrier relaxation. *Phys. Rev. B*, **71**:125327, 2005.
- [147] K. Král and Z. Khás. Electron self-energy in quantum dots. *Phys. Rev. B*, **57**:R2061, 1998.
- [148] M. Nedjalkov, I. Dimov, and H. Haug. Numerical studies of the markovian limit of the quantum kinetics with phonon scattering. *phys. stat. sol. (b)*, **209**:109, 1998.
- [149] H. Haug and S.W. Koch. *Quantum Theory of the Optical and Electronic Properties of Semiconductors*. World Scientific Publ., Singapore, 4. edition, 2004.
- [150] M. Betz, G. Göger, A. Laubereau, P. Gartner, L. Bányai, H. Haug, K. Ortner, C.R. Becker, and A. Leitenstorfer. Subthreshold carrier-LO phonon dynamics in semiconductors with intermediate polaron coupling: A purely quantum kinetic relaxation channel. *Phys. Rev. Lett.*, **86**:4684, 2001.
- [151] F. R. Gantmacher. *The theory of matrices*. AMS Chelsea Publishing, Providence, Rhode Island, 2000.
- [152] J.N. Franklin. *Matrix Theory*. Prentice-Hall, 1968.
- [153] K. Král, P. Zdeněk, and Z. Khás. Ultrafast carrier dynamics of resonantly excited InAs/GaAs self-assembled quantum dots. *Physica E*, **20**:290, 2004.
- [154] K. Král and P. Zdeněk. Stationary-state electronic distribution in quantum dots. *Physica E*, **29**:341, 2005.

Bibliography

- [155] A.V. Maleev, I.V. Ignatiev, I.Y. Gerlovin, I.E. Kozin, and Y. Masumoto. Temperature behavior of hot carrier dynamics in InP quantum dots. *Phys. Rev. B*, **71**:195323, 2005.
- [156] T.R. Nielsen, P. Gartner, and F. Jahnke. Many-body theory of carrier capture and relaxation in semiconductor quantum-dot lasers. *Phys. Rev. B*, **69**:235314, 2004.
- [157] N. Baer, S. Schulz, P. Gartner, S. Schumacher, G. Czycholl, and F. Jahnke. Influence of symmetry and Coulomb correlation effects on the optical properties of nitride quantum dots. *Phys. Rev. B*, **76**:75310, 2007.
- [158] Q.T. Vu, H. Haug, O. D. Mücke, M. Wegener, T. Tritschler, G. Khitrova, and H.M. Gibbs. Light-induced gaps in semiconductor band-to-band transitions. *Phys. Rev. Lett.*, **92**:217403, 2004.
- [159] Q.T. Vu, H. Haug, and S.W. Koch. Relaxation and dephasing quantum kinetics for a quantum dot in an optically excited quantum well. *Phys. Rev. B*, **73**:205317, 2006.
- [160] P. Borri, W. Langbein, S. Schneider, U. Woggon, R.L. Sellin, D. Ouyang, and D. Bimberg. Rabi oscillations in the excitonic ground-state transition of InGaAs quantum dots. *Phys. Rev. B*, **66**:81306, 2002.
- [161] J. Förstner, C. Weber, J. Danckwerts, and A. Knorr. Phonon-assisted damping of Rabi oscillations in semiconductor quantum dots. *Phys. Rev. Lett.*, **91**:127401, 2003.
- [162] K. Hennessy, A. Badolatu, M. Winger, D. Gerace, M. Atatüre, S. Gulde, S. Fält, E.L. Hu, and A. Imamoğlu. Quantum nature of a strongly coupled single quantum dot cavity system. *Nature*, **445**:896, 2007.
- [163] P. Michler, A. Imamoğlu, M.D. Mason, P.J. Carson, G.F. Strouse, and S.K. Buratto. Quantum correlation among photons from a single quantum dot at room temperature. *Nature*, **406**:968, 2000.
- [164] S.M. Ulrich, C. Gies, S. Ates, J. Wiersig, S. Reitzenstein, C. Hofmann, A. Löffler, A. Forchel, F. Jahnke, and P. Michler. Photon statistics of semiconductor microcavity lasers. *Phys. Rev. Lett.*, **98**:43906, 2007.
- [165] C. Gies, J. Wiersig, M. Lorke, and F. Jahnke. Semiconductor model for quantum-dot-based microcavity lasers. *Phys. Rev. A*, **75**:13803, 2007.
- [166] T. Schmielau. *Optische und Ein-Teilchen-Eigenschaften von Halbleitern*. PhD thesis, Universität Rostock, 2001.
- [167] M. Lorke. *Optical gain and laser properties of semiconductor quantum dot systems*. PhD thesis, Universität Bremen, 2008.

- [168] M. Lorke, T.R. Nielsen, J. Seebeck, P. Gartner, and F. Jahnke. Influence of carrier-carrier and carrier-phonon correlations on optical absorption and gain in quantum-dot systems. *Phys. Rev. B*, **73**:85324, 2006.
- [169] M. Lorke, F. Jahnke, and W.W. Chow. Anomaly in the excitation dependence of the optical gain of semiconductor quantum dots. *Phys. Rev. B*, **74**:35334, 2006.
- [170] M. Lorke, F. Jahnke, and W.W. Chow. Excitation dependence of gain and carrier induced refractive index changes in quantum dots. *Appl. Phys. Lett.*, **90**:51112, 2007.
- [171] W. Hoyer, M. Kira, and S.W. Koch. Influence of Coulomb and phonon interaction on the exciton formation dynamics in semiconductor heterostructures. *Phys. Rev. B*, **67**:155113, 2003.
- [172] W. Hoyer. *Quantentheorie zu Exzitonbildung und Photolumineszenz in Halbleitern*. PhD thesis, Philipps-University of Marburg, 2002.
- [173] G.J. Beirne, M. Reischle, R. Roßbach, W. Schulz, M. Jetter, J. Seebeck, P. Gartner, C. Gies, F. Jahnke, and P. Michler. Electronic shell structure and carrier dynamics of high aspect ratio InP single quantum dots. *Phys. Rev. B*, **75**:195302, 2007.
- [174] S. Nakamura. The roles of structural imperfections in InGaN-based blue light-emitting diodes and laser diodes. *Science*, **281**:956, 1998.
- [175] S.C. Jain, M. Willander, and J. Narayan. III-nitrides: Growth, characterization, and properties. *J. Appl. Phys.*, **87**:965, 2000.
- [176] S. Nakamura and S.F. Chichibu, editors. *Introduction to nitride semiconductor blue lasers and light emitting diodes*. CRC Press, 2000.
- [177] H. Kalt and M. Hetterich, editors. *Optics of semiconductors and their nanostructures*. Springer, Berlin, 2004.
- [178] J. Piprek, editor. *Nitride semiconductor devices - principles and simulation*. Wiley-VCH, 2007.
- [179] I. Vurgaftman and J.R. Meyer. Band parameters for nitrogen-containing semiconductors. *J. Appl. Phys.*, **94**:3675, 2003.
- [180] D.J. As and K. Lischka. Heteroepitaxy of doped and undoped cubic group III-nitrides. *phys. stat. sol. (a)*, **176**:475, 1999.
- [181] W.W. Chow and S.W. Koch. *Semiconductor-Laser Fundamentals*. Springer-Verlag, Berlin, 1. edition, 1999.

Bibliography

- [182] P. Lawaetz. Stability of the wurtzite structure. *Phys. Rev. B*, **5**:4039, 1972.
- [183] F. Bernardini and V. Fiorentini. Polarization fields in nitride nanostructures: 10 points to think about. *Appl. Surface Science*, **166**:23, 2000.
- [184] V. Fiorentini, F. Bernardini, and O. Ambacher. Evidence for nonlinear macroscopic polarization in III–V nitride alloy heterostructures. *Appl. Phys. Lett.*, **80**:1204, 2002.
- [185] D.A.B. Miller, D.S. Chemla, T.C. Damen, A.C. Gossard, W. Wiegmann, T.H. Wood, and C.A. Burrus. Band-edge electroabsorption in quantum well structures: The quantum-confined stark effect. *Phys. Rev. Lett.*, **53**:2173, 1984.
- [186] V. Fiorentini, F. Bernardini, F. Della Sala, A. Di Carlo, and P. Lugli. Effects of macroscopic polarization in III-V nitride multiple quantum wells. *Phys. Rev. B*, **60**:8849, 1999.
- [187] P. Waltereit, O. Brandt, A. Trampert, H.T. Grahn, J. Menniger, M. Ramsteiner, M. Reiche, and K.H. Ploog. Nitride semiconductors free of electrostatic fields for efficient white light-emitting diodes. *Nature*, **406**:865, 2000.
- [188] M.C. Schmidt, K.C. Kim, R.M. Farrell, D.F. Feezell, D.A. Cohen, M. Saito, K. Fujito, J.S. Speck, S.P. DenBaars, and S. Nakamura. Demonstration of nonpolar *m*-plane InGaN/GaN laser diodes. *Japanese Journal of applied Physics*, **46**:190, 2007.
- [189] H. Teisseyre, T. Suski, S.P. Łepowski, S. Anceau, P. Perlin, P. Lefebvre, L. Kończewicz, H. Hirayama, and Y. Aoyagi. Determination of built-in electric fields in quaternary InAlGaN heterostructures. *Appl. Phys. Lett.*, **82**:1541, 2003.
- [190] O. Marquardt, D. Mourad, S. Schulz, T. Hickel, G. Czycholl, and J. Neugebauer. A comparison of atomistic and continuum theoretical approaches to determine electronic properties of GaN/AlN quantum dots. *Phys. Rev. B*, **78**:235302, 2008.
- [191] F. Bernardini and V. Fiorentini. Macroscopic polarization and band offsets at nitride heterojunctions. *Phys. Rev. B*, **57**:R9427, 1998.
- [192] T.R. Nielsen, J. Seebeck, M. Lorke, P. Gartner, and F. Jahnke. Microscopic theory of carrier-carrier scattering in nitride based quantum-dot systems. *phys. stat. sol. (c)*, **3**:2038, 2006.
- [193] F. Bernardini, V. Fiorentini, and D. Vanderbilt. Polarization-based calculation of the dielectric tensor of polar crystals. *Phys. Rev. Lett.*, **79**:3958, 1997.
- [194] S. De Rinaldis, I. D'Amico, and F. Rossi. Intrinsic electric field effects on few-particle interactions in coupled GaN quantum dots. *Phys. Rev. B*, **69**:235316, 2004.

- [195] F.D. Sala, A. Di Carlo, P. Lugli, F. Bernardini, V. Fiorentini, R. Scholz, and J.-M. Jancu. Free-carrier screening of polarization fields in wurtzite GaN/InGaN laser structures. *Appl. Phys. Lett.*, **74**:2002, 1999.
- [196] T. Saito and Y. Arakawa. Electronic structure of piezoelectric $\text{In}_{0.2}\text{Ga}_{0.8}\text{N}$ quantum dots in GaN calculated using a tight-binding method. *Physica E*, **15**:169, 2002.
- [197] S. Schulz, S. Schumacher, and G. Czycholl. Spin-orbit coupling and crystal-field splitting in the electronic and optical properties of nitride quantum dots with a wurtzite crystal structure. *Eur. Phys. J. B*, **64**:51, 2008.
- [198] S. Schulz and G. Czycholl. Tight-binding model for semiconductor nanostructures. *Phys. Rev. B*, **72**:165317, 2005.
- [199] H. Dierks and G. Czycholl. Tight-binding calculations of the subband structures of zincblende-semiconductor [001] quantum wells. *Z. Phys. B*, **99**:207, 1996.
- [200] H. Dierks and G. Czycholl. Tight-binding calculation of linear excitonic absorption spectra of single quantum wells. *Journal of Crystal Growth*, **184**:877, 1998.
- [201] S. Schulz, S. Schumacher, and G. Czycholl. Semiconductor nanocrystals and embedded quantum dots: Electronic and optical properties. *phys. stat. sol. (b)*, **244**:2399, 2007.
- [202] W.H. Press, S.A. Teukolsky, and W.T. Vetterling. *Numerical recipes in FORTRAN* 77. University Press, Cambridge, 2nd edition, 1992.
- [203] W.H. Press, S.A. Teukolsky, W.T. Vetterling, and B.P. Flannery. *Numerical recipes in FORTRAN 90*. University Press, Cambridge, 2nd edition, 1996.
- [204] P. Hawrylak. Excitonic artificial atoms: Engineering optical properties of quantum dots. *Phys. Rev. B*, **60**:5597, 1999.
- [205] A. Kobayashi, O.F. Sankey, S.M. Volz, and J.D. Dow. Semiempirical tight-binding band structures of wurtzite semiconductors: AlN, CdS, CdSe, ZnS, and ZnO. *Phys. Rev. B*, **28**:935, 1983.
- [206] E. Anderson, Z. Bai, C. Bischof, S. Blackford, J. Demmel, J. Dongarra, J. Du Croz, A. Greenbaum, S. Hammarling, A. McKenney, and D. Sorensen. *LAPACK Users' Guide*. Society for Industrial and Applied Mathematics, third edition, 1999. URL <http://www.netlib.org/lapack/>.

Publications

Papers

- *Carrier-carrier and carrier-phonon scattering in the low-density and low-temperature regime for resonantly pumped semiconductor quantum dots*
J. Seebeck, M. Lorke, P. Gartner, and F. Jahnke,
phys. stat. sol (c) accepted for publication (2008)
(Conference paper NOEKS9)
- *Electronic shell structure and carrier dynamics of high aspect ratio InP single quantum dots*
G.J. Beirne, M. Reischle, R. Roßbach, W.M. Schulz, M. Jetter, J. Seebeck, P. Gartner, C. Gies, F. Jahnke, and P. Michler
Phys. Rev. B **75**, 195302 (2007)
- *Relaxation properties of the quantum kinetics of carrier-LO-phonon interaction in quantum wells and quantum dots*
P. Gartner, J. Seebeck, and F. Jahnke,
Phys. Rev. B **73**, 115307 (2006)
- *Influence of carrier-carrier and electron-phonon correlations on optical absorption and gain in quantum-dot systems*
M. Lorke, T.R. Nielsen, J. Seebeck, P. Gartner, and F. Jahnke,
Phys. Rev. B **73**, 85324 (2006)
- *Quantum kinetic theory of phonon-assisted carrier transitions in nitride-based quantum-dot systems*
J. Seebeck, T.R. Nielsen, P. Gartner, and F. Jahnke,
Eur. Phys. J. B **49**, 167 (2006)
- *Quantum kinetic theory of phonon-assisted carrier transitions in nitride-based quantum-dot systems*

J. Seebeck, T.R. Nielsen, M. Lorke, P. Gartner, and F. Jahnke,
phys. stat. sol (c) **3**, 2030 (2006)
(Conference paper ICNS6)

- *Microscopic theory of carrier-carrier scattering in nitride-based quantum-dot systems*
T.R. Nielsen, J. Seebeck, M. Lorke, P. Gartner, and F. Jahnke,
phys. stat. sol (c) **3**, 2038 (2006)
(Conference paper ICNS6)
- *Coulomb scattering in nitride-based self-assembled quantum dot systems*
T.R. Nielsen, P. Gartner, M. Lorke, J. Seebeck, and F. Jahnke,
Phys. Rev. B **72**, 235311 (2005)
- *Polarons in semiconductor quantum dots and their role in the quantum kinetics of carrier relaxation*
J. Seebeck, T.R. Nielsen, P. Gartner, and F. Jahnke,
Phys. Rev. B **71**, 125327 (2005)

Conference Contributions

(presenting author is indicated)

- *Theory for optical spectra of nitride quantum-dot systems* (talk),
J. Seebeck, M. Lorke, P. Gartner, S. Schulz, G. Czycholl and F. Jahnke,
IWN 2008, Montreux, Switzerland
- *The phonon bottleneck revisited at low temperatures* (poster),
J. Seebeck, P. Gartner, and F. Jahnke,
NOEKS9 2008, Klink, Germany
- *The phonon bottleneck revisited at low temperatures* (talk),
J. Seebeck, P. Gartner, and F. Jahnke,
DPG Frühjahrstagung 2008, Berlin, Germany
- *Quantum kinetics of polarons in semiconductor quantum dots* (talk),
J. Seebeck, P. Gartner, and F. Jahnke,
DPG Frühjahrstagung 2007, Regensburg, Germany

- *Quantum kinetics of polarons in semiconductor quantum dots* (talk),
J. Sebeck, P. Gartner, and F. Jahnke,
DPG Frühjahrstagung 2006, Dresden, Germany
- *Quantum kinetic description of LO-phonon relaxation of carriers in quantum wells and quantum dots* (talk),
P. Gartner, J. Sebeck, and F. Jahnke
NOEKS 2006, Münster, Germany
- *Quantum kinetic theory of phonon-assisted carrier transitions in nitride based quantum-dot systems* (talk),
J. Sebeck, T.R. Nielsen, M. Lorke, P. Gartner, and F. Jahnke,
ICNS6 2005, Bremen, Germany
- *Optical absorption in semiconductor quantum-dot systems* (poster),
M. Lorke, T.R. Nielsen, J. Sebeck, P. Gartner, and F. Jahnke
Progress in nonequilibrium Greens functions 2005, Kiel, Germany
- *Quantum kinetic effects in the optical properties of semiconductor quantum dots* (invited talk),
F. Jahnke, P. Gartner, M. Lorke, T.R. Nielsen, J. Sebeck
Progress in nonequilibrium Greens functions 2005, Kiel, Germany
- *Quantum kinetics of phonon-assisted carrier transitions in semiconductor quantum dots* (talk),
J. Sebeck, T.R. Nielsen, P. Gartner, and F. Jahnke,
CLEO/QELS 2005, Baltimore, USA
- *Quantum kinetics of polarons in semiconductor quantum dots* (talk),
J. Sebeck, T.R. Nielsen, P. Gartner, and F. Jahnke,
DPG Frühjahrstagung 2005, Berlin, Germany
- *Quantum kinetics of phonon-assisted carrier transitions in semiconductor quantum dots* (poster),
F. Jahnke, J. Sebeck, T.R. Nielsen, P. Gartner
ICPS 2004, Flagstaff, USA

Acknowledgments

I am grateful for the great support I have received from my supervisor Prof. Frank Jahnke. On the scientific as well as on the personal level it was a pleasure to work with him. Furthermore he made it possible to join many interesting international conferences and meet lot of interesting people.

For the pleasant and inspiring atmosphere, in addition to Prof. Frank Jahnke all other members of the semiconductor theory group are gratefully acknowledged. I thank Dr. Paul Gartner who always provided a quick answer to almost any question. The collaborations with Michael Lorke, Torben Nielsen, Christopher Gies and Stefan Schulz on different projects have been very fruitful. Stefan Schulz is also acknowledged for our exhausting training sessions in the Bremer Bürgerpark and some nice running competitions. I am also indebted to Hannes Kurtze for providing the experimental pump-probe spectra and inspiring discussions. The trip to New York after the CLEO/QELS conference in Baltimore together with Stefan Schumacher was really impressing. Furthermore, Dr. Jan Wiersig, Dr. Frithjof Anders, Sandra Ritter, Julia Unterhinninghofen, Norman Baer, Michael Buck, and Kolja Schuh also acknowledged for fruitful private discussions.

I also thank Klaus Bowe and Andreas Beuthner, who did a great job keeping our servers and computer clusters running, as well as our secretary Carmen Niemeyer-Zander.

Finally my parents and all of my friends are acknowledged for simply being there.